TECHNISCHE UNIVERSITÄT DARMSTADT

Time-Dependent Influence of Calcium Hydroxide, Alkali Hydroxides, and Sulfates on Pozzolanic Metakaolin Reactions: Experimental Investigations and Stoichiometric Modeling

Department of Civil and Environmental Engineering
Technical University of Darmstadt

Submitted in Fulfilment of the Requirements for the Degree of Dr.-Ing.

Kira Weise

Darmstadt 2024

Supervision: Prof. Dr. ir. Eduardus Koenders
Co-Supervision: Prof. Dr.-Ing. Thomas Matschei

Time-Dependent Influence of Calcium Hydroxide, Alkali Hydroxides, and Sulfates on Pozzolanic Metakaolin Reactions: Experimental Investigations and Stoichiometric Modeling

Author: Kira Weise
Dissertation (Location, Institution): Darmstadt, Technical University of Darmstadt
Date of Exam: 23.02.2024
Year of Publishing in TUprints: 2024

Acknowledgements

“Gratitude is the memory of the heart.” (citation from Jean Baptiste Massieu) and when I look back at the last years working on this thesis at the Institute of Construction and Building Materials, I feel great joy and thankfulness. I would like to acknowledge all those who have accompanied me along this way enriching my work through their personal and professional support.

First of all, I thank Prof. Dr. ir. Eduardus Koenders for his supervision of my thesis. I extremely appreciate that you have always supported me in my professional development and personal growth. Thank you very much for your trust and the freedom to contribute my own ideas throughout my work at your institute.

Additionally, I would like to thank my dear colleagues. The pleasant working environment at the institute is not only professionally enriching, but has also led to personal friendships.

My particular gratitude is addressed to Dr. Neven Ukrainczyk for his professional support along my PhD work. I especially enjoyed our intensive scientific discussions, that have highly enriched this thesis. Your outstanding personality is characterized by your comprehensive expertise, your intense interest in wide ranging research topics and your collaborative character. You are a unique enrichment for the whole institute.

I would especially like to thank Felix Berger, Conrad Ballschmiede and Sha Yang particularly for enriching our working life. Thank you very much for taking me out of intense scientific thoughts by regular coffee breaks and conversations about professional and private issues. This gratitude is additionally addressed to Aysen Cevik. You own an outstanding role at our institute that you enrich with your selfless, amiable and caring nature. Without exception, you help and support everyone at the institute and you take an honest interest in others' needs. Aysen, you significantly contribute to the positive atmosphere in our working environment.

Regarding your great support in my laboratory work, I specifically thank my dear colleges Yvette Schales and Helga Janning together with my student assistants, in particular Luca Marei Endell und Katharina Herrmann. Thank you very much for your great support during the realization of my experimental program as well as our technical conversations. Luciano Sambataro, I appreciate your Matlab assistance especially for the evaluation of the SEM/EDX data.

Dr. Frank Röser and Dr. Adrian Zimmermann, I would like to thank you for hiring me as a student assistant during my studies and for introducing me to the working environment at the Institute of Construction and Building Materials. My experiences in this time contributed significantly to my decision of starting the enriching path of a PhD after finishing my studies.

Last, but not least, my further thank is addressed with all my heart to my family and friends. Thank you very much for always being at my side, understanding and supporting me in all matters and loving me the way I am. My deepest gratitude goes to my parents for their unconditional love and support throughout my life. Thank you so much.

Abstract

The use of mortar and concrete is indispensable for civil engineering construction, but the cement production is highly energy intensive and causes vast CO_2-emissions. In this context, supplementary cementitious materials (SCMs) are one promising way of reducing the clinker content in cements leading to a more environmentally friendly binder material. In the last years, calcined clays have shown a great potential for the use as SCMs due to their large worldwide availability and lower CO_2-emissions compared to cement clinker. Their beneficial performance in binder systems is mainly driven by the pozzolanic reaction of metakaolin (MK), meaning the ability to react with calcium hydroxide (CH).

The pozzolanic MK reactions are influenced by several factors arising from the specific binder system. This research thesis mainly focusses on the CH availability, as well as the presence of alkali hydroxides and sulfates. The main aim is to understand in detail these influences und model pozzolanic MK reactions encompassing both short-term kinetics and long-term transformation processes.

The overall research concept comprises an extensive literature review, constituting the foundation of this thesis, two methodology studies addressing major challenges related to the analysis of the specific paste samples together with one article, discussing the major experimental results. Additionally, this work is complemented by a simplified stoichiometric and kinetic modeling of MK-CH systems.

For the experimental program, paste samples consisting of MK, CH, water, alkali hydroxides (KOH and NaOH) and/or sulfates (K_2SO_4 and Na_2SO_4) were prepared with two different MK/CH weight ratios of 0.33 and 1.0. Short-term analysis employed inductively coupled plasma optical emission spectrometry (ICP-OES), and pH measurements for pore solution as well as isothermal calorimetry, and in-situ X-ray diffraction (XRD) on selected paste samples. Long-term investigations up to 245 days with a reaction temperature of 40 °C include (quantitative) XRD, thermogravimetric (TGA) and scanning electron microscopy coupled with energy-dispersive X-ray spectroscopy (SEM/EDX). Especially for the high MK/CH ratio of 1.0, novel findings were generated, i.e. the potential formation of alkaline aluminosilicates and hindered pozzolanic MK reactions for the highest OH^-/CH weight ratio of 0.0307 as well as the deceleration of pozzolanic reactions with the incorporation of sulfates. Additionally, sulfates were detected in Si-rich hydrogarnet phases.

Experimental findings together with results from literature were used to characterize pozzolanic reaction products and stoichiometric equations, that were used for the development of a fundamental kinetic and stoichiometric reaction model. For the pozzolanic MK reaction, two separate reaction processes are identified forming C_4AH_{13} and C_2ASH_8. The reaction kinetics are determined by a reaction peak fitting of heat flow curves serving as input parameters in the developed model. The model allows to predict the phase assemblage of MK-CH systems over time validated with experimental results from thermogravimetric analysis (TGA), XRD and helium pycnometry (solid volume). With the help of the proposed model, the temperature dependency of the pozzolanic metakaolin reactions is analyzed, revealing an activation energy for the main (C_2ASH_8) pozzolanic reaction of 84 kJ/mol in the temperature range of 20 to 40 °C. The main model limitations are the fixed C-A-S-H and hydrogarnet compositions, that are discussed based on scanning electron microscopy along with energy-dispersive X-ray spectroscopy (SEM/EDX).

The experimental study provides a deeper understanding regarding the influences of CH availability, alkali hydroxides and sulfates on pozzolanic MK reactions, whereas the developed modeling approach covers the main reaction processes in these systems. This research thesis serves as a fundamental basis for further model extensions, e.g. the incorporation of sulfates and/or carbonates, and is supposed to find its use in the design of novel “low-carbon” binders in the future.

Table of Contents

1 Introduction

1.1 Research Background

The construction industry currently faces various challenges related to global warming and raw material shortages. One important aspect in this context are the high CO_2-emissions caused by the cement production that accounts for 4.5 % (2021) of the anthropogenic greenhouse gas emissions worldwide [1]. Additionally, the cement industry is the third-largest energy consumer globally with a total of 7 % (2018) of the industrial energy used [2]. This is particularly concerning, especially in consideration of a predicted further growth of cement production of approx. 12 - 23 % by 2050 (from 2018) [2]. Several efforts are taking place to account for a more environmentally friendly binder material [3]. A promising way in this context is to partially replace the clinker in the cements by alternative materials with a better CO_2 footprint [2, 4–6]. Among others, metakaolin and/or calcined clays in general have emerged as highly intriguing supplementary cementitious materials (SCMs) [7–9].

Mixed calcined clays benefit from a large availability worldwide [10] as well as lower calcination temperatures [7, 11, 12] and CO_2-emissions compared to cement clinker [13, 14]. The greatest challenge regarding the use of calcined clays as SCMs are large local variations in the compositions that influence the materials' reactivity and the overall performance in cementitious systems [7, 9, 11, 12, 15–18]. Even though all components of the mixed calcined clays play a role in the materials' performance [19, 20], metakaolin is the most reactive part and its amount mainly determines the calcined clay reactivity [7, 12, 16, 21].

Metakaolin (MK) refers to the clay mineral kaolinite that is calcined at temperatures of typically around 700 °C in laboratory scale [22–25] and up to approx. 850 °C in industrial calcination [26]. The dehydroxylation that takes place during the calcination process results in a structural disorder of metakaolin [24, 27–29] and is responsible for its highly pozzolanic reactivity [27–32], meaning the ability to react with calcium hydroxide (CH).

The advantageous performance of MK incorporated in cementitious systems is mainly due to its pozzolanic reactivity leading to the formation of additional hydration products [33–38]. "Optimum" replacement ratios of around 10 wt.-% to 15 wt.-% of cement by metakaolin were found, leading to the best results, e.g. regarding the compressive strengths and pore structure refinement in concrete and/or mortar [39–42]. Furthermore, the materials' durability can be enhanced, e.g. due to the consumption of CH that improves the sulfate resistance [43, 44] and a pore structure refinement that leads to lower water absorption rates [45, 46], an increased resistance against chloride penetration [41] as well as a delayed carbonation depths [46]. As established for cementitious systems, the materials' characteristics are mostly investigated up to 28 days [37, 47–49] and literature about long-term properties of metakaolin incorporated cement-based binders and/or its pozzolanic reactions is rare.

As cementitious systems represent a very complex surrounding with various influencing factors, the analysis of a materials' reactivity in more simplified and precisely controlled environments is a reasonable approach to fundamentally understand the respective reaction processes [49].

MK reacts with CH mainly forming calcium aluminate silicate hydrates (C-A-S-H) [27, 50–61] and C_2ASH_8 (stratlingite) [27, 50, 51, 53, 54, 56, 59, 61–67], whereas the formations of C_4AH_{13} [51, 53, 54, 57, 65, 66, 68–71] and hydrogarnet phases [51, 53, 54, 56, 65, 68, 69, 72] are controversially discussed in literature. The overall phase assemblage is influenced by several factors, like e.g. the metakaolin to calcium hydroxide weight ratio (MK/CH) [65, 73–75], secondary activators such as alkali hydroxides and sulfates [53, 62, 74–76], the reaction time [64] and temperature [69]. As C_4AH_{13} and C_2ASH_8 are thermodynamically unstable especially in the presence of CH [77], transformation reactions to more stable hydrogarnet phases may occur under certain conditions [53, 69, 75, 78]. Based on an extensive literature study [79], these processes were found to mainly occur for MK/CH values in the range of 0.3

to 0.6 [65, 68, 79], taking place in the long-term especially with excess supply of CH [69, 80, 81]. As these transformation reactions can negatively effect the materials' properties, like e.g. its durability, understanding the fundamental processes is of particular relevance. The novelty of this thesis lies in the systematically, time-depending and quantitative investigation of the pozzolanic metakaolin reactions including transformation processes and addressing the influence of CH availability, alkali hydroxides and sulfates.

Based on the findings in the simplified surrounding, this phenomenon could also be relevant in more complex (e.g. cementitious) systems. To quote an example, a significant decrease of the compressive strength from 28 to 90 days in metakaolin incorporated mortar was investigated with replacement ratios of 10 wt.-% and 15 wt.-% [39]. The reduction of compressive strengths in the long-term with excess supply of water (water to binder ratio of 0.6 compared to 0.4 of 0.5 [39]) and CH might be an indicator of transformation processes of metastable pozzolanic metakaolin reaction products to more phases, addressed in this work. The cited study [39] serves as an example revealing the relevance of the present research work indicating that the gained key fundamental findings might play a role in more complex surroundings.

The main aim of this research study is to understand in detail the time-dependent effects of CH availability, alkali hydroxides and sulfates on pozzolanic MK reactions and to model the main reaction processes in the short- and long-term by additionally accounting for phase transformations. Knowledge about the phase assemblage of metakaolin-modified systems is needed for the design of novel "low-carbon" binders in the future. The developed reaction model of this thesis is generic by purpose with the possibility of further transfers to more complex, e.g. cementitious systems, but it is not limited to that application.

1.2 Research Synthesis

The present work addresses the following two **research hypotheses**:

1. The availability of calcium hydroxide as well as the addition of alkali hydroxides and sulfates influence pozzolanic metakaolin reactions. The reaction kinetics and the phases assemblage of metakaolin-calcium hydroxide systems can experimentally be determined by isothermal calorimetry, thermogravimetric analysis (TGA), X-ray diffraction (XRD) and scanning electron microscopy coupled with energy-dispersive X-ray spectroscopy (SEM/EDX).
2. It is possible to estimate the phases assemblage in a system of metakaolin and calcium hydroxide by a simplified stoichiometric reaction model that accounts for pozzolanic reactions as well as phase transformations. By calibrating the pozzolanic reaction kinetics with short-term calorimetry measurements it allows to predict the long-term phases assemblage.

To verify these two hypotheses, the overall research work, including five publications, was designed according to the structure schematically shown in Figure 1.

In a first step, an extensive literature review was carried out regarding the hydrate phases formations in metakaolin-calcium hydroxide systems addressing the effect of alkali hydroxides, sulfates and carbonates. The review work in publication 1 (P1) [79] was needed to systematically study existing literature and to identify research gaps in this field. The formation of calcium aluminate silicate hydrates (C-A-S-H) and stratlingite (C_2ASH_8) was found as the main pozzolanic reaction, whereas the formation of C_4AH_{13} is controversially discussed. The excess supply of CH was identified as a relevant factor that determines transformation reactions from metastable to more stable phases and a range of the initially MK/CH weight ratio between 0.3 and 0.6 was found to favor these processes. The addition of alkali sulfates and/or carbonates lead to additional and/or different reaction products, whereas alkali hydroxides turned out to mainly effect the reaction kinetics. P1 constitutes section 2 of this thesis and builds a fundamental basis for the design of the experimental setup for the following work (Figure 1).

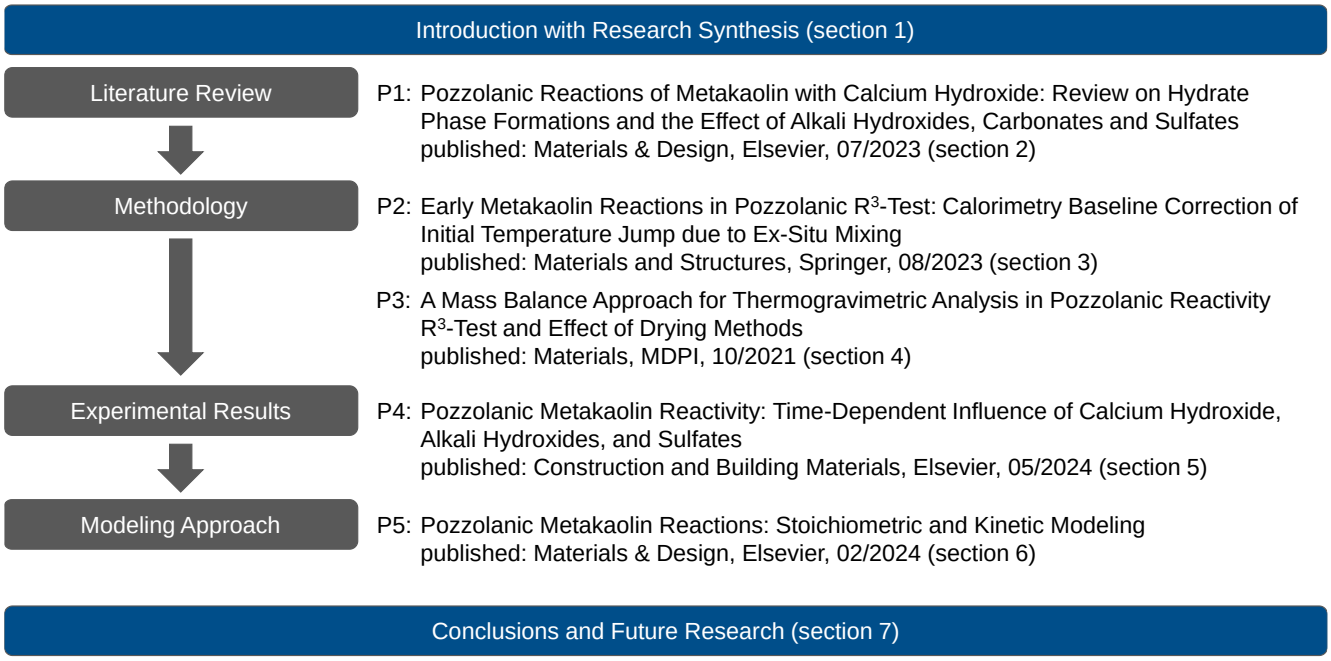

Figure 1: Structure of the present thesis highlighting the synthesis of the included publications.

Based on the literature review in P1, the experimental setup for this thesis was designed. A well-defined and controlled environment was selected that enables to separately analyze the respective factors on metakaolin-calcium hydroxide reactions. Paste samples consisting of metakaolin (MK), calcium hydroxide (CH) and water together with alkali hydroxides (KOH and NaOH) and sulfates (K_2SO_4 and Na_2SO_4) were prepared. To analyze the evolution of the phase assemblage over time, a drying procedure was applied to stop the hydration at specific reaction times up to 245 days [82]. Short-term analysis employed inductively coupled plasma optical emission spectrometry (ICP-OES), and pH measurements for pore solution as well as isothermal calorimetry, and in situ X-ray diffraction (XRD) on selected paste samples. Long-term investigations up to 245 days with a reaction temperature of 40 °C include (quantitative) XRD, thermogravimetric (TGA) and scanning electron microscopy coupled with energy-dispersive X-ray spectroscopy (SEM/EDX). Section 1.3 gives a comprehensive overview of the experimental studies of this thesis together with the microanalysis techniques applied.

For calorimetry testing, the elevated temperature of 40 °C together with in-situ mixing fails due to the lack of a proper paste homogenization. In this context, a novel isothermal calorimetric methodology was proposed in publication 2 (P2) [83] that accounts for early detection of reactivity responses with a user-friendly ex-situ mixing procedure. Knowledge about the very early reaction processes is important for the selective analysis of the individual peaks, especially for the highly reactive material (MK) used in this thesis in combination with alkali sulfates (rapid formation of ettringite). For the evaluation of TGA measurements, established normalization and calculation methods are known for cementitious systems, but they cannot be directly transferred to pastes comprising a large amount of calcium hydroxide as precursor material. To address this issue, a mass balance approach for the evaluation of TGA data was introduced in publication 3 (P3) [84]. P2 and P3 mainly address methodology aspects, needed for the further experimental work, building up sections 3 and 4 of the present thesis (Figure 1).

Publication 4 (P4), constituting section 5 of this thesis, provides systematical experimental investigations of the time-dependent influence of the CH availability as well as the presence of alkali hydroxides and sulfates on pozzolanic MK reactions. Two different initial MK/CH weight ratios of 0.33 and 1.0 were studied, clearly demonstrating and quantitatively describing long-term transformations from metastable C_2ASH_8 and C_4AH_{13} to more stable hydrogarnet phases with excess supply of CH (MK/CH = 0.33). The incorporation of alkali hydroxides and sulfates mainly show novel results for the higher MK/CH ratio of

1.0, namely a favored alkaline aluminosilicate formation with high OH^-/CH weight ratios (0.0307) and a slowing down of pozzolanic reactions with the incorporation of sulfates.
All of the above described studies are of special relevance for publication 5 (P5). It introduces a simplified stoichiometric and kinetic model for pozzolanic metakaolin reactions. The stoichiometric equations for the respective reactions were determined based on the literature review (P1) together with in-situ XRD measurements to enhance the understanding of short-term pozzolanic reaction products, whereas a fixed composition of the calcium aluminate silicate hydrates (C-A-S-H) was assumed. The reaction equations for the transformations of C_4AH_{13} and stratlingite to hydrogarnet were defined, the C-A-S-H composition of the products formed in these reactions was selected based on TGA results and isothermal calorimetry measurements were used to calibrate the pozzolanic reaction kinetics. The reaction model was validated with experimental results from qXRD, TGA and helium pycnometer measurements (total solid volume). Model limitations, especially the fixed C-A-S-H compositions, are discussed in depth based on SEM/EDX results. Additionally, the model allows to calculate the temperature dependency of the pozzolanic metakaolin reactions based on calorimetry measurements of varying isothermal conditions. The activation energy of the main (C_2ASH_8) pozzolanic reaction was determined to 84 kJ/mol in the temperature range of 20 °C to 40 °C validating the identified simple (short-term) reaction mechanisms. P5 constitutes section 6 of this thesis (Figure 1) and directly addresses the second research hypothesis outlined above.

Section 7 summarizes the main findings of this research work by directly answering the two hypotheses outlined above. The Supplementary Material for each publication is provided in section 8.

All **publications** as fundamental parts of this research work are listed below.

Publication 1 (P1):
Pozzolanic Reactions of Metakaolin with Calcium Hydroxide: Review on Hydrate Phase Formations and the Effect of Alkali Hydroxides, Carbonates and Sulfates
(published: Materials & Design, Elsevier, 07/2023, https://doi.org/10.1016/j.matdes.2023.112062)

Publication 2 (P2):
Early Metakaolin Reactions in Pozzolanic R^3-Test: Calorimetry Baseline Correction of Initial Temperature Jump due to Ex-Situ Mixing
(published: Materials and Structures, Springer, 08/2023,
https://doi.org/10.1617/s11527-023-02217-6)

Publication 3 (P3):
A Mass Balance Approach for Thermogravimetric Analysis in Pozzolanic Reactivity R^3-Test and Effect of Drying Methods
(published: Materials, MDPI, 10/2021, https://doi.org/10.3390/ma14195859)

Publication 4 (P4):
Pozzolanic Metakaolin Reactivity: Time-Dependent Influence of Calcium Hydroxide, Alkali Hydroxides, and Sulfates
(published: Construction and Building Materials, Elsevier, 05/2024,
https://doi.org/10.1016/j.conbuildmat.2024.136534)

Publication 5 (P5):
Pozzolanic Metakaolin Reactions: Stoichiometric and Kinetic Modeling
(published: Materials & Design, Elsevier, 02/2024, https://doi.org/10.1016/j.matdes.2024.112747)

The full-text publications are essential parts of this thesis. As they are embedded in the main text of this work, the articles are slightly adjusted to comply with the overall thesis layout as well as to provide

consistency in the wording. The content has not been modified and the original articles are open accessible via the given DOIs.

1.3 Experimental Overview

This section gives a general overview of all sample compositions included in this work together with the analysis techniques used. The abbreviations P1 - P5 refer to the five publications of this research thesis outlined above (section 1.2).

Paste samples were prepared, each consisting of an alkaline suspension mixed with metakaolin (or with a calcined clay in P3). The water to solid (solid = MK + CH) weight ratio was fixed to 1.2 analogous to the R³-test [85, 86] to avoid a stoppage of the reactions due to water shortages. The metakaolin to calcium hydroxide weight ratios applied (MK/CH) are 0.33 (P2 - P5) according to [85, 86] and 1.0 (P4, P5) to additionally demonstrate the effect of a reduced supply of CH (no significant transformation reactions expected). The experimental methodologies (P2, P3) are demonstrated on different calcined clay types whereas publications 4 and 5 concentrate on an industrially produced pure metakaolin (98 wt.-% amorphous content). The used metakaolin and calcined clays are summarized in Table 1 together with their product name and the supplying company.

Table 1: Overview of the used metakaolin and calcined clays in the experimental program.

Product Name	Suppling Company	P2	P3	P4 + P5
Metamax®	BASF SE	MK3		MK
PowerPozz® White	NEWCHEM GmbH	MK2	MK1	
Metaver® O	NEWCHEM GmbH	MK1		
Metaver® R	NEWCHEM GmbH		MK2	
Liament	Liapor GmbH & Co. KG		MC	

Variations of the alkaline suspension comprise the addition of secondary activators, namely alkali hydroxides (KOH and NaOH) and/or sulfates (K_2SO_4 and Na_2SO_4), whereas the suspension named as “0K“ does not contain any of those additional substances. The suspension named as “R3” (same as “0.32KOH_K2SO4” in P4) is based on [87] and contains potassium sulfate as well as potassium hydroxide. Analogously, suspension “0.32NaOH_Na2SO4” comprises of sodium hydroxide and sodium sulfate with the same SO_4^{2-}/MK and OH^-/MK weight ratios compared to “R3”. The suspensions “0.32KOH” and “0.32NaOH” contain potassium and sodium hydroxide with the same OH^-/MK weight ratio compared to “R3” (0.0077). In the suspensions “1.28KOH” and “1.28NaOH”, this ratio was increased to a four times higher value of 0.0306. An overview of the different alkaline suspensions together with the types of metakaolin and calcined clays used in the experimental program is provided in Table 2.

Table 2: Overview of the alkaline suspensions together with the type of metakaolin or calcined clay used in the experimental program.

Suspension	Metamax®	PowerPozz® White	Metaver® O	Metaver® R	Liament
0K	P4 + P5				
R3 (0.32KOH_K2SO4)	P2 + P4	P2 + P3	P2	P3	P3
0.32KOH	P2 + P4 + P5				
1.28KOH	P4 + P5				
0.32NaOH	P4				
1.28NaOH	P4				
0.32NaOH_Na2SO4	P4				

For this work, an extensive set of micro-analysis techniques was carried out to comprehensively characterize the kinetics and phases formations of the pozzolanic MK reactions both in the short- and long-term. Pore solution was extracted from the paste samples, pH values were measured and inductively

coupled plasma optical emission spectrometry (ICP-OES) was conducted. Additionally, fresh paste samples were tested with isothermal calorimetry for a duration of 7 days at 20 °C, 30 °C and 40 °C as well as with in-situ XRD for selected sample compositions. For the long-term analysis, the experimental program includes thermogravimetric analysis (TGA), X-ray diffraction (XRD) and scanning electron microscopy with energy-dispersive X-ray spectroscopy (SEM/EDX), carried out on powdered samples stopped with isopropanol after 2, 7, 56 and 245 days of reaction at 40 °C [82]. The overall testing program is summarized in Table 3. The used analysis methods are described in detail in section 3 and 4 together with sections 5.2.3 and 6.2.

Table 3: Overview of the analysis methods used in this thesis together with the testing times (d: days) and temperatures.

Methodology	**Type of sample**	**< 2d**	**2d**	**7d**	**56d**	**245d**
ICP-OES and pH*	Pore solution	20 °C				
Isothermal calorimetry	Fresh paste	20*, 30*, 40 °C	20*, 30*, 40 °C	20*, 30*, 40 °C		
In-situ XRD*	Fresh paste	~ 20 °C				
XRD	Dried powder		40 °C	40 °C	40 °C	40 °C
TGA	Dried powder		40 °C	40 °C	40 °C	40 °C
SEM/EDX*	Tablet		40 °C	40 °C	40 °C	40 °C

* Selected samples.

2 Publication 1: Literature Review

Publication 1 (Materials & Design, https://doi.org/10.1016/j.matdes.2023.112062):

Pozzolanic Reactions of Metakaolin with Calcium Hydroxide: Review on Hydrate Phase Formations and Effect of Alkali Hydroxides, Carbonates and Sulfates

Kira Weise[1,*], Neven Ukrainczyk[1], Eduardus Koenders[1]

[1] Technical University of Darmstadt, Institute of Construction and Building Materials, Germany.
* Corresponding author. E-mail address: weise@wib.tu-darmstadt.de.

Abstract: Metakaolin (MK) has emerged as a highly promising Supplementary Material in low carbon binders for the construction industry. In wide range of applications, from lime to cement-based materials, its hardening performance relies on the pozzolanic reactivity between MK and calcium hydroxide (CH), resulting in the formation of diverse calcium-aluminate/silicate hydrates. The reaction sequence is affected by specific conditions dictated by the binder system employed in various applications. To advance the design of binders that reduce the carbon emissions, a systematical review on MK-based reactions is crucial. This review encompasses a broad range of MK/CH ratios and examines the effect of alkali hydroxides, carbonates and sulfates. The focus is on the formation and stability of pozzolanic hydrate phases over time and under different curing temperatures. Additionally, the review addresses the characteristics that directly affect MK reactivity, such as the (calcined) clay structure and the dissolution of the reactants. The systematic findings shed light on the hydrate phase assemblage, enabling a better understanding of the reaction mechanisms in complex systems, like MK cementitious blends. The results of this review serve as a valuable foundation for the development of novel "low-carbon" binder designs and compositions for both cementitious and lime-based binders.

Keywords: metakaolin, calcium hydroxide, pozzolan, phase transformation, lime mortar, supplementary cementitious materials (SCM).

2.1 Introduction

Global warming and environmental constraints in the construction industry have accelerated the search for alternative low carbon binders. In this context, metakaolin showed a great potential for various applications in the construction industry [36, 41, 88–94]. The use of widely available calcined clays that contains a certain fraction of metakaolin (MK) as its most desired reactive component [7, 12, 16], can partly replace cement clinker in mortars and concrete [7, 8, 95–100], thereby reducing cement production and its associated CO_2 emissions [2]. Calcined clays display a wide range of chemical and mineralogical compositions [87, 96, 101–103]. While MK demonstrates superior pozzolanic reactivity [28, 81, 104], various calcined clay minerals may influence its binder potential [102, 105–107]. These minerals, although not the main focus of this review, should also be considered for specific applications. The incorporation of MK in cementitious systems improves the physical and mechanical properties [41, 45, 89, 108–114], mainly as a result of a pore structure refinement [45, 89, 109, 113–118] due to the space filling capacity of pozzolanic reaction products [28, 42, 45, 110, 114, 119, 120]. Furthermore, the addition of MK to lime-based binders, e.g. mortars for restoration and conservation purposes [121–127], can have positive effects, especially on the increasing rate of strength development as well as an improved durability [65, 122, 128–135]. The different applications all have in common that the chemical performance of MK is mainly driven by its pozzolanic reactivity, a chemical ability to consume calcium hydroxide (CH) and form pozzolanic hydrate phases. Depending on the specific system applied, further substances present can influence the reaction products formed.

This study concentrates on the reaction processes of MK with CH, not in Portland cement systems, with the aim of giving a fundamental review on the basic reactions complemented by the presence of alkali hydroxides, carbonates and sulfates. On the one hand, this approach is based on the concept of using a simplified model system, like e.g. designed for the R³-Test [85–87, 136], the Pozzolanic Reactivity Test (PRT) [137] and the lime mortar strength test [138], but extended for a wider range of MK/CH weight ratios. This knowledge may help to develop new binders and understand current Portland cement based systems. Through this focus, the current review article clearly distinguishes itself from substantial review work done over the last years, particularly most recent one from Zunino et al. with the focus on LC³-systems (Limestone Calcined Clay Cement) [81]. On the other hand, this approach offers the opportunity to use the obtained results as a valuable basis for a wider range of applications, like e.g. the development of novel lime mortar formulations.

MK is derived from the natural clay mineral kaolinite calcined at temperatures of around 700 °C [11, 16, 22, 23, 28, 139–141]. During this thermal activation, dehydroxylation [24, 28, 32] as well as further structural reorganization processes takes place [24, 28, 142], resulting in a (partly) amorphous structure [27–29], that leads to a significant increase in reactivity of the material [27–32].

MK reacts with calcium hydroxide (CH) mainly forming C-(A-)S-H, C_4AH_{13}, C_2ASH_8 (stratlingite) and $C_3AS_yH_z$ (hydrogarnet). Different factors may influence the formation of these hydrate phases, such as the metakaolin to calcium hydroxide weight ratio (MK/CH) [65, 73–75] as well as the curing time [64] and temperature [69]. Since C_4AH_{13} and C_2ASH_8 are thermodynamically unstable in alkaline environments or rather incompatible with CH [77], they convert to more stable hydrogarnet phases under certain conditions [53, 69, 75, 78]. The kinetics of the reactions between MK and CH are mainly influenced by the curing temperature [87] and secondary activators such as alkali hydroxides and sulfate [53, 62, 74–76].

If pastes of MK and CH contain additional carbonates and/or sulfates, further reaction products are formed in addition to those mentioned before. In the presence of carbonates, hemi- (Hc, $C_4Ac_{0.5}H_{12}$) and/or mono-carboaluminates (Mc, C_4AcH_{11}), designated as CO_3-AFm (CO_3-containing Aluminate-Ferrite-mono), have been identified [54, 56, 64, 76, 105, 143]. Incorporation of sulfates leads to a rapid formation of ettringite (designated as AFt; Aluminate-Ferrite-tetra) [62, 76, 105, 106], which may convert to monosulfoaluminate (Ms, C_4AsH_{12}) with reaction time (in the absence of carbonates) [75, 87], depending on the amount of sulfates present [62]. In contrast, by reactions of MK and CH with sulfates and carbonates [87], ettringite can be stabilized by the formation of CO_3-AFm.

The present study will add to this with a systematic review of the reaction processes of MK with CH and clarifies the effect of alkali hydroxides, carbonates and sulfates. The focus is mainly on the formation of reaction products and their respective stability in an alkaline surrounding, their dependence on varying MK/CH ratio, curing time and temperature. However, in this study, the most important aspects of both the structure and dehydroxylation of kaolinite and the influence on adsorption and dissolution of MK in alkaline environments are presented as well, since they are necessary for a holistic understanding of the hydration reaction processes and phase formations. This review concludes with an extensive summary of the hydrate phases formed from MK reactions, complemented by a thorough identification of potential research gaps that need to be addressed in the future. All together it provides an extensive basis for a detailed understanding of pozzolanic metakaolin reactions along with alkali hydroxides, sulfates and/or carbonates that are needed for a targeted design of metakaolin-based low carbon binders.

The present review contains literature that was published until April 2023 and includes peer-reviewed journal papers published in English and German language. The applied review methodology for this study is provided in detail in the Supplementary Material.

Relevant notations and abbreviations of minerals employed in this study are summarized in Table 4.

Table 4: Formulas [144] and abbreviations of minerals used throughout this article.

Mineral	Chemical formula	Short notation	Abbreviation
Metakaolin	$Al_2O_3 \cdot 2\ SiO_2$	AS_2	MK
Calcium hydroxide	$Ca(OH)_2$	CH	CH
Calcium carbonate	$CaCO_3$	Cc	Cc
Calcium sulfate	$CaSO_4$	Cs	Cs
Ettringite	$Ca_6Al_2(SO_4)_3(OH)_{12} \cdot 26\ H_2O$	$C_6As_3H_{32}$	AFt
Monosulfoaluminate	$Ca_4Al_2(SO_4)(OH)_{12} \cdot 6\ H_2O$	C_4AsH_{12}	Ms (AFm)
Monocarboaluminate	$Ca_4Al_2(CO_3)(OH)_{12} \cdot 5\ H_2O$	C_4AcH_{11}	CO_3-AFm or Mc
Hemicarboaluminate	$Ca_4Al_2(CO_3)_{0.5}(OH)_{13} \cdot 5.5\ H_2O$	$C_4Ac_{0.5}H_{12}$	CO_3-AFm or Hc

2.2 Focus and Constrains

The aim of this review is to provide a state of the art on the available fundamental knowledge on hydrate phase formations from reactions of MK with CH as well as to clarify herein the effect of alkali hydroxides, carbonates and sulfates. The focus is on MK-CH systems while eliminating additional influencing factors arising in more complex (e.g. LC^3) systems. Nevertheless, the literature that address MK reactions in Portland cement systems has been considered in a minor extent as a specific example, but only when the relevant information was not exclusively related to such binder systems.

The present literature review is reported in section 2.3 to 2.5, where section 2.3 is addressing both the structure of kaolinite and metakaolin while discussing specifics regarding dehydroxylation and structural disordering processes during calcination as these aspects fundamentally determine the properties of MK. Section 2.4 briefly describes the main findings regarding the dissolution and adsorption characteristics of MK as they are relevant for the overall comprehension of the reaction processes and phase formations. Section 2.5 is the main section of this literature review, that concentrates on the hydrated phase formations in MK-CH systems (section 2.5.1) and describes the effect of alkali hydroxides (section 2.5.2), carbonates (section 2.5.3) and sulfates (section 2.5.4). As the focus herein is on the reaction products, emphasis is on the use of characterization techniques such as TGA/DTA and XRD[1], where strength and durability aspects were not considered. Section 2.6 briefly addresses existing modeling approaches in this field. In the context of the main objective to better understand the pozzolanic reaction mechanisms of MK in MK-CH systems and to enable a transfer of the gained knowledge to more complex systems (driven by pozzolanic reaction) in future, like e.g. blended cementitious systems and/or lime-based mortars, studies dealing with MK-based geopolymers were not in focus of this literature review. The key differences between a reaction process of pozzolanic hydration and geopolymerization are mainly the absence of a calcium source ($CaO \leq 10$ w.-% [146]) and the much higher alkali hydroxide/silicates concentration (e.g. $>>$ 1 M NaOH [147]) in geopolymers. Nevertheless, some selected studies on geopolymers were referred to in section 2.4 as well to discuss common aspects of MK solubility in alkaline solutions. Figure 2 systematically summarizes the setup of this review study and includes the numbers of the sections and paragraphs that contain the respective information. The distinction with MK-based geopolymers becomes clear through the limited MK/CH weight ratio of 2.0 (larger calcium source compared to geopolymers) and an alkali hydroxide concentration of less than 1 M (alkalinity is much lower compared to geopolymers). The results of this review study on hydrate phase formations were further analyzed in view of variations in MK/CH as well as curing times and temperatures.

[1] As most common measurements to determine the type and amount of pozzolanic reaction products [145].

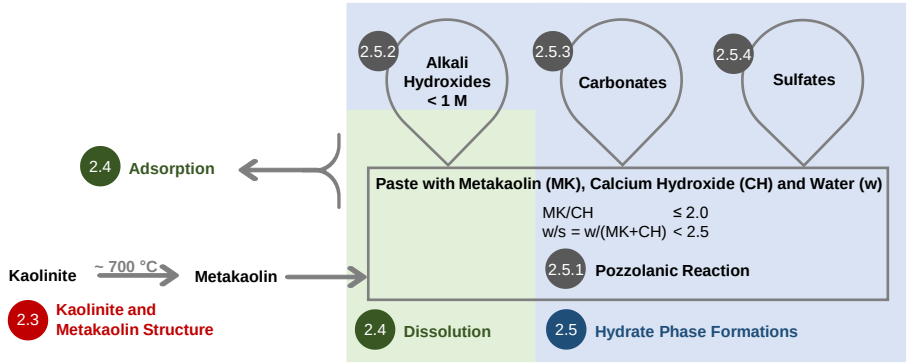

Figure 2: Graphical overview of the aspects addressed in this review study. The numbers show the sections addressing the respective topic.

In summary, the focus of this literature survey is as follows (see also Figure 2):

- **Hydrate phase formations** from reactions of MK with CH in suspensions (MK/CH ≤ 2.0 and w/s < 2.5, section 2.5.1) with the addition of alkali hydroxides (concentration < 1 M[2], section 2.5.2), carbonates (section 2.5.3) and sulfates (section 2.5.4).
- **The dissolution of MK and CH** affected by the addition of alkali hydroxides to the MK-CH system (section 2.4).

Note the following definition:

- The initial weight ratio of metakaolin (MK) to calcium hydroxide (CH) during sample preparation is indicated as **"MK/CH"** mainly to facilitate an easy comparison of different sample compositions in literature. It should be noted that this approach is a simplification and further aspects, particularly kinetic aspects additionally contribute significantly to the hydrate phase formations.

To implement the literature search shown in Figure 2, the following selection criteria for sample composition and curing conditions were applied:

- Lime paste samples containing MK, CH and water were considered (no mortar/concrete, so no incorporation of cement and/or sand and aggregates)
- Suspensions with water-to-solid mass ratio w/s < 2.5
- Relatively pure MK as summarized in Table S1-4 in the Supplementary Material ($SiO_2 + Al_2O_3 \geq 92.30$ %; $1.13 \leq SiO_2/Al_2O_3 \leq 1.41$ in MK and/or kaolin[3]; laboratory calcination temperature ≥ 700 °C)
- Initial weight ratios of MK to CH in pastes defined as MK/CH in this study of up to 2.0 (MK/CH ≤ 2.0)
- Alkali hydroxide concentration below 1 M
- Curing temperatures of 20 °C - 60 °C
- Age of samples up to 5 years

2.3 Kaolinite and Metakaolin Structure

The raw material kaolin has kaolinite or $Al_2(OH)_4Si_2O_5$ as one of the major mineral phases, which is a pure clay mineral composed of silicon tetrahedrons (T) and aluminum octahedrons (O), that build two layers (T-O, the so-called 1:1 clay) as shown in Figure 3 [24, 148]. The T-O layers are further linked into a stacking structure via hydrogen bonds and van der Waals forces, leading to kaolinite, disordered kaolinite and dickite structures depending on the type of stacking (dis)order [142]. SEM images of

[2] The concentration of alkali hydroxides was limited to < 1 M to stay in the range of pozzolanic reactions rather than geopolymerization (described above). Studies addressing MK based geopolymers are referred for a deeper understanding of general aspects regarding MK solubility in alkaline solutions in section 2.4 only.

[3] For pure MK SiO_2/Al_2O_3 can theoretically be calculated to $(2 \cdot 60$ g/mol $[SiO_2])/(102$ g/mol $[Al_2O_3]) = 1.18$.

kaolinite and metakaolin show the typical layered structure (Figure 4). The general platy morphology of kaolinite does not significantly change with the thermal treatment. Souri et al. reported only slight modifications, in particular more rounded particle edges and some agglomerations of platelets in irregular stacks [149] as shown in Figure 4.

MK is obtained by thermal activation (calcination) of the two layered aluminosilicate kaolinite at temperature ranges of 400 °C to 850 °C, typically around 700 °C in laboratory scale [22–25] whereas the ideal range for industrial calcination was reported as 700 °C to 850 °C [26]. During the thermal heating of kaolinite, different processes occur with increasing temperature as summarized by Hanein et al. [26]: dehydration, dehydroxylation and recrystallisation. Up to temperatures of approx. 300 °C, dehydration takes place. During this process, molecular water is released, that may be adsorbed, trapped within the clays pore structure and/or is associated with the interlayer cations [26]. Some other studies also reported a structural reorganization of the octahedral layers due to proton delocalization processes in the temperature range of 160 °C to 300 °C [150, 151] and from ~ 100 °C to 400 °C [139, 141], designated as pre-dehydration [139, 141] and pre-dehydroxylation [150, 151]. When further increasing the temperature, hydroxyl groups (OH^- ions) detach from the kaolinite layers, commonly named as dehydroxylation [24, 26, 28]. The temperature range in which dehydroxylation takes place may depend on the morphology and size of kaolinite mineral particles [23, 152], the structural layer stacking order of the raw material [23, 104, 142], possible impurities in the raw material [153] and heating conditions [154, 155]. The dehydroxylation of kaolinite starts at temperatures of around 350 °C [156], 400 °C [28, 139, 141, 150], 450 °C [22–24] and it continues up to 500 °C [150], 600 °C [28, 156], 650 °C [139, 141, 157], but being completed at around 700 °C [22–25, 27, 29, 32, 158]. Shvarzman et al. for example reported 95 % of dehydroxylation of kaolinite in the temperature range of 450 °C to 570 °C [23]. With further increasing temperatures (above ~ 800 °C), recrystallisation processes can occur [24, 141], that lower the reactivity of calcined kaolinite and should consequently be avoided in the production process.

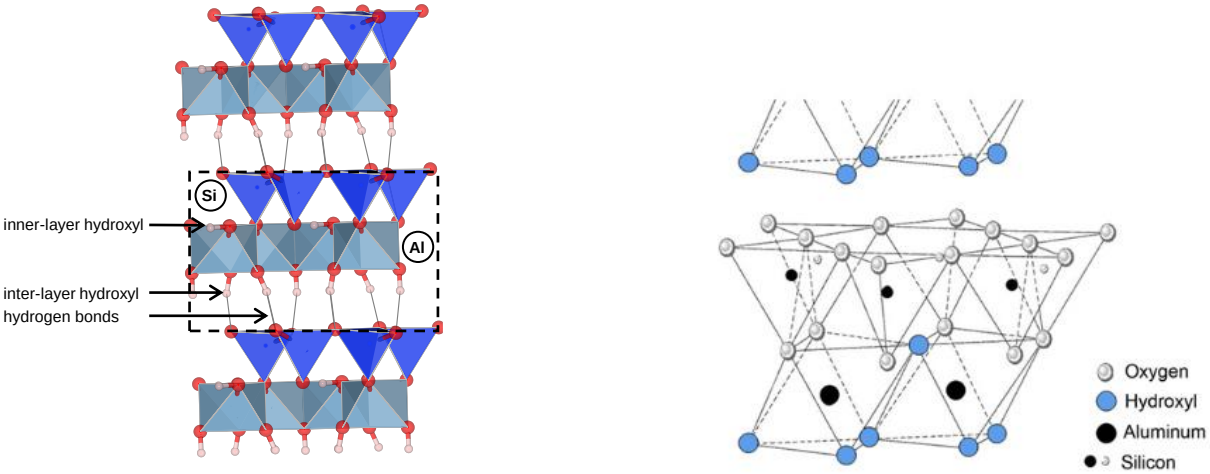

Figure 3: Layered structure of kaolinite consisting of silicon tetrahedrons and aluminum octahedrons with inner- and inter-layer hydroxyl groups shown in the unit cell (left: adapted from [24, 142], right: [159] © 2014 used with permission of Elsevier Science & Technology Journals from [159]; permission conveyed through Copyright Clearance Center, Inc..). The T-O layers (three shown in the left figure) are linked into a stacking structure via hydrogen bonds (shown in the figure) and van der Waals forces (not shown).

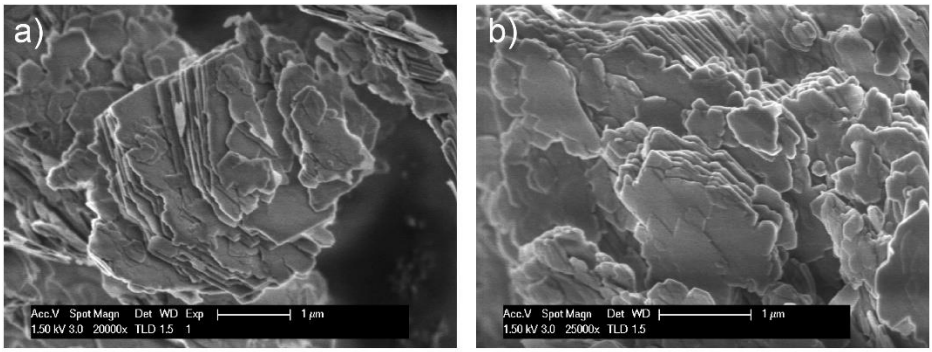

Figure 4: SEM image of (a) kaolinite and (b) metakaolin (kaolinite heat treated at 700 °C in a laboratory furnace) [149]. © 2015 used with permission of Elsevier Science & Technology Journals from [149]; permission conveyed through Copyright Clearance Center, Inc..

The dehydroxylation is one of the main processes during calcination of kaolinite that leads to a partially disordered state that increases the materials reactivity and is therefore described in more detail below. It should be noted, that even though dehydroxylation and "amorphization" are related processes, care should be taken not to mix them up [26]. Further increases in structural disorder were found with the heating after dehydroxylation was (almost) completed [28]. This phenomenon is further discussed at the end of this section.

According to the chemical formula given in eq. 1, the mass loss for full dehydroxylation of kaolinite can be calculated theoretically (stoichiometric mass loss) resulting in a value of 13.95 %[4], however, pure MK is industrially not so readily available in huge quantities [22, 25, 160]. Consequently, experimental measurements give lower values of e.g. 11.77 % [27] also due to impurities in the kaolin's raw material, namely illite and quartz in this case [27].

Eq. 1 shows the dehydroxylation of kaolinite to MK by using the commonly accepted chemical formula of ideal kaolinite and assuming full dehydroxylation [22, 30, 161, 162]. In addition, eq. 2 represents a chemical formula for kaolinite that displays the OH^- groups more clearly and allows partly dehydroxylation with remaining hydroxyl groups in the formed MK [139, 141, 150]. Setting the value x to zero gives the full dehydroxylation of kaolinite according to eq. 3 that is analogous to eq. 1, meaning the transformation of four hydroxyl groups into two water molecules, leaving two oxygen anions in the material as shown in eq. 4 [27, 163].

$Al_2O_3 \cdot 2\ SiO_2 \cdot 2\ H_2O$	$\rightarrow Al_2O_3 \cdot 2\ SiO_2 + 2\ H_2O$	[22, 25, 30, 161, 162]	(1)
$Al_2Si_2O_5(OH)_4$	$\rightarrow Al_2Si_2O_5(OH)_xO_{2-x} + (2 - x/2)\ H_2O$	[139, 141, 150]	(2)
$Al_2Si_2O_5(OH)_4$	$\rightarrow Al_2Si_2O_7 + 2\ H_2O$	[24, 26, 27]	(3)
$4\ OH^-$	$\rightarrow 2\ H_2O + 2\ O^{2-}$	[27, 163]	(4)
$AlO_2(OH)_4$	$\rightarrow AlO_4 + 2\ H_2O$	[31]	(5)

Where x is the amount of residual hydroxyl groups in MK (a low value of around 0.4 after thermal activation up to 650 °C [27, 141, 150]).

During calcination, MK retains the hexagonal platelet structure of kaolinite [24, 27], consisting of alternating, but disordered aluminum and silicate layers (Figure S1-2 in the Supplementary Material) [59]. The dehydroxylation process results in a decrease of MK layer thickness, from an average of ~ 110 nm in kaolinite to an average of ~ 95 nm in MK [32]. Aluminum (Al) transforms mainly from 6-coordination to 4- and/or 5-coordination due to the loss of water with little remaining 6-coordination (Figure 5 and Figure 6) [24, 27–31, 164] (e.g. change from 6- to 4-coordination following eq. 5), whereas silica remains in the 4-coordinated tetrahedra form, but rearranges slightly [24, 27] to accommodate the changes in aluminum structure [164]. The structural change is mainly driven by a reorganization of the aluminum layers, when Al migrates into vacant sites provided by the inter-layer

[4] (2 · 18 g/mol [H_2O])/(102 g/mol [Al_2O_3] + 2 · 60 g/mol [SiO_2] + 2 · 18 g/mol [H_2O]) · 100 %.

space followed by the deformation of the layers (Figure S1-2 in the Supplementary Material) [24]. Consequently, the thermal treatment destructs the crystalline order and creates a (partly) amorphous structure [24, 27–29] that results in a much higher reactivity of the material [27–32].

Along dehydroxylation, the reactivity of MK increases also due to the modification of the short-range order of Si in MK. ^{29}Si NMR studies [28] indicated that a range of neighboring arrangements are formed with Al in all three coordination states (IV, V, and VI), Figure 6 [165, 166]. In a kaolinite structure, the Al is octahedrally (Al^{VI}) coordinated, while in fully dehydroxylated (MK) case, the Al site is mainly tetrahedrally (Al^{IV}) coordinated as a result of 4 interactions via bridging oxygen with 2 Si and 2 Al neighbors (Figure 5 and Figure 6). In the partially dehydroxylated clay Al is mainly 5-coordinated (Al^{V}) [142], which is the most reactive Al state [29, 167]. Interestingly, Fernandez et al. identified an increase in 5-coordination Al with calcination between 600 °C and 800 °C after dehydroxylation seemed to be complete, leading to the conclusion that there must be another process, e.g. the modification of the short-range order of silicate units, besides dehydroxylation being responsible for the disordered state of MK [28]. Hanein et al. concluded that there is no complete amorphization of the structure, but the structural disorder as "loss of the lattice periodicity in the direction perpendicular to the structural layers" continues even after an almost complete dehydroxylation [26]. The structural disorder favors its dissolution in alkaline surroundings [27] so that MK can act as a source of silica and aluminum ions [30].

In summary, depending on the degree of dehydroxylation and (dis)order as well as the arrangement of the (nearest) neighbors in the structure of the MK vs. kaolinite, the reactivity could be linked to the dissolution of Al sites, which depends on the coordination numbers. Compared to other clay minerals, such as e.g. illite and montmorillonite, kaolinite contains on the one hand more OH^- ions and on the other hand, they are located at the edge of the structural layer (Figure 3), that favors dehydroxylation and consequently leads to an enhanced disorder of the structure after calcination as well as an increased amount of 5-coordinated Al at the surface of the layers which are exposed to the solution dissolving environment [28].

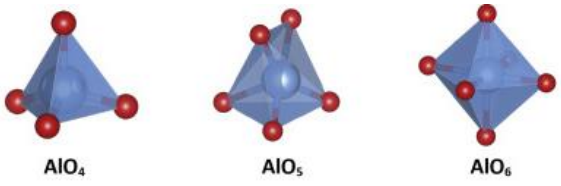

Figure 5: 4- (Al^{IV}), 5- (Al^{V}) and 6-coordination (Al^{VI}) of Al [168]. © 2019 used with permission of Elsevier Science & Technology Journals from [168]; permission conveyed through Copyright Clearance Center, Inc..

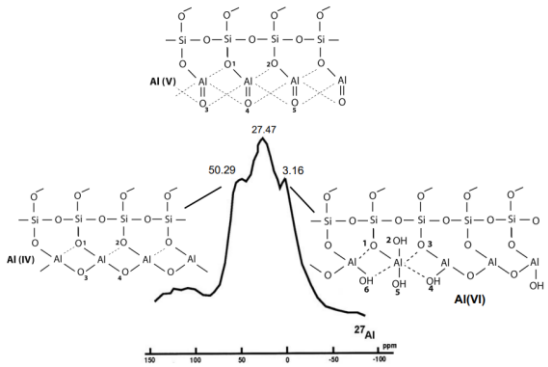

Figure 6: Three sequences constituting MK molecular structure, dotted line for coordination links, full line for chemical valence links. The numbers for oxygen and hydroxyl atoms provide the Al^{IV}, Al^{V} and Al^{VI} coordination parameters. [165, 166] © 2017 by Göller Verlag, Baden-Baden, Germany.

2.4 Dissolution and Adsorption

The pore solution of paste systems plays a major role for the evaluation of the reactivity and the formation of reaction products from binder materials. The analysis of the pore solution, can provide useful information about the dissolution behavior of the material and adsorption processes on the surface of particles, while both directly influencing the formation of reaction products [106]. Thus, to analyze the type of phases that precipitate during reaction processes, an understanding of the complex overall reaction mechanisms is needed, which involves the dissolution and adsorption as well as diffusion,

nucleation and growth aspects. Thus, all aspects need to be considered for the evaluation of the overall (as well as the individual) reaction mechanisms. Namely, results focusing solely on dissolution experiments cannot be linked directly to the formation of reaction products [107, 169], e.g. due to the adsorption phenomenon on calcined clay surfaces [107]. For that reason, the dissolution and adsorption mechanisms are further addressed in the following paragraphs.

In literature, the surface of calcined clay particles was found to have a strong affinity to adsorb ions from a pore solution [107]. The assumption of a negatively charged surface of calcined clays was interpreted from their negative zeta potentials measured in some studies [107, 159, 170–172] (e.g. in a synthetic cement pore solution: 0.4 g/L Ca^{2+}, 7.1 g/L K^{+}, 2.25 g/L Na^{+} and 8.29 g/L SO_4^{2-} at a pH of ~ 12.9 [170]). According to this, in systems incorporating CH, positively charged calcium ions (Ca^{2+}) present in the pore solution can adsorb on calcined clay particles [107, 159, 170, 172–175]. This phenomenon leads to a more intense consumption of CH [107] and additionally allows negatively charged PCE superplasticizer, e.g. commonly used in blended cementitious systems, to adsorb onto the clay surfaces [172]. In the simultaneous presence of a sulfate source in a system, several studies reported a subsequent adsorption of negatively charged sulfate ions (SO_4^{2-}) on the Ca^{2+} layer [107, 173, 175]. Beside adsorption on raw precursor's particles, sulfate ions can also adsorb on the surface of reaction products, e.g. C-(A-)S-H [140, 176–178]. In specific applications, such as in LC^3-systems, that can even be the main aspect explaining the influence of calcined clays on the sulfate balance [81, 179].

Physical properties of a material, like e.g. the surface area, may additionally influence the ion adsorption, leading to changes in the pore solution and consequently effect the dissolution and reaction behavior [107].

The overall composition of the pore solution, e.g. the change of Si/Al ratio as a result of MK dissolution in a respective system, directly affects the precipitation of reaction products as well as the reaction kinetics [76]. Thereby there is a general agreement in literature about a more intense solubility of MK with a higher pH [106] and accordingly a higher alkali hydroxide content [31, 76, 180–184].

In alkaline environments, the dissolution of MK (eq. 6 - 8), that involves breakage of covalent oxo-bridging of silicates and mostly ionic bonds of the aluminates, releases silicate and aluminate aqueous species [182]. Dissolution is a hydrolysis reaction where bridging oxygens (Si-O-Si or Si-O-Al of the solids) are attacked (i.e. protonated) by H_2O, which is further promoted by alkalis and hydroxyl anions [165]. This may occur simultaneously to hydrolysis/condensation (oligomer ⇌ monomer) reactions in solution. The reactions outlined in eq. 6 to 8 [169, 182, 185] are used in literature not only to explain the geopolymer formation [169, 182, 185], but also to describe the reaction mechanisms of MK with CH (and sulfate addition) [62]. With increasing alkalinity, silicate species according to eq. 8 become dominant as shown in eq. 9 [157, 185–187] and vice versa [182].

$$Al_2O_{3\,(s)} + 3\,H_2O + 2\,OH^- \rightarrow 2\,Al(OH)_4^- \quad [62, 182] \quad (6)$$

$$SiO_{2\,(s)} + H_2O + OH^- \rightarrow [SiO(OH)_3]^- \quad [62, 157, 182] \quad (7)$$

$$SiO_{2\,(s)} + 2\,OH^- \rightarrow [SiO_2(OH)_2]^{2-} \quad [62, 182] \quad (8)$$

$$[SiO(OH)_3]^- + OH^- \rightleftharpoons [SiO_2(OH)_2]^{2-} + H_2O \quad [157] \quad (9)$$

The dissolution behavior of MK is also dependent on the calcination temperature as shown by Boonjaeng et al. by testing calcination temperatures from 650 °C to 800 °C in different NaOH solutions (0.01, 0.1, 1, 3, 5 and 10 M NaOH) [147]. Although the results showed dependence on the NaOH concentration, no general quantification was possible, despite a clear result that MK exhibits higher solubility compared to kaolinite [147], underlining the general accepted fact of higher reactivity due to clay amorphization/dehydroxylation [27–32, 188]. Garg and Skibsted [29] reported the initial dissolution rate to be constant at approx. 38 μmol/L/h (Figure 7 (B)) for both Al and Si, during the first 24 hours in highly diluted systems (w/s = 4000). They also found that the solubility of MK in 0.1 M NaOH

solution is highest when MK is calcined at 700 °C compared to 500 °C and 900 °C [29], which is in agreement with other studies about the "optimal" calcination temperature of around 700 °C [27, 29, 32, 158].

The Si/Al ratio from dissolution of MK was stated in various studies to be close to 1.0 (i.e. suggesting congruent dissolution) as examined in different alkaline solutions [76, 107, 169, 181, 184, 189] for up to 180 days [76]. The rate of Al and Si dissolution at 25 °C was almost constant up to 20 hours and decreased up to 48 hours (1 g MK in 400 mL solution containing 0.1 M NaOH and 0.5 M KOH with pH = 13.5) [107]. Another study reported a linear dissolution behavior within the first 24 hours, approaching equilibrium values for later ages (Figure 7 (A) for up to 80 days; 0.25 g MK in 1 L 0.1 M NaOH solution with pH = 13.0) [29]. The authors identified a strong relation of the rate of dissolution and the degree of undersaturation as MK dissolves very fast in the beginning of the experiment and dissolution slows down as it approaches equilibrium, provided in Figure 7 (B) [29]. This finding could be also due to kinetic factors besides thermodynamic ones (how far from equilibrium concentrations), like e.g. the formation of protective layers on particles surfaces and/or an inhibitory effects caused by Al ions in the solution [29, 190]. Garg and Skibsted also found that the Si/Al ratio in a solution was different depending on the calcination temperature during MK production [29]. Namely, Si/Al ratio was reduced from 0.97, 0.89 to 0.67 when the temperature increased from 500 °C, 700 °C and 900 °C. This led to the following two hypothesis as proposed by the authors: 1) Al sites are less stable (more distorted) than Si sites and change coordination number at 700 °C (compared to 500 °C), and 2) at 900 °C, two separate calcination products, with different Si/Al ratios, may potentially coexist [29].

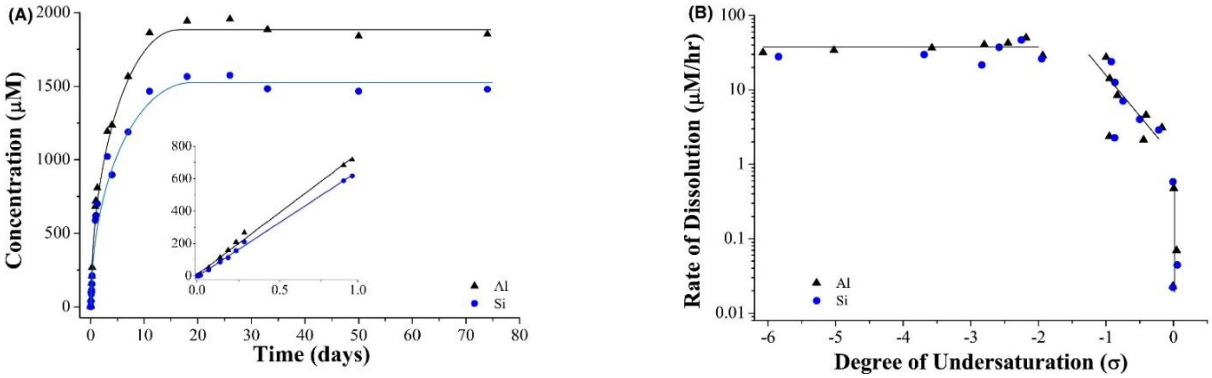

Figure 7: (A) Long-term dissolution kinetics of MK in a 0.1 M NaOH solution, the inset shows the data for the first day (B) Rate of Al and Si dissolution from the samples shown in (A) as a function of undersaturation degree of the surrounding solution [29]. © 2019 used with permission of BLACKWELL PUBLISHING American Ceramic Society from [29]; permission conveyed through Copyright Clearance Center, Inc..

Nevertheless, the reviewed studies do not fully agree regarding the preferred solubility of Si or Al from MK evaluated with respect to the measured ion concentration in the solution. Some studies reported a faster and more intense dissolution of Al from MK compared to Si (Figure 7 (A)) [29, 62, 182]. Various explanations for this phenomenon can be found in literature [63, 169, 191]. On the one hand, it could be due to stronger binding of Si in MK especially at the beginning of solubility experiments [169] and/or soluble Al ions adhering to Si rich regions in the MK structure, leading to an inhibition of Si solubility [191]. On the other hand, the reason could be an immediate precipitation of hydrate phases from soluble Si, which attach to the undissolved MK particles, followed by an inhibition of further dissolution of Si [63]. Fernández et al. examined the dissolution of 1 g calcined paper sludge, containing 33 % MK in addition to high amounts of calcite (66 %), in 75 mL of saturated CH solution at 40 °C for up to 360 days [63]. They found high concentrations of Al ions, and conclude that a) MK degrades strongly and b) the aqueous aluminate shows difficulties in incorporation into the hydrate phases formed [63]. In contrast, Hajimohammadi et al. [180], they found a higher concentration of Si compared to Al within the first 4 days of MK dissolution in a 0.1 M NaOH solution [180]. Higher Si solubility from MK were also reported by other authors for very high alkaline conditions (e.g. 8.0 M NaOH solution) [182] and at later ages, namely after approx. 10 h at 25 °C in 5 M and 8 M NaOH solution [169].

Regarding the dissolution of Al from MK, Garg and Skibsted [29] were the first to provide a strong experimental evidence for the preferential dissolution and a high reactivity of 5-coordinated aluminum in MK, whereas 4-coordinated aluminum dissolves more slowly due to a higher structural stability [29]. This finding could explain the general agreement in literature about 5-coordinated aluminum being the most reactive site in MK [167].

In literature, alkali hydroxide addition is found to accelerate the MK reactivity [192] probably due to the enhanced dissolution with increasing alkali hydroxide content [76, 193]. Hajimohammadi and van Deventer analyzed MK dissolution in NaOH solutions and could only detect a slight increase of the maximum (equilibrium) Al and Si ion concentration in solution for higher NaOH concentrations (0.05 M to 0.3 M) [180]. Regarding the impact of alkali hydroxide concentration on the dissolution of solid precursors, Sun and Vollpracht [194] discussed the following two-sided effect: a) higher alkali hydroxide concentrations accelerate dissolution due to more OH^- present and b) more reaction products are formed, which can deposit on the surface of dissolving precursors and act as a barrier that affects dissolution and diffusion [194].

The difference in dissolution behavior of MK in NaOH and KOH solutions was further investigated showing that the extent of dissolution is higher in NaOH rather than in KOH solutions with the same molar concentrations [181, 184], even for higher pH values in KOH solutions [184]. Panagiotopoulou et al. [181] explained this result by the higher charge density (smaller size) of Na^+ compared to K^+, which leads to a better stabilization of silicate monomers and dimers in a solution, as the interaction between cation and anion pairs is more intense, resulting in an increased dissolution rate [181, 195]. The high charge density cation, such as Na^+, promotes more the hydrolysis reaction in comparison to the low charge density cation K^+. Additionally, Scherb et al. [184] investigated an enhanced alkali uptake by MK in NaOH solutions compared to KOH and concluded that this uptake also weakens the MK structure leading to a more intense dissolution [184].

Deng et al. investigated MK-CH pastes made with a w/s ratio of 5.0 by varying $CaSO_4$ and Na_2SO_4 contents, finding a strong dependence of the type of activators on the dissolution characteristics of aluminum as well as on the coordination number of aluminum in the reaction products [62]. The presence of sulfates in solutions seems to accelerate the dissolution of aluminum from MK [62], probably due to the fast precipitation of ettringite as further discussed in section 2.5.4.

The presence of sulfates was also found to result in a more intensified CH dissolution and consequently a stronger MK reaction, e.g. based on bound water content obtained by TGA [107]. In contrast, very high alkaline solutions impede CH dissolution due to the common ion effect of OH^- species [53, 59, 147, 183].

Another parameter that influences the adsorption and dissolution behavior is the particle size distribution and consequently the surface area of the raw materials [107]. In general, the higher particle surface area generated e.g. by milling [187], increases not only the dissolution, that leads to an increased reactivity [188], but also the adsorption. In contrast, Hajimohammadi and van Deventer found slightly lower dissolution rates for MK with increasing milling time, due to a reaggregation of the particles [180]. Scherb et al. investigated the morphological evolution of MK particles in water and alkaline solutions (dosage by weight: 10 wt.-% of KOH and NaOH in the solution) using SEM images [184]. They found a reduction in particle size due to the dissolution process [184]. Especially the samples in NaOH solution showed a clear change in morphology, having a reduced mean particle size as shown in Figure 8 [184].

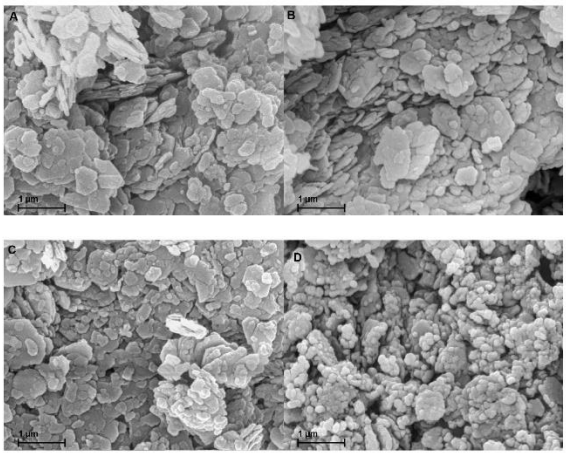

Figure 8: Morphological changes of MK in different solutions shown in SEM images (a: MK, b: MK-H_2O, c: MK-KOH, d: MK-NaOH) [184]. © 2020 by Scherb et al. (licensee MDPI, Basel, Switzerland).

Additionally, Romero and Garg recently investigated the morphological changes of MK when exposed to NaOH solutions with optical microscopy [32]. Their results show a decrease in MK layer thickness after dissolution in a 1 M NaOH solution. Raw kaolinite particles, that were not thermally activated, show a quite different behavior. Upon exposure to the NaOH solution, the kaolinite layers slide over each other, resulting in an expansion along the particle length (Figure 9). In contrast, MK particles did not show layer-by-layer (sliding) exfoliation, but broke apart into randomly-oriented planes (Figure 10). Dissolution of MK in a 1 M NaOH solution leads to a significant reduction of the (single) layer thickness (from an average of ~ 95 nm to an average of ~ 75 nm) [32]. The study gives novel insights into the dissolution process of MK particles, demonstrating no exfoliation, but disintegration and a thinning process of individual stacking layers.

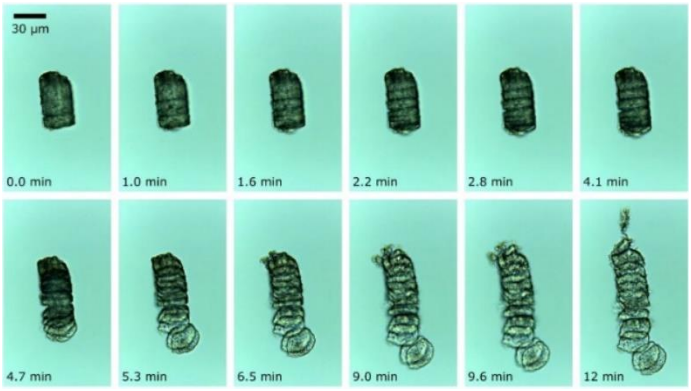

Figure 9: Kaolinite layers slide over each other leading to an expansion along the particle length when exposed to a 1 M NaOH solution [32]. © 2022 used with permission of Elsevier Science & Technology Journals from [32]; permission conveyed through Copyright Clearance Center, Inc..

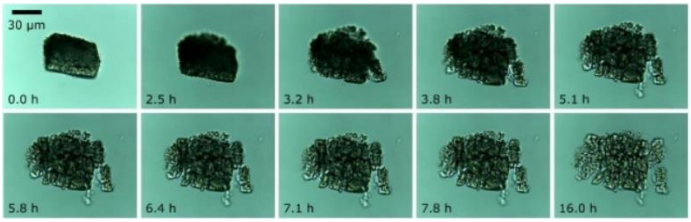

Figure 10: MK particles break apart in randomly-oriented planes and the layer thickness is significantly reduced when exposed a 1 M NaOH solution [32]. © 2022 used with permission of Elsevier Science & Technology Journals from [32]; permission conveyed through Copyright Clearance Center, Inc..

2.5 Hydrate Phase Formations

2.5.1 Pozzolanic Reaction

Reaction Processes and Main Influencing Factors

In this study, the pozzolanic reaction is defined according to DIN EN 197-1 representing the reaction processes between aluminosilicate (here only MK), CH and water [23]. Several studies identified C-S-H (calcium silicate hydrates), C_4AH_{13}, $C_3AS_yH_z$ (hydrogarnet) and/or C_2ASH_8 (stratlingite) as possible hydration products precipitating in this reaction [51, 53, 54, 56, 57, 65, 68–70, 72, 74]. In 1983, Murat defined the following three basic equations for the pozzolanic reaction of MK ($Al_2O_3 \cdot 2\ SiO_2$, short: AS_2) [51]:

$$AS_2 + 6\ CH + 9\ H \rightarrow C_4AH_{13} + 2\ C\text{-}S\text{-}H \quad [51]\ (10)$$

$$AS_2 + 5\ CH + 3\ H \rightarrow C_3AH_6 + 2\ C\text{-}S\text{-}H \quad [51]\ (11)$$

$$AS_2 + 3\ CH + 6\ H \rightarrow C_2ASH_8 + C\text{-}S\text{-}H \quad [51]\ (12)$$

AS_2:	Metakaolin ($Al_2O_3 \cdot 2\ SiO_2$)
CH:	Calcium hydroxide ($Ca(OH)_2$)
H:	Water (H_2O)
C-S-H:	Tobermorite or CSH_I (0.8-1.5 $CaO \cdot SiO_2 \cdot$ 0.5-2.5 H_2O), that also may including some Al incorporation C-(A-)S-H, as discussed later
C_4AH_{13}:	Tetracalcium aluminate hydrate
C_3AH_6:	Tricalcium aluminate hydrate
C_2ASH_8:	Hydrated gehlenite

In the same study he confirmed the formation of C_2ASH_8, C-S-H and small quantities of C_4AH_{13} as the main reaction products for ambient curing temperatures with XRD and DTA measurements [51]. Eq. 10 to 12 are derived based on stoichiometric considerations using a calcium (CaO) to silicate (SiO_2) ratio (C/S) of C-S-H as 1.0. Authors of subsequent studies partly adjusted the equations proposed by Murat regarding C/S. De Silva and Glasser e.g. identified C-S-H and C_4AH_{13} as the main reaction products arising in MK-CH systems [75]. Consequently, they simplified the reaction equation for their calculations as shown in eq. 13, forming C-S-H with a C/S of 2.0 and allowing only the formation of C_4AH_{13} as an aluminate phase [75].

$$AS_2 + 8\ CH + 7.34\ H \rightarrow C_4AH_{13} + 2\ C_2SH_{1.17} \quad [75]\ (13)$$

More recently, Zunino et al. proposed eq. 14 for the reaction of MK with a saturated portlandite solution assuming ideal compositions of the hydrate phases and using the illustrative C-A-S-H composition $C_{1.5}A_{0.1}SH_4$ [81].

$$AS_2 + (6.2 - 3.1a)\ CH + (12.0 - 4.6a)\ H \rightarrow (2\text{-}a)\ C_{1.5}A_{0.1}SH_4 + a\ C_2ASH_8 + (0.8 - 0.9a)\ C_4AH_{13} \quad [81]\ (14)$$

In literature, all four reaction products arising from eq. 10 to 12, viz. C-S-H, C_4AH_{13}, $C_3AS_yH_z$ and C_2ASH_8 are identified to be formed by a pozzolanic MK reaction, as also summarized in Table S1-3 in the Supplementary Material. C-S-H and the two (metastable) phases C_2ASH_8 and C_4AH_{13} are often identified as the main reaction products (from MK-CH pastes) in literature [54, 64, 69, 196]. Under some specific conditions further discussed below, $C_3AS_yH_z$ is formed as a stable cubic hydrogarnet phase [57, 65, 68, 69, 74]. However, in all studies not every phase is found at the same time. Especially some of the calcium aluminate hydrates are not stable and can transform into different phases with time under specific conditions. The decomposition of some calcium aluminate hydrates can lead to the liberation of CH (an increase was noted up to 90 days in [65], maximum CH at 56 and 90 days in [54]), that needs to be taken into account for the evaluation of pozzolanic reactivity based on CH consumption.

Subsequently, it is of particular interest to better understand under which conditions the individual phases form and whether they are stable or transform to more stable phases. In the following sections these questions will be discussed by systematizing existing studies in this field.

The type and amount of hydrated phases formed is dependent on the sample compositions, mainly through MK/CH [64, 65, 73–75, 147] and changes with reaction time [64]. There is a tendency of an increasing amount of C-S-H [64] and aluminate phases, namely $C_3AS_yH_z$ [50], C_2ASH_8 [64] and C_4AH_{13} [58, 64] with increasing MK/CH [54], but a generalization at that point can be misleading as the specific investigated ranges of MK/CH need to be further taken into account. Additionally, MK/CH influences the reaction rate, as higher MK/CH lead to a more rapid CH consumption (MK/CH of 2.0 compared to 1.0) [72]. Regarding the curing conditions, Azeredo et al. observed that pozzolanic reactions of MK are faster in moist air (RH ~ 100 %) at 22 °C rather than curing at dry air (RH ~ 65 %) [72]. Avet et al. studied the effect of curing temperatures (pastes containing calcined clays, CH and limestone) and found that the total heat release after one day at 40 °C was comparable to six days at 20 °C [87]. The authors also found no major change in phase assembly between these two curing temperatures, with the exception of ettringite that was less or even absent in systems with limestone at 40 °C [87]. They explained this result by the accelerated pozzolanic reaction of MK and the higher solubility of ettringite at increasing temperatures [87]. Other studies reported a temperature dependency of phase formations, viz. higher temperatures of around 60 °C favor the formation of hydrogarnet phases (direct formation and/or transformation from metastable phases) as further described below [64, 69]. Regarding phase formations in general, the microstructure development seems to be an additional influencing parameter, as it determines the available space in a matrix (pore structure) as well as the degree of reaction of the binder components. For example, an enhanced precipitation of hemi- (Hc, $C_4Ac_{0.5}H_{12}$) and monocarboaluminates (Mc, C_4AcH_{11}) was observed from the reaction of MK with limestone in LC^3-systems with w/b of 0.8 compared to 0.4 [143].

Reaction Products

Calcium silicate hydrates (**C-(A-)S-H**) of varying compositions (also including some Al, discussed later) precipitate from the reaction of MK with CH [27, 50–61]. Due to their low crystallinity [197], these phases are difficult to determine explicitly based on XRD, but other techniques like e.g. TGA and SEM enable their identification [50].

C-S-H was detected already at early stages as the main product of a reaction between MK and CH at 20 °C, 40 °C and 60 °C [59, 71]. With further reaction time, other phases, especially aluminate hydrates, like stratlingite, C_4AH_{13} and hydrogarnet (mainly at higher temperatures of ~ 60 °C) [71] are formed, as further discussed in the following sections.

Scherb et al. identified C-S-H formation after 10 h, that intensified up to 30 h in MK-CH systems mixed with a combined 0.1 M NaOH and 0.5 M KOH alkaline solution (pH = 13.5) at 25 °C (Figure 11, MK/CH = 1.0) [107]. In their study, the authors observed an intense heat release in calorimetry after 2 h (peak maximum ~ 3 mW/g_{solid}; Figure 11) associated with the dissolution of MK and CH. Afterwards, the dissolution of MK continues with a relatively constant rate, whereas CH dissolution accelerates again from 15 to 25 h that is correlated with an enhanced C-S-H formation (Figure 11) [107]. Frías and Cabrera detected C-S-H (using XRD and DTA) after two days, whereas aluminate phases (C_2ASH_8 and C_4AH_{13}) appeared after 9 days at 20 °C (no addition of alkali hydroxides) [53]. An earlier C-S-H formation was found already at 6 h with a curing temperature of 60 °C [74]. After 12 h and 21 h, besides C-S-H, other phases like stratlingite, C_4AH_{13} and hydrogarnet were detected as well [74]. Consequently, the nucleation time and rate of C-S-H precipitation accelerates/increases with curing temperature and the presence of secondary activators like alkali hydroxides and/or sulfate.

The temporal change of C-S-H composition [63] is difficult to determine accurately. De Silva et al. analyzed samples of MK with CH and different MK/CH ratios of 0.5 to 7.6 cured at 55 °C for 90 days with electron microscopy [69]. They found a general tendency of a decreasing C/S ratio from a

maximum of 2.1 to a minimum of 0.7 with an increasing MK/CH according to Figure 12 [69], and was supported by thermodynamic modeling of the pozzolanic reaction of pure SiO_2 with different amounts of added CH (C/S = 0.7 for CH/SiO_2 of 0.61 and 1.7 for CH/SiO_2 of 1.98) [137]. Additional results show some aluminum incorporation in C-S-H phases, increasing with MK/CH ratio, namely A/S increases from 0.03 up to 0.43 (Figure 12) [69]. Wang et al. reported a C/S ratio of 1.5 and C/A of 3.3 (i.e. calculated A/S of 0.45) for their MK-CH systems with MK/CH of 1.0 and cured at 20 °C [66]. C-S-H formation from the reaction of MK (calcined paper sludge having 14 % kaolinite in the raw material) in a saturated CH solution indicated an increase in C/S ratios from 1.6 to 2.5 with time (from 1 to 360 days) [63]. As data regarding C/S ratios is rare for (cement-free) MK-CH systems, values obtained from cementitious paste systems serve as a guidance. In cement pastes containing MK, C-S-H show lower C/S ratios from 1.0 (50 % MK) to 1.6 (20 % MK) [198] or around 1.43 (20 and 40 % MK) [192, 199] compared to a reference cement hydration (without MK) of around 1.6 to 1.9 [200] (1.6 [201], 1.75 [202], 1.77 [199]). Consequently, C/S ratios of around 1.0 [75] and 1.7 [107] were used for modeling calculations of MK reactions in literature.

The formation of C-S-H is generally known to be the most important phase for developing mechanical and durability properties of the materials, namely increase in compressive strength and reduction in transport properties (porosity, pore size distribution and pore connectivity) [113, 147, 203].

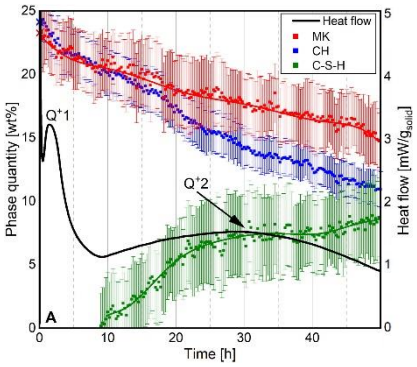

Figure 11: Phase quantification and heat flow of MK-CH (Q+1: dissolution of MK and CH, Q+2: formation of C-S-H) [107]. © 2021 used with permission of Elsevier Science & Technology Journals from [107]; permission conveyed through Copyright Clearance Center, Inc..

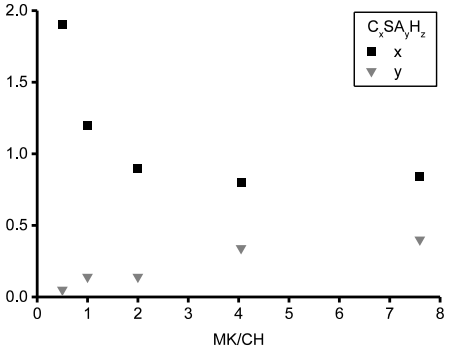

Figure 12: Composition of amorphous $C_xSA_yH_z$ with varying MK/CH ratios cured at 55 °C for 90 days, z not determined (data from [69] – mean values are shown).

C_2ASH_8 is a metastable [55, 57, 74] (thermodynamically unstable in the presence of CH [80, 81]) calcium aluminum silicate hydrate phase, named stratlingite or gehlenite hydrate and reported in many publications to be one of the or even the main reaction product formed in MK-CH systems [27, 50, 51, 53, 54, 56, 59, 61–67]. Its formula was reported based on analytical electron microscopic data as $C_2A_{(0.9\text{-}1.2)}S_{(0.9\text{-}1.3)}H_8$ with curing temperatures of 55 °C and MK/CH of 2.0 and higher [69]. Its occurrence in MK-CH systems is (besides kinetic aspects) mainly dependent on the MK/CH ratio (used as a parameter to compare different studies in this article) that is further discussed below. For MK/CH ratios of 0.2 or lower, stratlingite was not detected at ambient temperatures, even not after 1.5 years [54, 65, 68], but it was found in pastes with MK/CH between 0.3 and 7.6 [51, 53, 54, 56, 65, 68, 69, 72]. More intense stratlingite formation was observed in pastes with increasing MK content (MK/CH = 0.5, 1.0 and 2.0 cured at 38 °C for two months [204, 205] and MK/CH = 0.05 - 1.0 cured at 20 °C for 180 days [68]). However, for higher MK/CH ratios, Serry et al. found progressively less stratlingite formation with increasing MK/CH [50][5]. The authors explained that more stratlingite forms with decreasing MK/CH due to more calcium ions in pastes with lower MK/CH leading to a higher pH so that $[SiO_4]^{4-}$ enters into solution more easily, thus transforming C_3AH_6 into stratlingite [50]. This is in agreement with the results from Azeredo et al. (MK/CH of 1.0 and 2.0) [72] that support the preferred formation of stratlingite and

[5] Care should be taken when comparing MK/CH ratios, as Serry et al. prepared samples with clay (containing 75 % kaolinite) and CH with clay/CH ratios of 1.0 to 4.0 and calcined these samples at 800 °C [50]. The thermal activation leads to the dehydration and dehydroxylation of kaolinite and also a decomposition of CH and consequently to different MK/CH ratios in the sample preparation.

silica-containing hydrogarnet ($C_3AS_yH_z$) instead of C_3AH_6 by systematic studying the addition of SiO_2 in CaO-Al_2O_3-H_2O systems [78].

Stratlingite formation at ambient temperatures was detected already from the first day on [54, 68], up to 1.5 years [65] for MK/CH ratios larger than 0.2, whilst increasing up to 180 days, especially for MK/CH of 1.0 and 2.0 [54, 56, 65, 68]. Other studies reported an increase up to 120, 270 and 360 days of curing (MK/CH of 0.5, 1.0 and 2.0) [53, 56, 206], in agreement with De Silva and Glasser, who stated that stratlingite becomes more stable with decreasing calcium content [69]. Likewise, Silva et al. detected an increase of stratlingite for MK/CH of 1.0 up to 6 months followed by an almost constant amount up to 1.5 years [65]. For lower MK/CH of 0.3 to 0.6, a decrease was noted from 28 days onwards [65], supporting the hypothesis of hydrogarnet formation from stratlingite in the presence of CH, which will be further discussed below.

With increasing curing temperatures, the formation of stratlingite can be accelerated, but metastability makes this more complicated. At 60 °C, it formed already after 6 and 12 hours with MK/CH of 1.0 [70, 74]. However, other authors found that stratlingite persists in all mixtures only at 20 °C (MK/CH = 0.5 - 7.6), while at 55 °C only for MK/CH of 2.0 and higher (2.0, 4.0 and 7.6) [69]. This confirms that stratlingite is unstable at higher temperatures especially for MK/CH between 0.5 and 1.0, already after three days of curing. This is in line with observations regarding the formation of more stable hydrogarnet phases, as a result of transformation of stratlingite in the range of MK/CH between 0.3 and 1.0 at higher temperatures.

It should be noted, that the exact quantification of stratlingite with thermogravimetric analysis is challenging/not possible as its mass loss in thermal analysis is overlapping with the one from C_4AcH_{11} [56, 64, 65] in the temperature ranges of 140 °C - 200 °C [58], 160 °C - 220 °C [54], 150 °C - 250 °C [64] and 180 °C - 265 °C [207], respectively. Additionally, in some publications, stratlingite is not detected with XRD in the first days of hydration [53, 56], that could probably be due to its low degree of crystallinity at that particular age [56]. The amount of phases, in general, is also dependent on the relative humidity. Azeredo et al. detected C_2ASH_8 besides monocarboaluminate only in samples cured in moist air (RH ~ 100 %) at 22 °C, whereas in dry air (RH ~ 65 %), no C_2ASH_8 was detected [72]. Several studies reported a high mechanical resistance and strength of stratlingite [64, 208], so that the formation of this phase can generally be evaluated as beneficial for most applications.

To summarize, stratlingite formation (in MK and CH pastes), depends (besides kinetic aspects) mainly on the MK/CH ratio (used for comparison in this study, further discussed below), namely it was detected for MK/CH above 0.3 [54, 65, 68], in particular for 0.3 to 0.6, already after one day [54, 68] up to 1.5 years [65] at ambient temperatures with an increase up to 28 days and a further decrease at later ages [65]. These findings agree very well with the transformation of (metastable) stratlingite into more stable hydrogarnet in the presence of CH, for MK/CH between 0.3 and 0.6 from 28 days onwards at ambient temperatures, accelerated by temperatures [69]. For MK/CH of 1.0 and higher, stratlingite was detected from the first day up to 1.5 years with an increasing amount up to 180 days that remains almost constant afterwards, at ambient temperatures [54, 56, 65, 68].

At that point it should again be noted that the parameter MK/CH was used in this study to facilitate the comparison of different sample compositions used in the reviewed literature. This approach is a simplification and particularly kinetic aspects as well as the microstructure development additionally contribute to the hydrate phase formations. Nevertheless, the parameter MK/CH gives a good indication of mixture compositions that favor the coexistence of stratlingite and CH that promotes transformation reactions to more stable hydrogarnet phases.

C_4AH_{13} is an even more metastable [51, 53, 55, 74] calcium aluminate hydrate (than stratlingite) [54, 59–61, 64, 71, 206]. Its appearance in some studies in the initial stage of MK-CH pastes was explained by the metastable phenomenon due to supersaturation of the aqueous phase with respect to CH [69],

regardless of the MK/CH ratio (MK/CH = 0.05 – 1.0 [68]) and/or temperature [74]. Due to the relatively fast(er) transformation and the generally low stability, C_4AH_{13} was not detected for MK/CH of 0.5, 1.0 and 2.0 cured at ambient temperatures after two months [56, 66]. However, the difficulty in detection by XRD should be mentioned here, due to small amounts present [66] and/or low crystallinity [53, 57, 66, 70] and overlapping reflection peaks, mainly with C_2ASH_8 and C_4AcH_{11} [51, 53, 70]. Peak overlaps are also a challenge for the derivative of TG analysis, namely with C-S-H (25 °C – 150 °C [64], 110 °C [54], 150 °C [75]), C_2ASH_8 and C_4AcH_{11} (220 °C – 280 °C [58], 265 °C [207], 280 °C [75]), especially for longer curing times (123 days) [57, 71]. Another reason for the lack of C_4AH_{13} was attributed to carbonation, that destabilizes this phase due to the formation of carboaluminates [66].

However, most studies agree about the instability of C_4AH_{13} at ambient temperatures [51, 54, 64, 65, 68, 69], where this phase was observed from about first day up to approximately 28 or 56 days, but not beyond [64, 65, 68]. The phase transformation after a certain time is explained in literature by the formation of hydrogarnet especially at higher temperatures, namely at 40 °C and 55 °C [59, 69] and/or possibly another phase like $Ca_2Al(OH)_7 \cdot 6.5\ H_2O$ [65, 68]. The formation of $Ca_2Al(OH)_7 \cdot 6.5\ H_2O$ was detected by XRD in pastes with MK/CH of 0.05 to 1.0 at 23 °C after 14 and 28 days in parallel to the decomposition of C_4AH_{13} [65, 68]. The formation and further transformation of C_4AH_{13} were found to be accelerated by the incorporation of secondary activators, like e.g. NaOH [59]. Other studies reported, that C_4AH_{13} does not disappear with curing time up to 120 and 360 days (MK/CH = 1.0 at 20 °C) [53, 206]. A possible explanation for this was given by Rojas and Cabrera, proposing a relation of the stability of C_4AH_{13} with the presence of CH [71]. They observed by thermal analysis that C_4AH_{13} was present up to 180 days, while CH was completely consumed after 90 days, leading to the conclusion, that C_4AH_{13} might be stable in the absence of CH (MK/CH = 1.0 at 20 °C) [71]. In contrast, a decrease of C_4AH_{13} was detected with increasing MK/CH from 0.5 to 4.0 at 20 °C, whereas at 55 °C this trend was not clear [69]. This was explained by the increased Si release with higher MK/CH leading to the preferred formation of silicon containing aluminate phases. Moreover, although the curing temperature has influence on the stability of C_4AH_{13}, this phase was still detected as a metastable phase up to and as long as 123 days and 60 months at 60 °C with MK/CH of 1.0 [57, 74].

Several studies detected **hydrogarnet ($C_3AS_yH_z$)** formation in MK-CH pastes [57, 59–61, 65, 68–70, 74, 209], typically via transformation reactions of the metastable phases C_2ASH_8 and C_4AH_{13} [53, 59, 69, 75, 78, 209]. A decrease of C_2ASH_8 [64, 65] and C_4AH_{13} [64, 69] with time was linked to the formation of hydrogarnet investigated especially at higher temperatures of 40 °C and 55 °C [59, 69] (transformation reactions can also occur at ambient temperatures as discussed below), demonstrated by Martínez-Ramírez and Frias for curing times of 34 and 123 days at 60 °C and MK/CH of 1.0 [209]. The following equation for the transformation reaction of the two metastable phases to a stable cubic phase was proposed in literature [59, 210]:

$$C_2ASH_8 + C_4AH_{13} \rightarrow 2\ C_3AS_{0.5}H_5 + 11\ H \qquad \text{[59, 210, 211]} \quad (15)$$

$C_3AS_{0.5}H_5$: Hydrogarnet

Although there is an agreement in the literature about C_2ASH_8 and C_4AH_{13} being metastable (in the presence of CH) [51, 53, 55, 57, 74, 212], the mechanism behind hydrogarnet formation is controversially discussed. The transformation reactions seem to depend on the presence of CH [65, 69, 78, 213], reported mainly for curing temperatures of 50 °C or higher [58, 69, 70, 209, 212], but also for ambient temperatures [50, 65, 68]. In contrast, some authors indicate that hydrogarnet may form directly at higher temperatures [57, 70, 71, 74, 212]. Cabrera and Rojas showed that hydrogarnet is formed without a decrease of C_2ASH_8 and C_4AH_{13} from 30 h to 9 days with MK/CH of 1.0 at 60 °C [74]. And even for further curing times (up to 123 days), the authors could not find any evidence of further C_2ASH_8 and C_4AH_{13} transformation [71].

Hydrogarnet is a special group of cubic garnet minerals where the $[SiO_4]^{4-}$ tetrahedra are partially or completely replaced by OH^- [214]. The general formula of hydrogarnet is

$(Ca_3(Al,Fe)_2(SiO_4)y(OH)_4(3-y);\ 0 < y < 3)$ [214, 215] that includes different minerals with their respective end members summarized in Figure 13. The incorporation of iron (Fe) in hydrogarnet phases is of minor importance in relatively pure systems, where preferred incorporation of silicon (Si) plays a dominant role [59, 69, 78]. Thus, hydrogarnet is referred to as $C_3AS_yH_z$ with $z = 2 \cdot (3 - y)$ in this study. De Silva and Glasser gave different elemental compositions of hydrogarnet depending on MK/CH for samples cured at 55 °C [69], showing an increase of Si incorporation when MK/CH rises from 0.5 to 1.0 ($y = 0.26 - 0.34$ to $y = 0.48 - 0.9$) [69]. Hydrogarnet is a stable phase at temperatures of 20 °C and higher [214].

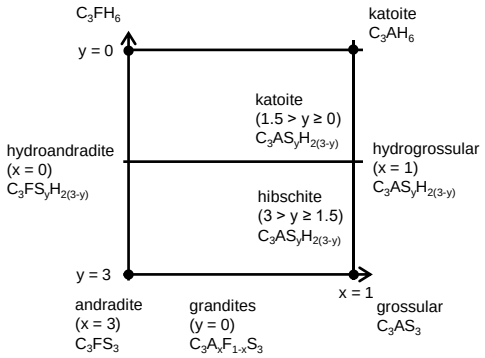

Figure 13: Nomenclature of minerals of the hydrogarnet group (figure adopted from [214]; nomenclature recommended by [216]).

The presence of hydrogarnet (in MK-CH systems) was especially found at 50 °C or higher [58, 69, 70, 209]. Frías et al. carried out an extensive study with MK/CH of 1.0 at 60 °C for up to 15 years [55, 57, 210]. In the first days of reaction (21 and 30 h), both the metastable and (cubic) stable phases coexist as directly formed from the reaction of MK with CH, not indicating any transformation at this age [55]. From 30 h up to 9 days, hydrogarnet was also found to coexist with C_2ASH_8 and C_4AH_{13}, still indicating a direct reaction of hydrogarnet from MK and CH [74]. After seven days, Žemlička et al. detected hydrogarnet in samples with MK/CH ratios (recalculated from reported MK/CaO values) of 0.38 and 0.76 cured at 50 °C with 95 % of relative humidity for seven days, but not in samples with higher (1.51 and 3.78) or lower (0.15) ratios (CaO used was limestone calcined at 1100 °C), whereas stratlingite was found in pastes with higher MK/CH only [58], indicating transformation reactions. For longer curing times of 34 and 123 days at 60 °C, a total transformation was reported with MK/CH of 1.0 [209]. These findings are in line with results of ambient curing temperatures, addressed in the next paragraph, and can be explained by the instability of C_2ASH_8 in the presence of CH leading to the formation of more stable hydrogarnet phases. In contrast, other studies showed hydrogarnet formation at higher temperatures (55 °C) even for MK/CH of 2.0 [69], whereas samples stored at ambient temperature did not show any hydrogarnet formation due to the absence of CH [69, 72, 217]. For MK/CH higher than 2.0, hydrogarnet was not observed, neither for ambient curing temperatures nor at 55 °C [69].

Several studies did not detect any formation of hydrogarnet at ambient temperatures of 20 °C to 25 °C and curing times up to 90, 180 and 360 days, respectively [53, 54, 56, 64, 69, 71] leading to the conclusion that higher temperatures are needed for the transformation reaction to take place. In some of these studies, different MK/CH were tested (0.2 and 1.0 in [54, 64]; 0.5, 1.0 and 2.0 in [56]), leading to the assumption that MK/CH does not influence this result (no significant transformation), at least not in the investigated range. In contrast, Serry et al. could identify hydrogarnet in pastes with lower lime contents (80 wt.-% kaolin and 20 wt.-% CH activated at 800 °C) indicating that hydrogarnet may be formed at ambient temperatures if MK/CH is high, possibly due to a lower pH value [50]. Gameiro et al. and Silva et al. investigated the formation of katoite (C_3AH_6), a low silica hydrogarnet (Figure 13), for a range of MK/CH between 0.3 and 0.6 for samples cured at ambient temperatures and 95 % relative humidity after 28 days (mainly after 180 days [65]) increasing up to 1.5 years [65, 68]. They explained their findings with the instability of C_2ASH_8 in the presence of CH leading to the formation of a more stable hydrogarnet phase. This is supported by Rojas and Sánchez de Rojas [70] results, showing that hydrogarnet formation is directly related to the CH content meaning that hydrogarnet increases when

CH decreases, while both phases remain constant from 34 to 123 days of curing [70]. In contrast, in pastes with MK/CH of 1.0, no CH is present at the same time as C_2ASH_8 and consequently, no hydrogarnet is formed [51, 53, 54, 56, 65, 68, 69, 72]. For lower MK/CH (0.05 to 0.2) no hydrogarnet was detected as no C_2ASH_8 was formed in these pastes [54, 65, 68]. De Silva and Glasser described the phase assemblage of samples with MK/CH between 0.5 and 7.6 at 20 °C and 55 °C [69]. At 20 °C, no hydrogarnet was formed, whereas it was detected at 55 °C for MK/CH of 0.5 and 1.0 after three days, whereas for MK/CH of 2.0 after 28 days [69]. At ambient temperatures, the tested MK/CH of 0.5 to 7.6 seem to be too high for transformation reactions to hydrogarnet (lack of CH) and/or the latest testing time (180 days) too short. Another reason for the lack of hydrogarnet phases in these samples could be the dense microstructure that (kinetically) impedes transformation reactions. With a curing temperature of 40 °C (MK/CH of 1.0), the transformation reaction of C_2ASH_8 and C_4AH_{13} was observed, more clearly in NaOH activated systems [59].

At longer curing times (34 and 123 days), Frías et al. found that metastable phases co-exist with hydrogarnet and they are almost completely transformed to stable phases after 123 days [55, 210]. Another study reported only C-S-H and hydrogarnet remain as main phases after 90 days of curing [59]. After 15 years, degradation of the initial compounds C-S-H, C_4AH_{13}, C_2ASH_8 and hydrogarnets was observed together with the formation of new phases like calcite and calcium zeolites mainly of the gismondine type [210].

To summarize, hydrogarnet forms (in MK-CH pastes) via the transformation reaction at ambient temperatures, while at around 55 °C it may from in two different ways: 1) in the first days it precipitates directly from the solution (coexisting with metastable phases) and 2) at longer times via transformation of the metastable phases for MK/CH of 0.38 to 2.0 [58, 69, 209] (lack of information for MK/CH = 0.3). However, for higher MK/CH no hydrogarnet was observed even at higher temperatures [69], possibly due to the lack of CH. At ambient temperatures, the transformation reaction is very slow and no hydrogarnet was observed except for the critical range of MK/CH between 0.3 and 0.6 [65, 68], due to the coexistence of C_2ASH_8 and CH, that favors the transformation [65, 69, 78, 213], observing hydrogarnet from 28 days onwards [65, 68]. For MK/CH less than 0.3, the lack of C_2ASH_8 prevents the formation of hydrogarnet at ambient temperatures [54, 65, 68] and for MK/CH of 1.0 and above, no hydrogarnet forms due to the absence of CH [51, 53, 54, 56, 65, 68, 69, 72]. These findings are based on MK-CH systems without sulfates, whereas if sulfates are present in the pastes, hydrogarnet can also form due to transformation processes from monosulfoaluminate [59], that is further discussed in section 2.5.4.

The transformation reactions can have negative effects on porosity, and thus the mechanical resistance and durability of mortars, especially at later curing ages [59, 65, 70]. Consequently, the discussion presented above demonstrates the need for a careful selection of the binder composition, especially regarding MK/CH, to avoid the detrimental effects of the transformation reactions in long terms.

Calcium Hydroxide Consumption

As the pozzolanic reactions (eq. 10 to 12) consume CH, this is often used to estimate the degree of the reaction. Although the consumption of CH measured over time can give useful information about the reaction kinetics and phase formations, it is dependent on many factors that are difficult to differentiate from each other. Namely the change in reaction stoichiometry is mainly dependent on the reaction products formed [218] as well as their phase compositions, like e.g. C/S in C-(A-)S-H. Besides, if sulfates are present in the system, ettringite and AFm phases precipitate, that further consumes CH [62, 143]. Additionally, the carbonation processes (mainly favored in systems with lower MK/CH [64]) also consumes CH and should be separately taken into account in the evaluation of experimental data, e.g. as shown in [65, 219]. Furthermore, the transformation and/or decomposition processes of aluminate phases, e.g. the decomposition of C_4AH_{13} after 28 or 56 days [54, 64], can partially induce the further liberation of CH as exemplarily shown in Figure 14 [54, 61, 64, 68]. When not differentiating between the specific phases formed, only general tendencies can be provided from the CH consumption in MK

reactions. With the Chapelle test, a consumption of 1.3 g [220, 221] to 1.5 g [87] CH per gram (of very reactive) MK was measured.

Several studies reported the consumption of CH when reacting with MK [53, 56, 68, 71, 72, 87, 104], that is dependent on the formed products explained above and consequently influenced by different factors like e.g. curing conditions (temperature and moisture), w/s, MK/CH as well as the presence of secondary activators like sulfates and/or alkali hydroxides [59]. The present study outlines only the main tendencies regarding CH consumption as found in MK-CH systems. In Figure 14, the maximum value for consumed CH expressed in percentage of the initial amount of CH is strongly dependent on the MK/CH ratio [68]. The data from different studies is summarized in Figure 16 for a curing time of 28 days at ambient temperatures [56, 68, 104]. The amount of consumed CH (as percentage of the initial amount of CH) rises with increasing MK/CH as a result of a decreasing amount of initial CH in the mixture. With MK/CH of 1.0 the entire amount of CH is consumed after 28 days [56]. The data from Figure 16 was used to calculate the consumed CH normalized to the initial amount of MK, that is shown in Figure 17. With increasing MK/CH ratio the amount of consumed CH in reaction products decreases after 28 days. After that time, CH is fully consumed for MK/CH of 1.0. Regarding different curing temperatures, Rojas and Cabrera reported an accelerated CH consumption in the first days at 60 °C compared to 20 °C, but for later ages, CH was not fully consumed, as shown in Figure 18 (94 % after 123 days) [71], possibly due to a diffusion limitation mechanisms in dense microstructures [222, 223]. Avet et al. found that for higher MK/CH ratios (1.0 - 3.0), CH is consumed at 20 °C after 4 days at the latest, observed by a plateau in calorimetry (Figure 15) and the absence of XRD peaks of CH [87]. As the samples included small amounts of additional alkali hydroxide and sulfate (SO_3/MK = 0.06 and K_2O/MK = 0.08), CH consumption was faster compared to systems without secondary activators. The acceleration of CH consumption due to the addition of alkaline activators was also shown in other studies (at 40 °C), together with a more enhanced CH consumption for higher w/s ratios (0.80 vs. 0.35) [59].

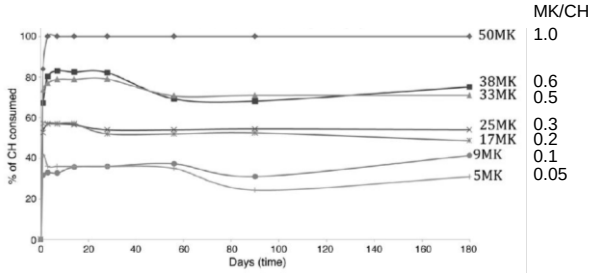

Figure 14: Consumed CH in samples with different MK/CH cured at 20 °C [68]. © 2012 used with permission of Elsevier Science & Technology Journals from [68]; permission conveyed through Copyright Clearance Center, Inc..

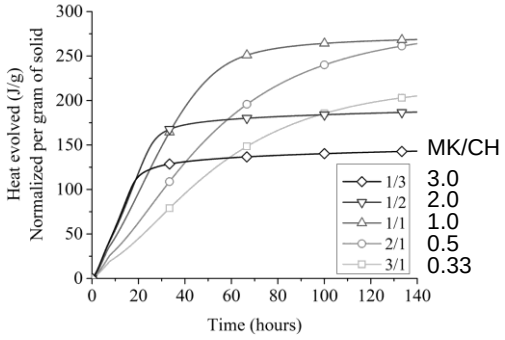

Figure 15: Heat evolved for different MK/CH at 20 °C (MK/CH = 1.0, 2.0 and 3.0 reach a plateau due to the absence of CH) [87]. © 2016 used with permission of Elsevier Science & Technology Journals from [87]; permission conveyed through Copyright Clearance Center, Inc..

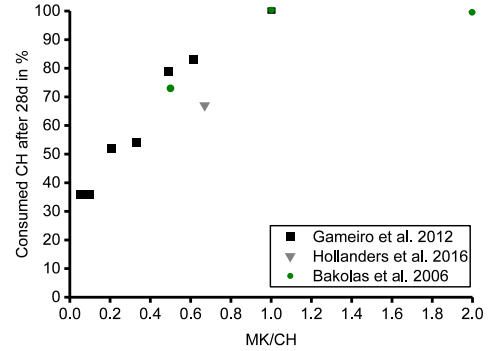

Figure 16: Consumed CH after 28 days in % at ambient temperatures [56, 68, 104].

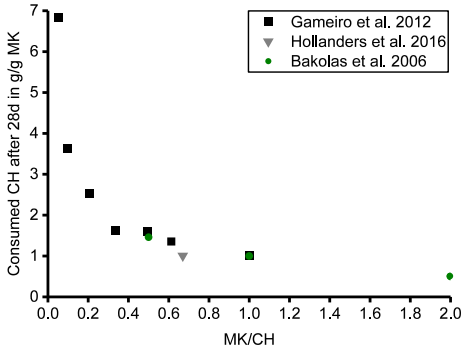

Figure 17: Consumed CH after 28 days calculated in g/g MK at ambient temperatures [56, 68, 104].

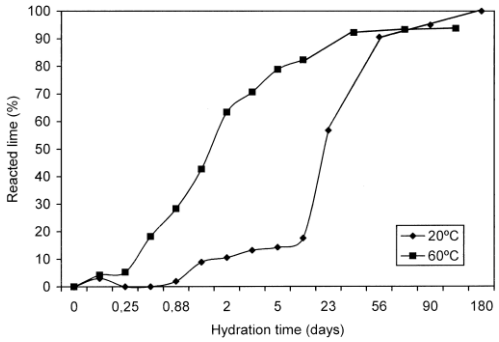

Figure 18: Consumed CH in % at 20 °C and 60 °C with MK/CH of 1.0 [71]. © 2002 used with permission of Elsevier Science & Technology Journals from [71]; permission conveyed through Copyright Clearance Center, Inc..

2.5.2 Effect of Alkali Hydroxides

The addition of alkali hydroxides (concentration < 1 M) mainly influences the dissolution of MK and CH as described in detail in section 2.4. Two opposite phenomenon occur: a) MK dissolution is enhanced with increasing alkali hydroxide content [31, 76, 180–184] whereas b) CH dissolution is impeded due to the higher pH [53, 59, 147, 183]. The changes in dissolved ions from MK and CH should affect the kind of hydrate phases formed, but information regarding this specific phenomenon is rare in literature. In one study, different reaction products were identified when comparing different aqueous solutions (H_2O vs. 0.5 M NaOH) for the preparation of MK-CH samples [75]. Whereas C-S-H with C/S of approx. 1.0 was the main reaction product in both samples, C_4AcH_{11} and C_4AH_{13} were formed in the first day of reaction in samples prepared with water, whereas in NaOH activated systems additional C_2ASH_8 was detected [75]. This can be explained by the extended silica solubility range of MK with increasing pH (outlined above), resulting in a higher amount of dissolved silica in the solution leading to the precipitation of C_2ASH_8. A recent study [137] found no significant impact of alkali type (varying molarities 0 – 2 M of KOH vs. NaOH) on the long-term reactivity of different SCMs with calcium hydroxide.

2.5.3 Effect of Carbonates

When carbonates are present in MK-CH systems, additional products occur in the main reactions, namely hemi- (Hc, $C_4Ac_{0.5}H_{12}$) and/or monocarboaluminates (Mc, C_4AcH_{11}) [54, 56, 61, 64, 66, 76, 105, 143]. In this study, these carboaluminates are indicated as CO_3-AFm. They were observed regardless of the source of carbonates, being present either as carbon dioxide (contamination) from air exposure [58, 72], or in the raw materials CH [56, 61, 66, 72, 107, 224] and/or MK [225] and/or from systematic addition of calcium carbonate (Cc) [87, 137].

The formation of Hc and Mc from the reaction of MK with Cc and CH can generally be described with the following reactions:

$AS_2 + 0.5\ Cc + 3.5\ CH + 8.5\ H \rightarrow C_4Ac_{0.5}H_{12}$ [143] (16)

$AS_2 + Cc + 5\ CH + 8\ H \rightarrow C_4AcH_{11} + 2\ C\text{-}S\text{-}H$ [226] (17)

Cc: Calcium carbonate ($CaCO_3$)
$C_4Ac_{0.5}H_{12}$: Hemicarboaluminate (Hc)
C_4AcH_{11}: Monocarboaluminate (Mc)

According to eq. 17 and stoichiometry calculations, Mc forms from a MK/Cc mass ratio of approximately 2.0 [218]. In some studies, Mc and Hc are reported to be stable at 25 °C as carbonate provides thermodynamic stabilization for the AFm phase [144, 227, 228]. When comparing these two CO_3-AFm phases, Mc is more stable [191], whereas the stability of Hc is controversially discussed depending on further aspects, like e.g. the presence of calcite (not stable) [144] as well as foreign anions such as chloride, sulfate or hydroxides (stabilization due to replacement ions) [229]. In contrast to CO_3-AFm, the stability of monosulfoaluminate (Ms) is marginal at ambient temperatures [144, 227], and will be further discussed in section 2.5.4.

In general (results coming from cementitious systems), the formation of CO_3-AFm was reported to result in a pore refinement by space filling [103, 143, 218] and consequently has positive effects on mechanical properties. The CO_3-AFm precipitation was also found to be dependent on the available space in the porous system (mainly forms in larger pores) [103, 143] and could slow down reaction rates due to the porosity refinement [143]. These remarks (coming from studies dealing with LC^3-systems, but also seem valid for MK-CH systems) demonstrate the importance of kinetic aspects as well as the microstructure development on the hydrate phase formations in experiments, that often cannot solely be explained by stoichiometric rules.

A detailed investigation of the influence of Cc on MK reactivity in MK-CH systems is rare in literature. Results are mainly available only for small amounts of carbonates, originating from the impurities in the used MK and/or CH (e.g. 5 % of Cc in the CH used in [56]) and/or originating from atmospheric carbon dioxide [54, 56, 72]. When the used CH was contaminated with Cc, more Mc was found e.g. in pastes with lower MK/CH (0.5, 1.0 and 2.0 tested at 25 °C) [56].

With ongoing hydration several authors observed a slight decrease of Mc [54, 56, 68, 72, 207], leading to the assumption, that it decomposes with time. Bakolas et al. e.g. identified the precipitation of Mc from 3 to 14 days, but not beyond 14 days (MK/CH of 1.0 and 2.0) [56]. Also Gameiro et al. explained the liberation of CH at 56 and 90 days with a possible decomposition of Mc and C_4AH_{13} [54]. The influence of Cc addition on the amount of free CH, due to the precipitation of phases like CO_3-AFm, was also mentioned by Matschei et al. [144]. As possible reaction products arising from the decomposition of Mc, calcium aluminate hydrates ($Ca_2Al(OH)_7 \cdot 6.5\ H_2O$) and/or hydrocalumite ($Ca_4Al_2CO_3(OH)_{12} \cdot 5\ H_2O$ [219]) were reported in literature [219, 230]. Azeredo et al. found that a decline of Mc seems to be dependent on MK/CH [72]. Mc decreases strongly over time with MK/CH of 2.0, but only slightly with a lower MK/CH of 1.0 [72]. The authors explained this finding with the higher MK content, resulting in more aluminum available in the system that can form C-A-H phases leading to a lower calcium content to form calcium carbonate phases like CO_3-AFm [72]. With a lower MK/CH (and consequently more CH in the samples) more available calcium ions can contribute to the formation of Mc [72]. Similar observations were found in other studies, showing a stronger decrease of Mc with a higher MK/CH ($0.5 < 1.0 < 2.0$) [56, 72]. For a low MK/CH of < 0.3, even a gradual increment of Mc could be detected up to 1.5 years [65]. In contrast, Žemlička et al. observed Mc and C_4AH_{13} particularly for high MK/CH [58]. These opposite findings could be due to different carbonation reactions, e.g. Mc can also arise from reactions of amorphous C-(A-)S-H, C-S-H gel and CH with atmospheric carbon dioxide and is not necessarily a reaction product of MK with CH and Cc only [58].

2.5.4 Effect of Sulfates

When a sulfate source is present in the MK-CH system, ettringite (also referred as “AFt” in literature) is formed [58, 61, 62, 66, 67, 76, 87, 105–107] according to eq. 18 [62, 75, 224], besides the pozzolanic

reaction products described above. Ettringite forms already in the first hours [59, 107] before the precipitation of C-S-H and aluminate phases like C_4AH_{13} and/or C_2ASH_8 [58, 59, 75]. Due to its needle-like structure the formation of ettringite is responsible for an increase of compressive strength of MK-CH systems when sulfates are present [58, 61]. The rate of ettringite formation is mainly dependent on the availability of sulfates, that varies with the kind of sulfate source and its respective solubility [59, 75]. Scherb et al. reported a constant rate of ettringite formation until the sulfate carrier was completely dissolved after approx. 20 h (Figure 20) [107]. If no carbonates are present in the system and with sulfate consumption, ettringite transforms with increasing dissolution of aluminum from MK into monosulfoaluminate (Ms, C_4AsH_{12}, also "AFm" in literature) according to eq. 19 [59, 62, 66, 75, 87] as supported by thermodynamic modeling [137]. This transformation reaction is reported to be endothermic [75], thus explaining the occurring peak/shoulder in the calorimetry rate curves. A complete reaction of gypsum was reported after one day with MK/CH of 1.0, a w/s ratio of 0.8 and a molar ratio of SO_3/Al_2O_3 of 0.1 at 40 °C, followed by the development of Ms [75]. In literature, a sequence of reactions occurring during the first day cured at 40 °C was described as follows: a) formation of ettringite, b) formation of C-S-H and C_4AH_{13} and c) transformation of ettringite to Ms [59].

$$2\ Al(OH)_4^- + 6\ Ca^{2+} + 3\ SO_4^{2-} + 26\ H_2O + 4\ OH^- \rightarrow C_6As_3H_{32} = \text{ettringite} \quad [75, 224] \quad (18)$$

$$C_6As_3H_{32} + 4\ Al(OH)_4^- + 6\ Ca^{2+} + 6\ OH^- \rightarrow 3\ C_4AsH_{12} + 8\ H_2O \quad [75] \quad (19)$$

Stoichiometrically, the stabilization of Ms was proposed by Zunino et al. according to eq. 20 in the presence of CH and calcium sulfate (Cs) [81].

$$AS_2 + 5.4\ CH + 0.8\ Cs + 12\ H \rightarrow 2\ C_{1.5}A_{0.1}SH_4 + 0.8\ C_4AsH_{12} \quad [81] \quad (20)$$

Ms itself is thermodynamically metastable (Matschei et al. reported a lower limit of thermal stability at ~ 5 °C [231] and lower stability at 25 °C [144], whereas Damidot and Glasser found an increased stability at > 45 °C [232]) where a possible transformation into hydrogarnet phases was reported in [59]. The sulfate liberated with this transformation was temporarily incorporated in C-S-H and subsequently released to the pore solution, leading to an increase in sulfate content [59].

Deng et al. found, that the A/S ratio of C-A-S-H phases decreases with increasing sulfate concentration [62] possibly due to the preferred incorporation of aluminum in ettringite and Ms formation. With an increasing amount of sulfate in the system, more ettringite [61, 224] and Ms is formed (Figure 19), while Na_2SO_4 vs. $CaSO_4$ leads to similar reaction products [62]. Avet et al. tested different SO_3/MK ratios (0.02, 0.04, 0.06 and 0.08) with a fixed K_2O/MK ratio of 0.08, observing ettringite being formed after one day only in the samples with the two highest SO_3 contents [87]. Besides, sulfate seems to increase the aluminum dissolution from MK, that leads to an enhanced formation of C-A-S-H phases as shown in Figure 19 and generally to a higher amount of aluminum in hydrate phases [62]. Some studies report that with the incorporation of sulfate in MK-CH systems, no or less stratlingite was detected [62, 66, 224]. This could be explained by the formation of Ms from stratlingite in the presence of gypsum according to eq. 21 [62, 66]. The liberated SiO_2 from this phase transformation could possibly react further with CH to C-S-H phases [62, 66]. In systems with high amounts of sulfate, e.g. 8 wt.-%[6] gypsum, Ms can further react to ettringite according to eq. 22 [66]. A similar finding was observed for C_4AH_{13}, that was not detected or only in traces in sulfate activated MK-CH systems [59].

$$C_2ASH_8 + CaSO_4 \cdot 2\ H_2O + 1.67\ Ca(OH)_2 + 2\ H_2O \rightarrow C_4AsH_{12} + C_{0.67}SH_{1.67} \quad [66] \quad (21)$$

$$C_4AsH_{12} + 2\ (CaSO_4 \cdot 2\ H_2O) + 16\ H_2O \rightarrow C_6As_3H_{32} \quad [66] \quad (22)$$

In contrast to these general findings, Scherb et al. recently published an article showing an ettringite stabilization after 20 h of curing without the formation of Ms or CO_3-AFm up to 50 h in MK-CH systems with MK/CH of 1.0, w/s of 1.0 with an alkaline solution containing 0.1 M NaOH and 0.5 M KOH (pH =

[6] (of the solids).

13.5) and 10 wt.-% of the solids being replaced by anhydrite at 25 °C (Figure 20) [107]. The aluminum released from MK seems to be incorporated in C-S-H phases after the maximum amount of ettringite is reached [107]. The authors assumed that the rate and the amount of released aluminum from MK is not enough at early ages of hydration in their experimental setup (up to 50 h at 25 °C) to form Ms [107], underlining the relevance of kinetic aspects for the assemblage of hydrate phases formed. No CO_3-AFm was formed due to the low Cc content (3.5 wt.-% impurities in the used lime) [107], further discussed in section 2.5.5. Figure 20 summarizes the phase assemblage and the heat flow over time, showing a rapid dissolution of MK and CH in the first 2 h, subsequently slowing down and accelerating again between 15 h to 25 h (MK) and 15 h to 30 h (CH), respectively [107]. Anhydrite dissolves continuously up to 15 h followed by a slight acceleration up to a complete dissolution after 20 h [107]. During anhydrite dissolution, a small amount of gypsum precipitates, but dissolves up to 20 h [107]. Ettringite is formed from 2 h onwards up to 20 h and stays almost constant up to 50 h [107].

The main differences in phase formations with and without sulfate addition in MK-CH systems is graphically shown in Figure 21. Deng et al. identified stratlingite as the main reaction product besides C-A-S-H in systems without sulfate, whereas with sulfate, ettringite, AFm and C-A-S-H was formed while stratlingite was not detected (MK/CH = 3.75 - 4.0, w/s = 5.0, 50 °C, 28 d, continuously stirred) [62].

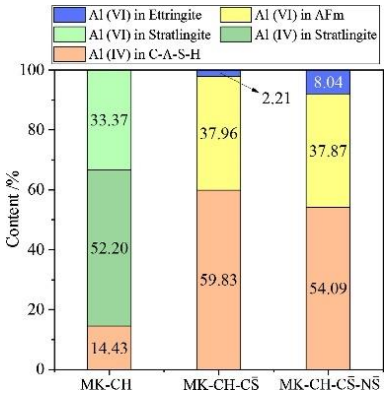

Figure 19: Phases formed in MK-CH systems with CS̄: $CaSO_4$ and NS̄: Na_2SO_4 (MK/CH = 3.75 - 4.0, w/s = 5.0, 50 °C, 28 d, continuously stirred, MK-CH-CS̄: SO_4/MK (weight ratio) = 0.047 and MK-CH-CS̄-NS̄: SO_4/MK = 0.065) [62]. © 2020 used with permission of Elsevier Science & Technology Journals from [62]; permission conveyed through Copyright Clearance Center, Inc..

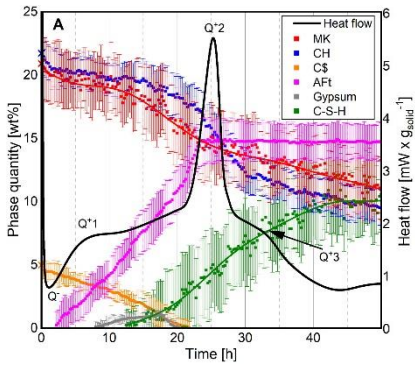

Figure 20: Phase quantification and heat flow of MK-CH-C$ with C$: anhydrite (Q+1: formation of ettringite and gypsum, Q+2: accelerated ettringite formation, Q+3: change in dissolution rate of MK and CH as well as formation of C-S-H) [107]. © 2021 used with permission of Elsevier Science & Technology Journals from [107]; permission conveyed through Copyright Clearance Center, Inc..

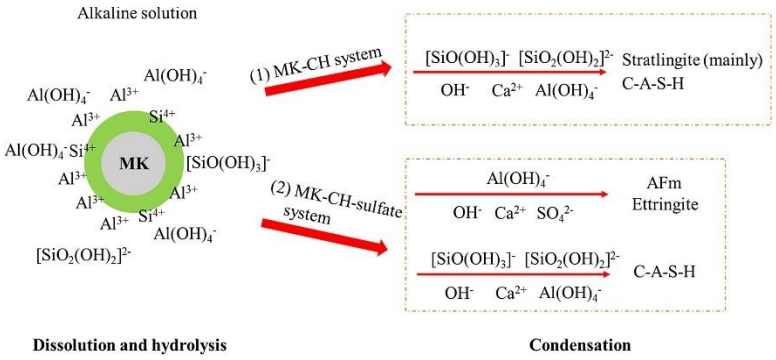

Figure 21: Schematic diagram of dissolution, hydrolysis and precipitation (condensation) processes in MK-CH and MK-CH-sulfate systems [62]. © 2020 used with permission of Elsevier Science & Technology Journals from [62]; permission conveyed through Copyright Clearance Center, Inc..

2.5.5 Interaction of Alkali Hydroxides, Carbonates and Sulfates

This section reports a limited number of results that have been documented in the literature regarding interaction processes of the simultaneous presence of alkali hydroxides, carbonates and sulfates in MK-CH systems.

When combining sulfate with NaOH in MK-CH systems (0.5 M NaOH compared to H_2O), no significant effect on the composition of the reaction products was observed, but the reaction rates were accelerated [75]. As outlined in section 2.5.2, effects on ion solubility with increasing pH due to alkali hydroxide addition could probably change the preferred formation of hydrate phases, but detailed information is lacking to date.

For the simultaneous presence of sulfates and significant amounts of (added) carbonates, different phase formations were investigated compared to the findings explained in section 2.5.3 and 2.5.4. Rapidly formed ettringite [75, 76, 107] is stabilized by carbonates [87], as the transformation of ettringite to Ms is suppressed by the formation of more stable [144, 227] CO_3-AFm phases (Hc and Mc) [76, 87, 107, 143, 173, 218] as stoichiometrically expressed according to eq. 23 [81].

$$AS_2 + 5.4\ CH + 0.4\ Cc + 1.2\ Cs + 20\ H \rightarrow 2\ C_{1.5}A_{0.1}SH_4 + 0.4\ C_4AcH_{12} + 0.4\ C_6As_3H_{32} \quad [81] \quad (23)$$

At this point it should be noted, that the occurring reaction processes are dependent on the specific amounts of sulfates and carbonates in a MK-CH system [66]. Because of this the Cc/SO_4 weight ratio will be used as a basis for comparison further in this study. The following data in wt.-% refers to the respective weight percentage of the solids in the samples. For a very low Cc/SO_4 weight ratio of 0.22 (MK/CH of 1.0 with 3.5 wt.-% Cc in the lime used and 5 wt.-% anhydrite) ettringite was stabilized, but neither Ms (discussed in section 2.5.4) nor CO_3-AFm was detected [107]. The authors concluded, that the Cc content was too low for a CO_3-AFm formation during early hydration up to 50 h [107]. Another study also investigated a favored ettringite formation rather than Ms and CO_3-AFm for a Cc/SO_4 weight ratio of 0.52 (MK/CH of 1.0 with 5 wt.-% Cc in the lime used and 8 wt.-% gypsum), and concluded that Ms can transform to ettringite in systems with high amounts of added gypsum (section 2.5.4) [66]. For a Cc/SO_4 weight ratio of 1.08 (MK/CH of 1.0 with 5 wt.-% Cc in the used lime and 4 wt.-% gypsum), Wang et al. observed Ms in samples cured at 20 °C for two months, whereas lower amounts of stratlingite and Mc (compared to samples without sulfate) and no Hc were detected [66]. A decrease in stratlingite with more sulfate was explained by the reaction of stratlingite with gypsum to form Ms, while dissolved SiO_2 reacted with CH to form C-S-H phases as outlined in eq. 21 [66]. With a higher Cc/SO_4 ratio of 7.7 (MK/CH of 0.33 with 10.78 wt.-% added Cc and 2.54 wt.-% K_2SO_4), Avet et al. reported the stabilization of ettringite along with the formation of CO_3-AFm as outlined above [87].

The same authors investigated different alkali hydroxide contents in their samples and found ettringite formation only for lower alkali hydroxide contents, namely K_2O/MK ratios of 0.06 and 0.08 compared to 0.1 and 0.12, when SO_3/MK was fixed to 0.06 [87]. They observed an enhanced pozzolanic reaction with higher alkali hydroxide contents and explained the increased CO_3-AFm rather than ettringite formation (Figure 22) due to the higher exponent of the OH^- activity in Hc (5 compared to 4 [233]) with increasing pH [87, 234].

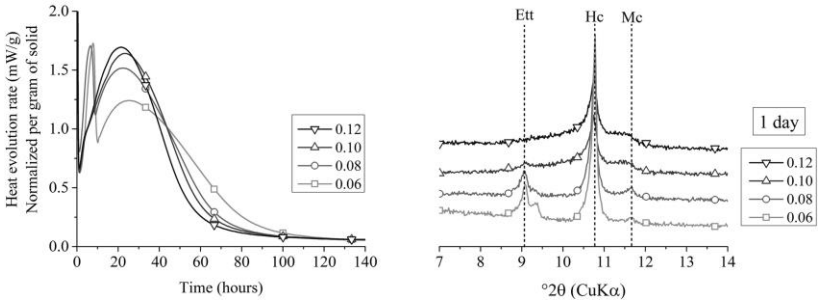

Figure 22: Heat evolution and XRD after 1 day of samples with varying K_2O/MK ratios and fixed SO_3/MK of 0.06 at 20 °C (Ett: Ettringite) [87]. © 2016 used with permission of Elsevier Science & Technology Journals from [87]; permission conveyed through Copyright Clearance Center, Inc..

2.6 Mathematical Modeling Outlook

Thermodynamic (TD) modeling is a scientific method to predict the development of long-term reaction products in equilibrium-state [137, 233, 235, 236]. Due to this equilibrium-state restriction, employing TD calculations for studying transformation reactions is challenging. Most recently, Bharadwaj et al. [137] used thermodynamic modeling to interpret pozzolanic reactivity tests, including metakaolin. Modeling approaches for reactivity of SCMs in cement blends were summarized by Skibsted and Snellings [237]. To improve thermodynamic modeling of SCM reactivity, additional data should focus on structure, dissolution, and kinetics to develop comprehensive physics-based models that accurately predict fundamental material properties and account for the reaction kinetics. An analytical dissolution rate model, applicable to a broad spectrum of phases, such as kaolinite to basaltic glass, which share chemical and structural similarities with common pozzolanic precursors, could be employed for metaclays and vitrified slags. Atomistic modeling methods have recently emerged and turned out to be a very powerful approach to understand the microstructure and it's relation to reactivity. Izadifar et al. [75] used ab-initio computations to study the impact of thermal activation on kaolinite structure and layer stacking providing inputs for further reactivity modeling. For example, Izadifar et al. [208] presented an ab-initio computational approach for obtaining the activation energies required for the dissolution of metakaolin (MK) providing a methodology for missing input data to predict the mesoscopic dissolution rate. Gong et al. [238] exerted atomistic simulations to generate detailed microstructural representations for various synthetic glasses. In another study, Gong and White [239] developed two microstructural descriptors related to reactivity in alkaline environments: average metal-oxygen dissociation energy (AMODE) and average self-diffusion coefficient (ASDC). However, atomistic or meso-scale computations have not yet been applied to model the intrinsic reactivity processes.

2.7 Summary of Findings

The main results of this review study are summarized in Figure 23 along with a comprehensive list of findings. The formation of C_2ASH_8, C_4AH_{13} and $C_3AS_yH_z$ are ranked according to different MK/CH ratios and summarized in Table S1-2 with additional details provided in Table S1-3 of the Supplementary Material.

In this review study, the MK/CH ranking can also be considered as a simplified approach for scientists to account for different oxide compositions of the initial mix (mainly CaO, SiO_2 and Al_2O_3) and the associated hydrate phase formations. However, some kinetic aspects as well as the microstructure development may significantly contribute to the hydrate phase formation as well. Moreover, when comparing various MK/CH ratios another relevant factor is the degree of reaction of both MK and CH. This may influence the hydrate phase formation and determines the availability of educts, e.g. CH, that can further participate in (trans)formation reactions over time.

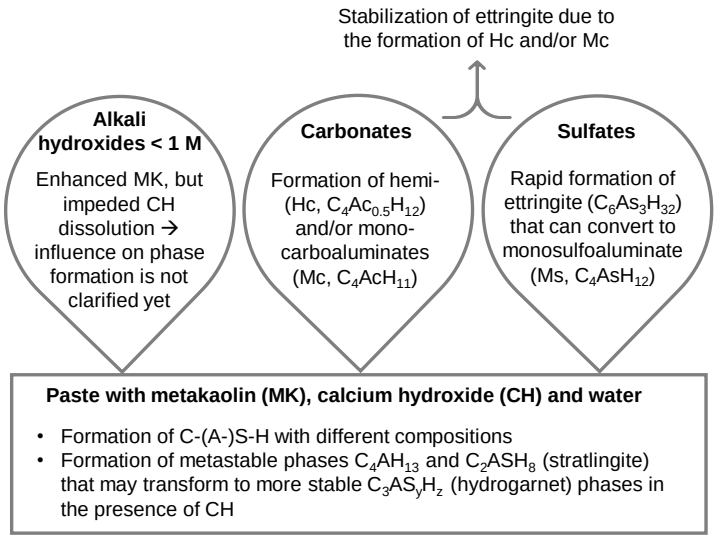

Figure 23: Summary of hydrate phase formations in MK-CH systems with added alkali hydroxides, carbonates and sulfates.

1) Most studies identified **C-(A-)S-H** phases as amorphous reaction products due to the pozzolanic reaction of MK [27, 50–59]. C-(A-)S-H has varying compositions from the first day on [54, 56, 68], up to the longest tested period of 5 years [57]. In general, a decrease in C/S (from 1.70 to 0.85) of the C-S-H phases with increase in MK/CH (0.5 to 2.0) due to the increasing amount of soluble Si from MK was detected (after 90 days of reaction at 55 °C) [69]. With higher MK/CH (2.0 to 7.6 [69]), the C-A-S-H composition shows an increased incorporation of aluminum.

2) **Stratlingite (C_2ASH_8)** was detected for a MK/CH ratio of 0.3 or higher, but not for lower ratios [54, 65, 68]. In the range of 0.3 to 0.6 [65, 69], between 1 day and 28 days its amount increased [56, 68], followed by a decrease up to 1.5 years [65], which was due to the formation of hydrogarnet in the presence of CH [65, 68]. For pastes with higher MK/CH ratios (1.0 - 2.0), stratlingite was observed [51, 53, 69, 72] with an increase from 1 day up to 180 days [54, 56, 65, 68], and remains stable afterwards (up to 1.5 years [65]) as the available CH for transformation reactions is lacking.

3) From the reviewed literature, the presence of **C_4AH_{13}** in MK-CH systems is not quite evident. In some studies, C_4AH_{13} was observed from 1 day to approx. 28 days [51, 53, 54, 65, 68, 69], and possible transformation processes to hydrogarnet and/or $Ca_2Al(OH)_7 \cdot 6.5\ H_2O$ were reported as well [54, 65, 68]. Some publications do not report C_4AH_{13} formation possibly due to its small amount [66], low crystallinity [53, 57, 66, 70] and/or a possible overlapping with other hydrate phases in TGA/XRD [51, 53, 57, 70, 71]. Increasing amounts with time up to 360 days [53, 206] and constant values afterwards were reported for MK/CH of 1.0 and related to the absence of CH [71].

4) **Hydrogarnet ($C_3AS_yH_z$)** phases were not detected for low MK/CH (0.05 to 0.2) [54, 65, 68] that correspond well with the absence of stratlingite in that particular range. Within the MK/CH range of 0.3 to 0.6, hydrogarnet was observed from 28 days up to 1.5 years [65, 68] due to transformation reactions of stratlingite and C_4AH_{13} [65, 68, 70]. For higher MK/CH (1.0 – 2.0), hydrogarnet was not detected [51, 53, 54, 56, 65, 68, 69, 72] as the amount of remaining CH is too low for transformation reactions.

5) The incorporation of **secondary alkali hydroxides** in a solution (concentration < 1 M NaOH and/or KOH), mainly leads to an accelerated MK dissolution [31, 76, 180–184], especially during the first days [59] and consequently to an increased pozzolanic reaction of the material [59, 76, 87, 192, 193]. The corresponding increase in pH enhances the dissolution rate of MK [31, 76, 180–184], but inhibits CH dissolution [53, 59, 147, 183]. This opposing effect can influence the hydrate phase formations, that needs to be further addressed in future research.

6) When introducing **carbonates** to the system, either as impurities in raw materials or curing/aging under atmospheric carbon dioxide, CO_3-AFm in the form of Hc and Mc were formed [54, 56, 64, 66, 76, 105, 143]. In several studies, these phases were mainly detected from the first day to approx. 14 or 28 days [54, 56] decreasing or missing at later curing times [65, 68, 72], indicating a decomposition with curing time that leads to a liberation of CH [54, 144], especially with higher MK/CH ratios [72].

7) The addition of **sulfate** (to MK-CH systems) leads to a rapid formation of ettringite [58, 62, 66, 76, 87, 105–107] that later may transform to Ms (depending on the sulfate content), if no carbonates are present [62, 66, 75, 87]. Ms may transform to hydrogarnet at later ages [59]. When additionally significant amounts of carbonates are incorporated in the paste, ettringite is stabilized [87, 107] and CO_3-AFm forms instead of Ms [76, 87, 107, 143, 173, 218]. Besides, sulfate accelerates MK dissolution and thus the early stage of pozzolanic reaction [62]. At later ages, sulfate reduces (or completely eliminates) stratlingite [62, 66, 224], due to the transformation reaction into Ms [62, 66].

8) **Temperature** (55 °C - 60 °C vs. 20 °C - 25 °C) mainly influences the kinetics of reactions leading to an accelerated phase formation [69, 70, 74, 87] and favoring a more stable hydrogarnet [58, 69, 70]. At temperatures of around 60 °C, hydrogarnet may precipitate directly [55, 74], while the transformation reactions (C_2ASH_8 and C_4AH_{13}) were detected in a MK/CH range of 0.38 - 2.0 [58, 69, 209] (lack of information for MK/CH = 0.3), whereas this range narrows at ambient temperatures to MK/CH of 0.3 - 0.6, explained by a lack of CH for MK/CH of 1.0 and higher [51, 53, 54, 56, 65, 68, 69, 72]. The narrower range in MK/CH for the transformation reaction identified in this review study could possibly be traced back to the investigated values of MK/CH in the specific studies (more research needed) e.g. for MK/CH of 0.6 to 1.0. Another explanation would be an increase of all reaction rates with temperature, that may lead to the coexistence of CH and stratlingite for MK/CH of 1.0 and higher.

2.8 Conclusions and Future Work

The main findings, summarized in section 2.7, highlight the formation and stability of reaction products affected by parameters such as MK/CH ratio, curing time, and temperature. By incorporating this information and addressing research gaps, input parameters for modeling approaches can be obtained to design and validate metakaolin-based binders. These models would integrate thermodynamics, kinetics, and microstructural aspects, offering scientific and engineering tools for tailoring binder compositions and understanding hydration/pozzolanic reactions affected by raw material selection, alkali additions, w/s ratios, and curing conditions.

Following research gaps are identified that should be addressed in future research:

- Type of alkali hydroxide (e.g. NaOH vs. KOH) on the dissolution of MK, especially differentiating between the effect of pH and alkali type;
- opposing effect of alkali hydroxides on the hydrate phase formations, namely due to a) enhanced MK dissolution with increasing alkali hydroxide content and b) impeded CH dissolution due to a higher pH;
- transformation of metastable hydrate phases formed in the temperature range between 20 °C and 60 °C, especially regarding the formation of hydrogarnet (via direct precipitation and/or transformation reactions);
- quantifying hydrate phases formed for varying amounts of sulfates and/or carbonates (e.g. for different SO_4/MK, Cc/MK and Cc/SO_4 ratios), while also addressing the kind of sulfate and/or carbonate sources (e.g. Na_2SO_4 vs. K_2SO_4);
- C-(A-)S-H stoichiometric compositions (e.g. C/S and C/A ratios), microstructures, alkali binding capacity and thermodynamic parameters;

- mathematical models combining chemical thermodynamics with kinetics (reaction and mass transfer rates) to link e.g. the consumed CH (readily obtained by TGA measurements) with the formed reaction products and microstructure, while also including the transformation reactions, i.e. coexistence of metastable and stable phases.

3 Publication 2: Isothermal Calorimetry

Publication 2 (Materials and Structures, https://doi.org/10.1617/s11527-023-02217-6)

Early Metakaolin Reactions in Pozzolanic R³-Test: Calorimetry Baseline Correction of Initial Temperature Jump due to Ex-situ Mixing

Kira Weise[1,*], Neven Ukrainczyk[1], Eduardus Koenders[1]

[1] Technical University of Darmstadt, Institute of Construction and Building Materials, Germany.
* Corresponding author. E-mail address: weise@wib.tu-darmstadt.de.

Abstract: The increasing concerns regarding global warming and the scarcity of raw materials in the construction industry have led to a growing need for alternative low-carbon binders to partially replace ordinary Portland cement. To assess the suitability of pozzolans as supplementary cementitious materials (SCMs), the R³-test has been introduced and successfully validated for a wide range of materials. This test provides an opportunity to analyze the reactivity classification and study the reaction mechanisms and kinetics of novel SCMs in a well-controlled environment. In this study, the focus lies on evaluating the early reactions of lime paste samples through isothermal calorimetry tests conducted at 40 °C. However, conventional mixing methods present experimental challenges. In-situ mixing fails to achieve proper paste homogenization, while ex-situ mixing results in a temperature difference at the start of testing due to the elevated testing condition of 40 °C. To address these concerns, a novel calorimetric methodology is proposed for early detection of reactivity responses. The main concept involves establishing a baseline correction for the temperature difference caused by ex-situ mixing, which is calibrated using an inert sample. This correction allows for the extraction of the heat generated by the early reactions. Combined with the Tian time correction, this methodology enables the evaluation of early reactions in lime paste samples measured with isothermal calorimetry at 40 °C within the first 100 minutes after mixing. The effectiveness of this methodology was demonstrated by evaluating the early reactions and the impact of potassium sulfate on three different types of metakaolin.

Keywords: R³-test; isothermal reaction calorimetry; Tian correction; metakaolin; supplementary cementitious materials; early pozzolanic reactions.

3.1 Introduction

The increasing global interest in alternative binder materials is due to global warming and raw material shortages in the construction industry. In order to assess the suitability of novel materials for the use as supplementary cementitious materials (SCMs) standardized testing procedures are needed [240, 241]. In this context, Avet et al. introduced the R³-test (rapid, relevant, reliable) in 2016 [87] that was further optimized and validated over a wide range of materials [85, 86]. With the R³-test it is possible to classify the raw materials by testing their reactivity in an alkaline suspension after seven days stored at 40 °C [86]. The reactivity can be measured through various testing procedures. Meanwhile, determining the bound water content using an oven test, as well as calculating the overall heat release from isothermal calorimetry, have been suggested [85, 240].

In addition to the defined composition of the R³-samples, a wider variety of sample compositions can be utilized to acquire more comprehensive insights into the mechanisms and kinetics of the pozzolanic reactions of specific SCMs. The main objective of this approach is to investigate the SCM reactions in a well-defined and controlled environment. Emphasis is on comprehending the fundamental phase (trans)formations and their kinetic behavior while minimizing the influence of additional factors that may be present in more complex cementitious systems. For this purpose, isothermal calorimetry seems to be a promising testing procedure. When conducting calorimetry at 40 °C with lime paste samples similar to the R³-test, two main experimental issues were identified, namely a) in-situ mixing challenges

to achieve a good homogenization as the alkaline suspension cannot be introduced by a syringe and b) ex-situ mixing leads to a temperature difference due to the elevated testing temperature of 40 °C. Even when the materials are preconditioned at 40 °C prior to mixing, practically it is challenging to provide reproducible conditions for each sample as the sample temperature inevitable drops during the mixing process. Mixing in a water bath seems like another opportunity, but is elaborated and intermediate steps are also difficult to control. To omit the initial heat release peaks that are affected by thermal equilibration of the sample the R³-test procedure (used to classify different SCMs according to their total reactivity) recommends to calculate the cumulative heat release starting from 1.2 h (72 min) after mixing [85]. Mixing the samples at 40 °C using a water bath, did not change the test results from 72 min onwards [85], indicating that the temperature difference effect does not affect the data gained after 72 min.

For a deeper understanding of the reaction mechanisms and kinetics of novel SCMs, especially for fast reacting materials, the very early reactions occurring within the first 72 min of the experiment could be of interest. To address the temperature difference effect during the early testing times, this article provides an experimental testing procedure for lime paste samples similar to R³-samples with isothermal calorimetry and introduces a novel methodology approach. It proposes to mix the samples ex-situ, in order to achieve good homogenization, but at ambient temperature, where an inert sample of the alkaline suspension (without added SCM) is used for a baseline correction. The methodology is based on separating the temperature difference effect, obtained from an inert sample and subtract it from the reactive one to obtain the heat generation response related to the early reaction processes. In isothermal calorimetry, the accurate recording of fast reaction processes can be influenced by a time-lag resulting from the thermal inertia between the sample and the calorimeter instrument. To address this issue, the Tian correction method has been introduced in the existing literature [242, 243]. Whenever employing the Tian correction method for the time-lag between initial and actual recording of the isothermal calorimetry, the rapidly liberated reaction heat of these lime paste samples can be monitored during the initial 100 min after mixing. This approach turned out to be very successful when studying fast reactions in calorimetry at a temperature of 40 °C. The method was demonstrated by evaluating the reproducibility of a baseline and early reaction mechanisms using three different types of metakaolin, as well as exploring the impact of potassium sulfate on the metakaolin reaction. Initial reactions of metakaolin with calcium hydroxide as well as with sulfates and/or carbonates are of particular interest, as various hydrate phases may form and transform that influence the binders performance, e.g. in terms of rheology [244, 245]. In lime-based pastes with metakaolin, sulfate incorporation rapidly forms ettringite [58, 61, 62, 66, 67, 76, 87, 105–107], which may convert to monosulfoaluminate (C_4AsH_{12}; AFm) [59, 62, 66, 75, 87] depending on sulfates and reaction time, while additional carbonates stabilize ettringite by the formation of hemi- and monocarboaluminates ($C_4Ac_{0.5}H_{12}$ and C_4AcH_{11}; CO_3-AFm) [76, 87, 107, 143, 173, 218].

3.2 Experimental Program

R³-samples consist of an alkaline suspension homogeneously mixed with a powdered SCM. As the focus of this study is on the early reactions (first 100 min), metakaolin was chosen as SCM in this study due to its high pozzolanic reactivity and the ability to form early ettringite in the presence of sulfates [58, 59, 61, 62, 66, 67, 76, 87, 105–107]. To demonstrate different intensities of early reactions, three different metakaolin were used and the alkaline suspension was prepared with (mix design according to [87, 240]) and without potassium sulfate.

The composition of 100 g suspension (R3) is outlined in Table 5 [87, 240] and consist of powdered calcium hydroxide (≥ 96 %), potassium hydroxide pellets (≥ 85 %), powdered potassium sulfate (≥ 99 %), and deionized water. For the preparation of 100 g suspension, potassium hydroxide pellets (KOH) were dissolved in 7 g deionized water for 15 min using a magnetic stirrer [84, 246]. In the next step, dissolved potassium hydroxide was homogenized with the remaining components (calcium hydroxide, potassium sulfate, and the remaining deionized water) using an electric mixer for another

15 min [84, 246]. To evaluate the effect of sulfates in the first minutes of reaction, an additional alkaline suspension was prepared without potassium sulfate according to Table 5 (0.32KOH).

To study the temperature jump effect on inert samples, eight calorimetry samples of alkaline suspension (without SCM) were prepared with (R3) and without (0.32KOH) potassium sulfate (4 for each suspension). The weighing for the reactive samples was chosen to 20.0 g ± 0.3 g. Equivalent heat capacities of inert samples were obtained by adjusting the weight of each type of inert suspension (R3 and 0.32KOH) to match the heat capacity of the reactive samples, namely 18.56 g ± 0.1 g for R3 and 18.39 g ± 0.1 g for 0.32KOH (_1). To analyze the effect of deviations from that target value, the following weights for three more samples for each inert suspension were chosen as 16.0 g ± 0.3 g (_3), 18.0 g ± 0.3 g (_2) and 20.0 g ± 0.3 g (_4), respectively. To study the potential impact of different inert samples on the baseline correction curve, an additional test series, named “inerts”, was conducted. This series also includes water samples as a control for the R³-suspensions (without SCM). Three specimens were measured for each type of inert sample, and the weighing process was adjusted accordingly to achieve the same heat capacity for each sample.

Three types of industrially produced metakaolin were used in this study. They differ mainly in their amount of amorphous content (MK1 ~ 68 wt.-% < MK2 ~ 83 wt.-% < MK3 ~ 98 wt.-%.) as well as the amount and type of incorporated impurities. Their chemical compositions are summarized in Table 6. Thermogravimetric analysis (TGA) of the raw materials shows a mass loss of around 2.2 wt.-% for MK1 in the DTG-curve between ~ 450 °C and 700 °C (Figure S2-1 in the Supplementary Material) indicating a lower calcination temperature (< 450 °C) that leads to a lower dehydroxylation degree compared to MK2 and MK3. Powder X-ray diffraction (XRD) results confirm the presence of remaining kaolinite in MK1 together with impurities like quartz, cristobalite and goethite (Figure 24). Other minerals present as impurities in MK2 comprise of muscovite, quartz and anatase, whereas MK3 is an almost pure metakaolin with only small traces of muscovite and anatase (Figure 24). TGA of the raw materials was carried out with “STA 449 F5 Jupiter” from NETZSCH (Selb, Germany) with nitrogen as an inert gas. 40 - 50 mg of powdered sample was placed in alumina crucibles, heated up to 40 °C, kept constant for 30 min and then heated up to 1000 °C at a constant heating rate of 20 °C per minute. XRD of the three metakaolin was carried out with “Bruker D2 Phaser” from Bruker Corporation (Billerica, USA), configured with CuKα1,2 radiation (40kV and 10mA), linear Lynxeye detector (5 degrees opening). All raw material samples were measured with 0.02 two theta step size and measurement time of 2 seconds per step.

Table 5: Composition of 100 g alkaline suspension with (R3) [87] and without (0.32KOH) potassium sulfate.

Suspension	$Ca(OH)_2$	K_2SO_4	KOH	H_2O
R3	37.77 g	1.48 g	0.32 g	60.43 g
0.32KOH	38.34 g	-	0.32 g	61.34 g

Table 6: Amorphous contents and chemical compositions of the used metakaolin in wt.-%.

	Amorphous	SiO_2	Al_2O_3	Fe_2O_3	CaO	MgO	Na_2O	K_2O	TiO_2
MK1*	~ 68	53-54	41-44	<0.5	n/a	n/a	n/a	<1.0	n/a
MK2	~ 83	53.0	42.2	2.4	<0.5	<0.5	<0.5	<0.5	1.8
MK3*	~ 98	52.3	45.2	<0.5	<0.5	<0.5	<0.5	<0.5	1.7

* Chemical compositions according to the manufacturer.

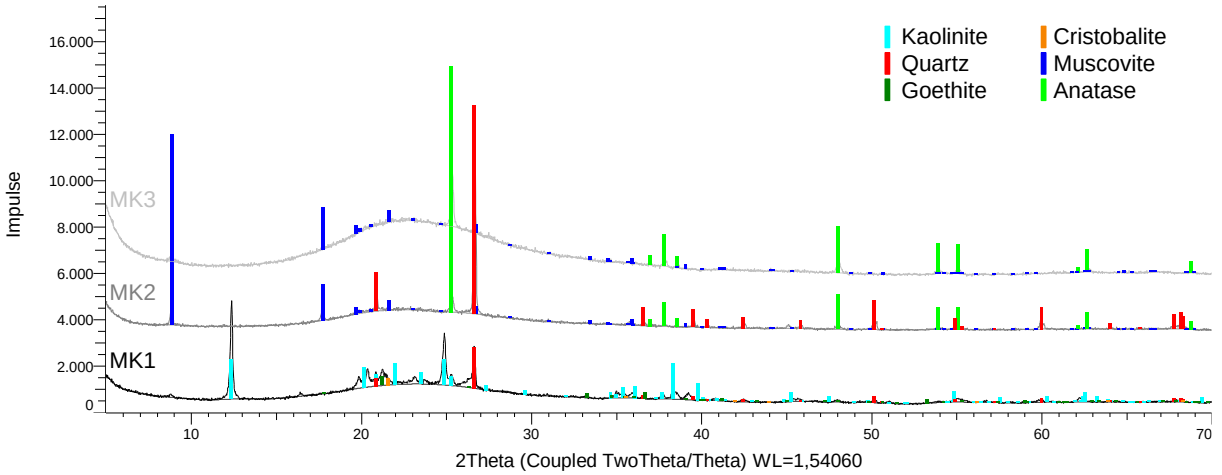

Figure 24: Powder X-ray diffractogram and qualitative analysis of the three different metakaolin samples used in this study (bottom: MK1, middle: MK2 and top: MK3).

Both the alkaline suspension and the reactive samples, which are a mixture of the suspension and metakaolin, were prepared in a temperature-controlled laboratory at approx. 20 °C, and the metakaolin used in the mixing process was also stabilized (overnight) at the same temperature. For the samples with potassium sulfate (_R3), 50 g suspension (R3, Table 5) was mixed with 6.30 g metakaolin (MK1, MK2 and MK3) according to [87] for 3 min with an electric stirrer [84]. The samples without potassium sulfate (_0.32KOH) were prepared with 6.39 g per 50 g suspension (0.32KOH, Table 5) to keep the metakaolin (MK) to calcium hydroxide (CH) weight ratio at 0.33 as well as the water to binder ratio (binder = MK + CH) constant at 1.2. Furthermore, to evaluate the repeatability of the proposed methodology, a test series named “MK3_Rep” was introduced, consisting of three similar specimens. The metakaolin type MK3 in combination with the suspension R3 (as defined in Table 5) was used for this series. For each reactive sample in this study, 20 g ± 0.3 g was weighed in the calorimetry plastic ampoule and placed immediately in the measurement channel chamber. The temperature at sample placement in the calorimeter was not measured to minimize the time-lag between mixing and sample placement, aiming to reduce temperature differences between the inert and reactive samples. After sufficient stabilization time (overnight) of the components, each sample was weighed for 3 minutes ± 30 seconds, recording the mass with a tolerance of 0.001 g. The initial sample temperature (during sample loading) could slightly vary due to the mixing procedure and initial dissolution reactions within the first 3 minutes. The proposed short and consistent mixing procedure minimized the first effect and was considered in the baseline correction. The second effect provided an approximate indication of the heat of reaction. Therefore, small deviations in sample temperatures from the room temperature had negligible effects on the baseline correction. This was confirmed by calculating the temperature difference between the initial temperature and the testing temperature of 40 °C for the inert samples, as shown in Table 7 and discussed in detail in section 3.3.1. The temperatures were calculated using eq. 24 and heat flow measurements, as direct experimental measurement of these temperatures posed challenges.

„MC CAL“ from C3 Prozess- und Analysentechnik GmbH (Haar, Germany) was used for the calorimetry measurements. The device was preconditioned and calibrated at 40 °C, water was used as a (differential) reference sample and data was collected every 30 s for 7 days. For some parts of this study, data was collected every 1 s, namely for the tests to determine the Tian constant (section 3.3.2) as well as for an additional test series (sample named by adding the suffix “_ats”, data shown in section 3.4), where MK3 with and without potassium sulfate was tested a second time.

3.3 Methodology

The calculation approach assumes, that the initial temperature jump effect could be obtained as a baseline measurement of an inert sample and subtracted from the reactive one. The effect is due to the

lower sample temperature of ~ 20 °C compared to the testing temperature of 40 °C, that enables a convenient ex-situ sample preparation at ambient temperatures with all samples having the same initial temperature. As discussed in section 3.3.1, to ensure accuracy and consistency, an additional inert sample (here: alkaline suspension without SCM) with a similar heat capacity as the reactive samples must be employed for the baseline correction that accounts for the initial temperature jump. This can be achieved by adjusting the sample weighing accordingly. The type of inert material was found to have no significant effect on the proposed methodology, as demonstrated in Figure 26 (comparison between water and suspension) and discussed in section 3.3.1.

3.3.1 Baseline Correction due to Initial Temperature Jump

Due to the temperature difference of ~ 20 °C, when the sample was mounted, there is a significant drop in the measured heat flow to highly negative values. This is followed by an exponential increase in the signal until it approaches zero (for the inert sample) that takes approx. 100 min.

To verify this approach, the temperature difference of ~ 20 °C can mathematically be calculated from the heat generated in the experiment by using the fundamental caloric equation (eq. 24). Table 7 summarizes the temperature differences of the eight inert samples calculated from the measurement data as integral over the first 100 min, resulting in a mean value of - 20.1 °C and a standard deviation of 0.7 °C.

$$Q = cp \cdot m \cdot \Delta T \tag{24}$$

Q: (Measured integral) heat in J.
cp: Specific heat capacity in J/(g·K).
m: Mass in g.
ΔT: Temperature difference in K.

Table 7: Calculated temperature difference at time of sample mounting in °C calculated from eq (1) and measured integral heat over the first 100 min resulting in a mean value of -20.1 °C (s = 0.7 °C).

Suspension	0.32KOH	R3
Calculated temperature difference	-19.5 (_1)	-20.0 (_1)
	-20.8 (_2)	-19.7 (_2)
	-21.6 (_3)	-19.8 (_3)
	-19.9 (_4)	-19.1 (_4)

Testing of inert samples with different heat capacities in this study shows that the temperature adjustment in terms of time and intensity is dependent on the samples heat capacity. The heat capacity was calculated by multiplying the individual mass of the sample with the specific heat capacity, determined according to the sample composition while assuming specific heat capacities for solids (0.80 J/(g·K)) and water (4.18 J/(g·K)). The temperature equilibration speed, called time constant in this study should not change significantly within the acceptable deviations of the masses. A higher deviation in masses is desirable to lower the weighting time to minimize changes in sample (room) temperature. To calibrate the initial baseline and the time constant (analogously to the Tian constant determination in section 3.3.2) several inert samples, that have a range of heat capacity comparable (+ 4.5 J/K and – 7.1 J/K) to the reactive samples (52.4 J/K - 53.5 J/K) have been tested. Results show small deviations for the range marked with a red circle in Figure 25 (+ 4.5 J/K and – 1.3 J/K). As the exact weighing is practically not possible in a short time period, the mass (i.e. heat capacity) is a critical factor for the good calibration. According to Figure 25, the inert sample should have a similar heat capacity compared to the reactive samples and the weight needs to be calculated prior to analysis. Thus, small variations in heat capacity due to weighing accuracy can be corrected mathematically using a multiplication factor (see *C-factor* below). The validity of this approach is strengthened by the results obtained from the “inerts” test series. In this series, six inert samples comprising of three water samples and three samples of alkaline suspension with comparable heat capacities were examined in detail. The mean values of these baselines, each normalized to the respective sample heat capacity, are shown in Figure 26 together with the standard deviations. Figure 26 illustrates only minor deviations within the

first 5 to 10 minutes of the experiment, confirming that the choice of inert material has no significant impact on the (normalized) baseline. Thus, the consistent results obtained from the “inerts” test series further substantiate the robustness of the proposed approach. The results also demonstrate that higher deviation of heat capacity from the reactive sample has a significant impact on the calibration of the time constant; resulting in the two outliers observed for the ”too low” heat capacity (Figure 25). Furthermore, to ensure accurate results, it is recommended to measure both the inert and the reactive samples within the same test series. This will guarantee identical temperatures for both material storage and sample preparation as this methodology is sensitive to small temperature variations. It even holds for temperature-controlled rooms, where slight variations in temperature may occur, even as the water temperature used to clean the mixing equipment, which should be taken into consideration as well.

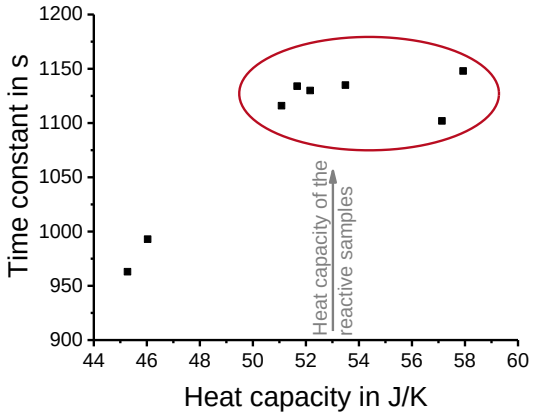

Figure 25: Time constants determined (according to the Tian method) for different inert samples calculated from the start of the measurement with ΔT ~ 20 °C. Inert samples in the (relatively small) heat capacity range of the reactive samples (marked with a red circle) show a similar time dependent behavior.

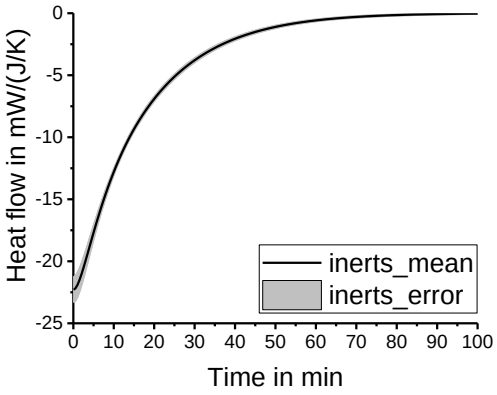

Figure 26: Temperature difference effect as mean value (inerts_mean) and standard deviation (inerts_error) of six inert samples from the “inerts” test series including 3 water samples and 3 with alkaline suspension with heat capacities in the range of the reactive.

The proposed interpretation utilizes raw calorimetry data beginning with the lowest (most negative) value, incorporating effects from both the temperature adaption (of inert and reactive samples) and heat generated by the reactive samples. To extract the heat generated specifically by the reaction processes, one must eliminate the baseline effects of the temperature jump. This is achieved by calibrating the inert sample and using it as a baseline for comparison with the reactive samples. The baseline signal is then subtracted from the reactive samples signal to obtain the heat generated specifically by the reaction processes. For this calculation, the (slightly) different heat capacities of the reactive and the inert samples need to be addressed, arising from the specified mass measurement tolerance (and weighing time limits). For this purpose, the *C-factor* was defined according to eq. 25. The specific heat capacities (*cp*) of the inert (exemplarily shown on suspension “R3” according to Table 5) and the reactive (12.59 g SCM in 100 g suspension according to [87]) samples can be calculated according to eq. 26 and eq. 27 by taking into account the respective sample compositions as well as the assumed specific heat capacities for solids (0.80 J/(g·K)) and water (4.18 J/(g·K)). Eq. 27 is based on the R³-sample composition consisting of 100 g suspension (R3) along with 12.59 g metakaolin.

$$C\text{-}factor = \frac{C_{\text{reactive}}}{C_{\text{inert}}} = \frac{cp_{\text{reactive}}}{cp_{\text{inert}}} \cdot \frac{m_{\text{reactive}}}{m_{\text{inert}}} \tag{25}$$

C-factor:	Defined calculation factor to address the (slightly) different heat capacities of the reactive and inert sample due to (time) limited mass measurement accuracy.
C:	Heat capacity in J/K.
cp:	Specific heat capacity in J/(g·K).
m:	Weight of the sample in g.
inert:	Referring to the inert sample.
reactive:	Referring to the reactive sample.

$$cp_{\text{inert}} = 0.3957 \cdot 0.80\ \text{J/(g·K)} + 0.6043 \cdot 4.18\ \text{J/(g·K)} = 2.8425\ \text{J/(g·K)} \quad (26)$$

$$cp_{\text{reactive}} = cp_{\text{inert}} \cdot \frac{100}{112.59} + 0.80\ \text{J/(g·K)} \cdot \frac{12.59}{112.59} = 2.6141\ \text{J/(g·K)} \quad (27)$$

With the help of the *C-factor* and following the assumptions explained above, the heat flow of the reactive sample induced by dissolution and reaction processes can be calculated according to eq. 28.

$$\dot{Q}_{\text{inert-corrected}} = \dot{Q}_{\text{raw}} - \textit{C-factor} \cdot \dot{Q}_{\text{inert,raw}} \quad (28)$$

$\dot{Q}_{\text{inert-corrected}}$: Data of heat flow in mW (baseline corrected due to initial temperature jump).
$\dot{Q}_{\text{raw}}$: Raw data of heat flow in mW (started from lowest value).
$\dot{Q}_{\text{inert,raw}}$: Raw data of heat flow of the inert sample in mW (started from lowest value).

3.3.2 Tian Correction

To account for the time-lag caused by thermal inertia effects between the samples and the calorimeter instrument, the Tian correction method [242, 243] is particularly necessary, especially for rapidly changing reaction rates observed during the initial stage of the experiment. The Tian constant plays a crucial role in this correction method, as it characterizes the exponential decay of a signal. Specifically, it represents the time required for the signal to decrease from any given value to 36.8 % (exp(-1)) of that value [243]. Incorporating the Tian correction ensures accurate alignment of the signals and compensates for the thermal inertia effects, allowing for more accurate interpretation of the experimental data.

One option to determine the Tian (time) constant is to thermally disturb a sample when the heat flow is constant or low, e.g. by quickly lifting and again placing the ampoule in the calorimeter [243]. The 12 calorimetry ampoules, with heat capacities ranging from 45.3 J/K to 57.9 J/K, were promptly removed from the chamber and then reinserted at the end of the measurement after 7 days. Moreover, different “lifting” times (time between lifting the sample and again placing it in the chamber) were investigated, namely 1, 6, 13 and 30 s, to address two opposing effects. First, the “lifting” time should be short to minimize a temperature difference due to sample cooling outside the chamber. Second, if the “lifting” time is too short, other effects, like e.g. cooling the stoppers and convection, become too dominant. The Tian constants are calculated individually for each calibration measurement, analyzing the exponentially decaying signal. As the Tian constant represents the time that the signal needs to decrease from any value to 36.8 % (exp(-1)) of that value [243], the curves were normalized to the lowest (initial) value and assuming an exponential relationship ($\dot{Q}_{\text{normalized}}(t) = -\exp(-t/\tau)$), the Tian constant τ was determined for a heat flow of -exp(-1) where time $t = \tau$ [243] (Figure 27). The results as mean values over 12 samples with measurement uncertainty (± one standard deviation) are visualized in Figure 28. The standard deviation decreased remarkably from a “lifting” time of 1 s to 6 s. To reduce the influence of (initial) convection for the Tian constant determination, the mean value of 759.4 s from this experiment (6 s) was further used for the Tian correction in this study.

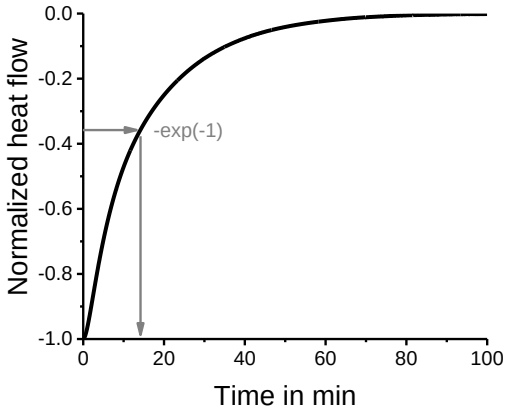

Figure 27: Tian constant determination (Data of R3_1 shown exemplarily for 30s "lifting" measurement; heat flow normalized between the null-baseline and -1 as the lowest measured value).

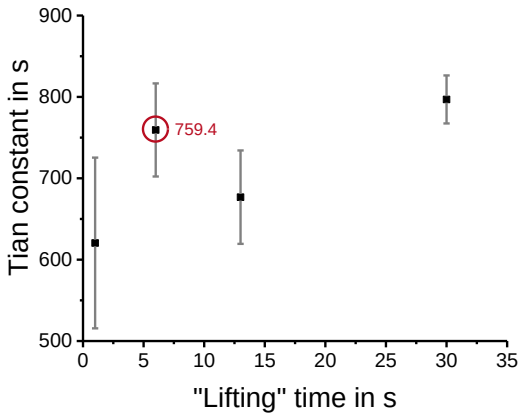

Figure 28: Tian constants as mean values over 12 replicate measurements for different "lifting" times (Tian constant used for the correction in this study marked in red).

The heat flow values of each sample $\dot{Q}$ were Tian-corrected with the Tian constant τ (= 759.4 s) according to eq. 29.

$$\dot{Q}_{\text{Tian-corrected}} = \dot{Q}_{\text{inert-corrected}} + \tau \cdot \frac{d\dot{Q}_{\text{inert-corrected}}}{dt} \tag{29}$$

$\dot{Q}_{\text{Tian-corrected}}$: Tian corrected heat flow in mW.
$\dot{Q}_{\text{inert-corrected}}$: Data of heat flow in mW (baseline corrected due to initial temperature jump).
τ: Tian constant.

3.4 Results and Discussion

Figure 29 shows the heat flow of all tested sample compositions up to 100 min calculated according to the proposed new methodology approach described in section 3.3. Heat flow results are normalized per gram of metakaolin. Up to three peaks are visible in the first 100 min depending on the sample composition. The first exothermic peak (1) occurs within the first approx. 25 min and seems to be due to the dissolution of metakaolin. The second peak (2) occurs as a smaller hill in between the two other peaks for MK2 and is visible in the data for MK3 with and without potassium sulfate as a shoulder on the third peak. MK1 does not show this characteristic. The third peak (3) occurs from approx. 25 min (depending on the sample composition) to 100 min. When comparing the three different metakaolin types, MK1 shows no distinct peaks in this initial time frame, but the first dissolution (peak 1). When no potassium sulfate is present in the sample (MK3 + 0.32KOH suspension = MK3_noK2SO4), peak 2 appears approx. 10 min earlier. MK2 and MK3 have similar intensities of peak 3, but for MK2 the peaks (2 and 3) start slightly earlier and overlap more. For the MK3 sample without potassium sulfate (MK3_noK2SO4), peak 3 is lesser pronounced and earlier compared to MK3 with sulfates. As the characteristic pattern of these three peaks is observed to be independent of the sulfate presence, they cannot be due to ettringite formation only, but indicate to other reaction processes, like e.g. hemi- and/or monocarboaluminate formation due to carbon dioxide contamination from air exposure [54, 56, 61, 64, 66, 76, 105, 143].

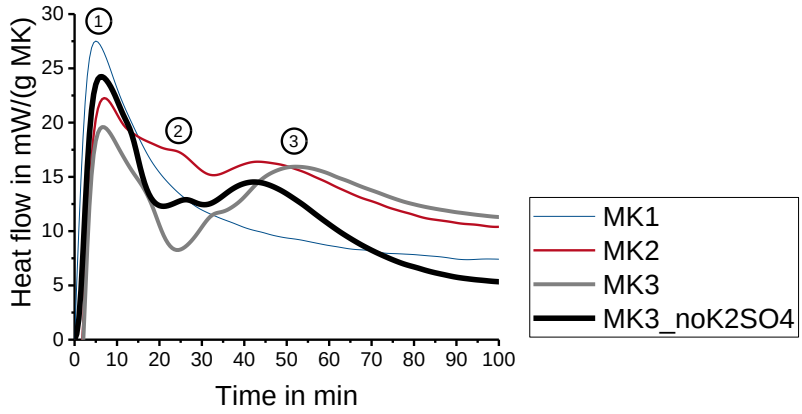

Figure 29: Initial heat flow in mW/(g MK) of all tested sample compositions (MK1-MK3 and MK3 without potassium sulfate) up to 100 min.

To further demonstrate the capability of using the proposed novel methodology, the reproducibility of the sample preparation was qualitatively investigated on two test series incorporating MK3 samples with and without potassium sulfate (additional test series named as _ats). The sample preparation process (suspension and reactive sample) in the additional test series (_ats) was even more precisely controlled with the aim to minimize carbonation contamination due to air exposure. Figure 30 compares the results of both test series. The first peak within the first 25 min (1) occurred in both test series with a comparable peak intensity but a slightly broader shape in the second test series (_ats). The broader first peak leads to the appearance of the second peak (2) as a shoulder on the first one. The third peak (3) is clearly present in the first test series, while not visible in the data originating from the additional test series (_ats). Thus, the third peak could be attributed to carbonate formations (hemi- and/or monocarboaluminates), arising from carbon dioxide exposure during sample preparation.

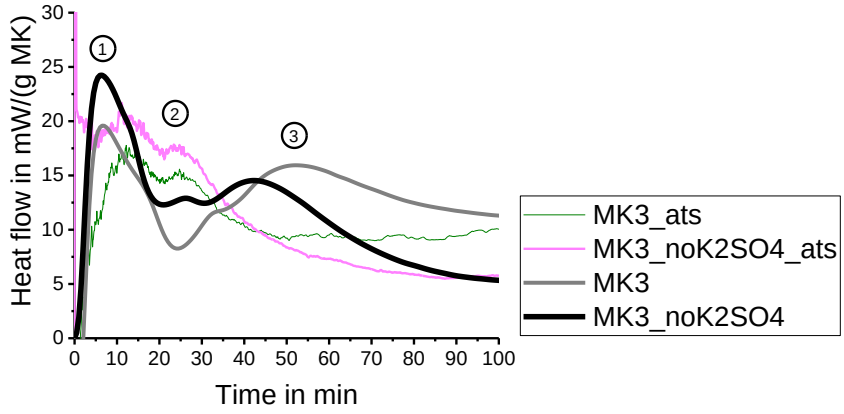

Figure 30: Comparison of the heat flow of MK3 samples with and without (_noK2SO4) potassium sulfate originated from different test series (additional test series named as _ats) up to 100 min.

The heat flow of all tested sample compositions is shown in Figure 31 for up to 36 h with characteristic peak formations. In general, the intensity of the heat flow increases with the amount of amorphous metakaolin content according to the following order: MK3 > MK2 > MK1 (in agreement with amorphous content by XRD results, Table 6). From 100 min up to 36 h, all samples, except from MK1, show two main peaks. The first peak is composed of multiple different sub-peaks for samples with sulfates, while the maxima of both main peaks are higher with potassium sulfate. The increased heat flow with potassium sulfate, especially within the first 12 hours (a), demonstrates their importance on the early reactions of metakaolin. It can be explained by higher rates of dissolution [62, 107] together with ettringite formation [58, 59, 61, 62, 66, 67, 76, 87, 105–107]. Without potassium sulfate, the last peak (b) is broader and shifted to later ages.

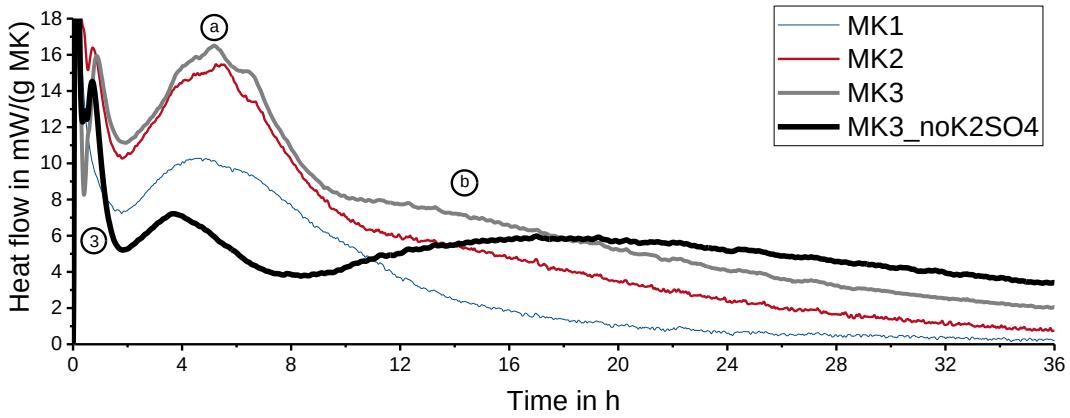

Figure 31: Heat flow of all tested sample compositions up to 36 h at 40 °C.

To qualitatively prove the presence of the peaks identified within the first 100 min with the proposed methodology (calorimetry at 40 °C), additional calorimetry measurements were carried out at 20 °C with MK3 with and without potassium sulfate. As there is no significant temperature difference of the initial sample temperature compared to the testing temperature and the reactions proceed much slower at 20 °C, the proposed methodology for data treatment was not that critical. The results are shown in Figure 32. Qualitatively, the heat flow curves at 20 °C (Figure 32) and 40 °C (Figure 31) show similar shapes with the peaks occurring more separated and at later ages at 20 °C. The first peak observed at 40 °C from approx. 25 min to 100 min (3) was also observed (within the first 12 h) in the measurement at 20 °C, validating the presence of that heat flow peak that becomes detectable with the help of the proposed methodology.

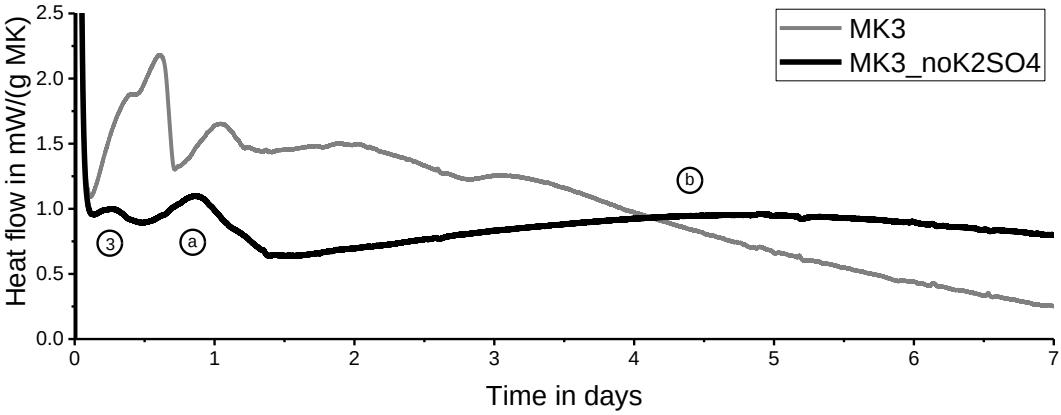

Figure 32: Heat flow of MK3 with and without (_noK2SO4) potassium sulfate up to 7 days at 20 °C.

As reaction kinetics are strongly temperature dependent and the temperature adaption from 20 °C to 40 °C takes approx. 100 min, the sample preparation in this study will result in different recorded signals compared to a sample preparation at elevated temperatures. Each sample first adapts to the testing temperature, so that the first reactions are slightly slower compared to a continuous measurement at 40 °C. The sample mounting with a large temperature difference is not in line with the general recommendations regarding calorimetry measurements [247]. However, as the elevated testing temperature of 40 °C is a specific characteristic of the R³-test, where a proper mixing can only be achieved ex-situ, the proposed methodology offers a user-friendly approach for addressing the practical challenges. The temperature adaption from 20 °C to 40 °C in the calorimetry leads to highly negative heat flow values in the beginning, followed by an exponential decaying signal that slightly overshoots the zero baseline before it stabilizes. This observation can be explained by the disturbed heat sink temperature that needs some time to restore [243]. As it is a physical phenomenon, it occurs in the inert

as well as the reactive samples, so it can be eliminated with the described correction calibration (subtraction of the inert from the reactive sample).

The proposed methodology offers a user friendly approach to effectively observe the early reactions of SCMs, here specifically tested on metakaolin in a controlled testing environment. More specifically, the materials considered in this testing environment are metakaolin (MK), portlandite (CH), alkali hydroxides and sulfates. The overall heat release data is shown in Figure 33 and summarized for different reaction times in Table 8. Employing the proposed methodology led after 100 min to a cumulative heat release that ranges between 69.1 J/(g MK) and 86.8 J/(g MK), depending on the composition of the sample and the type of metakaolin. Table 8 reveals that during the initial 100 min of testing, MK1 (MK3) exhibits 15.7 % (7.8 %) of the total heat released over a 7-day testing period. In Table 8, a comparison between the results obtained with and without (see *) the proposed methodology while excluding data from the first 72 min showed no significant difference in heat release. Contrarily to the regular R^3-testing procedure [85], it should be noted that all results from this study are without preconditioning the raw materials at 40 °C before sample mixing. Moreover, the proposed methodology is of particular relevance whenever investigating the early reactions that occur within the first 72 min. Its importance lies in understanding the initial stages of SCM reactivity rather than being essential for the overall SCM reactivity, as discussed in section 3.1. Moreover, the proposed methodology enables a precise data analysis, including reaction kinetics and separation of peaks.

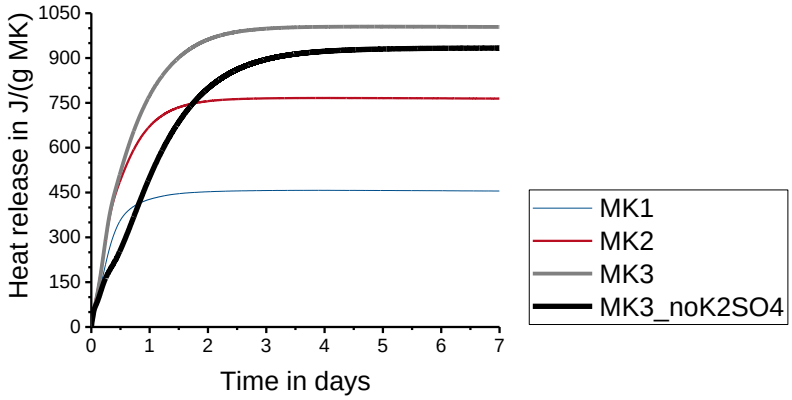

Figure 33: Cumulative heat release in J/(g MK) of all tested sample compositions (MK1-MK3 and MK3 without potassium sulfate) up to 7 days.

Table 8: Summary of cumulative heat release (Q) after different reaction times and relative standard deviation (in %) calculated from the MK3_Rep test series.

	MK1	MK2	MK3	MK3 _noK2SO4	Relative standard deviation
Q(10 min) in J/(g MK)	13.7	8.9	7.6	10.9	51.1 %
Q(72 min) in J/(g MK)	56.9	68.1	57.5	58.7	12.7 %
Q(100 min) in J/(g MK)	69.7	86.8	77.8	69.1	10.0 %
Q(7 d) in J/(g MK)	445.5	764.8	1003.8	933.0	2.7 %
Q(100 min)/Q(7 d) · 100 % in %	15.7	11.4	7.8	7.4	
Q(7 d) - Q(72 min) in J/(g MK)	398.6	696.7	946.3	874.3	
Q(7 d) - Q(72 min)* in J/(g MK)	399.6	701.8	952.1	877.1	

*Data not corrected according to this study.

The repeatability of this experimental approach was assessed by three additional samples of MK3 in the R3 suspension (MK3_Rep test series). The mean heat flow values along with the corresponding standard deviations are shown in Figure 34 up to 100 min reaction time. The results indicate significant deviations within the first 10 minutes, but show more consistent values with elapse of reaction process. The relative standard deviations of the total heat release at different reaction times are presented in the last column of Table 8. The data highlights that the heat recorded within the first

10 minutes provides a rough estimate, showing a variability of 51.1 %. However, as time progresses, the repeatability of the heat release measurements improves significantly. After 100 minutes, the variability decreases to only 10.0 %, and after 7 days, it further decreases to 2.7 %. This highlights the reliability and consistency of the measurements with increasing reaction time.

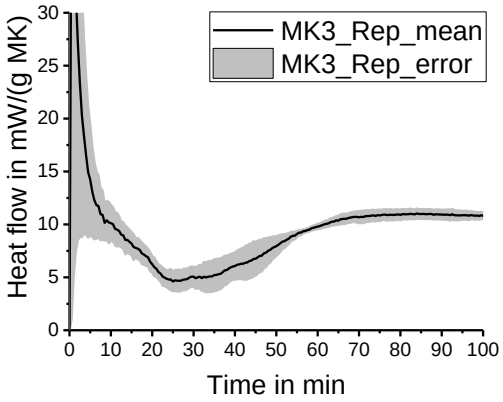

Figure 34: Mean value of heat flow (MK3_Rep_mean) and standard deviation (MK3_Rep_error) of three replicates of MK3 tested in R3 suspension (test series “MK3_Rep”).

3.5 Conclusion

A new methodology has been developed for testing lime paste samples similar to R³-samples in calorimetry, which allows for identifying early reaction-induced heat flow in samples that is typically undisclosed. To achieve good homogenization, the samples were ex-situ mixed at ambient temperature. To correct for the initial temperature jump (testing temperature at 40 °C), an inert sample (here: alkaline suspension without SCM, but other inert materials are also possible) was used to establish a baseline. By applying the Tian correction to account for fast reaction processes, the proposed methodology allows for the quantification of the reaction heat (kinetics) in lime paste samples measured in calorimetry at 40 °C, even within the first 100 minutes, using a feasible ex-situ mixing process. This approach enables quantitative evaluation of early reaction kinetics of R³ and similar lime paste samples, as demonstrated by studying the effects of three different metakaolin types (MK1, MK2 and MK3) and potassium sulfate addition. All three metakaolin types displayed a significant initial reaction peak within the first 25 minutes. Furthermore, the heat flow curves of MK2 and MK3 exhibit two additional peaks in the first 100 minutes after mixing. These characteristic peaks were also present for MK3 without potassium sulfate, although they appeared less intense (particularly peak 3) and earlier (peaks 2 and 3). The proposed methodology can be employed in future research and is recommended to explore the initial early reactions of metakaolin and/or other SCMs in controlled testing environments. This investigation is crucial for comprehending the fundamental phase (trans)formations that play a decisive role in determining various properties, such as the workability and placement (fresh rheological) characteristics of lime and/or alternative cement-based binders.

4 Publication 3: Thermogravimetric Analysis

Publication 3 (Materials, https://doi.org/10.3390/ma14195859):

A Mass Balance Approach for Thermogravimetric Analysis in Pozzolanic Reactivity R³-Test and Effect of Drying Methods

Kira Weise[1,*], Neven Ukrainczyk[1], Eduardus Koenders[1]

[1] Technical University of Darmstadt, Institute of Construction and Building Materials, Germany.
* Corresponding author. E-mail address: weise@wib.tu-darmstadt.de.

Abstract: The reactivity of supplementary cementitious materials (SCMs) is a key issue in the sustainability of cement-based materials. In this study, the effect of drying with isopropanol and acetone as well as the interpretation of thermogravimetric data on the results of an R³-test for evaluation of the SCM pozzolanic reaction were investigated. R³-samples consisting of calcium hydroxide, potassium hydroxide, potassium sulfate, water, and SCM were prepared. Besides silica fume, three different types of calcined clays were investigated as SCMs. These were a relatively pure metakaolin, a quartz-rich metakaolin, and a mixed calcined clay, where the amount of other types of clays was two times higher than the kaolinite content. Thermogravimetric analysis (TGA) was carried out on seven-day-old samples dried with isopropanol and acetone to stop the reaction processes. Additional calorimetric measurement of the R³-samples was carried out for evaluation of the reaction kinetics. Results show that drying with isopropanol is more suitable for analysis of R³-samples compared to acetone. The use of acetone results in increased carbonation and TGA mass losses until 40 (isothermal drying for 30 min) and 105 °C (ramp heating), indicating that parts of the acetone remain in the sample, causing problems in the interpretation of TGA data. A mass balance approach was proposed to calculate calcium hydroxide consumption from TGA data, while also considering the amount of carbonates in the sample and TGA data corrections of original SCMs. With this approach, an improvement of the linear correlation of TGA results and heat release from calorimetric measurement was achieved.

Keywords: pozzolanic reactivity R³-test; supplementary cementitious materials (SCMs); pozzolan; calcined clay; metakaolin; silica fume; thermogravimetric analysis (TGA); isopropanol; acetone; reaction calorimetry.

4.1 Introduction

Concrete with cement as binder is still one of the most used construction materials worldwide [248], which is also reflected by the enormous global cement production that was estimated at around four billion tons in 2018 [249]. The massive production of Ordinary Portland cement (OPC) is responsible for emitting enormous amounts of androgenic CO_2 caused by both fossil fuel burning and decarbonation of limestone [250]. Lowering these impacts can generally be achieved by lowering the amounts of cement clinker in concrete and/or by replacing it with more environmentally-friendly alternatives [251]. Common supplementary cementitious materials (SCMs) such as fly ash, silica fume or ground granulated blast-furnace slag are mainly employed for this purpose. However the availability fly ash, but also ground granulated blast-furnace slag, are becoming rare due to a worldwide reduction of the number of coal fired electricity plants and shortages on the world market, respectively [252]. From this it has become clear that the search for alternative SCMs for partial replacement of OPC, is vital. Possible alternative SCM materials for their use in cementitious systems, strongly depend on their potential reactivity, which drives the need for descriptive reactivity tests. For this reason, different testing procedures are used for measuring the reactivity of SCMs, as there is still no universally valid testing procedure available. To meet the general interest for a rapid, relevant and reliable test, Avet et al. first introduced the R³-test for evaluation of the pozzolanic reactivity of calcined kaolinitic clays in 2016 [87]. They developed a test environment for the pore solution of cementitious systems by using calcium hydroxide, potassium

hydroxide, potassium sulfate and water [87]. Bound water was determined using oven thermal treatment and heat flow measurements were carried out by using isothermal calorimetry on R³-samples [87]. This approach enabled to evaluate the pozzolanic reaction of SCMs independently of the specific cement properties. In the following years, the R³-test was developed further and extended with additional testing procedures like portlandite consumption measured with thermogravimetric analysis (TGA) and chemical shrinkage [253]. The R³-test was employed for evaluating the reaction behavior of many different kinds of SCM such as, besides calcined clays, also ground granulated blast-furnace slag, silica fume and fly ash [253–257].

For some of these reactivity test methods, e.g. TGA, drying of the samples is needed to stop the reaction processes prior to analysis. In a round robin test carried out by Snellings et al. different stoppage methods were tested on cement paste samples [258]. The solvent exchange method was found to perform best regarding the composition and preservation of pores in cementitious samples compared to oven, vacuum and freeze drying [258, 259]. Zhang et al. compared different solvents for drying of cement paste samples prior to the thermogravimetric analysis [260]. In their study, the order of mass loss in the temperature range of 600 °C to 1000 °C that refers to carbonates was the following: Acetone > ethanol > tetrahydrofuran > isopropanol [260]. In a similar study, Röser has chosen acetone treatment, against drying with isopropanol, freeze drying and microwave drying as the best possible method for hydration stoppage of cement paste samples for thermogravimetric analysis [261].

For the reaction stoppage of R³-samples, some research groups [253, 257, 262, 263] followed the drying procedure with isopropanol suggested by Snellings et al. for cement paste samples [264]. Blotevogel et al. used a combination of isopropanol and acetone treatment to stop the reaction processes in R³-samples [254]. And in contrast, Suraneni and Weiss did not use any drying procedure in their study as they calculated the amount of $Ca(OH)_2$ only, as any hydration stoppage would complicate the interpretation of test results [255].

As various drying methods for R³-samples are employed in literature, this study aims to compare the effect of drying with acetone and isopropanol on the thermogravimetric results on the following R³-tests; calcium hydroxide consumption and the amount of chemically bound water. The samples were prepared, dried and analyzed in a well-defined testing program that followed strict time tables, which is especially relevant for drying and thermogravimetric testing of the samples. Calorimetric measurement of the R³-samples was used for evaluation of the thermogravimetric test results.

The work starts with a detailed explanation of the procedure needed for interpretation of thermogravimetric data from R³-test, following a precise description of the mass balance approach. Calcium hydroxide consumption as well as the amount of chemically bound water was calculated according to a procedure that both takes into account the amount of carbonates in the sample and TGA data corrections of original SCMs.

4.2 Materials and Methods

4.2.1 Materials

In the experimental program, samples for the R³-tests were prepared containing R³-suspension and different SCMs. The SCMs employed in this study were silica fume (SF) and three different types of calcined clay, which were a relatively pure metakaolin (MK1), another with 46 wt.-% metakaolin and around 40 wt.-% quartz impurities (MK2) and finally, a mixed calcined clay (MC) with an amount of 25 wt.-% kaolinite in the raw material. The chemical composition of used SCMs is shown in Table 9.

The used silica fume (SF) contains 97 wt.-% of SiO_2 (Table 9). Rietveld refinement of X-ray diffraction using Topas version 5 software from Bruker (Billerica, USA) spiked with 10 % corundum resulted in 91 wt.-% amorphous material, with a specific density of around 2.2 g/cm³ and a specific surface of 150000 – 300000 cm²/g stated in the Elkem Data Sheet [265]. The mean particle size is around 0.15 μm.

Table 9: Chemical composition of SCMs in wt.-% (evaluated on pressed tablets by X-ray fluorescence analysis).

SCM	SiO_2	Al_2O_3	Fe_2O_3	CaO	MgO	Na_2O	K_2O	TiO_2	Other
SF	97.02	0.55	0.21	0.32	0.49	0.18	0.98	0.00	0.25
MK1	52.95	42.18	2.38	0.05	0.07	0.00	0.31	1.77	0.29
MK2	58.80	32.79	3.50	2.35	0.17	0.06	0.35	1.80	0.18
MC	51.44	22.31	9.95	7.01	2.78	0.34	3.49	1.19	1.49

The relatively pure industrial type of metakaolin MK1 is produced by grinding calcined kaolinite rich clay originating from secondary geological deposits (not known), with a specific density of 2.6 g/cm³ and a specific surface of 200000 cm²/g (BET). MK1 is a commercial product produced by industrial-scale calcination and grinding. It was calcined in an industrial-scale Herreshoff furnace (multiple-hearth), where in each hearth the temperature and time of calcination were precisely controlled (assumed to be <~750 °C) to ensure high reactivity. The corresponding qualitative X-ray diffraction result is shown in Figure 35, while the Rietveld refinement analysis resulted in an amorphous content of 83 wt.-% (~metakaolin), 10 wt.-% quartz, 5 wt.-% muscovite and 2 wt.-% anatase.

The second metakaolin MK2 is less pure compared to MK1 and contains impurities mainly of quartz. The qualitative X-ray diffraction diagram is shown in Figure 36, resulting in 46 wt.-% of amorphous material (~metakaolin), 40 wt.-% quartz, 10 wt.-% muscovite and 2 wt.-% calcite. Moreover, MK2 has a specific density of 2.5 g/cm³ and a specific surface of 160000 cm²/g (BET).

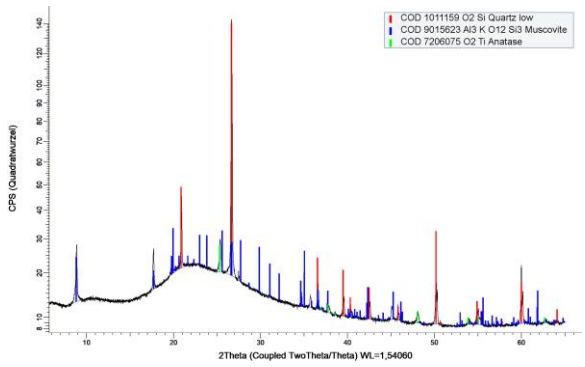

Figure 35: Powder X-ray diffractogram and qualitative analysis of metakaolin (MK1).

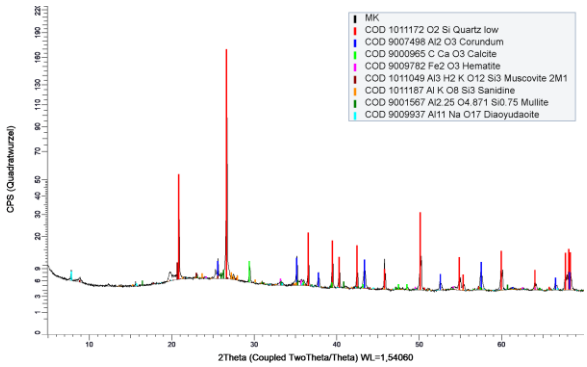

Figure 36: Powder X-ray diffractogram and qualitative analysis of metakaolin (MK2).

The raw clay used for the mixed calcined clay MC used was mined in the region of Unterstürmig in northern Bavaria (South part of Germany) and is a 180 million year old clay from the age of Lias. It was calcined industrially in a rotary kiln at around 650 °C and milled afterwards (more details can be found in [266]). The raw clay consists mainly of 25 wt.-% kaolinite, 30 wt.-% mica, 11 wt.-% illite, 6 wt.-% chlorite and 18 wt.-% quartz [267] and stored as grey-brown powder in small size bags. According to Liapor GmbH & Co. KG, the largest grain diameter of the mixed calcined clay is ≤ 100 μm and the amount of particles smaller than 32 μm is over 90 wt.-%. The specific density is 2.63 g/cm³, bulk density 1.00 g/cm³, and the specific surface area according to BET is 55000 cm²/g. X-ray diffraction indicates persistence of illite and mica (muscovite) peaks, showing that kaolinite is transformed to amorphous material during calcination, but 2:1 of the clay stays semi-crystalline.

4.2.2 Sample Preparation

Samples for the R³-tests were mixed with an alkaline suspension (R³-suspension) proposed by Li et al. and Avet et al. that mimics the alkaline pore solution of cement paste [87, 253]. The R³-suspension contains powdered calcium hydroxide (≥ 96 %), potassium hydroxide in flakes (≥ 85 %), powdered potassium sulfate (≥ 99 %) and deionized water. The composition is shown in Table 10. Firstly, potassium hydroxide flakes (KOH) were dissolved in 7 g deionized water for 15 minutes using a magnetic stirrer. In a second step, dissolved potassium hydroxide was homogenized with the remaining

constituents (calcium hydroxide, potassium sulfate and the remaining deionized water) using an electric mixer for 15 minutes.

Table 10: Composition of 100 g alkaline R³-suspension.

$Ca(OH)_2$	K_2SO_4	KOH	H_2O
37.77 g	1.48 g	0.32 g	60.43 g

Subsequently, 100 g of alkaline R³-suspension was mixed with 12.59 g of powder SCM for five minutes using an electric stirrer. The ratio, i.e. 12.59/100, was taken from investigations of Avet et al. [87]. Additionally, a reference mix was prepared containing R³-suspension only (without SCM). The mixed lime for TGA measurements was poured in 10 ml sealed polypropylene containers for each SCM and stored in an oven at 40 °C for seven days. After that, the reaction process was stopped by drying the samples with two different solvents (isopropanol and acetone). For each SCM three samples were dried with isopropanol and three with acetone.

The drying procedure with isopropanol was carried out according to Snellings et al. [258, 264]. R³-samples of 3 g ± 0.05 g were crushed to pieces smaller than 1 mm and immersed in 100 ml of isopropanol for 15 minutes while stirring the suspension manually with the help of a glass stick. In a next step, the suspension was poured gently on a Büchner filter letting the isopropanol percolate. The residue was rinsed with 20 ml of isopropanol and twice with 20 ml of diethyl ether. The residue was placed on a watch glass and dried for 8 minutes ± 30 seconds in an oven at 40 °C.

For the drying procedure with acetone 3 g ± 0.05 g of the R³-sample was gently hand-milled and washed three times with 5 ml acetone (> 99.5 %) while continuing milling according to Röser and Weise [246, 261, 268]. For the reference sample (R³-suspension without SCM) seven times of 5 ml acetone were needed to dry the samples.

Prior to analysis, the samples were stored in a desiccator over silica gel and soda lime according to Snellings et al. [264]. Isopropanol samples were gently hand-milled just before thermogravimetric testing (< 5 minutes).

The samples dried with isopropanol were indicated as “ISO” and with acetone “ACT”. They were numbered according to the order of sample preparation and TGA measurement. The samples ISO_1 and ACT_1 were tested at the same day as reaction stoppage. Thermogravimetric analysis of both samples ISO_2, ACT_2, ISO_3 and ACT_3 was conducted the next day, respectively, which was in line with the recommendations of Snellings et al. [264]. The order of TGA measurement was the following: ISO_1, ACT_1, ISO_2, ACT_2, ISO_3 and ACT_3. The used original materials (SCMs) were measured with thermogravimetric analysis separately.

For the calorimeter tests, lime samples were mixed as described above and directly placed in the calorimeter chamber, which was preconditioned at 40 °C. The heat release was measured for a duration of 7 days.

4.3 Measurement Methods

For analyzing the reaction processes of the R³-samples, the samples were tested both by TGA and by calorimetry.

For thermogravimetric analysis (TGA) "STA 449 F5 Jupiter" from NETZSCH was employed. The crucibles consisted of alumina and were filled with 40 mg – 50 mg powder material. To avoid oxidation, nitrogen was used as an inert gas. The samples were first heated up to 40 °C and kept constant at this temperature for 30 minutes. Subsequently, each sample was heated up to 1000 °C at a constant heating rate of 20 °C per minute.

For the calorimetric measurements “MC CAL” from C3 Prozess- und Analysentechnik was employed. For this, 20 g of R³-sample was prepared at room temperature and placed in the calorimeter ampoule that was preconditioned at 40 °C. Measurements of heat release of the R³-samples were carried out for seven days. The reference sample was used for the calculation of the specific heat capacity.

4.4 A Mass Balance Approach for TGA in Pozzolanic Reactivity R³-Test

For the interpretation of thermogravimetric data, the sample mass inside the sealed container is assumed to remain constant during the reaction processes. Pozzolanic reactions of SCM turns parts of calcium hydroxide and water into hydration phases. As a result, reaction products are formed that contain a certain amount of chemically bound water. As calcium carbonate was detected in the R³-samples, mainly resulting from the drying procedure of the samples after seven days, these were considered for interpretation of test results as well. Determining the actual amount of carbonates in the sample is needed to exactly calculate the consumption of calcium hydroxide by SCMs [269]. Based on these simplified schematic considerations a mass balance approach from the thermogravimetric data of the lime samples containing SCM, water, calcium hydroxide, potassium hydroxide and potassium sulfate is subsequently proposed.

In a first step, all thermogravimetric data is corrected to the measured mass at 40 °C (*m40*) according to eq. 30, so that 100 wt.-% sample is related to a temperature of 40 °C,

$$x^* = \frac{x}{m40} \cdot 100\ \% \tag{30}$$

x^*: Corrected TGA value in wt.-%;
x: Any TGA data (mass or mass loss) in wt.-%;
$m40$: Mass at 40 °C taken from TGA in wt.-%.

This approach follows the assumption that mass loss from room temperature up to 40 °C is caused by remaining solvents and consequently mainly referring to the drying procedure [261].

In the proposed mass balance approach, the measured mass at 1000 °C (*m1000*) is used to standardize the results to the reference value of g/100 g SCM. The remaining mass at 1000 °C (*m1000*) consists of the following anhydrous components (*Anhydrous*): Anhydrous parts of unreacted SCM, anhydrous parts of reaction products, CaO from $Ca(OH)_2$, K_2SO_4 and K from KOH. With the information of the initial masses from the testing program and the stoichiometric considerations it is possible to calculate the amount of SCM related to *m1000* (*SCM_Anhydrous*),

$$\begin{aligned} Anhydrous = {} & \frac{mix\_SCM}{mix\_solid} \cdot m1000\_SCM^* + \frac{mix\_Ca(OH)2}{mix\_solid} \cdot 100\ \% \cdot \frac{56}{74} + \frac{mix\_K2SO4}{mix\_solid} \cdot 100\ \% \\ & + \frac{mix\_KOH}{mix\_solid} \cdot 100\ \% \cdot \frac{39}{56} \end{aligned} \tag{31}$$

$$SCM\_Anhydrous = \frac{\text{mix\_SCM}}{\text{mix\_solid}} \cdot 100\ \% \cdot \frac{100\ \%}{\text{Anhydrous}} \tag{32}$$

Anhydrous: Amount of anhydrous components in g/100 g *mix_solid* calculated according to eq. 31;
mix_solid: Mass of solid components in the mix design of the testing program in g;
mix_y: Mass of component y (SCM, $Ca(OH)_2$, K_2SO_4 or KOH) in the mix design of testing program in g;
*m1000_SCM**: Corrected mass at 1000 °C taken from TGA of pure SCM in wt.-%;
SCM_Anhydrous: Amount of SCM in g/100 g *Anhydrous* calculated according to eq 32.

The numbers in eq. 31 as well as later in eqs. 33, 34 and 36, result from the molar masses of CaO (56 g/mol), $Ca(OH)_2$ (74 g/mol), K (39 g/mol), KOH (56 g/mol), H_2O (18 g/mol), $CaCO_3$ (100 g/mol) and CO_2 (44 g/mol), respectively.

In the next step, the corrected thermogravimetric data according to eq. 30 is analyzed to determine the amount of $Ca(OH)_2$, $CaCO_3$ and *w*, which summarizes the amount of physically and chemically bound

water (without water in calcium hydroxide) as well as remaining organic solvents and free water in the sample. The results are standardized to the unit g/100 g SCM by using eq. 32. The mass loss caused by the dehydroxylation of calcium hydroxide in a temperature range of around 400 °C to 500 °C (in line with literature [9, 253, 268, 270]) was determined with the tangential method according to Lothenbach et al. [271]. The amount of $CaCO_3$ was calculated according to [272, 273] with the mass loss between 600 °C and 750 °C (in line with literature [247, 268, 274–277]) using the stepwise method,

$$Ca(OH)_2 = \frac{ML\_Ca(OH)2^*}{m1000^*} \cdot 100 \cdot \frac{74}{18} \cdot \frac{100}{SCM\_Anhydrous} \quad (33)$$

$$CaCO_3 = \frac{ML\_CaCO3^*}{m1000^*} \cdot 100 \cdot \frac{100}{44} \cdot \frac{100}{SCM\_Anhydrous} \quad (34)$$

$$w = \frac{m40^* - m600^* - ML\_Ca(OH)2^*}{m1000^*} \cdot 100 \cdot \frac{100}{SCM\_Anhydrous} \quad (35)$$

$Ca(OH)_2$: Amount of calcium hydroxide in the sample in g/100 g SCM;
*ML_Ca(OH)2**: Corrected mass loss between approx. 400 °C – 500 °C determined with the tangential method from TGA in wt.-%;
*m1000**: Corrected mass at 1000 °C taken from TGA in wt.-%;
SCM_Anhydrous: Amount of SCM in g/100 g *Anhydrous* calculated according to eq. 32;
$CaCO_3$: Amount of calcium carbonate in the sample in g/100 g SCM;
*ML_CaCO3**: Corrected mass loss between 600 °C – 750 °C determined with the stepwise method from TGA in wt.-%;
w: Amount of physically and chemically bound water (without water in calcium hydroxide) as well as remaining organic solvents and free water in the sample in g/100 g SCM;
*m40**: Corrected mass at 40 °C taken from TGA in wt.-%;
*m600**: Corrected mass at 600 °C taken from TGA in wt.-%.

Pozzolanic reactivity is often described by the consumption of calcium hydroxide (*Consumption CH*). With the thermogravimetric data of a R³-test it is possible to calculate this value. Consumption of $Ca(OH)_2$ represents the difference between the initial $Ca(OH)_2$ in a mix design and the amount of $Ca(OH)_2$ in a sample at testing time, as defined in [253, 255]. Additionally, the proposed mass balance approach of this study takes into account those parts of $Ca(OH)_2$ that are bound in $CaCO_3$ during drying or even during heating of the thermogravimetric measurement as stated by Taylor and Turner [278]. This basic approach was already suggested before by Kim and Olek for interpretation of thermogravimetric data of cement paste samples [269]. To calculate the amount of bound $Ca(OH)_2$ in a carbonation process the amount of $CaCO_3$ in the sample according to eq. 34 needs to be corrected with the value of $CaCO_3$ in original SCM. Moreover, the possible amount of $Ca(OH)_2$ in SCM reduces the consumption of $Ca(OH)_2$ by SCM and needs to be taken into account according to eq. 36,

$$Consumption\ CH = \frac{mix\_Ca(OH)2}{mix\_SCM} \cdot 100 - Ca(OH)_2 - (CaCO_3 - ML\_CaCO3\_SCM^* \cdot \frac{100}{44}) \cdot \frac{74}{100} - ML\_Ca(OH)2\_SCM^* \cdot \frac{74}{18} \quad (36)$$

Consumption CH: Consumption of calcium hydroxide by pozzolanic reaction of the SCM in g/100 g SCM;
mix_y: Mass of component *y* (SCM or $Ca(OH)_2$) in the mix design of testing program in g;
$Ca(OH)_2$: Amount of calcium hydroxide in the sample in g/100 g SCM;
$CaCO_3$: Amount of calcium carbonate in the sample in g/100 g SCM;
*ML_CaCO3_SCM**: Corrected mass loss between 600 °C – 750 °C determined with the stepwise method from TGA of original SCM in wt.-%;
*ML_Ca(OH)2_SCM**: Corrected mass loss between approx. 400 °C – 500 °C determined with the tangential method from TGA of original SCM in wt.-%.

For reasons of comparability, *Consumption CH* was also calculated without considering the carbonation processes and TGA data of the original SCM according to eq. 37,

$$Consumption\ CH\ (Common) = \frac{mix\_Ca(OH)2}{mix\_SCM} \cdot 100 - Ca(OH)_2 \quad (37)$$

Consumption CH (Common): Consumption of calcium hydroxide by pozzolanic reaction of the SCM in g/100 g SCM calculated without considering carbonation and TGA data of pure SCM;
mix_y: Mass of component y (SCM or $Ca(OH)_2$) in the mix design of testing program in g;
$Ca(OH)_2$: Amount of calcium hydroxide in the sample in g/100 g SCM.

4.5 Results and Discussion

The derivative of a TG-curve (DTG) of the reference sample indicates that drying with acetone results in an increased amount of carbonates (mass loss from 600 °C to 750 °C, Figure 37) compared to the samples dried with isopropanol according to the procedures described in section 4.2.2.

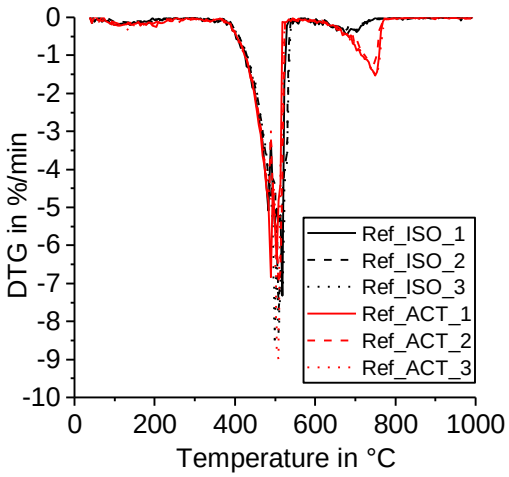

Figure 37: DTG – Reference (R^3-suspension without SCM) dried with isopropanol (ISO) and acetone (ACT).

Evaluation of the reference sample results in a calculated amount of calcium carbonate ($CaCO_3$) of 9.85 wt.-% with acetone drying and 3.39 wt.-% when isopropanol was used to stop reaction. The amount of calcium hydroxide ($Ca(OH)_2$) in the samples was 83.48 wt.-% for acetone drying and 91.63 wt.-% with isopropanol. The larger amount of $CaCO_3$ and the decrease in $Ca(OH)_2$ with the use of acetone for drying was already reported earlier by Taylor and Turner [278]. They observed an aldol condensation reaction of acetone in alkaline environment at room temperature. The sorbed and newly formed organic substances are less volatile than acetone and yield carbonate ions on heating during a thermogravimetric measurement (200 °C to 600 °C) [271, 278, 279]. Kim and Olek pointed out that drying cement paste samples before grinding, as it was done in the isopropanol treatment in this study, results in less carbonation compared to drying samples after grinding, like the acetone treatment described in this paper [269]. The sum of $CaCO_3$ and $Ca(OH)_2$ in the reference samples is less for samples dried with acetone compared to isopropanol that indicates that free water as well as parts of the solvent remains in the samples dried with acetone. This effect may cause problems in interpretation of TGA data.

Figure 38 to Figure 41 show the DTG-curves of the R^3-samples with silica fume (SF), metakaolin (MK1 and MK2) and mixed calcined clay (MC). Especially the results with mixed calcined clay (Figure 38) support the observation investigated in the reference sample that drying with acetone increases the formation of carbonates (mass loss from 600 °C to 750 °C). Similarly, Kim and Olek have shown enhanced carbonation in acetone treated cement paste samples [269]. For stronger pozzolanic reactions like for silica fume and metakaolin, more $Ca(OH)_2$ is consumed by SCM and consequently less $Ca(OH)_2$ remains for carbonation. As the investigated mixed calcined clay (MC) is the weakest pozzolan in this study, the effect of the remaining free water when dried with acetone is visible for these samples as similar to the reference one. When looking at the mass loss from 40 °C to 105 °C, Figure 38 clearly shows that free water remains in the samples after drying with acetone. It decreases with time in the exicator as mass loss reduces with the sequence MC_ACT_1, MC_ACT_2 and MC_ACT_3.

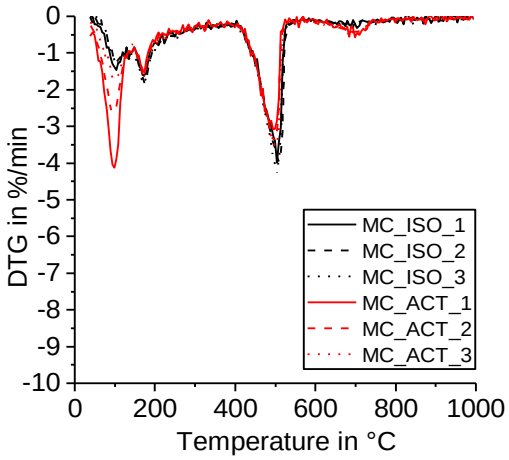

Figure 38: DTG – R³-sample with mixed calcined clay (MC) dried with isopropanol (ISO) and acetone (ACT).

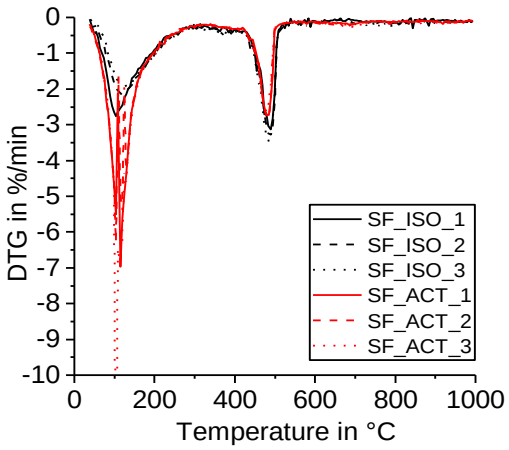

Figure 39: DTG – R³-sample with silica fume (SF) dried with isopropanol (ISO) and acetone (ACT).

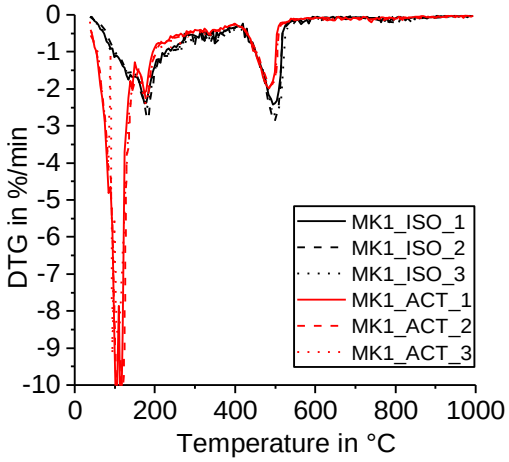

Figure 40: DTG – R³-sample with metakaolin (MK1) dried with isopropanol (ISO) and acetone (ACT).

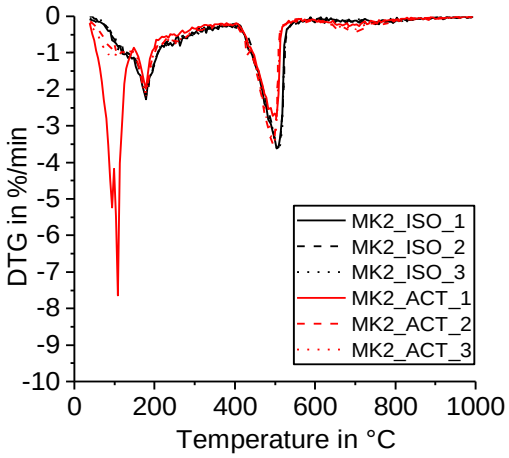

Figure 41: DTG – R³-sample with metakaolin (MK2) dried with isopropanol (ISO) and acetone (ACT).

Some samples that were dried with acetone show strong deviations in the DTG-curve in the temperature range of around 40 °C to 150 °C (e.g. Figure 39). This could be due to some remaining acetone or adol polycondensated products [278] in the samples that may affect the thermogravimetric measurement. Overall, the measured TGA data show a larger mass loss from room temperature to 40 °C for samples dried with acetone compared to isopropanol, which supports the results outlined above that some acetone (derived products [278]) and free water is remaining in these samples before testing.

The results achieved from evaluation of TGA data following the above explained mass balance approach are shown in Figure 42 for both drying with acetone and isopropanol. Value *w*, which summarizes the amount of physically and chemically bound water (without water in calcium hydroxide) as well as remaining organic solvents and free water is larger in samples dried with acetone compared to isopropanol. In literature, this value is often used to describe the amount of 'chemically' bounded water in reaction products of cement paste samples [258, 261, 268], but as outlined above, R³-samples dried e.g. with acetone or isopropanol (according to the described procedure) still contain some organic solvent and free water remaining that is per definition included in the calculation of value *w* according to eq. 35. Infrared spectroscopy data from Zhang and Scherer [280] demonstrate that isopropanol also remains strongly sorbed by cement hydration products after oven drying. The comparison of the drying methods is not strictly focused on the effect of isopropanol vs. acetone, as the drying procedures are done differently. The purpose of the comparison in this paper is on the effect of the methods. This study considers the effect of drying R³-samples (with isopropanol and acetone done in different ways) on the

results achieved with thermogravimetric analysis (TGA) using a newly proposed mass balance calculation approach.

Following the results of *Consumption CH* and drying with acetone (red symbols in Figure 42), pozzolanic reactivity could be rated as SF > MK1 > MK2 > MC. Even though the proposed mass balance approach considers carbonation, the results differ for the two solvents employed. This finding is in contrast to observations of Kim and Olek for cement paste samples [269]. They reported nearly identical results for the amount of $Ca(OH)_2$ when using the modified interpretation of TGA data analogous to the proposed mass balance approach in this study [269]. Moreover, Kim and Olek also stated that if significant carbonation takes place, it cannot be compensated by a modified interpretation of thermogravimetric data [269]. These findings encourage that an appropriate choice of drying procedure is essential to achieve reliable thermogravimetric results in cement pastes as well as in R³-samples.

Figure 43 shows a zoom in of Figure 42 for the samples dried with isopropanol. It can be noted that the distribution of values is smaller when evaluating *Consumption CH* compared to *w* referring to the standard deviation shown in Figure 43. This finding is in line with results for cement paste samples from Snellings et al. [258]. In a round robin test, they found that interlaboratory reproducibility was better for the analysis of calcium hydroxide content compared to the amount of chemically bound water determined by thermogravimetric analysis [258], that corresponds to the calculation of value *w* in this study for R³-samples. Snellings et al. explained this phenomenon by a larger sensitivity of the bounded water content to changes in the drying procedure of the samples [258]. Additionally, value *w* calculated according to eq. 35 also includes the amount of remaining organic solvents and free water in the sample, that is strongly influenced by the drying procedure. Regarding *Consumption CH* and drying with isopropanol (black symbols in Figure 42 and Figure 43), pozzolanic reactivity can be ordered as MK1 > SF > MK2 > MC.

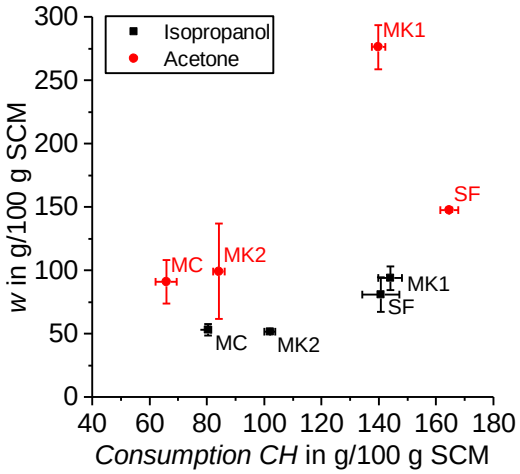

Figure 42: *w* and *Consumption CH* (acetone and isopropanol).

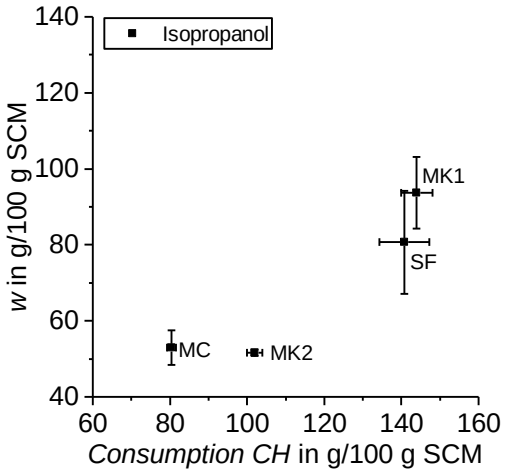

Figure 43: Zoom in of Figure 42: *w* and *Consumption CH* (isopropanol).

This sequence could be validated with calorimetry results as shown in Figure 44. The total heat release up to seven days at 40 °C for all tested SCMs are in the range of 350 J/g SCM for the mixed calcined clay (MC) and 757 J/g SCM for the relatively pure metakaolin employed in this study (MK1). The tested silica fume has a total heat release of 603 J/g SCM (SF) and the metakaolin with quartz impurities 452 J/g SCM (MK2). Consequently, all of the tested SCMs can be categorized in a high range of heat release (> 250 J/g SCM) according to Snellings and Kamyab [257]. Compared to the other pozzolans in this study, the mixed calcined clay (MC) shows the weakest reactivity. During calcination of clays kaolinite is transformed to amorphous material, with a 2:1 ratio of the clays staying semi-crystalline. It is known that the clay structure significantly affects their pozzolanic reactivity [267]. More specifically calcined 1:1 (sandwich layer = tetrahedral-octahedral = TO) clays like metakaolin are more reactive

than calcination of other clays such as illite, muscovite (mica) (2:1, TOT) and chlorite (2:1:1, TOTO) [28, 104, 105, 267].

The calorimetric results in Figure 44 clearly show an early reaction of the two tested metakaolin (MK1 and MK2) compared to the heat development of the mixed calcined clay (MC) and silica fume (SF). The enhanced initial pozzolanic reaction of metakaolin that occurs within the first 48 hours was already reported by Beuntner [267] by comparing calorimetric measurements of a relatively pure metakaolin and a mixed calcined clay. Higher reactivity could be attributed to the more dissolvable Al from metakaolin. The Si/Al ratio in solution may also play a decisive role on reaction kinetics, in addition to the total content of the reactive phase. More reactive aluminate species may lead to an increase in reactivity [191]. This is also known in the process of polycondensation reaction, that aluminate species react more rapidly with silicate species than the reaction between two silicate species [281].

Figure 45 shows the correlation of *Consumption CH* with overall heat release from calorimetry test samples dried with acetone and isopropanol and evaluated with the proposed mass balance approach (*) as well as without (*Consumption CH (Common)*): Calculation of calcium hydroxide consumption without considering carbonation and TGA data of the original SCMs).

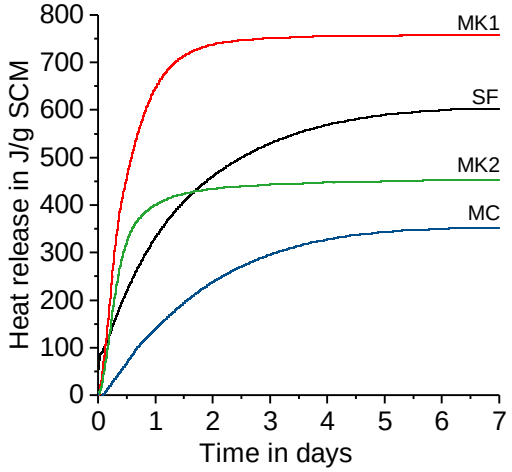

Figure 44: Results of calorimetry test of R³-samples.

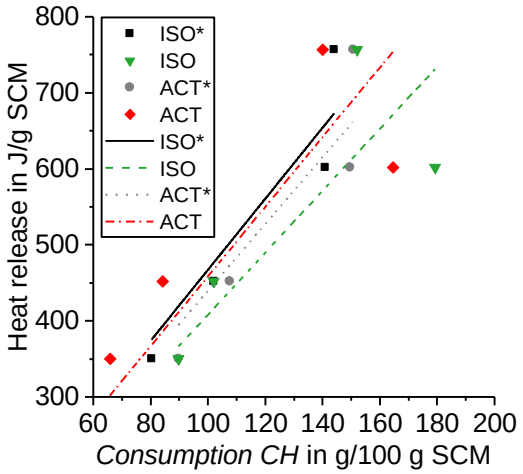

Figure 45: Correlation of heat release and *Consumption CH* (acetone and isopropanol) — Used abbreviations are outlined in Table 11.

Table 11 summarizes the regression accuracy values R^2 from the linear correlation of *Consumption CH* and total heat release. The intersection with the y-axis was set to zero, similar to the approach from Suraneni and Weiss [255]. Drying with isopropanol results in a slightly higher R^2 value compared to reaction stoppage with acetone. When the mass balance approach of TGA data is applied, R^2 is even higher as compared to the commonly used technique without taken into account carbonation and TGA data of original SCM. When comparing these two evaluation techniques, the percentual increase of R^2 is a little higher for acetone treated samples (3.2 %) compared to isopropanol (2.8 %). As drying with acetone results in an increased carbonation, incorporating these effects in the evaluation of TGA data result in a somehow larger effect as for drying with isopropanol with lesser amount of $CaCO_3$. Data from Suraneni and Weiss show a R^2 value of 0.94 for the linear regression of the same parameters generated with tests on different SCMs, as summarized in Figure 46 [255]. The amount of carbonates and TGA data of original SCM in the interpretation of their thermogravimetric test results was not explicitly taken into account [255].

Table 11: Summary of the linear correlation Heat release = x · *Consumption CH*.

Drying	Mass Balance Approach of TGA Data	Abbreviation	R^2	Gradient x
Isopropanol	New proposal	ISO*	0.988	4.67
Isopropanol	Common	ISO	0.961	4.08
Acetone	New proposal	ACT*	0.985	4.40
Acetone	Common	ACT	0.954	4.58

Table 11 shows also the calculated gradients for the different linear fits, and show a range between 4.08 (ISO) and 4.67 (ISO*). Taking into account the drying method with isopropanol and the proposed mass balance approach of this study (ISO*), the results indicate a heat of reaction of 467 J/g for the reacted calcium hydroxide, that refers to 34.56 kJ/mol calcium hydroxide for the tested SCMs. This result is in very good (8% relative error) agreement with Suraneni and Weiss calculated a value of 31.67 kJ/mol based for their test results [255]. Newman reported a heat of reaction for the reaction of calcium hydroxide with silica gel and water of 10.3 kcal, that corresponds to around 43 kJ/mol [282]. The value for the reaction enthalpies between SiO_2 and/or Al_2O_3 and calcium hydroxide during a pozzolanic reaction of SCMs is mainly depending on the exact reaction that takes place. Reaction enthalpies calculated with the thermodynamic software GEMS are in the range of 26 to 35 kJ/mol [255].

Figure 46 shows the test results of this study, dried with isopropanol and calculated with the new proposed mass balance approach for TGA data (ISO*), along with the results from Suraneni and Weiss [255]. The SCMs analyzed in this study (marked with stars and labelled in bold in Figure 46) are mainly located directly on the linear fitted line through the data from these authors [255]. Following the classification proposed by Suraneni and Weiss, the calcined clay (MC) and the metakaolin with quartz impurities (MK2) are classified as pozzolanic SCMs [255]. The investigated silica fume (SF) as well as the relatively pure metakaolin (MK1) are located in the upper pozzolanic area. MK1, that has the highest amount of Al_2O_3 (42.18 wt.-%) of the investigated SCMs, is located above the dashed line that confirms the outcome from Suraneni and Weiss [255]. They concluded that the pozzolanic reaction of aluminum rich phases release more heat compared to silicon rich ones [255].

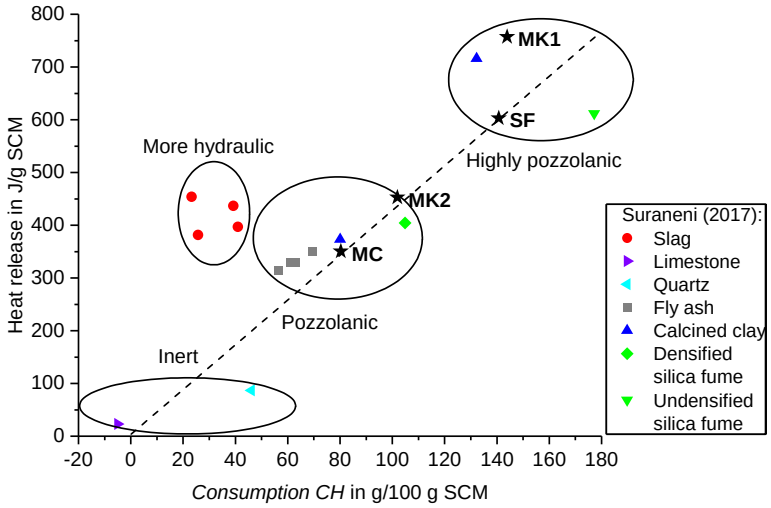

Figure 46: Results of this study SF, MK1, MK2 and MC, (ISO*: Dried with isopropanol and calculated according to the proposed mass balance approach) shown in the figure adapted from Suraneni and Weiss [255].

4.6 Conclusions

This study considers the influence of drying R³-samples with isopropanol and acetone (done in different ways) on the results achieved with thermogravimetric analysis (TGA) using a new calculation approach. A mass balance approach is proposed for the measured thermogravimetric (TG) data from R³-tests that

considers both the carbonation of samples and TG data of the original SCMs. From the results of this study, the following conclusions can be drawn:

1. The drying procedure with acetone described in this paper, resulted in some free water, sorbed acetone and/or acetone derived organic polycondensates [278] to remain in the samples that may affect the TGA data and its interpretation.
2. TG results of dried samples with the isopropanol method showed less carbonates and a better correlation with calorimetric test results compared to samples dried with the acetone method. Thus, the drying method with isopropanol (instead of acetone) and use of the proposed mass balance approach is recommended for TGA of R^3-test.
3. The order of reactivity is the same for calorimetric measurement and TGA regarding the consumption of calcium hydroxide in samples dried with isopropanol: MK1 > SF > MK2 > MC.
4. The incorporation of carbonation and TGA data of original SCMs in the evaluation of TG data of R^3-samples improves the correlation between calcium hydroxide consumption from TGA and the heat release determined with a calorimetric measurement.

5 Publication 4: Experimental Results and Discussion

Publication 4 (Construction and Building Materials, https://doi.org/10.1016/j.conbuildmat.2024.136534):

Pozzolanic Metakaolin Reactivity: Time-Dependent Influence of Calcium Hydroxide, Alkali Hydroxides, and Sulfates

Kira Weise[1,*], Luca Marei Endell[1], Neven Ukrainczyk[1,*], Eduardus Koenders[1]

[1] Technical University of Darmstadt, Institute of Construction and Building Materials, Germany.
* Corresponding authors: weise@wib.tu-darmstadt.de, ukrainczyk@wib.tu-darmstadt.de.

Abstract: In the quest for environmentally sustainable binders within the construction industry, metakaolin (MK) has emerged as a highly promising material. Its reactivity and hardening performance encompass a wide range of applications, spanning from lime to cement-based materials. This performance is primarily underpinned by the pozzolanic reaction with calcium hydroxide (CH), leading to the formation of various calcium aluminate silicate hydrates. The intricacies of the hydration kinetics and resultant reaction products hinge on several factors woven into the specifics of the binder type. This study investigates the influence of CH availability, explored through initially mixed MK/CH weight ratios of 0.33 and 1.0. Furthermore, the study examines the impact of introducing alkali hydroxides (KOH and NaOH) and/or sulfates (K_2SO_4 and Na_2SO_4) on the pozzolanic reactions. Short-term analysis employed inductively coupled plasma optical emission spectrometry (ICP-OES), and pH measurements for pore solution as well as isothermal calorimetry, and in-situ X-ray diffraction (XRD) on paste samples. Long-term investigations extended to 245 days at 40 °C, incorporating XRD, thermogravimetric (TGA) and scanning electron microscopy coupled with energy-dispersive X-ray spectroscopy (SEM/EDX). Results provide insights into the kinetics of phase assemblage and compositions of C-A-S-H gels, highlighting the transformation of metastable C_2ASH_8 and C_4AH_{13} to stable Si-rich hydrogarnet phases, incorporating sulfate, under excess CH conditions. Higher MK/CH enriches Si/Ca, Al/Ca, enhancing C-A-S-H gels, while KOH addition further boosts Al/Ca ratios.

Keywords: Metakaolin; pozzolanic reaction kinetics; metastable phase transformations; isothermal calorimetry; SEM/EDX, ICP-OES.

5.1 Introduction

Global warming and raw material shortages in the construction industry have intensified global research into more environmentally friendly binders. In this context, metakaolin (MK) has emerged as a highly promising material [36, 41, 88–94], suitable for use in lime [121–127] and cement-based systems [7, 8, 96–100]. MK is derived from the natural clay mineral kaolinite, which undergoes calcination at temperatures of around 700 °C [11, 22, 23, 139–141]. This thermal activation leads to dehydroxylation [24, 32] and subsequent structural reorganization processes [24, 142], resulting in a (partly) amorphous [27, 29] and reactive structure [27, 29–32]. The hardening performance of MK in various binder systems is primarily driven by its pozzolanic reaction with calcium hydroxide (CH) [81, 104], resulting in the formation of various calcium aluminum silicate hydrates [42, 45, 79, 110, 114, 119, 120].

In MK-CH systems, the reaction kinetics, hydrate phase formations, and their long-term transformations from metastable to more stable phase configurations depend on various influencing factors related to the specific binder system for a given application. These factors include the initial metakaolin to calcium hydroxide weight ratio (MK/CH) [49, 65, 73–75], curing time [64], temperature [69] and secondary activators [49, 53, 62, 74–76]. A recent study [49] investigated the influence of CH availability, alkali hydroxides and sulfates on the hydration processes of several supplementary cementitious materials, including metakaolin (MK). In addition to the results published for reaction times up to 28 days at 27 °C

[49], this article contributes to the research field by covering investigations of short- and long-term reaction processes. Additionally, this study allows to compare the effect of different alkali hydroxide (KOH and NaOH) and sulfate types (K_2SO_4 and Na_2SO_4).

MK reaction with CH predominantly forms amorphous C-A-S-H phases [27, 49–61] and stratlingite (C_2ASH_8) [27, 49–51, 53, 54, 56, 59, 61–67]. In [79], it is discussed that stratlingite is thermodynamically unstable in the presence of CH and may slowly transform into more stable hydrogarnet phases (C_3AH_6) in the long-term [53, 59, 69, 75, 78, 209]. C_3AH_6 is used as one hydrogarnet representative in this study, including hydrogarnet phases with incorporated silicon. Similarly, the formation of C_4AH_{13} was reported in some publications [51, 53, 54, 65, 68, 69], along with possible transformation processes to more stable phases [54, 65, 68].

Understanding these long-term transformation reactions is crucial, as they can adversely affect the material's durability properties, such as porosity, leading to a degradation of the overall materials performance.

The addition of alkali hydroxides to MK-CH systems primarily results in an increase in the pH value of the solution, accelerating MK dissolution [31, 76, 180–184] and pozzolanic reaction [59, 76, 87, 192, 193]. In contrast, the increase in pH inhibits CH dissolution [53, 59, 147, 183] due to the common ion effect [53, 59, 147, 183]. While the literature has not conclusively clarified the influence of this opposing effect on MK pozzolanic reactions, the present study provides deeper insights into this aspect.

The addition of sulfates to MK-CH systems is reported to lead to rapid formation of ettringite [58, 62, 66, 76, 87, 105–107]. Ettringite may transform into monosulfoaluminate (depending on the sulfate content) in the absence of carbonates [49, 62, 66, 75, 87]. If carbonates are present in the system, ettringite is stabilized [87, 107] and carbonate-containing AFm phases are formed instead of monosulfoaluminate [76, 87, 107, 143, 173, 218].

In the present study, the effect of calcium hydroxide availability (initial MK/CH weight ratios of 0.33 and 1.0), as well as the incorporation of alkali hydroxides (KOH and NaOH) and sulfates (K_2SO_4 and Na_2SO_4), on pozzolanic MK reactions is investigated in the short and long-term, up to 245 days, and at a reaction temperature of 40 °C. In the short-term, defined up to two days of reaction at 40 °C in this study, elements in the pore solution were detected with inductively coupled plasma optical emission spectrometry (ICP-OES), whereas the reaction kinetics as well as phase formations and transformations are analyzed by isothermal calorimetry and in-situ X-ray diffraction (XRD). The reaction products in the long-term, defined as reaction times greater than two days at 40 °C, are mainly characterized by thermogravimetric analysis (TGA), quantitative X-ray diffraction (qXRD) and scanning electron microscopy coupled with energy-dispersive X-ray spectroscopy (SEM/EDX).

This article systematically investigates pozzolanic MK reactivity, highlighting novel long term experimental results proving transformation reactions of metastable MK reaction products (C_2ASH_8 and C_4AH_{13}) to more stable hydrogarnet phases (C_3AH_6) under excess CH conditions. The experimental results presented in this study serve as a fundamental basis for the development of MK reaction models, facilitating the design of novel MK-based "low-carbon" binders in the future.

5.2 Materials and Methods

5.2.1 Materials

For the present study, paste samples were prepared by mixing an alkaline suspension (main part is calcium hydroxide) with powdered metakaolin. The industrially produced highly pure metakaolin used has an amorphous content of approx. 98 wt.-% with the chemical composition shown in Table 17. Powdered calcium hydroxide (CH ≥ 96 %), potassium hydroxide pellets (KOH ≥ 96 %, NaOH ≥ 98 %) as well as powdered potassium and sodium sulfate (K_2SO_4 ≥ 99 %, Na_2SO_4 ≥ 99 %) from Carl Roth

GmbH & Co. KG (Karlsruhe, Germany) together with deionized water were used for the preparation of the alkaline suspension.

Table 12: Chemical composition of the used metakaolin in wt.-% according to the manufacturer.

	SiO_2	Al_2O_3	Fe_2O_3	CaO	MgO	Na_2O	K_2O	TiO_2
MK	52.3	45.2	0.42	0.04	0.04	0.22	0.15	1.7

The sample compositions vary in the MK/CH weight ratio (0.33 and 1.0), the type and amount of added alkali hydroxides (KOH and NaOH) as well as the addition of alkali sulfates (K_2SO_4 and Na_2SO_4) as shown in Table 13. The water to solid (MK+CH) ratio was set to 1.2. The OH^-/MK weight ratios from the addition of KOH and NaOH were fixed to 0.0077 [87] (0.32KOH and 0.32NaOH) and 0.0306 (1.28KOH and 1.28NaOH). The samples with incorporated sulfates have a fixed SO_4^{2-}/MK weight ratio of 0.0648 according to the samples used for the R^3-test for reactivity classification [87].

Table 13: Sample weight ratios (OH^- refers to the additionally added OH^- from KOH or NaOH).

Sample	MK/CH weight ratio	OH^-/MK weight ratio	OH^-/CH weight ratio	Molarity (moles OH^-/L)	SO_4^{2-}/MK weight ratio	SO_4^{2-}/CH weight ratio
0.33MK_0K	0.33	0	0	0	0	0
0.33MK_0.32KOH	0.33	0.0077	0.0025	0.09	0	0
0.33MK_1.28KOH	0.33	0.0306	0.0102	0.38	0	0
0.33MK_0.32KOH_K2SO4	0.33	0.0077	0.0025	0.09	0.0648	0.0216
0.33MK_0.32NaOH	0.33	0.0077	0.0025	0.09	0	0
0.33MK_1.28NaOH	0.33	0.0306	0.0102	0.38	0	0
0.33MK_0.32NaOH_Na2SO4	0.33	0.0077	0.0025	0.09	0.0648	0.0216
1MK_0K	1.0	0	0	0	0	0
1MK_0.32KOH	1.0	0.0077	0.0077	0.19	0	0
1MK_1.28KOH	1.0	0.0306	0.0307	0.75	0	0
1MK_0.32KOH_K2SO4	1.0	0.0077	0.0077	0.19	0.0648	0.0648
1MK_0.32NaOH	1.0	0.0077	0.0077	0.19	0	0
1MK_1.28NaOH	1.0	0.0306	0.0307	0.75	0	0
1MK_0.32NaOH_Na2SO4	1.0	0.0077	0.0077	0.19	0.0648	0.0648

5.2.2 Sample Preparation

For the alkaline suspensions, the alkali hydroxide pellets were firstly dissolved in a part of the deionized water for 15 min using a magnetic stirrer [84, 246]. Secondly, the alkali hydroxide solution was homogenized with the remaining components (CH, alkali sulfates and the remaining deionized water) with the help of an electric mixer for 15 min [84, 246]. For the preparation of the reactive samples, 100 g alkaline suspension was homogenized with MK by using an electric mixer for 5 min [84] (3 min for calorimetry and in-situ XRD samples [83]). The fresh paste samples were directly used for isothermal calorimetry testing as well as for in-situ X-ray diffraction (selected sample compositions as outlined in Table 14).

To extract the pore solution, centrifugal containers were filled with 50 g of fresh paste for each sample composition (samples with MK/CH = 0.33 only), sealed and stored at ambient temperatures of ~ 20 °C. Centrifuge „Multifuge X3 FR“ from Thermo Fisher Scientific Inc. (Waltham, USA) was used to collect the pore solution of the samples after 30 minutes, 3, 5, 24 and 48 hours. The samples were centrifuged with 4000 rotations per minute at 20 °C. In a next step, the pore solution that sediments on top of the solids was pressed through a filter syringe with a pore size of 2–3 μm. The following sample preparation for the inductively coupled plasma optical emission spectrometry (ICP-OES) is based on DIN EN ISO 11885 [283]. The obtained pore solution was weighted and pH was measured with a device from Mettler-Toledo GmbH (Gießen, Germany). For the acidification of the solution prior to testing, nitric acid (68 % with a density of 1.41 g/cm³) was added with an acid/solution weight ratio of approx. 0.07.

Subsequently, the pH was measured again to check the required value of < 1.0 according to DIN EN ISO 11885. The acidified samples were stored in sealed polypropylene containers at 20 °C. Prior to testing, 1 mL of the sample solution was diluted with 9 mL of water. In a next step, 1 mL of 68 % nitric acid and 1 mL of 37 % hydrogen peroxide was added and the solution was heated up at 105 °C for one hour to accelerate the degradation of organic components. Water evaporated in this step is refilled afterwards to a total sample volume of 10 mL.

Additionally, to study the long-term effects, polyethylene containers were filled for each sample with 10 g ± 0.1 g of the fresh paste [82], sealed and stored at 40 °C in a ventilated oven [84–87]. After 2, 7, 56 and 245 days, the whole sample (10 g) was gently crushed and grinded in an agate mortar along with 10 mL isopropanol. An aliquot of 3 g ± 0.05 g of the grinded sample was taken before the isopropanol was completely evaporated and immediately placed in 50 mL of isopropanol [82] followed by the drying procedure recommended for cement paste samples according to Snellings et al. [258, 264]. The samples were dried in a desiccator for at least 12 hours, but less than 2 days and gently hand-milled before TGA and XRD testing. For the SEM/EDX measurements, tablets with a diameter of 6.5 mm were prepared by placing 0.05 g of powdered sample in the hydraulic press tool from Enerpac (Menomonee Falls, Wisconsin) and pressing for 1 min with 2 kN (~ 60 N/mm²).

5.2.3 Methodology

For a detailed understanding of the reaction mechanisms, the obtained pore solution was tested after 30 minutes, 3, 5, 24 and 48 hours with inductively coupled plasma optical emission spectrometry (ICP-OES) and the pH value was determined. Isothermal calorimetry measurements were carried out at 40 °C for seven days and in-situ X-ray diffraction (XRD) was performed on selected samples at ambient temperatures (~ 20 °C). The dried powder obtained from samples reacted at 40 °C was used for thermogravimetric analysis (TGA) and X-ray diffraction (XRD) after 2, 7, 56 and 245 days. The powder was additionally pressed into tablets that were used for scanning electron microscopy coupled with energy-dispersive X-ray spectroscopy (SEM/EDX). An overview of the performed analysis techniques is given in Table 14 together with the assignment to the short- (ST, results in section 5.3.1) and long-term (LT, results in section 5.3.2) definition of this article.

Table 14: Overview of analysis techniques, samples, reaction temperatures and testing times (min: minutes, h: hours, d: days, ST: short-term, LT: long-term).

Methodology	Sample	Temperature	Testing times	ST/LT
Calorimetry	Fresh paste	40 °C	≤ 7d	ST
ICP-OES and pH*	Pore solution	20 °C	30min, 3h, 5h, 24h and 48h	ST
In-situ XRD**	Fresh paste	~ 20 °C	≤ 90h	ST
TGA	Dried powder	40 °C	2d, 7d, 56d, 245d	LT
XRD***	Dried powder	40 °C	2d, 7d, 56d, 245d	LT
SEM/EDX*	Tablets	40 °C	7d, 245d	LT

* All samples with MK/CH = 0.33 only.
** Selected samples only: 0.33MK_0.32KOH, 1MK_0.32KOH, 0.33MK_0.32KOH_K2SO4 and 1MK_0.32KOH_K2SO4.
*** Quantitative XRD (qXRD) for samples with MK/CH = 0.33 without incorporated sulfates only.

Inductively Coupled Plasma Optical Emission Spectrometry

„SPECTRO ARCOS ICP-OES“ from SPECTRO Analytical Instruments GmbH (Kleve, Germany) was used for inductively coupled plasma optical emission spectrometry (ICP-OES). The following elements were determined: Ca, Al, Si, Na, K and S.

Isothermal Calorimetry

For calorimetry testing, “MC CAL“ from C3 Prozess- und Analysentechnik GmbH (Haar, Germany) was used with preconditioning and calibration at 40 °C. Data was collected every 30 s for 7 days [83]. The sample preparation as well as the calculation of the heat flow curves for the reactive samples was performed according to the proposed procedure in [83]. The signals recorded within the first 25 minutes

after mixing were assigned to dissolution processes [83] and consequently excluded for the calculation of the reaction heat releases. To link the gained information from in-situ XRD measurements to the heat flow peaks from calorimetry, selected samples (0.33MK_0.32KOH and 0.33MK_0.32KOH_K2SO4) were additionally tested at isothermal conditions of 20 °C.

X-Ray Diffraction

"Bruker D2 Phaser" from Bruker Corporation (Billerica, USA), configured with CuK$\alpha_{1,2}$ radiation (40kV and 10mA), linear Lynxeye detector (5 degrees opening) was used for X-ray diffraction (XRD) measurements. The powdered samples were measured with 0.02 2θ step size in a 5–70 2θ range and a measurement time of 2 seconds per step. The phases used for the quantitative XRD (qXRD) analysis are exemplarily shown for 0.33MK_1.28KOH_2d and 0.33MK_1.28KOH_245d in Figure S4-1 in the Supplementary Material. As calcium hemicarboaluminate [284] has a similar structure compared to C_4AH_{13} (AFm phase with ½ CO_3^{2-} instead of OH^- as anion), it represents C_4AH_{13} very well [49] and was used for this phase in the present study due to the lack of information in existing databases. The stratlingite structure model provided by Santacruz et al. [285] well captures the diffractogram peaks, particularly the main peak at around 7 2θ (Figure S4-1 in the Supplementary Material). The qXRD analysis in this study was performed for the samples with MK/CH of 0.33 without added sulfates as internal standard method by Rietveld refinement using Topas version 5 software from Bruker (Billerica, USA), with the respective amount of CH in each sample from TGA results as internal standard.
Additionally, short-term in-situ XRD measurements were run with four selected samples only up to 30 h (1MK_0.32KOH and 1MK_0.32KOH_K2SO4 measured from 5 to 23 2θ every hour), 50 h (0.33MK_0.32KOH_K2SO4 measured from 5 to 33 2θ every two hours up to 44 h and 50 h) and 90 h (0.33MK_0.32KOH measured from 5 to 33 2θ every two hours up to 35 h and further measurement every four hours). Airtight sample holder with a dome like X-ray transparent cap from Bruker was used. The duration for a step size of 0.67 s/step resulted in single measurement run of 19 min followed by a (cooling) pause of 40 or 100 minutes, respectively. As the temperature in the measurement device cannot be adjusted, the in-situ XRD measurements were carried out at ambient temperatures of 20 °C, slightly heated up due to the X-rays applied (with enough pauses between regular measurements to avoid excess heat generation).

Thermogravimetric Analysis

"STA 449 F5 Jupiter" from NETZSCH (Selb, Germany) was used for thermogravimetric analysis (TGA), whereas nitrogen was chosen as the inert gas. 40–50 mg of dried powder sample was placed in alumina crucibles, firstly heated up to 40 °C, kept constant for 30 min and secondly heated up to 1000 °C at a constant heating rate of 20 °C per minute. The consumed CH (CH-consumption) as well as the chemically bound water (CBW) in hydration products were calculated in gram per 100 g MK according to [84] by applying the tangent method [247].

Scanning Electron Microscopy with Energy-Dispersive X-Ray Spectroscopy

"Zeiss EVO LS25" from Carl Zeiss AG (Oberkochen, Germany) was used for scanning electron microscopy coupled with energy-dispersive X-ray spectroscopy (SEM/EDX). The tablets were used for the measurements, the accelerating voltage was set to 15 kV [247], the working distance was fixed to 8.5 mm and the magnification was set to 4000x. For each sample, EDX point analysis was performed on five randomly chosen measuring areas each one consisting of 140 measured points (Figure S4-2 in the Supplementary Material) resulting in 700 measured points per sample. The dwell time per spot was set to 5 s and the distance between the measured spots was 5 μm [247]. The results are presented in Si/Ca-Al/Ca diagrams (mass ratios) allowing to qualitatively identify reaction products as well as remaining MK.

5.3 Results and Discussion

This section is split into short- and long-term segments, with a division marked by a set threshold of two days of reaction at 40 °C.

5.3.1 Short-Term Results and Discussion

In this study, the short-term is defined as the initial two days of the reaction at 40 °C. Despite conducting the isothermal calorimetry measurements up to seven days at 40 °C, the results are presented in this section (Figure 47 to Figure 50) because the primary reaction peaks manifest within the first two days.

The heat flow curves are depicted up to two days of reaction, while the heat release is illustrated up to seven days. Figure 47 clearly demonstrates the acceleration of the reactions with an increasing alkali hydroxide content for samples with MK/CH of 0.33, aligning with findings in the literature (MK/CH = 0.43 with NaOH addition) [49]. Sodium hydroxide (NaOH) addition induces a more intense acceleration compared to potassium hydroxide (KOH). This finding may be attributed to the more profound dissolution of MK in NaOH [181, 184], even with higher pH values of KOH solutions [184]. Notably, a slightly higher Al concentration was measured in the sample 0.33MK_0.32NaOH compared to 0.33MK_KOH in this study (Figure 52 (A)). Two explanations are considered for this phenomenon: firstly, the higher charge density of Na^+ due to its smaller size compared to K^+ promotes the hydrolysis reaction to a greater extent, leading to an increased dissolution rate [181, 195]. Secondly, Scherb et al. [184] reported enhanced alkali uptake by MK in NaOH solutions compared to KOH, possibly due to the smaller size of sodium ions (Na^+), weakening the MK structure and resulting in more intense dissolution [184].

In samples with sulfates, the first peak is characterized by heat flow “shoulders” indicating several overlapping reaction processes (Figure 48 (A)). The initial peaks are more pronounced compared to samples without sulfates, and the use of sodium instead of potassium again leads to more accelerated reactions. As shown in Figure 48 (B), samples with incorporated sulfates exhibit higher total heat releases after seven days (986 J/(g MK) for 0.33MK_0.32KOH_K2SO4 and 982 J/(g MK) for 0.33MK_0.32NaOH_Na2SO4) compared to those without sulfates (909 J/((g MK)) for 0.33MK_0.32KOH and 931 J/(g MK) for 0.33MK_0.32NaOH). The increased heat release in sulfate-containing samples can be explained by the additional formation of ettringite in an exothermic reaction. With a heat of reaction for the formation of ettringite of - 81.1 kJ/(mol SO_4^{2-}) [75], the additional heat generated by the formation of ettringite from the total amount of sulfates in this study can be calculated to be 55 J/(g MK) (= 81.1 kJ/mol · 0.0648 g/(g MK) / 96 g/mol · 1000). As reported elsewhere and shown in the in-situ XRD results in this study, ettringite can transform to monosulfoaluminate (depending on the sulfate content) in the absence of carbonates [49, 62, 66, 75, 87]. Assuming a heat of reaction for the endothermic transformation of ettringite (AFt) to monosulfoaluminate (Ms) of 89.5 kJ/(mol AFt) [75], an endothermic heat can be calculated to 20 J/(g MK) (= 0.0648 g/(g MK) / 96 g/mol / 3 · 89.5 kJ/mol · 1000) assuming the total conversion to Ms. In total, these calculations would results in a surplus of total heat release due to sulfate reactions (AFt formation and transformation to Ms) of 35 J/(g MK). Parashar and Bishnoi investigated an acceleration of ettringite formation with the simultaneous addition of NaOH and a later occurrence of heat flow peaks with increasing sulfate content [49].

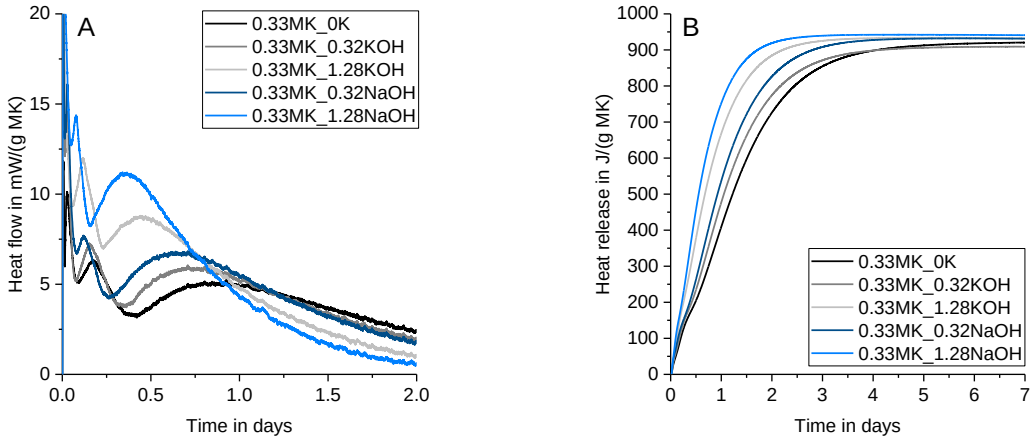

Figure 47: Heat flow curves (A) and heat release (B) from isothermal calorimetry measurements at 40 °C of all samples with MK/CH of 0.33 without added sulfates (Fig. S4-3 in the Supplementary Material shows the same results up to 7 days of reaction).

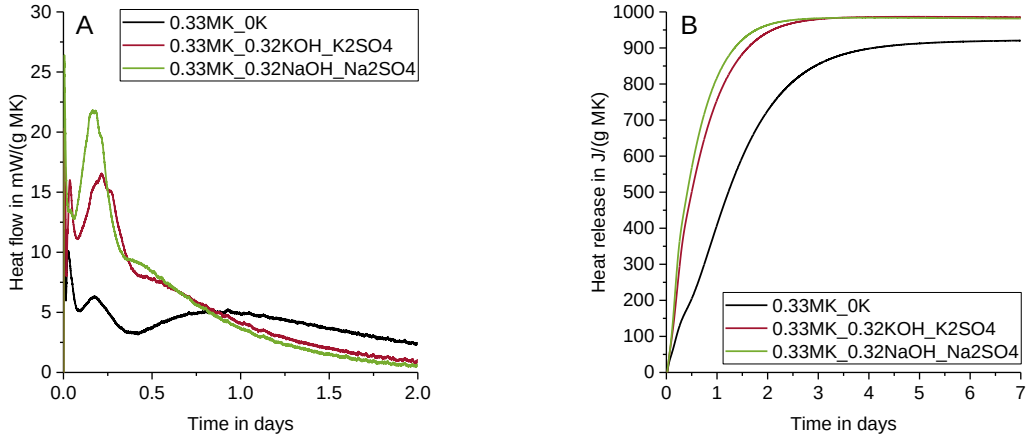

Figure 48: Heat flow curves (A) and heat release (B) from isothermal calorimetry measurements at 40 °C of all samples with MK/CH of 0.33 with incorporated sulfates and 0K.

Figure 49 displays the isothermal calorimetry results for samples with MK/CH of 1.0 without incorporated sulfates. Once again, the increase in alkali hydroxides accelerates the reactions. The first reaction peak is comparatively lower and less visibly pronounced than in samples with MK/CH of 0.33. The presence of sodium hydroxide (NaOH) leads to an even more pronounced acceleration than potassium hydroxide (KOH). Notably, the two samples with the highest alkali hydroxides content (1MK_1.28KOH and 1MK_1.28NaOH) exhibit a distinctive behavior. While they initially experience an accelerated peak evolution, there is a sharp subsequent decrease in the heat flow curve, resulting in a significantly lower total heat release from day one onwards. These samples, having the highest OH^-/CH weight ratios (Table 13), may impede CH dissolution and intensify MK dissolution, favoring the formation of alkaline aluminosilicates [197] over pozzolanic reaction products. Parashar and Bishnoi suggested a higher polymerization of C-A-S-H gels with increasing alkali content, potentially resulting in a passivation layer inhibiting further reaction processes [49].

In contrast, the incorporation of a low amount of alkali hydroxides (1MK_0.32KOH and 1MK_0.32NaOH) leads to an accelerated and even higher overall heat release after 7 days (Figure 49 (B)). However, the addition of sulfates results in an acceleration followed by a sharp decrease in the heat flow (Figure 50 (A)) and a lower total heat release (Figure 50 (B)). The sulfate reactions (AFt formation and transformation to Ms) consume significant amounts of calcium in the initial hours of the reaction, which is subsequently unavailable for later pozzolanic reactions in the samples with MK/CH of 1.0 due to limited availability of CH. Additionally, sulfate reaction products, mainly AFm phases, attach

on the surface of CH particles and hinder the further (and total) CH dissolution, as visible in the TGA results (Figure 58 (B)).

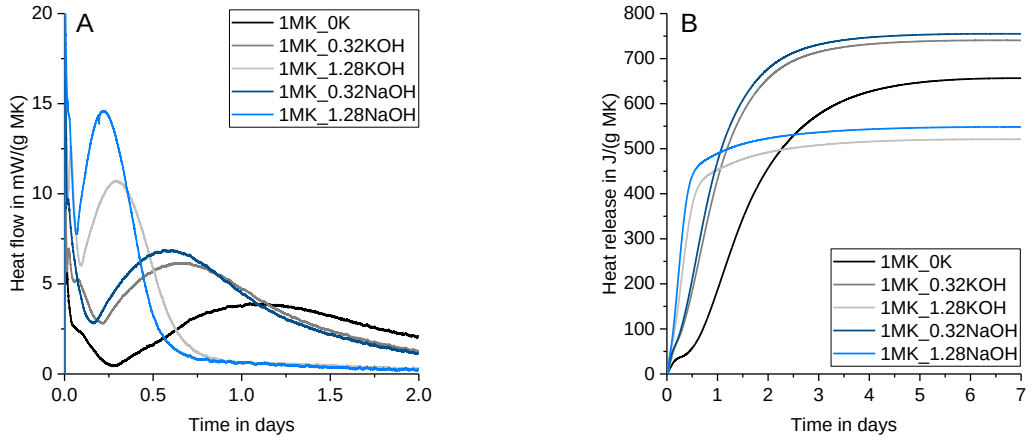

Figure 49: Heat flow curves (A) and heat release (B) from isothermal calorimetry measurements at 40 °C of all samples with MK/CH of 1.0 without added sulfates (Fig. S4-4 in the Supplementary Material shows the same results up to 7 days of reaction).

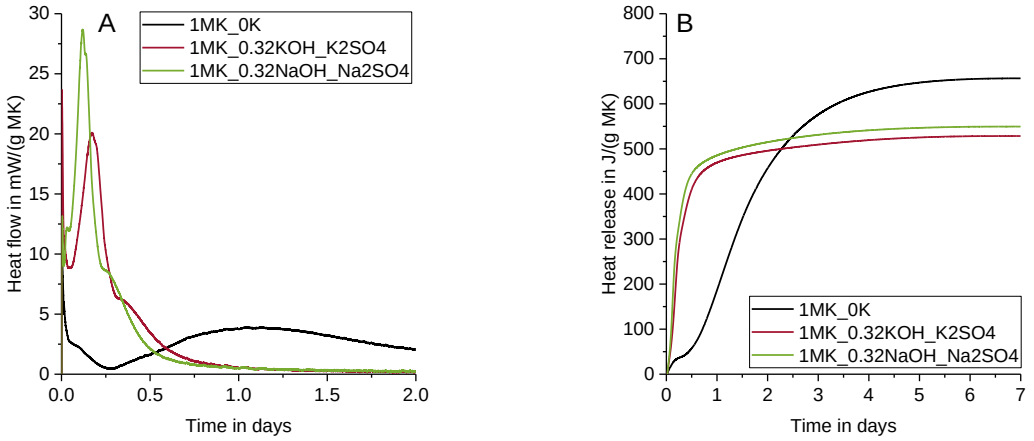

Figure 50: Heat flow curves (A) and heat release (B) from isothermal calorimetry measurements at 40 °C of all samples with MK/CH of 1.0 with incorporated sulfates and 0K.

In order to delve deeper into the impact of alkali hydroxide and sulfate additions on MK reactions, pore solutions from the samples were extracted following the procedure outlined in section 5.2.2. Subsequently, the pH values were measured, and the concentrations of soluble elements Ca, Al, Si, K, Na and S were determined. Table 15 provides a summary of the pH values from all samples with MK/CH of 0.33. The values are presented as mean values from five measurement times (30 min, 3 h, 5 h, 24 h and 48 h). Higher pH values were observed with an increase in alkali hydroxide (NaOH and KOH) content in the samples. Notably, samples containing potassium hydroxide (KOH) exhibited even higher pH values compared to those with sodium hydroxide (NaOH), despite having the same added OH^- content. This observation can be explained by potassium hydroxide being a stronger base due to the larger size of potassium (K^+) compared to sodium ions (Na^+), facilitating easier dissociation of OH^- ions. The addition of sulfates (0.32KOH_K2SO4 and 0.32NaOH_Na2SO4) resulted in increased pH values compared to the same samples without sulfates (0.32KOH and 0.32NaOH). This aligns with findings in the literature, which report a more pronounced CH dissolution with sulfates [107].

Table 15: pH values for the samples with MK/CH of 0.33.

Sample	pH*	Standard deviation
0.33MK_0K	12.90	0.03
0.33MK_0.32KOH	13.36	0.06
0.33MK_1.28KOH	13.90	0.06
0.33MK_0.32KOH_K2SO4	13.66	0.17
0.33MK_0.32NaOH	13.24	0.03
0.33MK_1.28NaOH	13.65	0.07
0.33MK_0.32NaOH_Na2SO4	13.40**	0.03

* Calculated as mean value from five measuring times (30min, 3h, 5h, 24h and 48h).

** Calculated as mean value from three measuring times (30min, 3h and 5h) as not enough solution was available for later ages.

Figure 51 to Figure 53 present the results obtained from inductively coupled plasma optical emission spectrometry (ICP-OES) measurements. The concentrations of Ca^{2+}, Si^{4+} and Al^{3+} are expressed in mg/L of pore solution, while the results for SO_4^{2-}, Na^+ and K^+ are presented as wt.-% based on the amounts of the respective elements in the individual sample compositions.

Figure 51 (A) clearly shows an impeded calcium hydroxide dissolution in samples with incorporated alkali hydroxides. This observation is attributed to the higher pH values (see Table 15), inducing the common ion effect that hinders CH dissolution [53, 59, 147, 183]. In sample 0K, without incorporated alkali hydroxides, the calcium concentration in the solution is approx. 800 mg/L after 30 minutes (the reaction time was initiated after mixing MK with alkaline suspension), decreasing to around 700 mg/L after two days of reaction. The reduction of calcium ions in the solution indicates pozzolanic reactivity in the sample. Samples with a small amount of added alkali hydroxides (0.32KOH and 0.32NaOH) exhibit a significantly reduced concentration of Ca^{2+}, with values of around 200 mg/L, further decreasing to approx. 50 mg/L in samples with higher amounts of alkali hydroxides (1.28KOH and 1.28NaOH). In samples with incorporated sulfates, the initial calcium concentration (after 30 minutes) is 317 mg/L (0.32NaOH_Na2SO4) and 383 mg/L (0.32KOH_K2SO4) and significantly decreases within the first day of reaction. The sharp decrease in calcium concentration in these samples indicates a rapid reaction to calcium-rich phases, i.e. ettringite formation.

Figure 51 (B) illustrates the concentrations of sulfate ions in the pore solutions for the two samples that contain K_2SO_4 and Na_2SO_4. The results were calculated in wt.-% based on the total amount of sulfates in the respective sample. After 30 minutes of reaction (directly starting after mixing procedure), 71 wt.-% (0.32KOH_K2SO4) and 75 wt.-% (0.32NaOH_Na2SO4) of the overall sulfate content in the sample was detected in the pore solution. This value is not 100 wt.-% as sulfate has already reacted within the first minutes and/or it may adsorb on precursor material, e.g. adsorption [107, 173, 175] on Ca^{2+} layer [107, 159, 170, 172–175] build on negatively charged [107, 159, 170–172] calcined clay particles [107, 173, 175], as well as on reaction products [140, 176–178]. The sulfate concentration in the pore solution decreases within the first day to values close to zero after 24 hours. The results indicate a complete consumption of the incorporated sulfates within the first day of reaction at 20 °C (no sulfate ions detected in the pore solution after 24 h). This finding agrees with in-situ XRD measurements (discussed below), showing a rapid formation of ettringite within the first 10 h, leading to the conclusion that the sulfate is consumed even earlier than 24 h (no linear behavior from 5 h to 24 h in Figure 51).

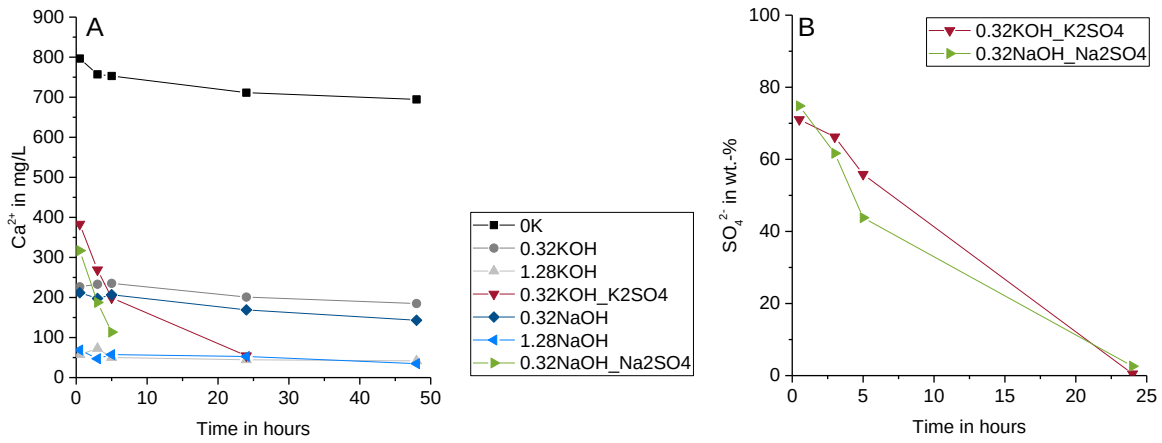

Figure 51: A: Calcium (Ca^{2+}) concentration in the pore solution in mg/L; B: Sulfate (SO_4^{2-}) concentration in the pore solution in wt.-% (100 wt.-% refers to the total amount of sulfate in the sample).

The aluminum (Al^{3+}) and silicon (Si^{4+}) concentrations in the solutions are outlined in Figure 52. Samples with the highest amounts of added alkali hydroxides (1.28KOH and 1.28NaOH) exhibit the highest concentrations, indicating the most intense MK dissolution. From 3 up to 40 hours, an increase in Al^{3+} and Si^{4+} concentration is observable. The inclusion of sulfates (0.33MK_0.32KOH_K2SO4 compared to 0.33MK_0.32KOH) leads to higher Al^{3+} and Si^{4+} concentrations in the solution, especially after 24 hours. Enhanced MK dissolution in the presence of sulfates has been reported in the literature [62] resulting in an acceleration of early pozzolanic reactions [62]. In their experiments, SO_4^{2-}/MK weight ratios of 0.047 and 0.065, comparable to the samples in this study (0.065), were applied, but SO_4^{2-}/CH was significantly higher with 0.177 and 0.244 (compared to 0.022 and 0.065) due to the fixed higher MK/CH of 3.75 [62]. Unfortunately, some data points for the sulfate containing samples are missing in Figure 51 (A), Figure 52 and Figure 53 as the amount of pore solution extracted, especially at later ages, was insufficient for analysis due to enhanced hardening performance in these samples.

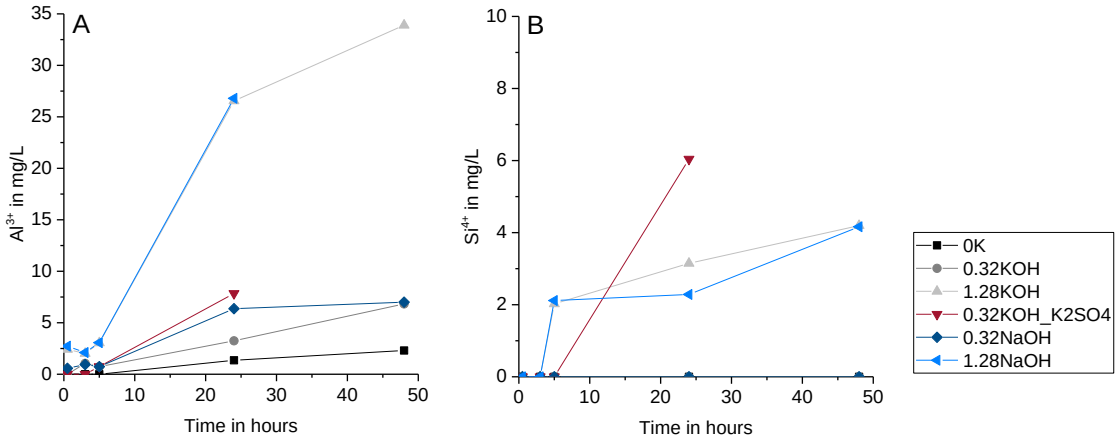

Figure 52: A: Aluminum (Al^{3+}) concentration in the pore solution in mg/L; B: Silicon (Si^{4+}) concentration in the pore solution in mg/L.

The concentrations of potassium (K^+) and sodium (Na^+) are shown in Figure 53 as weight percent (wt.-%) relative to the total amount of alkalis in the individual samples. In samples with added KOH and/or K_2SO_4, between 79 wt.-% and 94 wt.-% of the initial potassium was detected. Conversely, in the other samples, small amounts of potassium were observed, associated with MK dissolution. In these samples, approx. 25 wt.-% of potassium was observed, with 100 wt.-% of K^+ being related to the small amount of K_2O in MK according to Table 17. The results indicate a limited release of K^+ from MK, whereas the added KOH and K_2SO_4 dissolved to a greater extend. A similar trend is evident in the samples with added sodium in Figure 53 (B). Samples with incorporated NaOH and/or Na_2SO_4 exhibit a release of 72 wt.-% to 89 wt.-% of the initial amount of Na^+ in the sample. These values are slightly lower

compared to the K^+ concentrations in Figure 53 (A), supporting the easier dissolution of potassium hydroxide due to the larger size of potassium (K^+) compared to sodium ions (Na^+). The Na^+ concentrations in samples without added NaOH and/or Na_2SO_4 originate from the small amount of Na_2O in MK according to Table 17.

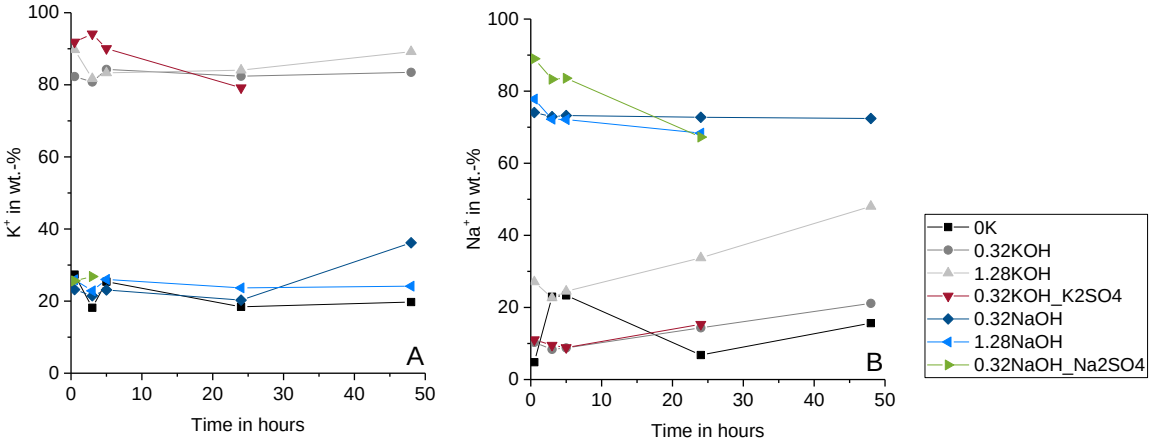

Figure 53: Potassium (K^+) (A) and sodium (Na^+) concentration in the pore solution in wt.-% (100 wt.-% refers to the total amount of potassium (A) or sodium (B) in the sample).

To track the formation of crystalline phases, in-situ XRD analyses were performed on selected sample compositions (see Table 14). Supplementary Material Figure S4-5 and Figure S4-6 present the results for sample 0.33MK_0.32KOH without added sulfates within the 10.1–12.0 2θ and 6.2–7.7 2θ ranges, respectively, over the reaction time. In the 10.1–12.0 2θ range (Figure S4-5 in the Supplementary Material), the earliest peaks emerge, with one peak at approx. 10.6 2θ starting to develop between 5 and 25 hours of reaction at ~ 20 °C. Another small peak appears even earlier, from 3 to 9 hours after sample preparation, at approx. 11.6 2θ. In this range, AFm phases with various specific compositions are reported in the literature [49, 144, 231, 284, 286–289]. Here, this peak might be assigned to C_4AH_{13} (AFm phase with OH^- as anion). From approx. 37 h after mixing, a characteristic peak at ~ 7.0 2θ starts to build up, as shown in Figure S4-6 in the Supplementary Material, and is assigned to stratlingite (C_2ASH_8) [49, 231, 285, 290]. The in-situ XRD results for sample 1MK_0.32KOH indicate that all three mentioned peaks occur slightly earlier for the higher MK/CH of 1.0 compared to 0.33 (Supplementary Material Figure S4-7 and Figure S4-8).

To correlate the information obtained from in-situ XRD with isothermal calorimetry peaks, selected samples (0.33MK_0.32KOH and 0.33MK_0.32KOH_K2SO4) were isothermally measured at 20 °C. The results presented in [291] (Figure S4-9 in the Supplementary Material) illustrate two reaction peaks for sample 0.33MK_0.32KOH, which can be linked to the formation of C_4AH_{13} (peak 1) and C_2ASH_8 (peak 2).

Figure 54 and Figure S4-10 in the Supplementary Material present the in-situ XRD measurements for sample 0.33MK_0.32KOH_K2SO4 (composition based on the R^3-test [87]). The initial peak emerges from 2 h onwards at approx. 9 2θ (Figure 54), associated with the formation of ettringite [292–294]. On closer examination, this peak exhibits a shift to slightly higher 2θ values (~ 9.1 2θ) from 10 h, which can be linked to monosulfoaluminate (Ms) phases with high water contents [286]. Between 8 h and 18 h, one distinctive peak at approx. 10.6 2θ appears (Figure 54), analogous to the formation of C_4AH_{13} in the sample without added sulfates (Figure S4-5 in the Supplementary Material). In 0.33MK_0.32KOH_K2SO4 this peak occurs slightly later (from 8 h) compared to sample 0.33MK_0.32KOH (from 5 h). In the sample with incorporated K_2SO_4, an additional peak at approx. 10.2 2θ builds up as a left-sided shoulder of the C_4AH_{13} peak after 16 h to 18 h of reaction, related to the formation of Ms [286]. Figure S4-10 in the Supplementary Material demonstrates the formation of C_2ASH_8 starting after ~ 38 hours, approximately at the same reaction time compared to the sample

without incorporated sulfates in Figure S4-6 in the Supplementary Material (0.33MK_0.32KOH). From 24 h onwards, the peak at ~ 9.1 2θ disappears, indicating a reduction in the amount of water-rich monosulfoaluminate (Ms). The release of water from monosulfoaluminate with time was observed in literature in calcium sulfoaluminate cements [295].

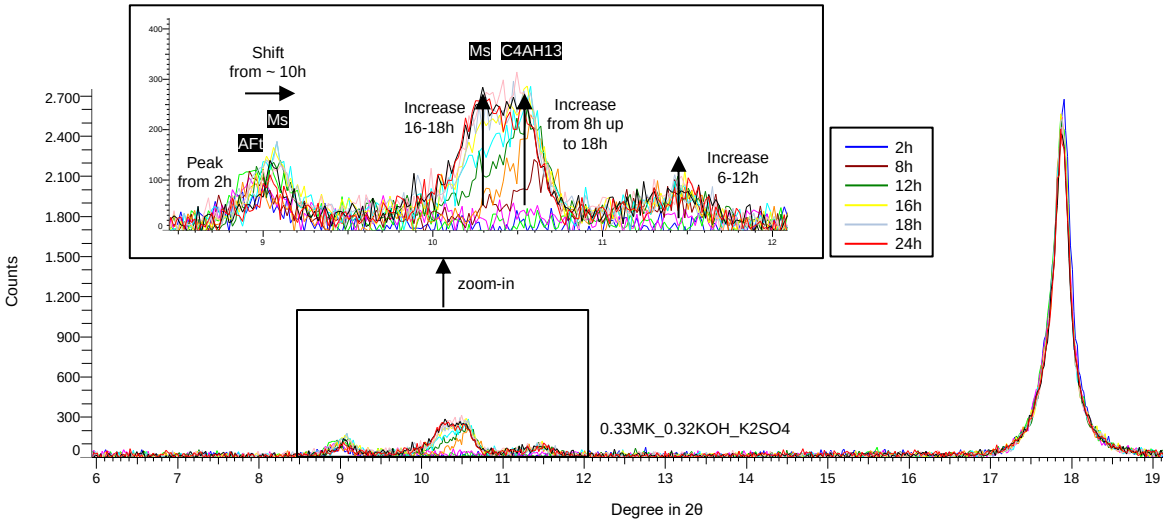

Figure 54: In-situ XRD results shown for 0.33MK_0.32KOH_K2SO4 from 2h up to 24h (data shown for every two hours).

Linking the phases detected in 0.33MK_0.32KOH_K2SO4 with in-situ XRD measurements to the heat flow curves is not as straightforward as in the samples without sulfates (Figure S4-9 in the Supplementary Material). Figure 55 shows the heat flow curves of the sample with K_2SO_4 measured at 20 °C and 40 °C (Figure S4-11 in the Supplementary Material shows the data up to 7 days). Several exothermic overlapping peaks are detected, possibly in the following order: a) formation of ettringite (AFt), b) C_4AH_{13} and c) C_2ASH_8 according to the in-situ XRD results. The large and broad peak with its maximum at approx. 12 h in the 40 °C measurement (peak c) could be related to the formation of C-A-S-H gels (together with C_2ASH_8). The transformation of ettringite (AFt) to monosulfoaluminate (Ms) is endothermic [75] and might be visible in the heat flow curve measured at 20 °C as indicated in Figure 55. According to [59], the transformation process is reported to occur after the formation of C_4AH_{13}.

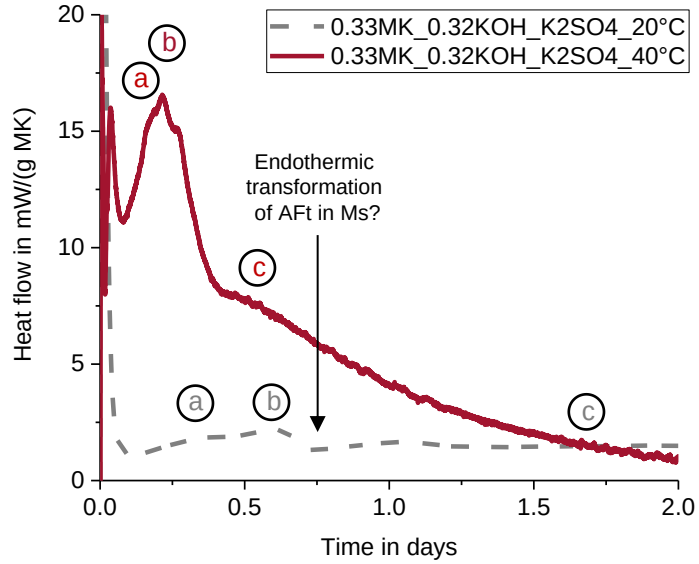

Figure 55: Isothermal calorimetry results shown for 0.33MK_0.32KOH_K2SO4 at 20 °C and 40 °C up to 2 days; peak a related to ettringite (AFt), peak b to C_4AH_{13} and peak c to C_2ASH_8 formation.

Figure 56, along with Figure S4-12 and Figure S4-13 in the Supplementary Material, presents the in-situ XRD results for sample 1MK_0.32KOH_K2SO4. This sample has an overall higher amount of aluminates compared to 0.33MK_0.32KOH_K2SO4 due to the higher MK/CH weight ratio, and consequently, the sulfate reactions (AFt and transformation to Ms) are more intense (Figure 56). Figure 56 shows the formation of ettringite (AFt) at approx. 9.0 2θ mainly in the first two hours, with constant peaks in this range up to 5 h. After 6–7 h of reaction, this peak starts to shift slightly to the higher value of 9.1 2θ, indicating transformation reactions to water-rich monosulfoaluminate (Ms). This peak further increases up to 8 h (Figure 56), followed by a decrease from 12 h onwards (Figure S4-12 in the Supplementary Material). Two additional peaks related to the formation of Ms [286] appear from 6 h, increasing up to 11 h at 9.9 and 10.3 2θ (Figure 56). From 4 h to 11 h another peak at 10.6 2θ, related to the formation of C_4AH_{13}, increases (Figure 56), followed by a slight decrease from 16 h onwards (Figure S4-12 in the Supplementary Material). The formation of C_2ASH_8 starts from approx. 17 h onwards (Figure S4-12 in the Supplementary Material) up to the end of the testing time after 50 h (Figure S4-13 in the Supplementary Material). This peak is significantly more intense compared to sample 0.33MK_0.32KOH_K2SO4 (Fig. S12 in the Supplementary Material) due to the higher MK/CH weight ratio [53, 54, 56, 65, 68, 69, 206].

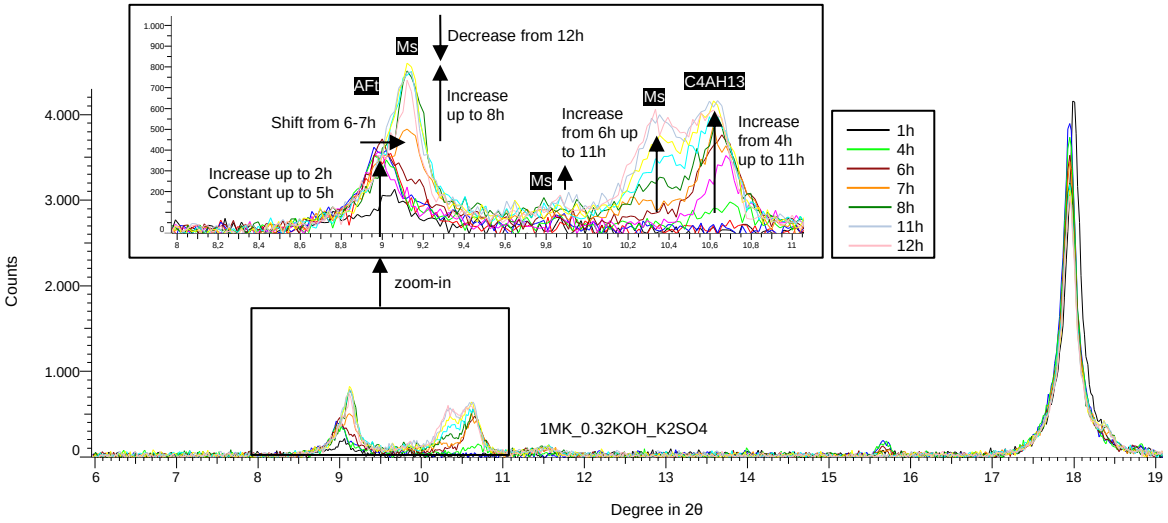

Figure 56: In-situ XRD results shown for 1MK_0.32KOH_K2SO4 from 1h up to 12h (data shown for every hour).

5.3.2 Long-Term Results and Discussion

The long-term phase of this study spans from 2 up to 245 days of reaction at 40 °C. This section presents and discusses the outcomes from thermogravimetric analysis (TGA), quantitative X-ray diffraction (qXRD) and scanning electron microscopy coupled with energy-dispersive X-ray spectroscopy (SEM/EDX).

Thermogravimetric analysis (TGA) was used to determine the chemically bound water (CBW) in reaction products (mass loss between 40 °C and 600 °C subtracted by the mass loss related to CH depletion) and the consumption of CH in the samples at specific testing times (2, 7, 56 and 245 days) [84]. Figure S4-14 in the Supplementary Material exemplarily shows the DTG-curve of sample 0.33MK_0K, with TG- and DTG-curves for all samples available in Figure S4-15 to Figure S4-42 in the Supplementary Material. Figure 57 depicts the evolution of the CBW and CH consumption over time, up to 245 days at 40 °C for samples with MK/CH of 0.33. In all samples, the CBW increases up to seven days of reaction representing an uptake of bound water and/or OH^- groups in hydrate phases, followed by a substantial decrease up to 245 days (Figure 57 (A)), indicating transformation processes of metastable C_4AH_{13} and C_2ASH_8 to more stable hydrogarnet phases (C_3AH_6). These transformations are in agreement with qXRD results for the MK/CH ratio of 0.33 discussed below and align with indications in literature in the MK/CH weight ratio range of 0.3–0.6 [65, 68, 70, 79]. The novelty of this paper lies in the systematically, time depending and quantitatively investigation of these transformation processes. The formation of

hydrogarnet phases in the long-term are additionally visible by an increasing peak in the temperature range of 250 °C to 400 °C [214, 296], as indicated in Figure S4-14 in the Supplementary Material. After 2 and 7 days of reaction, sulfate-containing samples exhibit higher CBW due to sulfate reactions (AFt formation and transformation to Ms). As these reactions consume a substantial amount of calcium, CH consumption is also higher in sulfate-containing samples, as shown in Figure 57 (B). Generally, CH consumption notably increases up to 56 days, followed by only slight increases for further reaction times up to 245 days, except for the two samples 0.33MK_0.32KOH and 0.33MK_1.28KOH. These two samples might be outliers, possibly due to inaccurate sample preparation and/or measurement after 245 days.

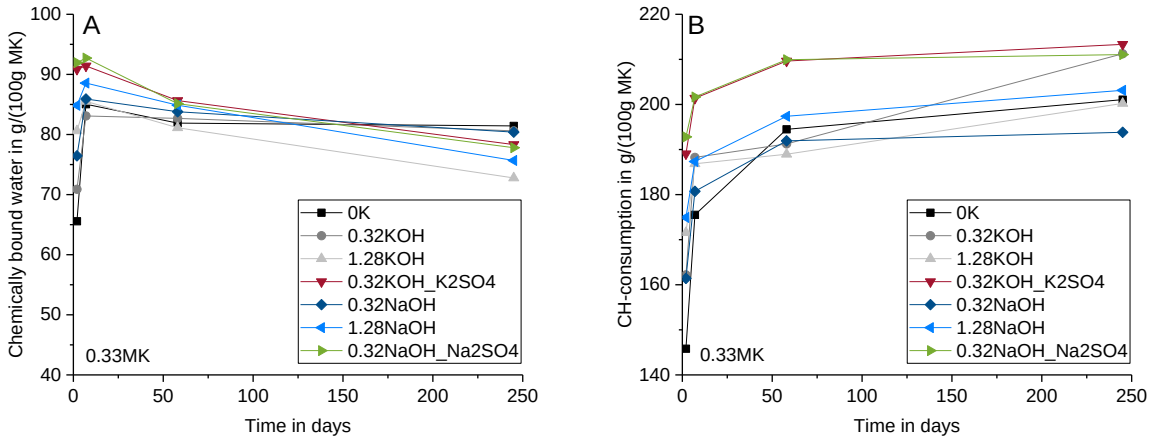

Figure 57: Chemically bound water in reaction products (A) and CH consumption (B) in samples with MK/CH of 0.33 (TGA).

Figure 58 shows the CBW in reaction products and the CH consumption over 245 days at 40 °C for the samples with MK/CH of 1.0. In contrast to samples with an MK/CH of 0.33, these samples exhibit a lack of CBW decreases over time, indicating no significant transformation reactions to hydrogarnet phases due to the absence of CH. Lower CBW values were generally measured in the samples with MK/CH of 1.0 compared to the samples with MK/CH of 0.33. The samples 1MK_1.28KOH and 1MK_1.28NaOH again show a significantly different behavior, i.e. much lower CBW values compared to the other samples (Figure 58 (A)). As explained in section 5.3.1, this observation may be attributed to the formation of alkaline aluminosilicates [197] instead of MK pozzolanic reaction products (C_4AH_{13} and C_2ASH_8). Samples 1MK_0K, 1MK_0.32KOH and 1MK_0.32NaOH display accelerated CH consumption compared to the other samples with MK/CH of 1.0 (Figure 58 (B)). In the samples with an MK/CH of 1.0, the addition of sulfates decelerates MK pozzolanic reactions, aligning with lower overall heat releases in calorimetry results (Figure 50 (B)). After 245 days, complete CH consumption occurs in the samples, resulting in a CH consumption of 100 g per 100 g MK (MK/CH = 1.0). This value is notably lower than in samples with an MK/CH of 0.33, emphasizing the impact of CH shortages and the prevention of transformation reactions from metastable C_4AH_{13} and C_2ASH_8 to more stable hydrogarnet phases.

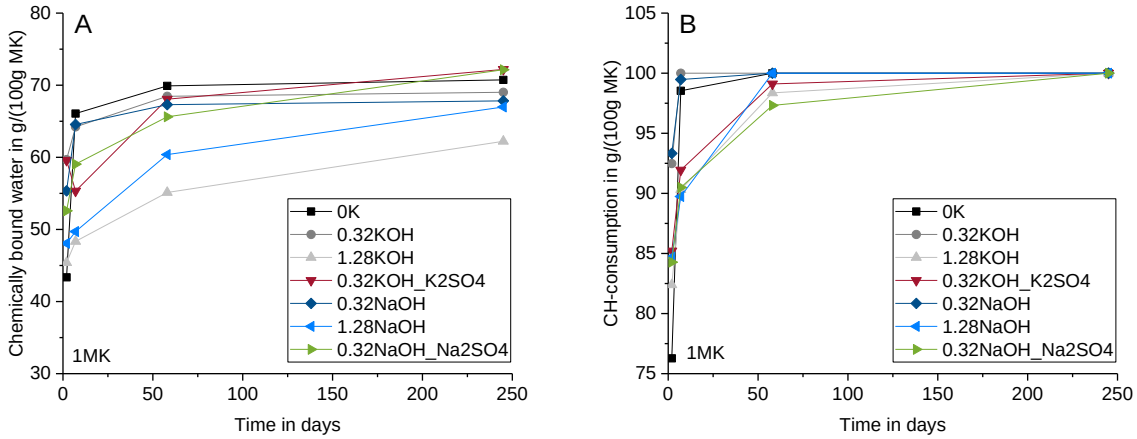

Figure 58: Chemically bound water in reaction products (A) and CH consumption (B) in samples with MK/CH of 1.0 (TGA).

Table 16 summarizes the quantitative X-ray diffraction (qXRD) results calculated for the samples with MK/CH of 0.33 without incorporated sulfates. They are normalized in gram per 100 g MK. The results indicate significant increases in hydrogarnet phases, particularly rich in Si represented by $C_3AS_{0.69}H_{4.62}$ in this study, with reaction time. Concurrently, TGA results reveal substantial decreases in chemically bound water over time, confirming that the formation of hydrogarnet phases can be attributed to transformation reactions. Although C_4AH_{13} slightly decreases or remains constant in some samples, its full identification in qXRD is challenging due to reflection peak overlap with other AFm phases, like carbonate containing AFm, resulting from CO_2 contamination during sample storage and hydration stoppage. The amount of C_2ASH_8 quantified from qXRD measurements is relatively low and does not change significantly with time. Moreover, C_2ASH_8 may have a partly amorphous structure and its reflection peak at approx. 30 2θ can overlap with C-A-S-H gels [297] (Figure S4-43 in the Supplementary Material). Consequently, values calculated for C_2ASH_8 lack conclusiveness. The amorphous content is predominantly associated with C-A-S-H gels, but considering the partly amorphous nature of stratlingite, the actual amount of C-A-S-H phases in the samples might be slightly lower than the values presented in Table 16, which do not change significantly with reaction time. Graphical qXRD results are provided in Figure S4-43 to Figure S4-47 in the Supplementary Material.

Figure S4-48 (MK/CH = 1.0) and Figure S4-49 in the Supplementary Material (MK/CH = 0.33) exemplarily demonstrate qualitatively the influence of sulfates on the XRD results in the long-term. The sulfate-containing results show additional peaks in the range of 9–11 2θ, related to sulfate containing phases, i.e. monosulfoaluminate (Ms). The peaks related to stratlingite around 7 and 14 2θ are lower in the samples with sulfates, but they are difficult to interpret quantitatively, as the samples differ in the amount of chemically bound water and consequently they do not have comparable sample masses. The samples with incorporated sulfates were not analyzed quantitatively (qXRD) due to difficulties in characterizing specific reaction products in that range.

Table 16: qXRD results for the samples with MK/CH of 0.33 (without sulfates) normalized per 100 g MK.

Sample	Time in days	CH*	C_4AH_{13}	C_2ASH_8	C_3AH_6	$C_3AS_{0.69}H_{4.62}$	Amorphous
0.33MK_0K	2	153.7	10.9	3.4	0.7	5.8	262.6
	7	121.6	11.3	2.4	0.7	15.3	295.3
	56	99.9	8.1	5.6	0.5	18.9	310.6
	245	96.5	8.6	4.8	0.7	30.9	299.6
0.33MK_0.32KOH	2	140.6	9.2	2.3	0.6	10.0	307.2
	7	116.1	9.3	2.3	0.6	10.2	312.7
	56	106.3	11.5	5.3	0.8	18.3	303.4
	245	82.5	9.5	5.3	0.8	35.1	307.2
0.33MK_1.28KOH	2	122.7	13.1	2.7	3.1	5.9	308.5
	7	113.3	13.8	2.3	4.4	7.2	310.5
	56	105.8	10.9	3.0	0.6	26.6	302.3
	245	100.6	7.2	0.0	6.7	32.5	294.0
0.33MK_0.32NaOH	2	140.5	11.0	2.5	0.6	2.4	287.6
	7	118.9	10.5	2.6	0.6	10.3	303.3
	56	106.3	10.8	3.4	0.8	17.5	307.7
	245	109.3	11.8	5.5	0.8	23.7	291.8
0.33MK_1.28NaOH	2	131.8	12.1	2.8	0.6	9.0	300.1
	7	117.1	10.3	3.0	0.6	12.2	308.9
	56	102.6	8.9	2.7	1.1	25.5	309.3
	245	95.9	6.3	0.0	6.5	31.5	299.3

* Determined by thermogravimetric analysis (TGA).

Figure 59 to Figure 63 show Si/Ca-Al/Ca diagrams (mass ratios) derived from scanning electron microscopy coupled with energy-dispersive X-ray spectroscopy (SEM/EDX) measurements. In this diagram, non-reacted samples would form an imaginary line with a slope of approx. 1.0 (indicated as grey dashed line in Figure 59 (A)), as CH alone does not contain silicon or aluminum, representing the zero point, and MK having a Si/Al weight ratio of ~ 1.0. Data points moving away from that imaginary line (Si/Al ~ 1.0) represent reaction products. Figure 59 shows the results for the two samples 0.33MK_0K and 0.33MK_1.28KOH after 7 and 245 days of reaction at 40 °C. The incorporation of KOH results in reaction products with higher Al/Ca ratios, noticeable as a shift of the measured points to the right side in the diagram. This shift may be attributed to elevated pH values from the presence of KOH, leading to more intense MK dissolution [31, 76, 180–184] and impeded CH dissolution [53, 59, 147, 183]. The triangle on the left side of the imaginary line with a slope of ~ 1.0 are assigned to C-A-S-H phases [247, 298] as Si/Al >> 1.0 (indicated in Figure 59 (B)), whereas data points moving to the right side in the diagram especially visible in Figure 59 (B) are related to hydrogarnet phases ($C_3AS_{0.69}H_{4.62}$ is exemplarily indicated in the diagram). This finding supports the theory of transformation reactions from metastable to more stable hydrogarnet phases in the samples with excess supply of CH (MK/CH = 0.33).

Figure 60 visualizes the results for the samples 1MK_0K and 1MK_1.28KOH after 7 and 245 days. Sample 1MK_1.28KOH significantly shows more data points in the upper right corner of the diagram, indicating non-reacted MK, especially after 7 days of reaction (Figure 60 (A)), when compared to 1MK_0K. The considerably higher OH^-/CH in that sample (Table 18) enhances MK and impedes CH dissolution, resulting in a diminishing pozzolanic reaction together with the possible formation of additional alkaline aluminosilicates [197]. The phases rich in Si and Al might also be zeolites, that were identified for long curing times and high temperatures in MK-CH systems [210].

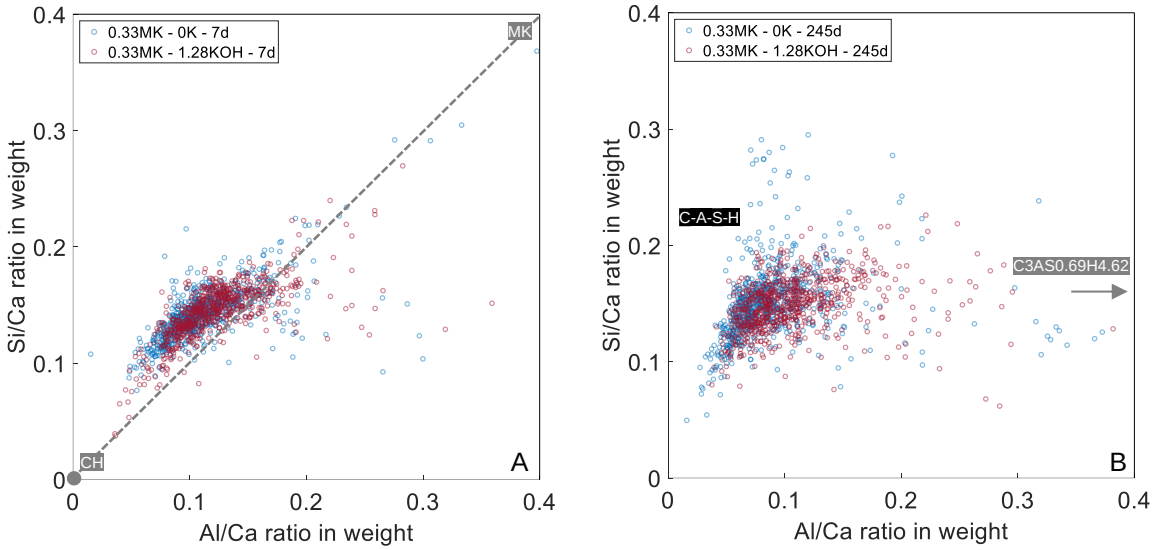

Figure 59: SEM/EDX results for 0.33MK_0K and 0.33MK_1.28KOH at 7 days (A) and 245 days (B) of reaction.

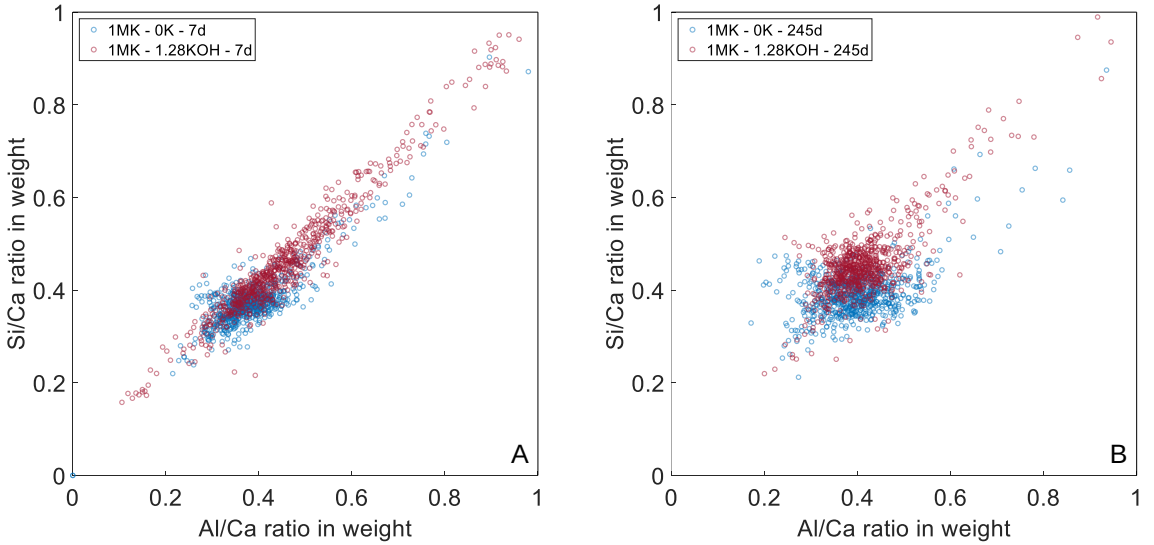

Figure 60: SEM/EDX results for 1MK_0K and 1MK_1.28KOH at 7 days (A) and 245 days (B) of reaction.

Examining the samples incorporating sulfates, Figure 61 (A) displays the outcomes for MK/CH of 0.33, while Figure 61 (B) for 1.0 after both 7 and 245 days. Notably, the data points after 245 days are more condensed compared to those after 7 days, indicating ongoing reactions from 7 days onwards, particularly evident in sample 1MK_0.32KOH_K2SO4 (Figure 61 (B)). Figure S4-50 in the Supplementary Material provides a comparative analysis of the measured data in samples with KOH after 245 days with MK/CH of 0.33 and 1.0. The left-sided triangle, denoted as C-A-S-H gels, distinctly illustrates higher Al/Ca and Si/Ca weight ratios for the higher MK/CH ratio of 1.0 compared to 0.33. This observation is ascribed to the overall increased silicon and aluminum levels and reduced calcium content in systems with higher MK/CH, aligning with literature in the MK/CH range of 0.5–7.6 [69]. Uptake of Al into C-S-H gel condenses bridging sites, enhances interlaminar chain cross-links, causing dimers to merge into pentamers and increasing aluminosilicate mean chain lengths at low Ca/(Si + Al) ratios [299].

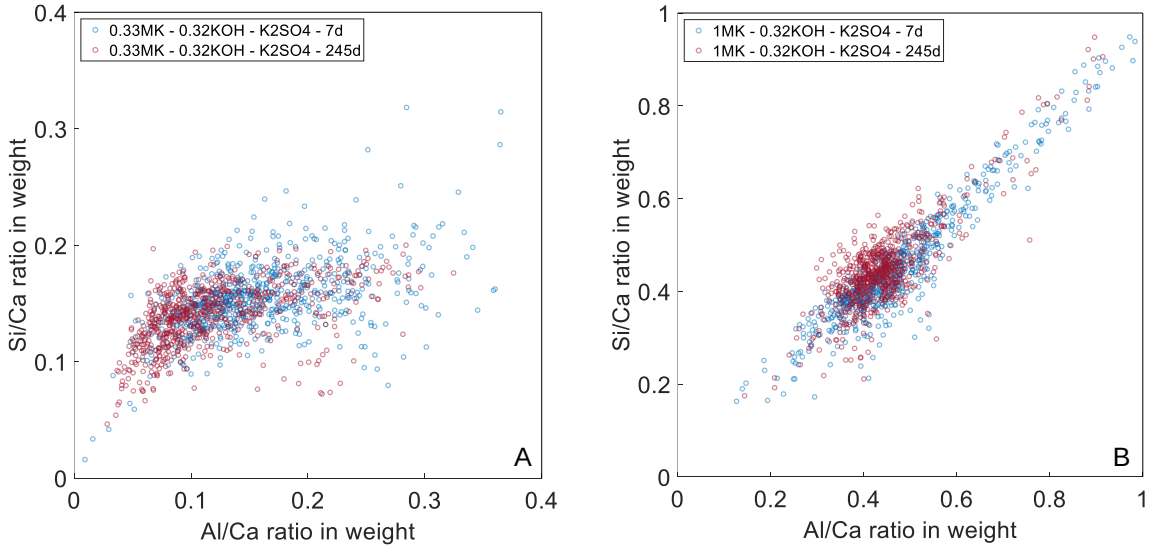

Figure 61: SEM/EDX results for 0.33MK_0.32KOH_K2SO4 (A) and 1MK_0.32KOH_K2SO4 (B) after 7 and 245 days of reaction.

The Si/Ca-Al/Ca diagrams, depicting mass ratios, offer a graphical means to highlight the distribution of specific elements within reaction products. In Figure 62, green circles pinpoint the presence of sulfate (S) in reaction products (S ≥ 0.5 wt.-% and 1.1 wt.-%). Similarly, Figure 63 emphasizes potassium (K) enrichment in formed phases, represented by red circles (K ≥ 1.8 wt.-% and 3.6 wt.-%). These threshold values were calculated based on the initial amount (S and K) in grams per 100 g of solids (MK + CH) in the initial mix design. As demonstrated in Figure 62, sulfates (≥ 0.5 wt.-%) are predominantly found in aluminum-rich reaction products, specifically in ettringite, hydrogarnet and/or monosulfoaluminate, indicated below an imaginary line with a slope of 1.0. Notably, data points with a high sulfate content concentrate in this area, indicating a sulfate enrichment in Si-rich hydrogarnet phases. Results from Okoronkwo and Glasser [300] confirm Si-free hydrogarnet instability with sulfate-bearing cement phases, yet suggest stability for various silica-substituted hydrogarnet solid solutions in conditions typical of blended cement systems. Moreover, sulfate (Fe, Mg) have been reported as incorporations in hydrogarnet formed in cement-based hydroceramic materials [301], as well as in Portland cements moist-cured at 85 °C [215], akin to their presence in natural garnet [216]. Conversely, potassium (K) tends to localize in silicon-rich products, primarily C-A-S-H phases positioned on the upper left side of Figure 63 (A and B). These findings align with reported alkali uptake of C-A-S-H phases in the literature [302–304], proving the validity of the applied methodology of element detection in reaction products by SEM/EDX measurements. The data presented in main part of this article corresponds to a reaction time of 245 days, with results after 7 days available in Figure S4-51 to Figure S4-54 in the Supplementary Material.

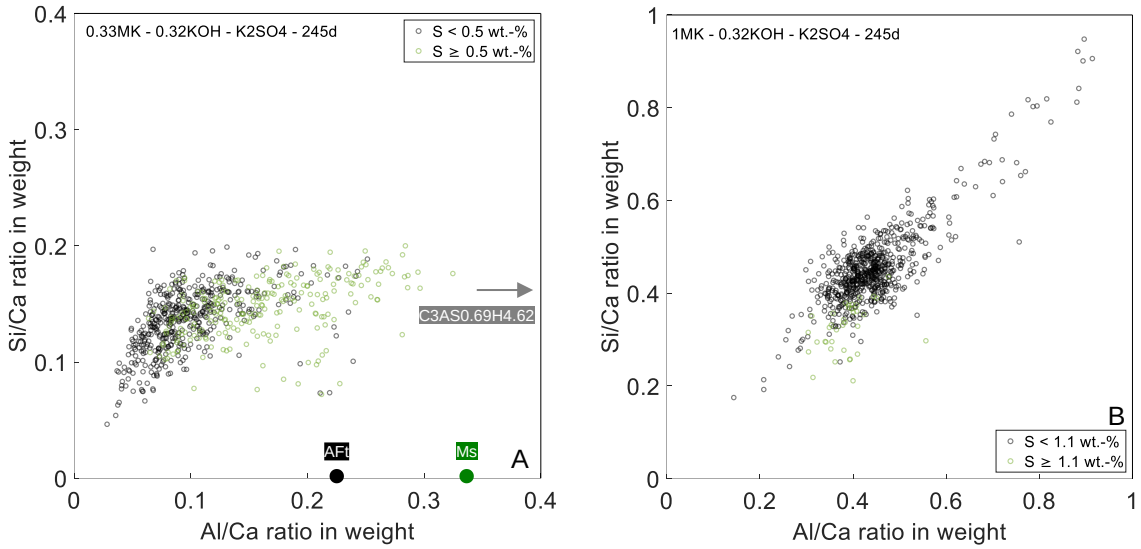

Figure 62: A: SEM/EDX results for 0.33MK_0.32KOH_K2SO4 after 245 days of reaction, green circles represent data points with S ≥ 0.5 wt.-%; B: SEM/EDX results for 1MK_0.32KOH_K2SO4 after 245 days of reaction, green circles represent data points with S ≥ 1.1 wt.-%.

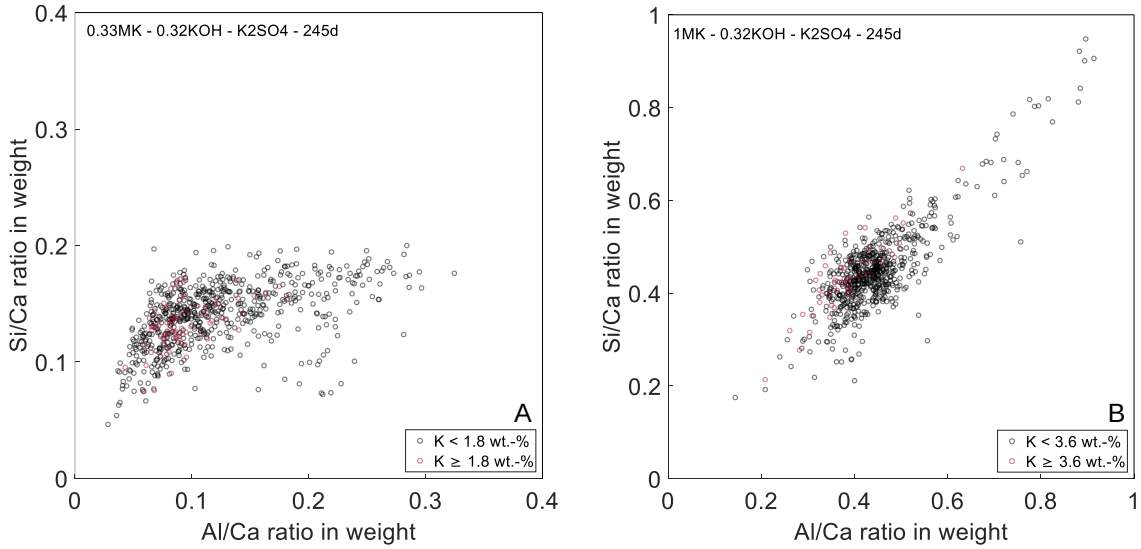

Figure 63: A: SEM/EDX results for 0.33MK_0.32KOH_K2SO4 after 245 days of reaction, red circles represent data points with K ≥ 1.8 wt.-%; B: SEM/EDX results for 1MK_0.32KOH_K2SO4 after 245 days of reaction, red circles represent data points with K ≥ 3.6 wt.-%.

5.4 Conclusions

This study systematically investigates the impact of calcium hydroxide (CH) availability, alkali hydroxides (KOH and NaOH), and sulfates (K_2SO_4 and Na_2SO_4) on both short and long-term pozzolanic MK reactions, using an extensive set of microanalysis techniques. The key findings are summarized as follows:

1. The inclusion of alkali hydroxides results in higher pH values, enhancing MK dissolution and impeding CH dissolution due to the common ion effect.
2. The pH values of the pore solution are higher with KOH than NaOH at fixed OH^-/MK weight ratios, attributed to the stronger base properties (easier dissolution due to larger potassium ions).
3. MK pozzolanic reactions exhibit acceleration with alkali hydroxides incorporation, particularly pronounced with NaOH compared to KOH.
4. Samples with the highest OH^-/CH weight ratio of 0.0307 (1MK_1.28KOH and 1MK_1.28NaOH) display distinct behavior, potentially related to the formation of alkaline aluminosilicates and hindered MK pozzolanic reactions.

5. Sulfates incorporation leads to rapid ettringite (AFt) formation, transforming into monosulfoaluminate, accelerating reaction processes with increased total heat release in MK/CH 0.33 samples. Conversely, sulfates decelerated pozzolanic MK reactions in higher MK/CH ratio (1.0) samples.
6. Excessive CH in MK/CH 0.33 samples prompts transformation reactions of metastable C_4AH_{13} and C_2ASH_8 into more stable (Si-rich) hydrogarnet phases, evident through reduced chemically bound water and quantitative XRD measurements.
7. SEM/EDX mapping reveals potassium (K) primarily in C-A-S-H phases and sulfates (S) in aluminum-rich products. Higher Si/Ca and Al/Ca ratios in C-A-S-H phases correlate with higher MK/CH ratios, while the addition of potassium hydroxide results in higher Al/Ca ratios in C-A-S-H phases.

This study provides fundamental knowledge into factors influencing pozzolanic MK reactions, which may serve the development of reaction models essential for designing novel MK-based binders in the future.

6 Publication 5: Stoichiometric and Kinetic Modeling

Publication 5 (Materials & Design, https://doi.org/10.1016/j.matdes.2024.112747):

Pozzolanic Metakaolin Reactions: Stoichiometric and Kinetic Modeling

Kira Weise[1,*], Neven Ukrainczyk[1,*], Eduardus Koenders[1]

[1] Technical University of Darmstadt, Institute of Construction and Building Materials, Germany.
* Corresponding authors: weise@wib.tu-darmstadt.de, ukrainczyk@wib.tu-darmstadt.de.

Abstract: In the pursue of environmentally-friendly binders for the construction industry, metakaolin (MK) has emerged as promising material, with its hardening performance primarily driven by pozzolanic reactions. However, in systems containing MK and calcium hydroxide (CH), transformation reactions from metastable to stable phases, particularly in excessive CH conditions, can adversely affect material properties. To anticipate these processes, this study introduces a stoichiometry-based reaction modeling approach for pozzolanic MK reactions, encompassing both short-term kinetics and long-term transformation processes. The primary pozzolanic reactions of MK are briefly outlined, highlighting two sequential, partially overlapping reactions forming C_4AH_{13} and C_2ASH_8. Short-term reaction kinetics are modeled using isothermal calorimetry measurements and deconvoluting the two reaction peaks. The model is in good agreement with experimental quantitative X-ray diffraction (qXRD), thermogravimetric analysis (TGA) and helium pycnometer (density, i.e. solid volume) results. Model limitations are discussed based on qualitative scanning electron microscopy with energy-dispersive X-ray spectroscopy (SEM/EDX) analysis. Leveraging the proposed model, the temperature dependency of pozzolanic MK reactions is analyzed, revealing an activation energy for the primary reaction of 84 kJ/mol. The model is intended to lay a foundation for designing innovative binder systems based on metakaolin, while paving the way for sustainable construction in the future.

Keywords: Metakaolin; reaction kinetics; stoichiometric model; phase assemblage; transformations; activation energy.

6.1 Introduction

The construction industry is facing major challenges related to global warming and raw material shortages. In this context, metakaolin (MK) has emerged as a very promising supplementary cementitious material for attaining low carbon binders [88, 89, 93, 305]. Its hardening performance, spanning from lime [121–123, 126, 127] to cement-based materials [96, 97, 99, 306], is primarily controlled by the pozzolanic reactivity between MK and calcium hydroxide (CH) [81, 104] and leads to the formation of various calcium aluminum silicate hydrates [45, 79, 110, 120]. The reaction kinetics, hydrate phase formations, and their long-term transformations from metastable to more stable phase configurations are affected by various conditions, including the initial metakaolin to calcium hydroxide weight ratio (MK/CH) [65, 73–75], curing time [64], temperature [69] and secondary activators [49, 62], which are all imposed by the binder system employed for a given application.

In binder systems, long-term transformation reactions can adversely affect their durability properties, such as porosity, while leading to a degradation of the overall material performance. Apart from predominantly amorphous C-A-S-H phases [49, 54, 55, 60], stratlingite (C_2ASH_8) is formed as the primary reaction product in the pozzolanic MK reaction [49, 62, 65, 66]. In [79], it is discussed that this

phase is thermodynamically unstable in the presence of CH and undergoes a slow transformation to more stable hydrogarnet phases (C_3AH_6) under certain conditions [53, 69, 78, 209]. The formation and/or transformation of C_4AH_{13} are subject of controversial discussions [79]. In the present study focus is on pozzolanic metakaolin reactions and long-term transformation processes for knowledge development and design of innovative low-carbon binders.

Assessing the phase assembly resulting from cement hydration or variations in composition can be achieved through either thermodynamic modeling [233, 307] or mass balance calculations [247] while assuming a relative stability of the hydrate phases. However, due to the challenges posed by metastable phases, kinetic constraints, and the variable stoichiometry of C-A-S-H phases, a simplified mass balance approach is conducted in the present study. This approach is not only computationally less expensive but aligns also directly with experimentally determined reaction kinetics.

Particularly, well-established boundary compositions for C-A-S-H, such as $C_{1.75}SH_4$, $C_{1.75}A_{0.05}SH_4$, $C_{1.3}A_{0.1}SH_3$, $C_{0.67}A_{0.05}SH_2$, $C_{0.67}SH_2$ detailed in [247], cover a wide range of data identified for various systems, including Portland cements (Ca/Si = 1.7 - 2.0; Al/Si = 0.05 - 0.1) [200], blended cements (Ca/Si = 1 - 1.5, Al/Si = 0.03 - 0.2) [308–310], and alkali-activated slags (Ca/Si = 0.7 - 1.0; Al/Si = 0.1 - 0.3) [311, 312]. These have been recently consolidated into a structural-consistent CASH+ sublattice solid solution model in [313]. In formulating simplified stoichiometric equations for this study, fixed C-A-S-H compositions were assumed to provide a broader potential model usage without the need of chemical speciation solvers. It is essential to emphasize that these fixed C-A-S-H compositions should be reevaluated in light of evolving data from various systems, as demonstrated here by the case of MK-CH.

In the present paper, a simplified stoichiometric reaction model is described that predicts the phase assemblage of metakaolin-calcium hydroxide pastes. In the model two separated pozzolanic reactions are considered along with the transformation process of C_2ASH_8 to hydrogarnet and C-A-S-H phases, mainly driven by the subsequent availability of CH.

Identification of reaction products and equations is based on an extensive literature review [79], supplemented by new results from in-situ XRD measurements to enhance the understanding of short-term pozzolanic reaction products. The experimental approach introduced in this study intentionally involves precisely controlled MK-CH systems to unravel the fundamental phase transformations while minimizing the influence of additional factors present in more complex ones [49], such as e.g. in cementitious systems. Pastes composed of MK, CH and water were prepared with varying amounts of potassium hydroxide for the kinetic aspects. A sample with an MK/CH ratio of 0.33, without the addition of potassium hydroxide, served as a calibration point for the stoichiometric reaction parameters. Isothermal reaction calorimetry measurements for various paste compositions were used to calibrate the kinetics of the pozzolanic metakaolin reactions. Validation of the model for samples with compositions different than the calibration sample was carried out using results from thermogravimetric analysis (TGA) and quantitative X-ray diffraction (qXRD). The model was further validated by helium pycnometer tests for the total solid volume measurements, while scanning electron microscopy coupled with energy-dispersive X-ray spectroscopy (SEM/EDX) was employed to discuss model limitations in depth, mainly the fixed C-A-S-H compositions. The overall research design is outlined in Figure 64.

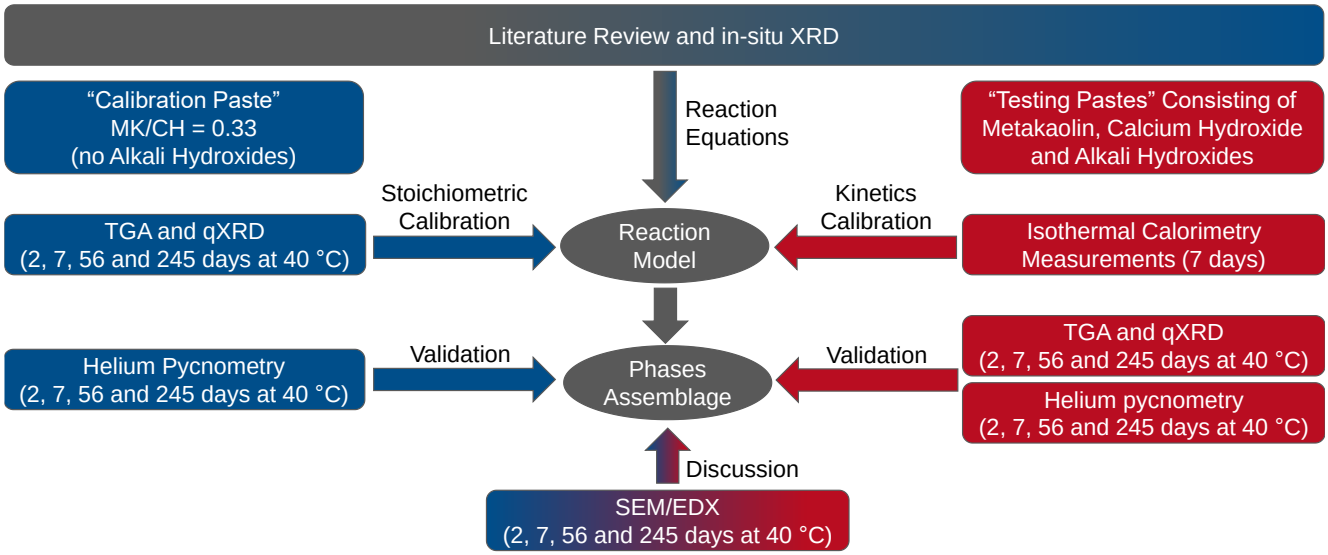

Figure 64: Overview of the research design of the present study; literature review in [79].

The proposed reaction model enables an estimation of the phase assemblage in metakaolin-calcium hydroxide pastes over time, for various sample compositions (MK/CH). To account for the reaction kinetics aspect, isothermal calorimetry measurements were employed for calibrating the reaction model. The model is intended for a simple analytical use without a need for speciation (chemical thermodynamic) solvers and as a starting point for more advanced modeling endeavors. The primary emphasis is on the simple modeling approach that combines stoichiometric calculations with the kinetics of pozzolanic metakaolin reactions with long-term transformation processes. This study provides a combined experimental and modeling approach for the design of innovative "low carbon" binders in the future.

6.2 Materials and Methods

6.2.1 Materials and Sample Preparation

Paste samples were prepared consisting of an alkaline suspension and powdered metakaolin. The metakaolin used was an industrially produced highly pure metakaolin (MetaMax®, BASF SE, Germany) with an amorphous content of approx. 98 wt.-% and 68 % of particle sizes $< 2\ \mu m$ (surface area is 14.2 m^2/g). The chemical composition, according to the manufacturer, is outlined in Table 17. Powdered calcium hydroxide (CH $\geq$ 96 %) and potassium hydroxide pellets (KOH $\geq$ 96 %) from Carl Roth GmbH & Co. KG (Karlsruhe, Germany) were used for the experiments.

Table 17: Chemical composition of the used metakaolin in wt.-%.

	SiO_2	Al_2O_3	Fe_2O_3	CaO	MgO	Na_2O	K_2O	TiO_2
MK	52.3	45.2	<0.5	<0.5	<0.5	<0.5	<0.5	1.7

The sample compositions that mainly vary in the MK/CH weight ratio (0.33 and 1.0) as well as the amount of added KOH are outlined in Table 18. The water to solid weight ratio (w/(MK+CH)) was set to 1.2. The OH^-/MK weight ratios coming from the additional incorporation of KOH were fixed to 0.0077 (0.32KOH) and 0.0306 (1.28KOH), respectively. The sample composition of 0.33MK_0.32KOH is based on the pozzolanic reactivity R^3-test [85–87] with the exclusion of sulfates as the reaction model focusses on the basic reactions in MK-CH systems only.

Table 18: Sample weight ratios and compositions of 100 g suspension plus metakaolin; OH^-/MK weight ratios refer to the added KOH only.

Sample	MK/CH weight ratio	OH^-/MK weight ratio	Calcium hydroxide (CH)	Potassium hydroxide (KOH)	Water (w)	Metakaolin (MK)
0.33MK_0K	0.33	0	38.46 g	-	61.54 g	12.82 g
0.33MK_0.32KOH	0.33	0.0077	38.34 g	0.32 g	61.34 g	12.78 g
0.33MK_1.28KOH	0.33	0.0306	37.97 g	1.28 g	60.75 g	12.66 g
1MK_0K	1.0	0	29.41 g	-	70.59 g	29.41 g
1MK_0.32KOH	1.0	0.0077	29.19 g	0.74 g	70.06 g	29.19 g
1MK_1.28KOH	1.0	0.0306	28.56 g	2.89 g	68.55 g	28.56 g

The suspensions were prepared according to [84]. Potassium hydroxide pellets (KOH) were firstly dissolved in a part of the deionized water for 15 min using a magnetic stirrer [84, 246]. Secondly, dissolved KOH was homogenized with the remaining components (CH and the remaining deionized water) with the help of an electric mixer for 15 min [84, 246]. For the preparation of the reactive samples, 100 g suspension was homogenized with the respective amount of MK with an electric mixer for 5 min [84] (3 min for calorimetry and in-situ XRD samples [83]). The fresh paste samples were directly placed in the calorimetry chamber and also used (selected sample compositions) for in-situ X-ray diffraction measurements. Additionally, for each sample composition, several polyethylene containers were prepared with 10 g ± 0.1 g of the fresh sample [82], sealed and stored at 40 °C in a ventilated oven [84–87]. After 2, 7, 56 and 245 days, the whole sample (10 g) of each composition was gently crushed and grinded in an agate mortar along with 10 mL isopropanol. Before the isopropanol was completely evaporated, an aliquot of 3 g ± 0.05 g of the grinded sample was taken and placed in 50 mL of isopropanol. After this pre-treatment [82], the drying procedure recommended for cement paste samples according to Snellings et al. [258, 264] was performed. The samples were dried in a desiccator for at least 12 hours, but less than 2 days and gently hand-milled. The powdered samples were used for XRD and TGA testing. For the SEM/EDX measurements, tablets with a diameter of 6.5 mm were prepared by placing 0.05 g of powdered sample in the hydraulic press tool from Enerpac (Menomonee Falls, Wisconsin) and pressing for 1 min with 2 kN (~ 60 N/mm²).

6.2.2 Thermogravimetric Analysis

Thermogravimetric analysis (TGA) was carried out with “STA 449 F5 Jupiter” from NETZSCH (Selb, Germany). Nitrogen was used as an inert gas, 40 - 50 mg of powdered sample was placed in alumina crucibles, heated up to 40 °C, kept constant for 30 min and then heated up to 1000 °C at a constant heating rate of 20 °C per minute. The consumed CH (CH-consumption) as well as the chemically bound water in hydration products (CBW) in the samples were calculated in gram per 100 g MK according to [84] by applying the tangent method [247].

6.2.3 X-Ray Diffraction

X-ray diffraction (XRD) measurements were carried out with a “Bruker D2 Phaser” from Bruker Corporation (Billerica, USA), configured with $CuK\alpha_{1,2}$ radiation (40kV and 10mA), linear Lynxeye detector (5 degrees opening). All samples were measured with 0.02 2θ step size in a 5-70 2θ range and a measurement time of 2 seconds per step. The phases used are exemplarily shown in Figure S5-1 in the Supplementary Material for 0.33MK_0K_2d. Due to its similar structure, calcium hemicarboaluminate [284] (AFm phase with ½ CO_3^{2-} instead of OH^- as anion) was found as a good representative of C_4AH_{13} [49] and was consequently used for this phase in the present study due to the lack of information on this in existing databases. For a better representation of the peak at approx. 7 2θ, the stratlingite structure according to Santacruz et al. [285] was used. The qXRD analysis in this study was performed as internal standard method by Rietveld refinement using Topas version 5 software from Bruker

(Billerica, USA). As an internal standard, the respective amount of CH in each sample was taken from TGA results.

Additionally, short-term in-situ XRD measurements were run with these two selected samples only up to 30 h (1MK_0.32KOH measured from 5 to 23 2θ every hour) and 90 h (0.33MK_0.32KOH measured from 5 to 33 2θ every two hours up to 35 h and further measurement every four hours). Airtight sample holder had a dome like X-ray transparent cap from Bruker. The duration for a step size of 0.67 s/step resulted in single measurement run of 19 min followed by a (cooling) pause of 40 or 100 minutes, respectively. The temperature in the measurement device cannot be adjusted, so that the in-situ XRD measurements were carried out at ambient temperatures of 20 °C, slightly heated up due to the X-rays applied (with enough pauses between regular measurements to avoid excess heat generation).

6.2.4 Isothermal Calorimetry

For calorimetry testing, "MC CAL" from C3 Prozess- und Analysentechnik GmbH (Haar, Germany) was used. The device was preconditioned and calibrated at 40 °C and data was collected every 30 s for 7 days [83]. The sample preparation as well as the calculation of the heat flow curves for the reactive samples was performed according to the proposed procedure in [83]. To link the gained information from in-situ XRD measurements to the heat flow peaks from calorimetry, selected samples (0.33MK_0K and 0.33MK_0.32KOH) were additionally tested at isothermal conditions of 20 °C (section 6.3). Furthermore, the same samples were tested at 30 °C isothermal condition for the fundamental discussion of the temperature dependency of the identified metakaolin pozzolanic reactions (section 6.5.4).

6.2.5 Scanning Electron Microscopy with Energy-Dispersive X-Ray Spectroscopy

Scanning electron microscopy coupled with energy-dispersive X-ray spectroscopy (SEM/EDX) was performed on the tablets with "Zeiss EVO LS25" from Carl Zeiss AG (Oberkochen, Germany). For the measurements, the accelerating voltage was set to 15 kV [247], the working distance was fixed to 8.5 mm and the magnification was set to 4000x. For each sample, EDX point analysis was performed on five randomly chosen measuring areas each one consisting of 140 measured points (Figure S5-2 in the Supplementary Material) resulting in 700 measured points per sample. The dwell time per spot was set to 5 s and the distance between the measured spots was 5 μm [247]. The results are presented in Si/Ca-Al/Ca diagrams (molar ratios). With known stoichiometric information of expected hydrate phases, reaction products as well as remaining MK can be qualitatively identified.

6.3 Experimental Identification of Pozzolanic Reaction Products

In-situ XRD measurements were carried out to determine the main reaction products formed in the pozzolanic reactions of metakaolin. The results are consequently linked to results from calorimetry measurements carried out at 20 °C and can further be referred to the elevated testing temperature of 40 °C. This section exemplarily discusses the results for the sample 0.33MK_0.32KOH whereas the results for 1MK_0.32KOH are given in the Supplementary Material (Figure S5-4 and Figure S5-5). Figure 65 and Figure S5-3 in the Supplementary Material show the in-situ XRD results in the range of 10.1 to 12.0 2θ and 6.2 to 7.7 2θ with reaction time. In the first range (Figure 65), one peak at approx. 10.6 2θ starts to build up from 5 to 25 hours of reaction at ~ 20 °C (slightly higher due to the X-rays applied). Another peak occurs even earlier from 3 to 9 hours after sample preparation at approx. 11.6 2θ. In this characteristic range, AFm phases of different specific compositions can be detected [49, 144, 231, 284, 286–289]. As an AFm phase with two OH^- as anion, C_4AH_{13} was referred to these peaks. From approx. 37 hours of reaction, one characteristic peak at ~ 7.0 2θ starts to build up as shown in Figure S5-3 in

the Supplementary Material that is assigned to stratlingite (C_2ASH_8) in literature [49, 231, 285, 290]. For the higher MK/CH of 1.0, all of the three mentioned peaks occur slightly earlier, as shown in Figure S5-4 and Figure S5-5 in the Supplementary Material.

The in-situ XRD results are further linked to the heat evolvement in calorimetry measurements. Figure 66 outlines the heat flow curves of the sample 0.33MK_0.32KOH at 20 °C and 40 °C. Both isothermal conditions result in two characteristic peaks as highlighted in the graph. The 20 °C data can be linked to the in-situ XRD measurements, as they were carried out at approximately the same temperature (slightly higher for in-situ XRD measurements due to X-ray application). In the calorimetry measurement at 20 °C, the first maximum is at ~ 21 h of reaction and the second one starts to build up after ~ 35 h. Based on the in-situ XRD results, they can be assigned to the formation of C_4AH_{13} (peak 1) and C_2ASH_8 (peak 2) along with C-A-S-H that cannot be identified by XRD due to its amorphous structure. As demonstrated in section 6.5.1, the samples with MK/CH of 1.0 show earlier peak evolutions in calorimetry data, that correlates well to the findings of in-situ XRD results (Figure S5-4 and Figure S5-5 in the Supplementary Material).

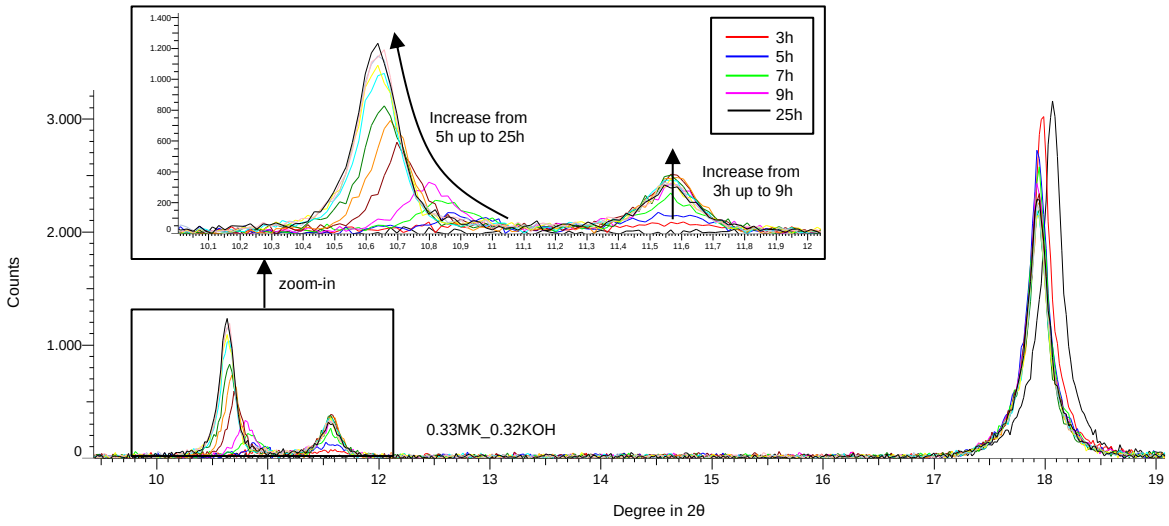

Figure 65: In-situ XRD results shown for 0.33MK_0.32KOH from 1h up to 25h (data shown for every two hours); peaks related to C_4AH_{13}.

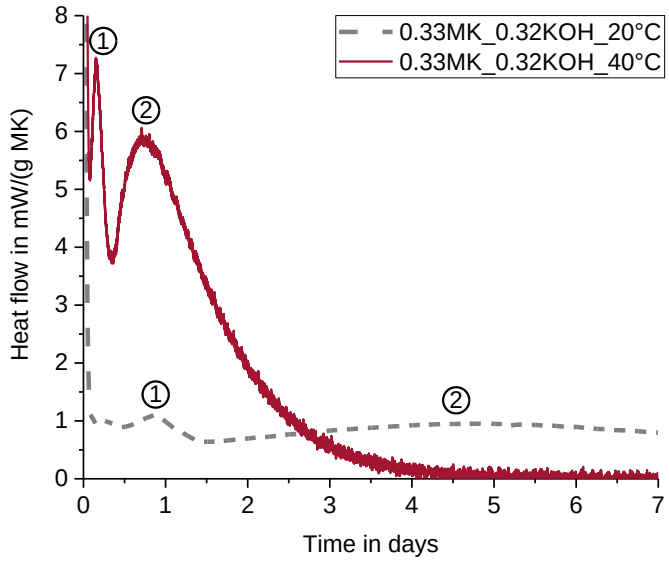

Figure 66: Isothermal calorimetry results shown for 0.33MK_0.32KOH at 20 °C and 40 °C; peak 1 related to C_4AH_{13} and peak 2 to C_2ASH_8 formation.

6.4 Model Description

The model assumptions, collectively summarized in section 6.4.3, outline the framework for understanding the pozzolanic reactions of metakaolin (MK) in the considered binder system. The assumptions involve the categorization of MK reactions into the formation of C_4AH_{13} and C_2ASH_8, along with C-A-S-H. The pozzolanic reaction kinetics are individually calibrated by the deconvolution and kinetic modeling of two heat flow peaks from calorimetry data and serve as input parameters for the reaction model (Figure S5-6 in the Supplementary Material). Additionally, transformation of metastable phases to more stable states are considered, and their parameters are derived from calibrations based on experimental results. The composition of pozzolanic C-A-S-H is fixed and independent of sample variations, while the density remains constant. The model assumes both a temperature-independent nature for the phases formed and the overall long-term degree of MK reactions within the studied temperature range of 20 °C to 40 °C. These assumptions collectively provide a foundation for the comprehensive analysis of metakaolin's behavior in sustainable construction binder systems. A detailed overview of the proposed model showing the input and output parameters is provided in Fig. S6, whereas a simplified scheme is given in Figure S5-7 in the Supplementary Material. The flow chart in Figure S5-6 explains in detail the stoichiometric and kinetic calculations within the provided MATLAB® code (documentation of the provided MATLAB® code is given in the Supplementary Material). The model combines reaction stoichiometry with its kinetics to establish the foundation for comprehending the quantitative relationships and rates that govern the pozzolanic reactions of MK. This combined approach is pivotal for elucidating the intricacies of the transformations, providing essential insights for the design and optimization of sustainable binder systems.

6.4.1 Stoichiometric Equations

Based on findings in literature [79] combined with the experimental results of this study outlined in section 6.3, the pozzolanic reaction of MK (MK reacting with CH) was split into two sequential, partially overlapping reactions forming both C_4AH_{13} (= first pozzolanic reaction; eq. 1) and C_2ASH_8 (= second pozzolanic reaction; eq. 2), as well as amorphous calcium aluminum silicate hydrates (C-A-S-H). The following briefly outlined primary (stoichiometric) reaction equations (eq. 1 and 2) were assumed in the reaction model describing the pozzolanic reaction of MK (short: AS_2) with CH to form C_4AH_{13} (eq. 1) and C_2ASH_8 (eq. 2) along with C-A-S-H. In general, the stoichiometric reaction model is designed to allow any C-A-S-H composition (eq. 1 and 2), but in the present study, $C_{1.5}A_{0.075}S_{0.75}H_{2.7}$ was assumed based on the experimental qXRD and TGA results of the calibration sample 0.33MK_0K.

$$AS_2 + n_1\,CH + x_1\,H \rightarrow y_1\,C_4AH_{13} + z_1\,C_cA_aS_sH_h \quad \text{(first pozzolanic reaction)} \quad (38)$$

$$AS_2 + n_2\,CH + x_2\,H \rightarrow y_2\,C_2ASH_8 + z_2\,C_cA_aS_sH_h \quad \text{(second pozzolanic reaction)} \quad (39)$$

$n_1 = 4(1-2a/s)+2c/s$
$x_1 = 9(1-2a/s)+2/s(h-c)$
$y_1 = 1-2a/s$
$z_1 = 2/s$
$n_2 = 2+(2a-c)/(a-s)$
$x_2 = 6+(6a+c-h)/(a-s)$
$y_2 = (1-2a/s)/(1-a/s)$
$z_2 = -1/(a-s)$

In literature [79], transformations from the metastable reaction products C_4AH_{13} and C_2ASH_8 to more stable hydrogarnet phases are reported for a MK/CH range of 0.3 to 0.6 [65, 68, 70]. For lower MK/CH (0.05 - 0.2), hydrogarnet phases were not detected due to the absence (or low amount) of C_2ASH_8 [54, 65, 68], whereas for higher MK/CH (1.0 - 2.0) the CH shortage hinders the transformation to hydrogarnet [51, 53, 54, 56, 65, 68, 69, 72]. The potential transformation of C_4AH_{13} into more stable

hydrogarnet phases was not considered in the reaction model due to the experimental challenges associated with discerning it (e.g. in XRD quantification) from calcium hemicarboaluminate [284]. The latter may be formed due to contamination with CO_2 exposure during the experiments, and is stable, i.e. does not transform into hydrogarnet. Still, the transformation of metastable C_4AH_{13} [51, 53, 55, 74] remains an intriguing aspect for future research. Eq. 40 was used to simulate the transformation of C_2ASH_8 with an excess supply of CH into hydrogarnet phases and C-A-S-H. The model accommodates the formation of katoite (C_3AH_6) and Si-containing hydrogarnet ($C_3AS_{0.69}H_{4.62}$) to address the inclusion of silicon in the hydrogarnet structure [59, 69, 78], particularly favored in binder systems rich in MK [69]. In the transformation reaction (eq. 40), the C-A-S-H phase was stoichiometrically defined as $C_{1.5}A_{0.075}S_{0.75}H_{2.7}$, aligning with the pozzolanic C-A-S-H phase described earlier. This was calibrated based on chemically bound water and CH consumption results obtained from TGA measurements for the sample 0.33MK_0K. The stoichiometric factors in eq. 40 depend on the specific C-A-S-H composition. Additionally, one factor must be assumed; here, y_4 was set to a value of 0.5.

$$C_2ASH_8 + n_3\ CH \rightarrow y_3\ C_3AH_6 + y_4\ C_3AS_{0.69}H_{4.62} + z_3\ C_{\underline{c}}A_{\underline{a}}S_{\underline{s}}H_{\underline{h}} + x_3\ H \quad (40)$$

$n_3 = 3 \cdot y_3 + 3 \cdot y_4 + \underline{c} \cdot z_3 - 2$
$x_3 = 8 + n_3 - 6 \cdot y_3 - 4.62 \cdot y_4 - \underline{h} \cdot z_3$
$y_3 = 1 - \underline{a}/\underline{s} - y_4 + \underline{a}/\underline{s} \cdot 0.69 \cdot y_4$
$y_4 = 0.5$ (assumed)
$z_3 = 1/\underline{s} - 0.69/\underline{s} \cdot y_4$

6.4.2 Kinetic Modeling

The two reactions in eq. 38 and 39 are identified as the pozzolanic reactions occurring in metakaolin-calcium hydroxide mixtures in the short-term whereas their kinetics were determined by isothermal calorimetry measurements [83]. The two peaks identified in calorimetry were assigned to these two equations based on results from in-situ XRD tests (section 6.3) and the calorimetry data was used to determine the degree of metakaolin reaction (α) in each of the two processes (see Figure 68). As the heat of each reaction per mole of metakaolin is not the same for the two equations, a linear link of the heat release to the degree of reaction is not possible. Consequently, the heat of reaction was calculated according to the Hess's law for both reactions and named H_i (with i = 1 and 2 for reactions outlined in eq. 38 and 39). For these calculations, the formation enthalpy of $C_{1.5}A_{0.075}S_{0.75}H_{2.7}$ was calibrated to a value of -2696 kJ/mol, assuming a metakaolin reaction degree of 0.96 after seven days of hydration at 40 °C in the calibration sample 0.33MK_0K within the calibration procedure. This assumption, derived from SEM/EDX results of sample 0.33MK_0K at 40 °C, supported by Figure S5-49 in the Supplementary Material, indicating limited non-reacted metakaolin. The near-complete pozzolanic reaction is inferred after 7 days at 40 °C, supported by calorimetry results (Figure 69), where heat flow approaches zero around 5 days. To provide a more realistic estimate, the theoretical degree of complete metakaolin reaction (1.0) was thus adjusted to 0.96, acknowledging that achieving complete metakaolin consumption is experimentally impractical. The value -2696 kJ/mol is in the range of several formation enthalpies of C-A-S-H phases reported in literature [233, 314], changing e.g. with the molar C/S ratio [313] and alkali incorporation [303]. It is important to clarify that, at this juncture, the assumed $C_{1.5}A_{0.075}S_{0.75}H_{2.7}$ phase should be understood as an approximative solid-solution phase representing multiple C-A-S-H phases with diverse compositions. A further discussion in section 6.5.5 elaborates on this assumption, highlighting that the formation enthalpy of -2696 kJ/mol cannot be attributed to a singular C-A-S-H phase. The formation enthalpy of MK was calculated to -3478 kJ/mol according to Hess's law by assuming a heat of dehydroxylation reaction of 272.44 J/g [315] and a kaolinite formation enthalpy of 4120.2 kJ/mol [316]. The calculated heat of reactions are H_1 = -257 kJ/mol and H_2 = -197 kJ/mol, respectively. The heat of reactions were used to calculate the degree of metakaolin

reaction (α) directly from the heat flow data. Even though results from microanalysis techniques reveal transformation reactions already within the first seven days (analysis timeframe of calorimetry measurements) for the samples stored at 40 °C, the transformation processes were disregarded in the kinetic calibration of the pozzolanic reactions in this model.

To model the reaction kinetics, a cement hydration model developed for CAC (calcium aluminate cement) hydration [317] was successfully adapted by implementing eq. 41, combining nucleation and growth (or interface) reactions m_1 and m_2 for precipitation of hydration products following by a mass transport mechanism m_3. The three parts of the kinetic model (m_1, m_2 and m_3) are graphically shown for the second pozzolanic reaction of 0.33MK_0K in Figure 67 (A).

$$\frac{d\alpha_i}{dt} = \frac{1}{1/m_1(\alpha_i)+1/m_2(\alpha_i)+1/m_3(\alpha_i)} = \frac{1}{1/(k_{1i}\cdot\alpha_i)+1/(k_{2i}\cdot(1-\alpha_i/\eta_i))+1/(k_{3i}\cdot\log(\eta_i/\alpha_i)^4\cdot(1-\alpha_i/\eta_i))} \quad (41)$$

m_1, m_2, m_3: Individual rates of modeling function.
i: Reaction index (i = 1: eq. 38 and i = 2: eq. 39).
α_i: Degree of metakaolin reaction i.
k_{1i}, k_{2i}, k_{3i}, η_i: Modeling parameters for reaction i; $k_{j,i}$ are reaction constants for mechanisms j = 1, 2, 3 and η_i is the limiting reaction *degree*.

The kinetic model explicitly models the two main pozzolanic reactions eq. 38 and eq. 39. The model for the first reaction does not approach asymptotically zero, as it simulates the growth of metastable hydrate that eventually stops nucleating due to preferences for more stable nucleates and at that stage is not limited by the mass transport mechanisms. The overall kinetic model combines the two $d\alpha/dt$ models (for 1st and 2nd peaks) by integrating them additively ($d\alpha/dt = d\alpha_1/dt + d\alpha_2/dt$; $\alpha = \alpha_1 + \alpha_2$) to finally (re)produce the measured heat curve. The kinetic parameters gained from the kinetic modeling (k_{1i}, k_{2i}, k_{3i}, η_i) serve as input parameters for the stoichiometric reaction model with explicit finite difference integration (MATLAB® code provided as a Supplementary File). The overall degree of metakaolin reaction (α) results from the addition of α_1 and α_2 as exemplarily shown for the sample 0.33MK_0K in Figure 68.

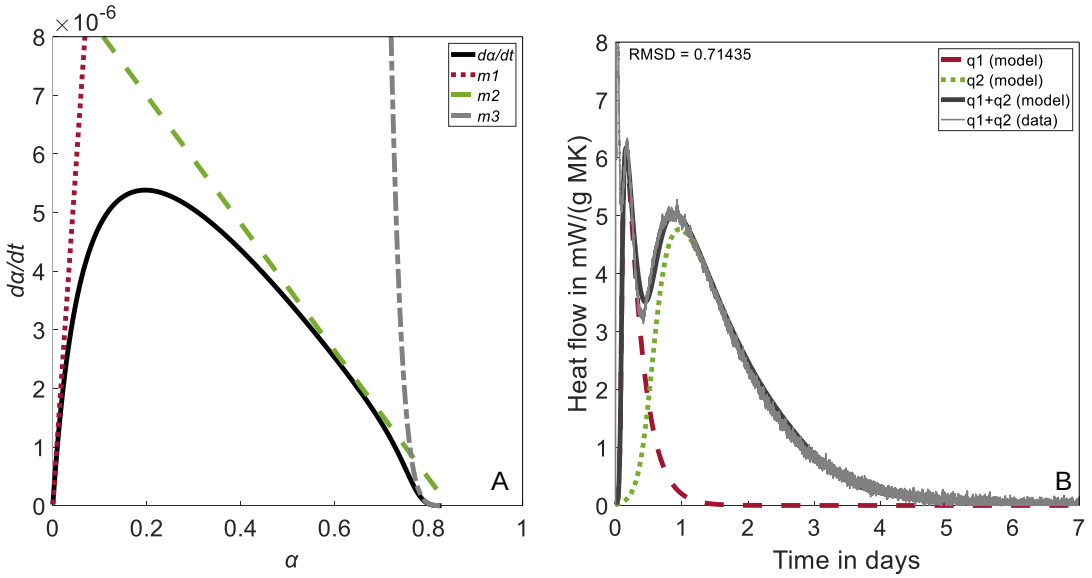

Figure 67: Kinetic modeling (exemplarily shown on sample 0.33MK_0K) (A: Kinetic modeling according to eq. 41 for the second pozzolanic reaction of 0.33MK_0K and B: Fitting of the calorimetry heat flow (q) measurement with kinetic model equation (first and second pozzolanic equation) with root mean square deviation (RMSD); $\alpha_1(1) = 5e^{-6}$ and $\alpha_2(1) = 40{\cdot}5e^{-6}$).

Given the intricate interdependencies among the formed reaction products, released heat, and the corresponding degree of metakaolin reaction, a simplified empirical approach (lognormal fitting) was employed in a first step providing initial values for the more detailed physically-based reaction model. The heat flow from the two reactions (eq. 38 and 39) in mW/(g MK) was separated by a fitting process with two lognormal functions solved by Levenberg Marquardt algorithm using OriginPro® (Figure S5-8 and Figure S5-9 in the Supplementary Material). This initial fitting process employed two lognormal (empirical) functions to mathematically describe the experimental data, enabling the separation of the two reaction processes. The correlation between the heat release of both individual reactions and their corresponding degree of reaction (α_i) are calculated based on the respective heat of reaction (i = 1: eq. 38 and i = 2: eq. 39). The gained fitting parameters (A_1, w_1, xc_1, A_2, w_2, xc_2) serve as initial basis for the more detailed physically-based reaction modeling according to eq. 41 [317]. The kinetic model equation is given in eq. 41, comprising simultaneously nucleation and growth and mass transfer (diffusion) mechanisms. With the help of the lognormal fitting parameters, the two individual reaction kinetics $d\alpha/dt$ were calculated and the results were fitted against the kinetic model given in eq. 41. For all samples with MK/CH of 0.33, the model is designed to allow a complete MK reaction (α = 1), whereas the maximum degree of MK reaction was reduced for the samples with MK/CH of 1.0. In these samples, the pozzolanic MK reactions stop due to a limitation of CH and consequently full MK reaction is not possible. The maximum α (α_max) for these samples was calculated as the following: 1) α after seven days was taken as a result of the initializing fitting step and 2) the possible further MK reaction was estimated based on the remaining CH in the samples after seven days from TGA measurements. For the sample 1MK_0.32KOH α_max was reduced to 0.7 to realize a better model fitting (adjusted parameter is the heat of formation of C-A-S-H according to Table S5-6 in the Supplementary Material). In a last step, the modeling parameters (k_{1i}, k_{2i}, k_{3i}, η_i) were refined to directly fit the experimental heat flow data as exemplarily shown for 0.33MK_0K in Figure 67 (B).

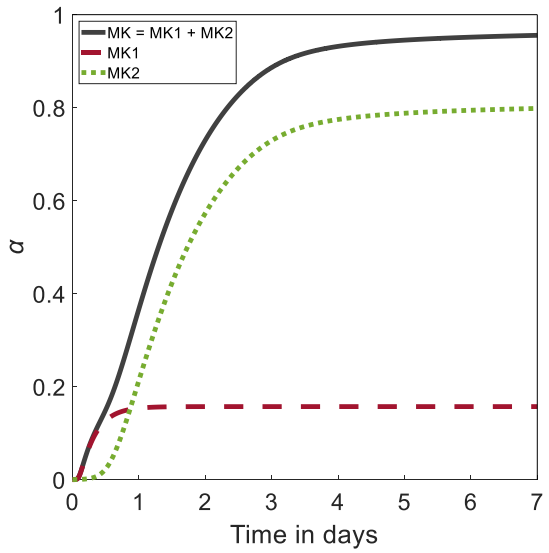

Figure 68: Degree of metakaolin reactions (0.33MK_0K), divided in the two reaction processes.

The reaction rate of the transformation reaction (eq. 40) was assumed to follow the kinetic equation shown in eq. 42. The transformation rate is calculated based on the amount of the respective phase with the exponent n giving the reaction order and multiplied by a rate constant (k). The calculation of the reaction rate for the transformation of stratlingite includes the total amount of CH as educt according to eq. 42 at the respective reaction time. The parameters k and n were approximated through calibration using TGA and qXRD results of the sample 0.33MK_0K (k = 10; n = 3). In delineating the kinetics of

transformation reactions, the utilization of stratlingite is directly proportional to the amount of hydrated phases being consumed, encompassing portlandite as well (as depicted in eq. 42). Notably, the elevated value assigned to the kinetic exponent ($n = 3$) suggest a potential impact of dissolution and precipitation reactions. Specifically, these reactions, influenced by the undersaturation (and supersaturation) of equilibrium ion concentrations in the pore solution [287], hydrate surface areas [318], and other intricate processes, may play a substantial role. A more intricate chemical thermodynamic portrayal of the solid-liquid solubility equilibrium is intentionally omitted in this context. However, for a more comprehensive understanding of the kinetics of phase transformations, a more detailed investigation is recommended in future research.

$$dC2ASH8 = k \cdot C2ASH8^{n} \cdot CH \tag{42}$$

dC2ASH8: Reacting moles of C_2ASH_8.
C2ASH8: Total amount of C_2ASH_8 in moles.
CH: Total amount of CH in moles.
n: Order of reaction with respect to C_2ASH_8.
k: Transformation rate constant for the transformation of C_2ASH_8.

6.4.3 Summary of Model Assumptions, Parameters and Calibration

The model assumptions explained in the previous sections are summarized as follows:

- The pozzolanic reactions of MK are divided into the formation of C_4AH_{13} and C_2ASH_8 along with C-A-S-H according to eq. 38 and 39.
- C_2ASH_8 was assumed to transform to more stable (Si-containing) hydrogarnet phases (C_3AH_6 and $C_3AS_{0.69}H_{4.62}$) according to eq. 40.
- The composition of the pozzolanic C-A-S-H as well as the one formed in the transformation process is calibrated to $C_{1.5}A_{0.075}S_{0.75}H_{2.7}$ based on 0.33MK_0K and fixed with respect to various other sample compositions and reaction times.
- The density of C-A-S-H is fixed to 2.0 [319] independent of the sample composition and reaction time.
- After seven days of reaction at 40 °C the degree of metakaolin reaction (α) is assumed in the first parameter estimation step (lognormal fitting) as 0.96 for the calibration sample 0.33MK_0K.
- The formation enthalpy of the pozzolanic C-A-S-H is calibrated to -2696 kJ/mol based on 0.33MK_0K and fixed for the other sample compositions reacted at 40 °C.
- The kinetics of the transformation reaction is indicatively calibrated with the qXRD and TGA results of the sample 0.33MK_0K ($k = 10$; $n = 3$).
- The kind of phases formed as well as the overall long-term degree of MK reactions are assumed to be independent of the temperature in the investigated range of 20 °C to 40 °C.

The stoichiometric equations as well as the reaction kinetics were calibrated as explained in detail in the sections 0 and 6.4.2. Table 19 summarizes the model parameters together with their respective calibrations. Apart from the fitting parameters for the pozzolanic reaction kinetics that need to be individually determined for each sample, the main model parameters were calibrated with the experimental data gained for the sample 0.33MK_0K. The input and output parameters of the proposed reaction model are schematically shown in Figure S5-6 in the Supplementary Material. The densities of the individual phases used for the calculation of the total solid volume are outlined in Table 20.

Table 19: Overview of the model parameters and their calibration.

Subject	Parameters	Calibration
C-A-S-H composition	c, a, s, h in pozzolanic $C_cA_aS_sH_h$ (eq. 38 and 39) and $\underline{c}$, $\underline{a}$, $\underline{s}$, $\underline{h}$ in transformation $C_{\underline{c}}A_{\underline{a}}S_{\underline{s}}H_{\underline{h}}$ (eq. 3)	TGA together with qXRD results for 0.33MK_0K: $C_{1.5}A_{0.075}S_{0.75}H_{2.7}$
Heat of reactions	Formation enthalpy of pozzolanic $C_cA_aS_sH_h$	Isothermal calorimetry (assumption: α = 0.96 after 7 days for sample 0.33MK_0K): -2696 kJ/mol
Kinetics of pozzolanic reactions according to eq. 38 and 39	Kinetic modeling parameters (k_{1i}, k_{2i}, k_{3i}, η_i) in eq. 41	Isothermal calorimetry individually for each sample (see Table 21)
Kinetics of transformation reaction according to eq. 42	k, n	TGA together with qXRD results for 0.33MK_0K

Table 20: Densities of the individual phases used for the calculation of the total solid volume.

Phase	Density in g/cm³	Reference
MK	2.64	Measured.
CH	2.24	Specification manufacturer [320] and measured.
C_4AH_{13}	2.05	[233, 321, 322]
C_2ASH_8	1.94	[321]
C_3AH_6	2.52	[214, 233, 321, 322]
C-A-S-H	2.00	[319, 322]

6.5 Results and Discussion

6.5.1 Kinetic Modeling

Isothermal calorimetry heat flow measurements at 40 °C are shown in Figure 69 (A: MK/CH = 0.33 and B: MK/CH = 1.0) with variations in the potassium hydroxide content, i.e. 0.32 and 1.28KOH respectively. Based on these results, the kinetic model outlined in eq. 41 was used to fit the heat flow curves. The modeling parameters are provided in Table 21, where higher k_{1i} indicate a more accelerated reaction, higher k_{2i} is related to a generally broader curve and η_i describes the maximum α_i for the individual reaction ($\eta_1 + \eta_2 = \alpha\_max$). To realize satisfying fitting of the calorimetry heat flow data, α_i vectors need to be carefully initialized for the two pozzolanic reactions, indicated as $\alpha_1(1)$ and $\alpha_2(1)$ in the figure captions. The kinetic modeling results are graphically shown in Figure 67 (B) for 0.33MK_0K and Figure S5-10 to Figure S5-18 in the Supplementary Material in comparison with the experimental heat flow data. The parameters of the initial lognormal fitting (A_1, w_1, xc_1, A_2, w_2, xc_2) for the heat flow peak separation for initializing the parameter estimation of the kinetic model, namely the two individual α_i, are outlined in Table S5-1 in the Supplementary Material.

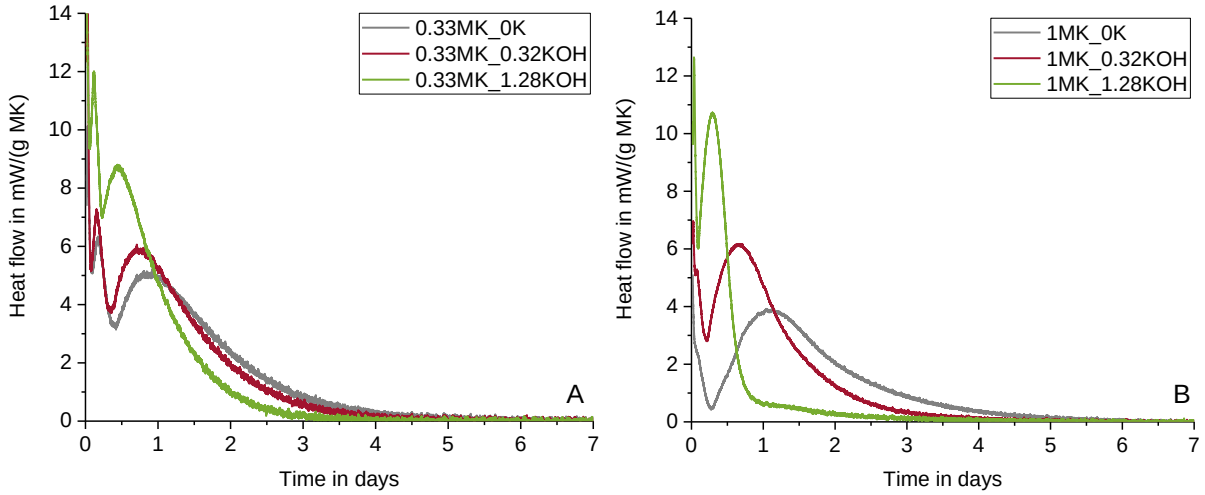

Figure 69: Heat flow curves of all samples with MK/CH = 0.33 (A) and MK/CH = 1.0 (B).

Table 21: Results of the kinetic fitting parameters (isothermal calorimetry 40 °C); $k_{31} = 0$ with root mean square deviation (RMSD)*.

Sample	k_{11}	k_{21}	η_1	k_{12}	k_{22}	k_{32}	η_2	RMSD
0.33MK_0K	9.3759e-04	9.3759e-06	0.1572	1.1702e-04	9.1656e-06	8.9656e-02	0.8428	0.71
0.33MK_0.32KOH	9.5947e-04	9.5947e-06	0.1418	1.4423e-04	1.0396e-05	0.030864	0.8582	0.91
0.33MK_1.28KOH	1.5079e-03	1.5079e-05	0.17807	2.0569e-04	1.4707e-05	0.09	0.82193	0.45
1MK_0K	3.5706e-03	3.5706e-06	0.026782	9.7636e-05	7.7881e-06	0.09	0.70322	0.15
1MK_0.32KOH	5.1863e-03	5.1863e-06	0.044156	1.7046e-04	1.0469e-05	0.09	0.65584	0.44
1MK_1.28KOH	1.2641e-02	1.2641e-05	0.072349	4.2074e-04	2.104e-05	0.0020225	0.50765	0.27

* Calculated in mW/(g MK) by comparing the modeled vs. experimental heat flow data starting from 25min.

In Figure 69, the calorimetry data and consequently the fitting parameters in Table 21 (larger k_{21}) and Table S5-1 in the Supplementary Material reveal a much more pronounced first peak (C_4AH_{13} formation) for the samples with an MK/CH of 0.33 compared to 1.0 and acceleration of both pozzolanic reactions with the incorporation of KOH. The reduced formation of the highly calcium-rich product C_4AH_{13} in the samples with a higher MK/CH ratio seems to be related to the proportionally reduced CH content. In these samples the heat flow peak is not as visible as for the lower MK/CH ratio of 0.33. Regarding the second peak (C_2ASH_8 formation) the incorporation of KOH in the samples with MK/CH of 0.33 leads to a clear acceleration of the reaction (increasing k_{12}), but the total peak area (A_2 in Table S5-1 in the Supplementary Material) is within the same range for all samples. In contrast to this, the sample 1MK_1.28KOH shows a very different behavior. The second peak occurs earlier compared to the other two samples with MK/CH of 1.0, but additionally, the total peak area is significantly reduced and the overall shape of the peak differs from the others. This phenomenon can possibly be explained by the additional formation of alkaline aluminosilicates [197] as a result of the extensively higher OH^-/CH ratio and the consequently higher MK and impeded CH dissolution due to a higher pH [53, 59, 147, 183]. In the present study, the OH^-/MK ratio was fixed, so that an increase in MK/CH leads to higher OH^-/CH, accordingly. Table 22 outlines the respective OH^-/CH ratios and molarities (moles KOH/liter).

Table 22: Overview of the OH^-/CH weight ratios in the samples with incorporated KOH (values in brackets show the respective molarities).

Sample	_0.32KOH	_1.28KOH
0.33MK	0.0025 (0.09 M)	0.0102 (0.38 M)
1MK	0.0077 (0.19 M)	0.0307 (0.75 M)

6.5.2 Phase Assemblage Modeling

This section shows the results of the modeled phase assemblage of the sample 0.33MK_0K, whereas the model outputs of all other sample compositions are given in the Supplementary Material in Figure S5-19 to Figure S5-23. The samples used in this study were selected to demonstrate and discuss both the accelerating effect of KOH and the impact of a CH shortage on the metakaolin pozzolanic reactions for higher MK/CH. The modeling outputs shown in this section and in the Supplementary Material are accompanied by the TGA and qXRD results that are part of the validation study (section 6.5.3), and allow a discussion on the phase assemblage at this point. The XRD results indicate an amorphous part of stratlingite and its reflection peak at approx. 30 2θ can overlap with C-A-S-H phases [297] (indicated for sample 0.33MK_0K_2d in Figure S5-24 in the Supplementary Material). In this context, the qXRD results should be interpreted with care (all qXRD results given in Figure S5-24 - Figure S5-27 in the Supplementary Material).

The modeling outputs for the sample with MK/CH of 0.33 are shown without KOH (0.33MK_0K) in Figure 70 and with KOH (0.33MK_0.32KOH and 0.33MK_1.28KOH) in Figure S5-19 and Figure S5-20 in the Supplementary Material. The results show a decrease of MK within the first approx. 7 days along with the consumption of CH forming C_4AH_{13}, C_2ASH_8 and C-A-S-H phases. A further consumption of CH in parallel to the formation of hydrogarnet phases is due to the transformation of C_2ASH_8 and leads to a more stable phase assemblage in the long-term (here: up to 245 days cured at 40 °C). The incorporation of KOH leads to an acceleration of the pozzolanic reactions as shown in Figure S5-28 in the Supplementary Material. In general, the model calculates a higher amount of C_4AH_{13}, and a lower amorphous content compared to the qXRD results. The differences of the modeled phases and the experimental data might be due to several factors, like e.g. differences in the composition of C-A-S-H phases, changes in the stoichiometric factors of the transformation reaction of C_2ASH_8 (eq. 40), the neglected transformation of C_4AH_{13} and/or different kinetics of the transformation reactions. All these factors mutually influence each other, so that only potential tendencies can be discussed, and not the individual factors separately. The incorporation of KOH might result in a reduced transformation of C_2ASH_8 due to a declining CH dissolution, that consequently results in a lower hydrogarnet content compared to the actual modeled amount. The C-A-S-H composition might additionally be changed by the presence of KOH, leading to variations in the stoichiometric equations (eq. 38 and 39) as well as the molar masses used for the calculation of the respective amount of phases in terms of mass (further discussed in section 6.5.5). Compared to the sample without KOH, qXRD results show a higher overall amorphous content, that might be due to potassium ions present as interlayer cations in C-A-S-H phases [313], along with lower amounts of C_4AH_{13} and C_2ASH_8.

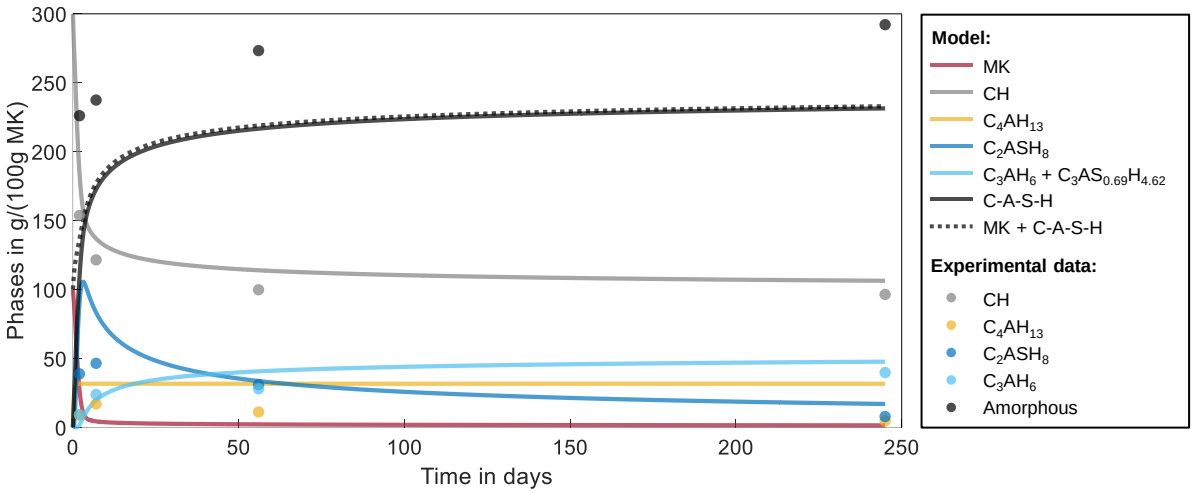

Figure 70: Modeled phase assemblage of 0.33MK_0K, dots are representing qXRD/TGA data.

As shown in Figure S5-29 (A) in the Supplementary Material, the proposed reaction model yields an overall metakaolin reaction degree of 0.69 after seven days of reaction at 40 °C for the higher MK/CH ratio of 1.0. The figure also shows the evolution of the two individual pozzolanic reactions for the first seven days. In Figure S5-29 (B) in the Supplementary Material, the impact of KOH on the overall degree of MK reaction with MK/CH of 1.0 is demonstrated for 0.32KOH and 1.28 KOH. Also here it can be observed that the addition of KOH leads to an accelerated pozzolanic reaction, where the sample with the highest amount of KOH (1MK_1.28KOH) shows a significantly lower overall degree of MK reaction, viz. reduced to a value of 0.53. In this sample, the additional formation of alkaline aluminosilicates [197] might result in a completely different phase formation compared to the other samples due to the significant higher OH^-/CH ratio, not covered by the present reaction model.

The modeled phase assemblage for the sample 1MK_0K along with the qXRD results at two days of reaction (further reaction times could not be evaluated with the executed internal standard approach due to the full consumption of CH) is shown in Figure S5-21 in the Supplementary Material up to 20 days, after which the results were constant. The predicted amount of C_2ASH_8 is considerably higher, while the amorphous portion is lower, in comparison to the data obtained from qXRD results after 2 days of reaction. It should be acknowledged, that these experimental results might be prone to significant errors due to the small amount of remaining CH in the samples, which was used for the internal standard quantification method (10.1 g in 1MK_0K, 3.1 g in 1MK_0.32KOH and 8.5 g in 1MK_1.28KOH). The phase assemblage stabilizes from the sixth day onward, as the CH in the sample is entirely consumed, resulting in no further significant transformation of C_2ASH_8.

The modeled reaction kinetics separated in the two pozzolanic reactions are shown for all samples in Figure S5-30 and Figure S5-31 in the Supplementary Material. The rapid and not asymptotical approach to zero of *da/dt* of the first reaction kinetics (eq. 38) is because it simulates the growth of metastable hydrate that eventually stops nucleating due to preferences for more stable nucleates and at that stage is not limited by the mass transport mechanisms. the kinetic curve is calculated considering only calorimetry data up to seven days, as further reactions (mainly transformation of hydrates) do not significantly consume MK anymore, shown by SEM/EDX and calorimetry. As the degree of reaction is linked to MK consumption, further improvement of the kinetic model would require another definition of the degree of reaction, linked to the stratlingite consumption. Whereas for the MK/CH ratio of 0.33, the first pozzolanic reaction is not significantly affected by a small amount of KOH (0.33MK_0.32KOH

relative to 0.33MK_0K), it is strongly affected by further increase of the alkali hydroxide content (sample 0.33MK_1.28KOH) leading to a strong acceleration, as shown in Figure S5-30 (A) in the Supplementary Material. For the second pozzolanic reaction, an accelerated reaction is observed already for a small amount of KOH (Figure S5-30 (B) in the Supplementary Material). However, in the first pozzolanic reaction, the overall amount of MK contributing to the reaction process is reduced with the higher MK/CH of 1.0 (Figure S5-31 (A) in the Supplementary Material), but the enhanced KOH content accelerated the reaction process and increased the total degree of reacting MK. Furthermore, higher reaction rates are observed for MK/CH of 1.0 compared to 0.33, that may be caused by an enhanced dissolution due to the higher amount of MK available. In the second pozzolanic reaction, MK reaction accelerated with increasing KOH content (Figure S5-31 (B) in the Supplementary Material). The sample 1MK_1.28KOH again shows a significantly different behavior, namely an pronounced acceleration of the reaction rate followed by a sharp decline. Consequently, this sample reached a significantly lower total degree of MK reaction as already shown in Figure S5-29 (B) in the Supplementary Material. An explanation of this phenomenon could be the significantly higher OH^-/CH ratio (Table 22), that could lead to an impeded CH dissolution due to the enhanced pH value of the solution.

6.5.3 Validation of Modeling Results

TGA and qXRD results of sample 0.33MK_0K were used to calibrate the model (thin lines in figures). Other sample compositions could optionally also be employed for validation to show a wider applicability of the model. As in the previous section, qXRD results were used for validation, in the present section results from thermogravimetric analysis (TGA) as well as helium pycnometry are used for comparison with the model outputs. From TGA data, the consumed CH (CH-consumption) as well as the chemically bound water (CBW) in reaction products was calculated [84] (TG- and DTG-curves of all samples are given in Figure S5-32 - Figure S5-43 and a summary of the TGA results is provided in Table S5-2 in the Supplementary Material). The results are used to validate the CH-consumption and CBW outputs of the proposed reaction model as shown in Figure 71 and Figure 73.

The model results for the consumption of CH are in a good agreement with the TGA data for the selected samples, viz. 0.33MK_1.28KOH and 1MK_0K (Figure 71 (A)). The consumed CH per 100 g MK for the sample with MK/CH of 1.0 reached a value of 100 g, meaning a complete consumption of CH within the first seven days of reaction is limiting further pozzolanic reactions. The samples with MK/CH of 0.33 show a much higher CH-consumption (MK reacting with CH) of approx. 200 g per 100 g MK in the long-term.

The chemically bound water (CBW) in the reaction products is outlined in Figure 71 (B) and shows good agreement between the model results and experimental data for the sample 0.33MK_1.28KOH. In particular, the amount of CBW in sample 1MK_0K up to seven days of reaction shows good agreement with the TGA data. The ongoing (slow) increase of experimental CBW results up to 245 days is not captured by the model. The overall MK reactions stopped after approx. seven days due to the complete consumption of CH. According to the TGA data, it seems like even though CH is fully consumed, free water can still be bound in reaction products in the long-term, mainly in C-A-S-H. As in the present model (section 6.4.3) the C-A-S-H composition is fixed, it does not change within the reaction time and consequently, the experimentally determined CBW in reaction products cannot be fully represented by the modeled phases for MK/CH of 1.0.

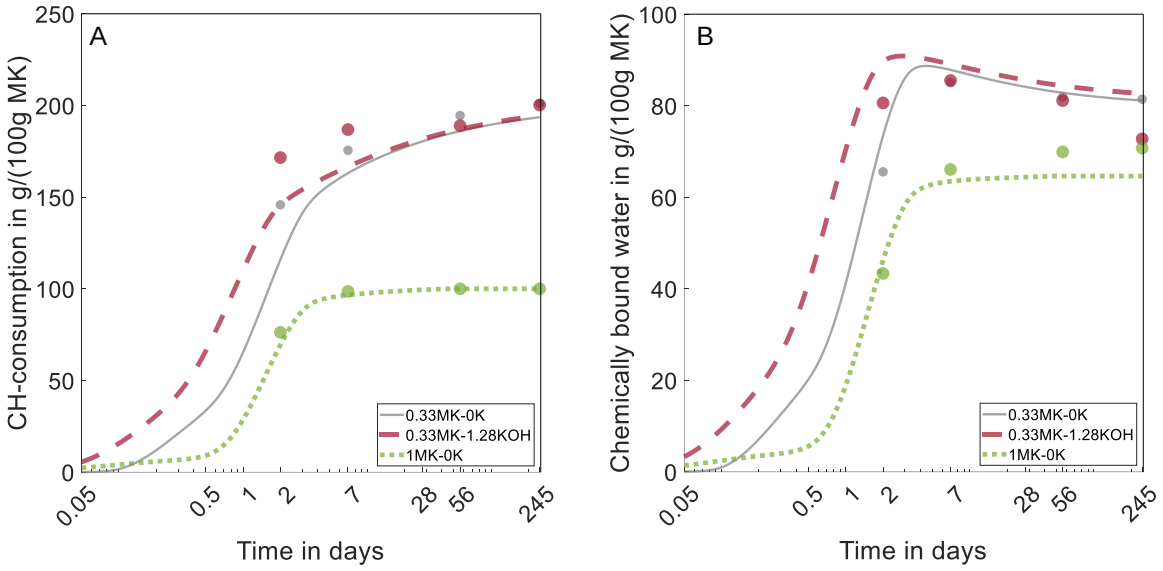

Figure 71: Model validation with TGA data (A: CH-consumption and B: chemically bound water in reaction products).

Helium pycnometry was used to determine the sample density (results of all samples are summarized in Table S5-3 of the Supplementary Material). When knowing the initial sample composition along with the chemically bound water in reaction products (CBW) from TGA measurements, the total volume of solid phases normalized per gram of MK was calculated and compared with the volume of the modeled phase assemblage (see Figure 72). For the two samples with MK/CH of 0.33, the experimental data clearly shows a decrease of the total solid volume with reaction time. These results highlight the critical aspect of transformation reactions that may negatively influence the materials properties. A decrease of the total volume of solid phases in hardened pastes can cause micro cracks that may result in durability problems [323–326]. Another interesting result is the lower total solid volume of the sample with incorporated KOH (0.33MK_1.28KOH) compared to the one without KOH (0.33MK_0K) as shown in Figure 72. This finding might be due to a lower C/S molar ratio in the C-A-S-H phases for the sample with KOH. This might increase the pH value followed by a more intense MK [31, 76, 180–184] along with an impeded CH dissolution [53, 59, 147, 183]. According to [327] a lower C/S is simultaneously accompanied by a reduced H/S molar ratio that consequently increases the C-A-S-H density [328]. A higher density with an increasing amount of silica in C-A-S-H was also reported elsewhere [329] whereas in contrast, other studies observed lower densities with decreasing C/S ratios [314, 322, 329]. The different findings in literature demonstrate the complexity of C-A-S-H compositions, and makes it difficult to give a clear statement on this mechanism.

A reduction of the total volume of solids is not visible in the experimental data for the sample with MK/CH of 1.0, confirming that no significant transformation reactions take place in the absence of CH. The decreasing volume with time for the samples with MK/CH of 0.33 is also predicted by the model, but to a much lesser extend compared to the pycnometer data. The modeled total volume is directly dependent on the densities of the individual phases (Table 20). In particular the assumed C-A-S-H density of 2.0 g/cm³ [319] that is not allowed to change within the reaction time (section 6.4.3) might be a reasonable explanation of this. Especially in the first days of reaction, the density of the C-A-S-H phases might be much lower and consequently, the volume of the solid phases much higher. An increase of the C-A-S-H density with reaction time is considered realistic in the investigated systems, e.g. due to a reduction of C/S [328, 329], but this is not covered in the present model.

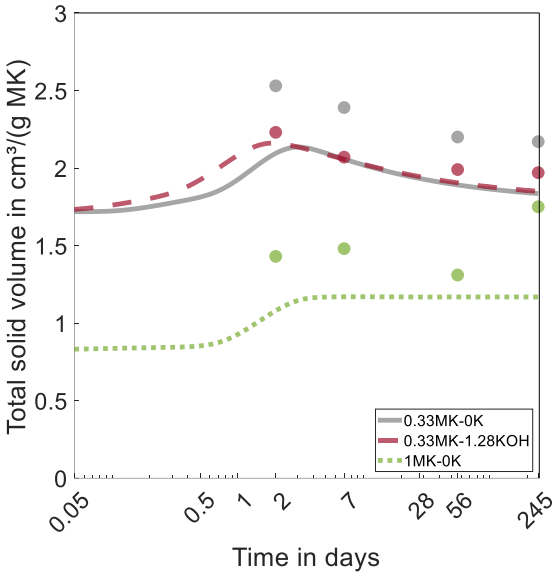

Figure 72: Model validation with helium pycnometry data (total solid volume).

Figure 73 and Figure 74 show the model results for the samples with MK/CH of 1.0 and different amounts of KOH in comparison with the experimental data. TGA data (Figure 73 (A)) shows a slightly accelerated consumption of CH for the lower amount of added KOH (1MK_0.32KOH), but a deceleration for the higher amount of KOH (1MK_1.28KOH). This trend is also visible in the modeled curves, but the CH-consumption of 1MK_1.28KOH is less pronounced in the model results when compared to the data. This observation might be due to the shape of the calorimetry curve for this sample and the difficulty of realizing a better lognormal fit as already explained in section 6.4.2 (see Figure S5-9 in the Supplementary Material). Figure 73 (B) shows the experimental and model results for the chemically bound water (CBW) in the reaction products of all samples with MK/CH of 1.0. The experimental data does not show a significant difference between the sample with and without a lower amount of KOH (1MK_0K compared to 1MK_0.32KOH), whereas the model predicts a slightly higher amount of CBW in sample 1MK_0.32KOH. The C-A-S-H phases in the sample with KOH might have a lower C/S molar ratio, due to an enhanced MK [31, 76, 180–184] and impeded CH dissolution [53, 59, 147, 183], that might consequently be accompanied by a reduced H/S ratio [327]. If the model H/S ratio would be lower compared to the sample without KOH, the model results for CBW would decrease as well, resulting in similar values of CBW for both samples as also observed from the TGA data. The same trends are visible from the model results and measured total solid volume (Figure 74). The measured value for the sample 1MK_0K after 56 days of reaction seems to be an outlier possibly due to incorrect sample preparation and/or measurement. The increase of CBW (Figure 73 (B)) and total solid volume (Figure 74) for reaction times larger than seven days are not covered by the model as the reactions are designed to stop after complete depletion of CH and the C-A-S-H composition is fixed with respect to time and sample composition.

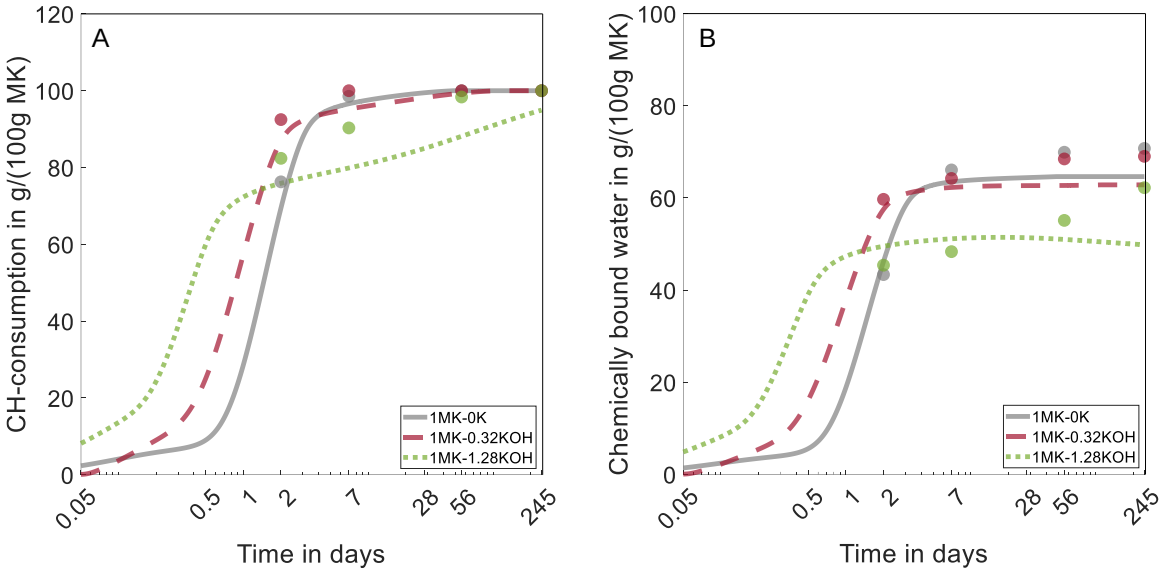

Figure 73: Model validation with TGA data (A: CH-consumption and B: chemically bound water in reaction products) for the samples with MK/CH of 1.0 and different amounts of KOH.

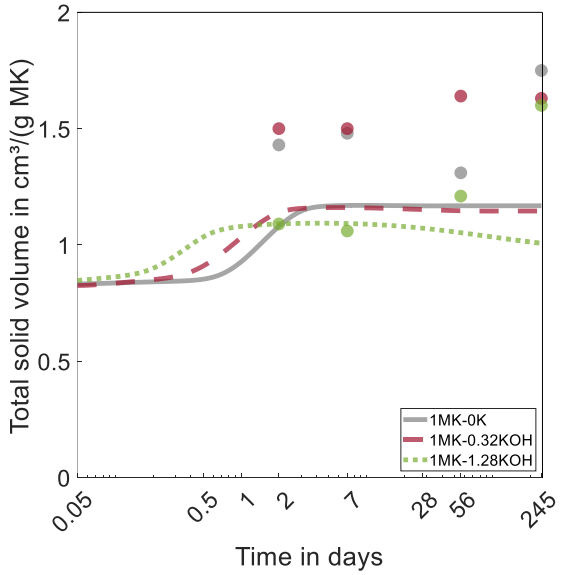

Figure 74: Model validation with helium pycnometry data (total solid volume) for the samples with MK/CH of 1.0 and different amounts of KOH.

6.5.4 Temperature Dependency

The proposed metakaolin reaction model utilizes calorimetry measurements as input for the pozzolanic reaction kinetics. Consequently, employing isothermal calorimetry measurements at temperatures other than 40 °C, to provide kinetic input parameters, enables predictions of the corresponding phase assemblage at the selected temperature.

In this study, measurements at 20 °C and 30 °C were conducted on selected samples to investigate the temperature dependency of pozzolanic metakaolin reactions and validate the proposed mechanisms by calculating the activation energy as a function of the degree of reaction. Reaction rates for the two individual pozzolanic metakaolin reactions outlined in section 6.4.1 were determined with the proposed reaction model as $d\alpha/dt$ for reactions at 20 °C, 30 °C and 40 °C (fitting parameters are provided in Table S5-4 and S5-5 in the Supplementary Material). As per section 6.4.3, the overall (long-term) degree of metakaolin reaction was assumed to be independent of the reaction temperature. Consequently, the

heat of formation of the pozzolanic C-A-S-H phase was calibrated for samples measured at temperatures that differ from 40 °C to achieve the same overall long-term degree of MK reaction (the respective values are summarized in Table S5-6 in the Supplementary Material).

The individual reaction rates are plotted against the degree of metakaolin reaction (α) in Figure 75 (A: peak 1 and B: peak 2). Figure 75 (A) shows the reaction rates for the first peak from calorimetry measurements related to the formation of C_4AH_{13} and C-A-S-H depending on the applied temperature. The reaction rates increase with higher temperatures in the range of 20 °C to 40 °C, and the degree of metakaolin reaction in this early stage also rises with temperature. The overall degree of MK reaction (α) for the first pozzolanic reaction (eq. 38, section 6.4.1) is lower compared to the second peak, correlating with the formation of C_2ASH_8 and C-A-S-H (eq. 39, section 6.4.1). The values range from approx. 0.04 at 20 °C to 0.16 at 40 °C. The degree of MK reacted in the second reaction (eq. 39, section 6.4.1) is much higher than in the first, following a clear trend consistent with the Arrhenius equation, allowing for the calculation of the activation energy of MK and the proposed reaction mechanism.

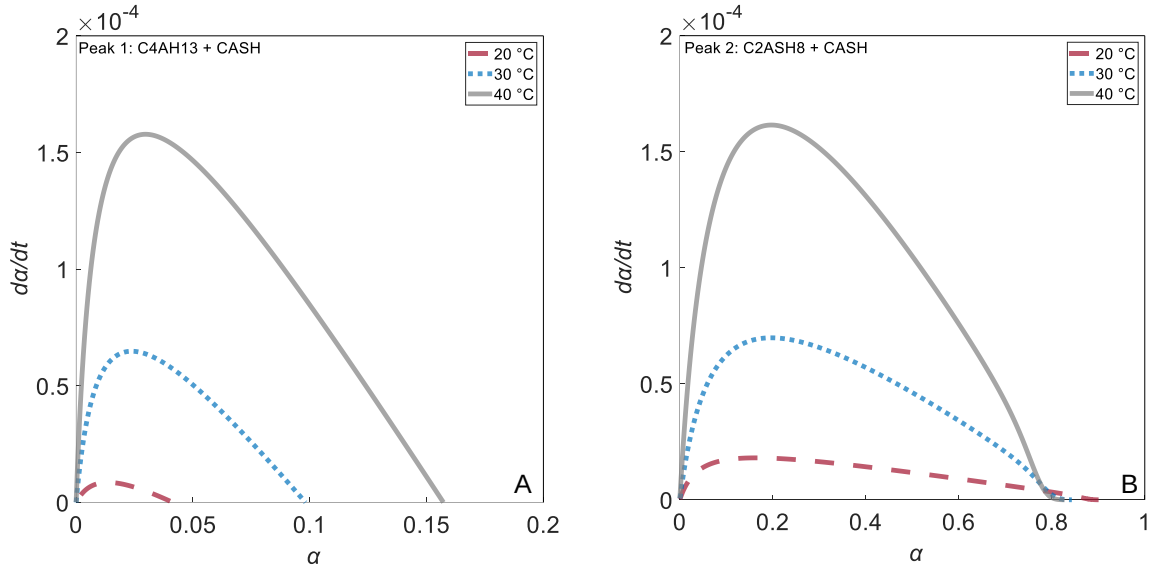

Figure 75: Modeled reaction rates ($d\alpha/dt$) of the sample 0.33MK_0K depending on the degree of metakaolin reaction (α) for the two proposed pozzolanic metakaolin reactions at 20 °C, 30 °C and 40 °C (A: Peak 1 and B: Peak 2).

The Arrhenius equation defines the reaction rate constant as an exponential function of the absolute temperature (as outlined in eq. 43).

$$k = A \cdot \exp(-Ea/(R \cdot T)) \quad (43)$$

k: Reaction rate constant.
T: Absolute temperature in K.
A: Arrhenius factor.
Ea: Activation energy for the reaction in J/mol.
R: Universal gas constant (8.31 J/(mol·K)).

With the knowledge of at least two reaction rate constants at two different reaction temperatures, the activation energy can be calculated. Figure 75 (B) indicates an Arrhenius temperature dependence of the second metakaolin reaction that forms stratlingite and C-A-S-H according to eq. 39. For this specific reaction, the activation energy was calculated for each degree of metakaolin reaction according to eq. 44 [330]. The result is shown for the sample 0.33MK_0K calculated with isothermal calorimetry data at 20 °C and 40 °C in Figure 76. Figure 76 suggests an activation energy of approx. 84 kJ/mol for the degree of reaction between 0.1 and 0.6 for the pozzolanic metakaolin reaction outlined in eq. 44.

$$Ea(\alpha) = R \cdot \log\left(\frac{d\alpha/dt\_T1(\alpha)}{d\alpha/dt\_T2(\alpha)}\right) \cdot \frac{T1 \cdot T2}{T2 - T1} \quad (44)$$

Ea: Activation energy for the reaction in J/mol.
R: Universal gas constant (8.31 J/(mol·K)).
T1: First temperature in K.
T2: Second temperature in K.
dα/dt_T1: Reaction rates determined as *dα/dt* from the reaction model at *T1*.
dα/dt_T2: Reaction rates determined as *dα/dt* from the reaction model at *T2*.

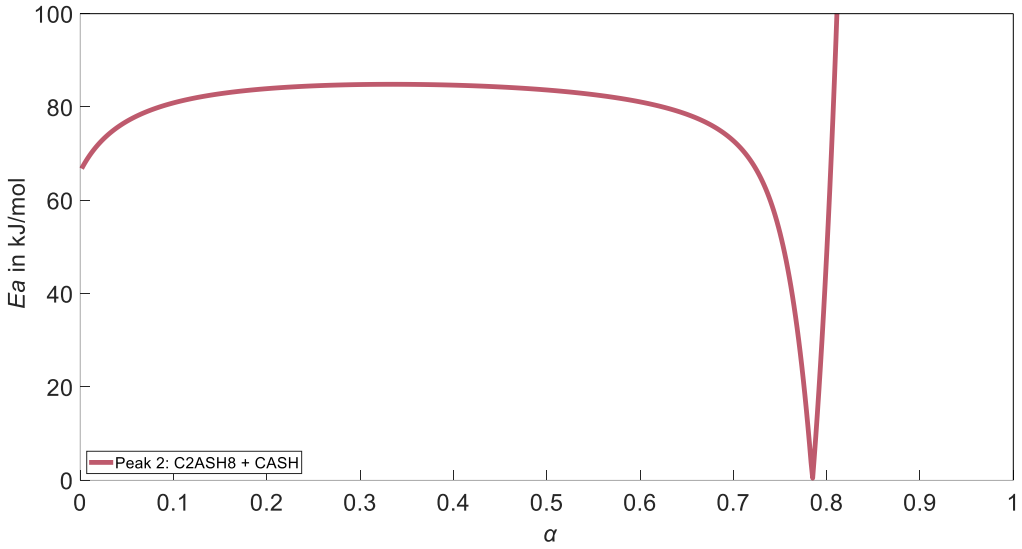

Figure 76: Calculated activation energy *Ea* for the sample 0.33MK_0K in kJ/mol for eq. 39 outlined in section 6.4.1 shown for the respective degree of metakaolin reaction (α); isothermal calorimetry data of 20 °C and 40 °C used for the calculation.

The similar procedure was conducted for the same samples at the temperatures of 20 °C and 30 °C as well as 30 °C and 40 °C. Additionally, a sample with added potassium hydroxide (0.33MK_0.32KOH) was analyzed in the same way (modeled reaction rates for peak 1 and peak 2 are given in Figure S5-44 and Figure S5-45 in the Supplementary Material). The calculated activation energies are summarized in Table 23 and graphically shown in Figure S5-46 and Figure S5-47 in the Supplementary Material.

Information on the activation energy of metakaolin in pozzolanic reactions is scarce in the literature. Ninov et al. proposed a decreasing activation energy from 71 to 45 kJ/(mol CH) for increasing reaction degrees between 0.2 and 0.6 [220]. These values are higher compared to the ones determined in this study when $C_{1.5}A_{0.075}S_{0.75}H_{2.7}$ is assumed as the average C-A-S-H phase ($n_2 = 2+(2a\text{-}c)/(a\text{-}s) = 4$): 84 kJ/mol / 4 = 21 kJ/(mol CH). A decrease in activation energy with an increasing degree of reaction is not evident from the data of this study. A recently published study [331] investigated the activation energy of MK dissolution differentiating between Al and Si dissolution at different pH values of the solution. For a pH value of 13, activation energies of 89 kJ/mol (Al) and 81 kJ/mol (Si) were reported [331]. In cement paste systems, activation energies of 46 kJ and 62 kJ/mol are reported with the addition of micro- and nano-silica as pozzolanic representatives [332]. In the present study, discrepancies in initial ($\alpha < \sim 0.02$) and end ($\alpha > \sim 0.7$) values are not considered, as they are highly sensitive to model implementations. The variations of the calculated activation energies for the same sample using data from different isothermal conditions (rows in Table 23) may arise due to the assumption of the long-term degree of metakaolin reaction being independent of the reaction temperature. The results could be improved by experimentally determining the exact amount of remaining MK in the samples and calibrating the model accordingly.

Table 23: Calculated activation energies at different temperatures for two samples with and without incorporated KOH.

Sample	20 °C - 30 °C	30 °C - 40 °C	20 °C - 40 °C
0.33MK_0K	102 kJ/mol	66 kJ/mol	84 kJ/mol
0.33MK_0.32KOH	75 kJ/mol	62 kJ/mol	69 kJ/mol

6.5.5 Model Limitations

The main limitations of the proposed stoichiometric reaction model lies in the assumed constant composition of C-A-S-H phases that develop in the pozzolanic reactions, before and during transformation from stratlingite to hydrogarnet. In this study, the C-A-S-H phase assumed for the pozzolanic reactions (eq. 38 and 39) and the transformation reaction of stratlingite (eq. 40), represented by $C_{1.5}A_{0.075}S_{0.75}H_{2.7}$ maintains fixed molar ratios of Ca/Si = 2.0 and Al/Ca = 0.1. The assumed C-A-S-H composition maintains constant throughout reaction time or specific sample composition in the proposed model, deliberating simplification chosen to mitigate model complexity.

Nevertheless, the actual composition of C-A-S-H is depending on the specific sample composition and undergoes changes over time. During the precipitation of synthetic C-A-S-H from CaO, $CaO{\cdot}Al_2O_3$, and silica fume (SiO_2), initial high Ca/Si molar ratios were observed, transforming into lower ratios within one day, depending on the target Ca/Si value, which ranged from 0.6 to 1.6 [333]. The same trend was found in cementitious LC^3-systems (limestone calcined clay cement), where the Ca/Si ratio decreases with advancing MK reaction, particularly after CH depletion [334]. In samples with a higher MK content, Al/Ca increased over time from 90 days to 3 years, while Ca/Si decreased [334]. Systems with a higher MK content exhibited a lower Ca/Si (1.37 compared to a maximum of 1.79 for the reference without MK) and a higher Al/Ca ratio (0.24 compared to a minimum value of 0.05 for the reference without MK) [109], for a hydration time of 3 years. The total amount of Ca in C-A-S-H increases slightly up to three years and even up to 10 years of hydration, indicating a slow redistribution of Si and Al [335] within the C-A-S-H [114]. Furthermore, a recently published study modeled an increase of Al/Ca and Si/Ca in C-A-S-H for higher degrees of MK reaction and replacement ratios of cement by MK [336]. It should be noted that even in cementitious systems, C-A-S-H phases are highly dependent on the specific binder composition [247], as values vary e.g. for Portland cements (Ca/Si = 1.7 - 2.0; Al/Si = 0.05 - 0.1) [200], blended cements (Ca/Si = 1 - 1.5, Al/Si = 0.03 - 0.2) [308–310], and alkali-activated slags (Ca/Si = 0.7 - 1.0; Al/Si = 0.1 - 0.3) [311, 312]. Consequently, these values can only be referred to for general tendencies, while for specific systems like MK-CH more detailed investigations are necessary.

The C-A-S-H composition not only influences stochiometric coefficients in the reaction equations but also the formation enthalpies [233, 313, 314] and densities of these phases [314, 319, 322, 328, 335, 337, 338]. A more in-depth scanning electron microscopy analysis coupled with energy-dispersive X-ray spectroscopy (SEM/EDX) was conducted on the samples in this study. The results, shown in Figure 77 and Figure 78 (and Figure S5-48 - Figure S5-50 in the Supplementary Material), based on Al/Ca vs. Si/Ca diagrams (molar ratios), show the individual chemical compositions of amorphous C-A-S-H phases [339]. In these diagrams, non-hydrated samples consisting of MK and CH result in an imaginary line with a slope of approx. 1.0, as CH alone does not contain silicon or aluminum, representing the zero point. Pure MK, without calcium, is found in the upper right corner (asymptotic approach infinity) [298]. As EDX analysis measures a certain area of the sample, data from one measured point will always include overlapping results, leading to a diffuse combination of phases [247, 298, 340]. Consequently, non-hydrated data of the investigated samples result in an imaginary line starting in the zero point and having a slope of the Si/Al ratio in MK (~ 1.0). Reaction products of MK and CH differ in their respective Si/Al ratio as well as the calcium content. Accordingly, data points move away from this line with

reaction time, as demonstrated in Figure 77 (A: 0.33MK_0K) and Figure S5-48 in the Supplementary Material (1MK_0K). Data points moving to the upper left side are assigned to C-A-S-H phases [247, 298] as Si/Al >> 1.0. The amount of these phases is increasing with time, especially for lower MK/CH of 0.33 (Figure 77 (A)). Data points in the upper right corner, representing non-reacted MK [298], are decreasing with reaction time. Additionally, the formation of hydrogarnet phases can be observed as well, and are increasing with time in Figure 77 (A: data points moving to the lower right corner), but not for higher MK/CH of 1.0 (Figure S5-48 in the Supplementary Material). These observations align with the proposed reaction model.

When comparing the data points assigned to C-A-S-H phases (upper left corner of the "triangle") for MK/CH of 0.33 and 1.0 (Figure 77 (B)), a clear trend emerges, showing an increase in Si/Ca and Al/Ca with higher MK/CH ratios. This pattern is attributed to the overall elevated amounts of silicon and aluminum and reduced calcium content in the systems. Figure 77 (B) further illustrates the specific compositions of the assumed C-A-S-H phases in the reaction model. The composition of $C_{1.5}A_{0.075}S_{0.75}H_{2.7}$, used as the C-A-S-H phase formed in the pozzolanic reactions of MK as well as the transformation of C_2ASH_8 to hydrogarnet phases, exhibits an Al/Ca molar ratio of 0.1 and Si/Ca of 0.5 (represented by a black circle with a grey infill in Figure 77 (B)).

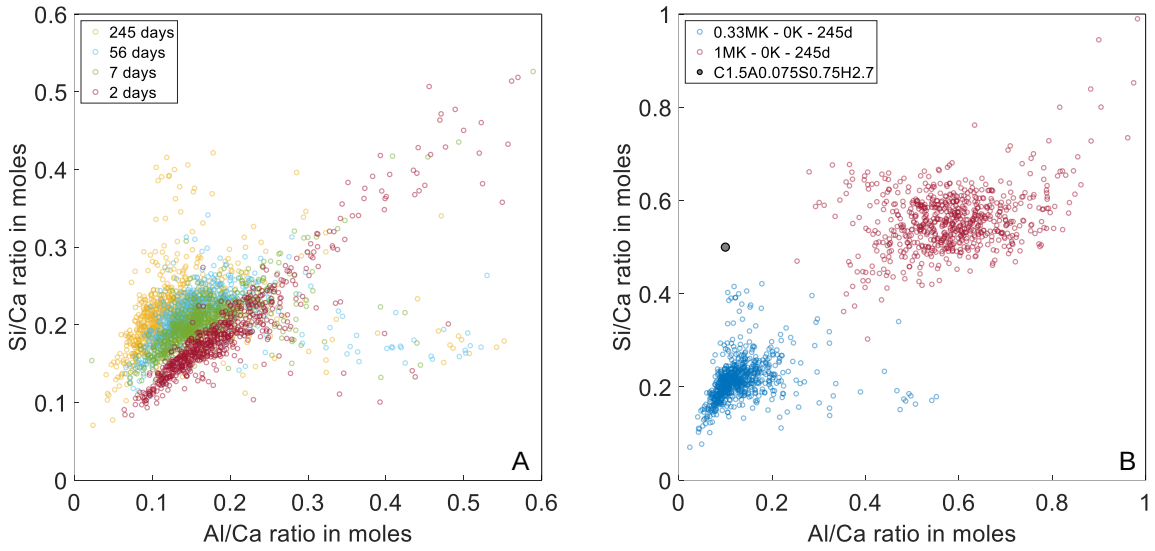

Figure 77: SEM/EDX results for 0.33MK_0K with reaction time (A) and 0.33MK_0K and 1MK_0K at 245 and C-A-S-H compositions of the modeled phases (B).

The effect KOH has on the composition of the reaction products is shown in Figure 78 for MK/CH of 0.33 (A) and 1.0 (B) after 245 days of reaction (data after 7 days is shown in Figure S5-49 and Figure S5-50 in the Supplementary Material). Across all sample compositions and the two chosen testing times, a noticeable shift of data points towards higher Al/Ca ratios was observed for samples with incorporated KOH. This shift can be attributed to elevated pH values resulting from the presence of KOH and intensified MK dissolution [31, 76, 180–184], while impeding CH dissolution [53, 59, 147, 183]. Particularly in sample 1MK_1.28KOH, there are significantly more data points in the upper right corner of the diagram, indicating non-reacted MK, especially after 7 days of reaction, when compared to 1MK_0K. The considerably higher OH^-/CH in that sample (see Table 22) enhances MK and impedes CH dissolution, resulting in a diminishing pozzolanic reaction aligning with the results from the reaction model described in section 6.4 together with the possible formation of additional alkaline aluminosilicates [197]. The SEM/EDX results vividly show variations of the C-A-S-H composition with

time and MK/CH weight ratio, highlighting the model limitations resulting from a fixed C-A-S-H composition.

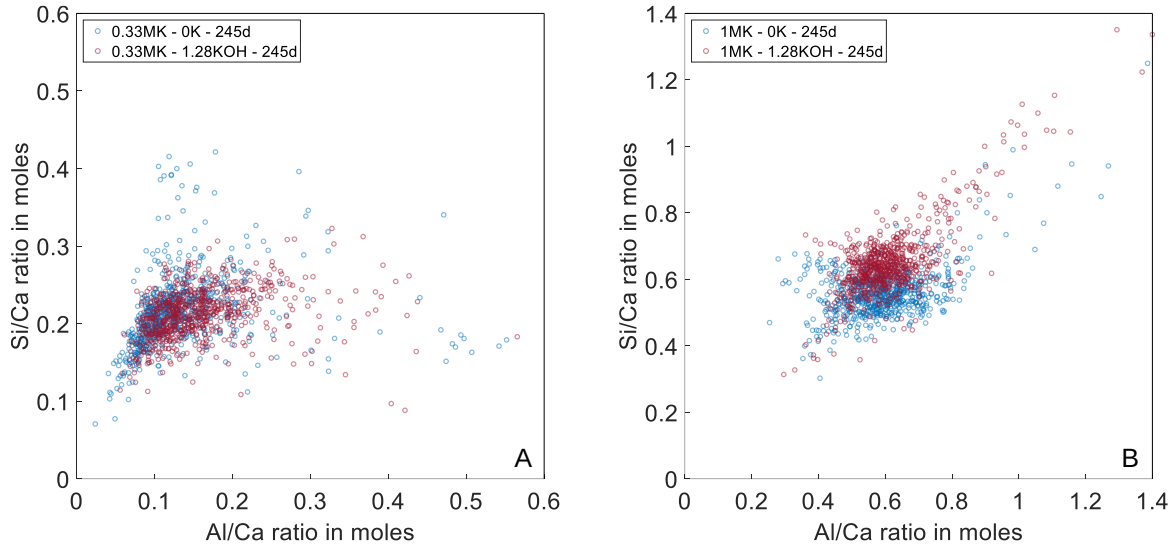

Figure 78: SEM/EDX results for 0.33MK_0K and 0.33MK_1.28KOH (A) and 1MK_0K and 1MK_1.28KOH (B) after 245 days of reaction.

Beyond the fixed C-A-S-H composition, the assumed transformation reaction pose a further constraint on the proposed model. As detailed in section 6.4.1, the composition of C-A-S-H forming in the transformation of C_2ASH_8 (eq. 40) was set as $C_{1.5}A_{0.075}S_{0.75}H_{2.7}$ in accordance with the pozzolanic C-A-S-H phase, calibrated based on experimental TGA results for the sample 0.33MK_0K and based on all other model assumptions (see section 6.4.3). The stoichiometric equation (eq. 40) and kinetics of the transformation reaction (eq. 42) in the proposed model remain constant across the reaction time and (initial) sample composition and can be considered as a rough estimation only. Further research is needed to refine the model in this regard. Additionally, disregarding possible transformations of C_4AH_{13} is a further limitation of the proposed model.

6.6 Conclusions

A relatively simple stoichiometric reaction model for pozzolanic metakaolin reactions was developed, encompassing several overlapping short-term as well as long-term transformation reactions. The model predicts the phase assemblage in metakaolin-calcium hydroxide reactions as a function of time and reaction degree, providing a valuable contribution to the design of innovative metakaolin-based binder systems. Calibration of reaction kinetics was performed through isothermal calorimetry measurements, validated by qXRD, TGA and helium pycnometer results. The discussion of the models' limitations includes relative elemental ratios resulting from SEM/EDX measurements, offering qualitative phase analysis and remaining MK amount. Key findings are summarized as follows:

- The proposed kinetic model, calibrated based on experimental calorimetry measurements, enables the separation of two partially overlapping reaction mechanisms, allowing to calculate the individual degrees of metakaolin reaction.
- The proposed stoichiometric reaction model predicts main reaction processes and estimates the phase assemblage over reaction time, including the long-term transformations.
- Pozzolanic reactions of metakaolin are separated into two equations, representing the formation of C_4AH_{13} and C_2ASH_8. The main pozzolanic reaction is the formation of stratlingite

and C-A-S-H, where the activation energy was calculated as 84 kJ/mol based on the model and isothermal calorimetry data (20 °C and 40 °C).

- Incorporation of potassium hydroxide accelerates reaction processes and reduces the activation energy of the pozzolanic metakaolin reaction to 69 kJ/mol (0.33MK_0.32KOH).
- A critical model simplification is the fixed definition the C-A-S-H composition, discussed in section 6.5.5. Results of SEM/EDX graphical mapping (relative elemental ratios) analysis, reveal increasing Si/Ca and Al/Ca in C-A-S-H phases with MK/CH (initial mix) ratios, and the addition of potassium hydroxide results in higher Al/Ca ratios in C-A-S-H phases.

Future research directions could include variations in C-A-S-H composition in the model and studying transformation reaction equations and kinetics in more detail. Extensions involving carbonates and/or sulfates are interesting aspects for further investigation.

7 Conclusions

The main conclusions of the present work address the two research hypotheses outlined in section 1.2. The first **research hypothesis (1)** can be answered as following with respect to the methodology aspects and experimental findings.

The main conclusions regarding the **methodology aspects** are:

- User-friendly ex-situ mixing of MK-CH pastes can be applied for isothermal calorimetry testing at 40 °C by using an inert sample for the baseline correction.
- The mass balance approach for the evaluation of thermogravimetric analysis (TGA) data, accounting for carbonation processes and the composition of the precursor material, is promising for R^3-samples with calcined clays.
- Using isopropanol (instead of acetone) for the drying procedure of the investigated samples led to more reliable TGA results due to a more effective solvent exchange, fewer carbonation and less interactions with reaction products.
- The phases selection for quantitative XRD analysis, i.e. the choice of the specific hydrogarnet phases, has a significant influence on the results and needs to be taken into account for interpretation of the results.
- The exact quantitative determination of the amorphous metakaolin content in hydrated paste samples is not possible with the microanalysis techniques applied in this work. Additional experiments, e.g. nuclear magnetic resonance spectroscopy (NMR), could give further details related to this aspect.
- Information about the structure and the degree of polymerization of C-A-S-H phases as well as alkaline aluminosilicates was not gained with the used analysis techniques. Further analysis, e.g. Fourier-transform infrared spectroscopy (FT-IR), would give further insights into these aspects.

The key findings related to the **pozzolanic metakaolin reactions** are:

- Based on isothermal calorimetry measurements and in-situ X-ray diffraction testing, the pozzolanic reactions of MK can be described by two reaction processes occurring in the following order: 1) formation of C_4AH_{13} and 2) formation of C_2ASH_8, both together with C-A-S-H.
- The formation of C_4AH_{13} is enhanced with higher calcium content (lower MK/CH) and with increasing temperature in the range of 20 °C to 40 °C.
- The activation energy for the main (C_2ASH_8) pozzolanic MK reaction was calculated to a value of 84 kJ/mol based on the proposed reaction model and isothermal calorimetry measurement data of 20 °C and 40 °C.
- As C_4AH_{13} and C_2ASH_8 are metastable reaction products, they transform to more stable hydrogarnet phases in the long-term, especially with excess supply of CH.

Novel results addressing the incorporation of **alkali hydroxides and sulfates** are:

- Pozzolanic MK reactions exhibit acceleration with alkali hydroxides incorporation, particularly pronounced with NaOH compared to KOH, with the same OH^-/MK weight ratio.
- Samples with the highest OH^-/CH weight ratio of 0.0307 (1MK_1.28KOH and 1MK_1.28NaOH) display distinct reaction mechanisms, potentially related to the formation of alkaline aluminosilicates and hindered pozzolanic MK reactions, not covered by the presented reaction model.
- Sulfate incorporation leads to a rapid ettringite (AFt) formation, transforming into monosulfoaluminate, accelerating reaction processes in samples with MK/CH of 0.33, but conversely, decelerating pozzolanic MK reactions in higher MK/CH ratio (1.0) samples.
- SEM/EDX mapping reveals potassium (K) primarily in C-A-S-H phases and sulfates (S) in aluminum-rich products, like in ettringite, monosulfoaluminate and in Si-rich hydrogarnet phases.

Based on the research work of this thesis, the second **research hypothesis (2)** can be answered as following:

- The kinetics of the pozzolanic metakaolin reactions can be determined experimentally by isothermal calorimetry measurements, serving as input parameters for the stoichiometric reaction model.
- A simplified stoichiometric and kinetic reaction model for MK-CH systems was developed, using input parameters from fitting of heat flow curves together with the initial MK/CH weight ratio. The model allows to predict the phase assemblage of these systems in the short- and long-term by covering the pozzolanic reactions as well as transformation processes.
- The model can be used to calculate physical characteristics, e.g. the development of the total solid volume with time, indicating critical volume reductions in the long-term.
- The main limitations of the model are the fixed C-A-S-H and hydrogarnet compositions as demonstrated with experimental results from scanning electron microscopy analysis along with energy-dispersive X ray spectroscopy (SEM/EDX). Based on these tests, Si/Ca and Al/Ca in C-A-S-H phases increase with MK/CH, the incorporation of potassium hydroxide leads to higher Al/Ca ratios and sulfates are incorporated in Si-rich hydrogarnet phases.
- The model serves as a basis for further research work, that would be needed for more precise predictions, especially allowing individual phases compositions as well as to account for the incorporation of alkali hydroxides, sulfates and/or carbonates.

Based on the findings outlined above, the following aspects for **future research** work are suggested:

- The specific phases characteristics as well as the reaction mechanisms of pozzolanic reactions in parallel to the formation of alkaline aluminosilicates, investigated especially for high OH^-/CH weight ratios, is an interesting research field.
- The stoichiometric equations as well as the kinetics of the transformation reactions need to be further studied in more detail by additionally accounting for individual phases selection in quantitative XRD analysis.
- In future research, the proposed simplified reaction model can be enlarged by allowing variations in the C-A-S-H and/or hydrogarnet compositions.
- Pore solution parameters, like e.g. the pH value, should be included in the reaction model to account for variations in the alkali hydroxide and sulfate content, influencing the phases formations especially for high MK/CH ratios.
- Extensions of the model, e.g. regarding the addition of carbonates and/or sulfates are interesting aspects for future work.
- In future research, work related to a transfer of the fundamental pozzolanic reaction model to more complex, e.g. cementitious, systems is of particular interest.

8 Supplementary Material

8.1 Publication 1

8.1.1 Review Methodology

This review covers literature published until April 2023. In the first step, thirteen works [51, 53, 58, 62, 63, 68, 69, 74, 75, 106, 107, 143, 173] were identified as the most relevant publications dealing with the reactivity of MK with CH in terms of the reaction products being formed. The articles are summarized in Table S1-1, which reflects the authors' preferences on the subject, ranging from some pioneering publications from 1983 to 1993 on the basic reaction processes between MK and CH [51, 69, 75], over more recent findings from 2001 to 2015, to the latest studies published from 2020 to 2022. The latter, also includes investigations of MK reactions in more complex systems such as cement pastes characterized by various simultaneously occurring influencing factors like sulfate, carbonates, alkalis and chlorides [53, 106, 143, 173]. Following the forward and backward citation search methods, the references of each main publication as well as the articles referencing them, resulted in a total number of 1085 articles (Table S1-1) that were screened using the online web platform "Web of Science" [341]. The respective results were refined by the search term "metakaolin or MK" and skimmed by reading abstracts and conclusions to identify the articles addressing the topic of this review study. This process was followed by a detailed reading and comparative study of the articles leading to further literature from each of the cited studies, all used to identify articles relevant as input for systematizing the knowledge.

In addition, relevant articles were searched in the "Web of Science" database using the following search syntax terms: *AB=((metakaolin OR "calcined kaolin") AND ("calcium hydroxide" OR "lime" OR "Ca(OH)2" OR "portlandite") NOT geopolymer)*, whereas the abbreviation AB stands for the respective abstract of the articles. The search resulted in 478 publications (15th May 2023), the number of which is shown chronologically in Figure S1 up to the end of 2022, illustrating the increasing research interest and relevance of this topic over the last years. The titles and abstracts of all 478 articles were scanned and the relevant literature was selected for the present review study. The literature review includes peer-reviewed journal papers published in English and German language.

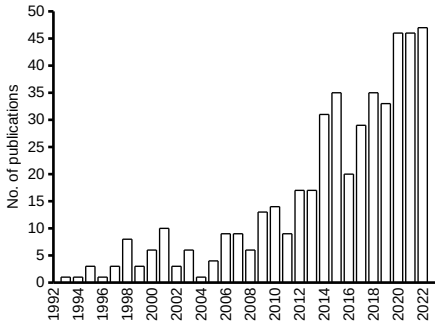

Figure S1-1: Chronologically sorted number of publications that match following search criteria syntax: AB=((metakaolin OR "calcined kaolin") AND ("calcium hydroxide" OR "lime" OR "Ca(OH)2" OR "portlandite") NOT geopolymer) [342].

8.1.2 Supplementary Figures

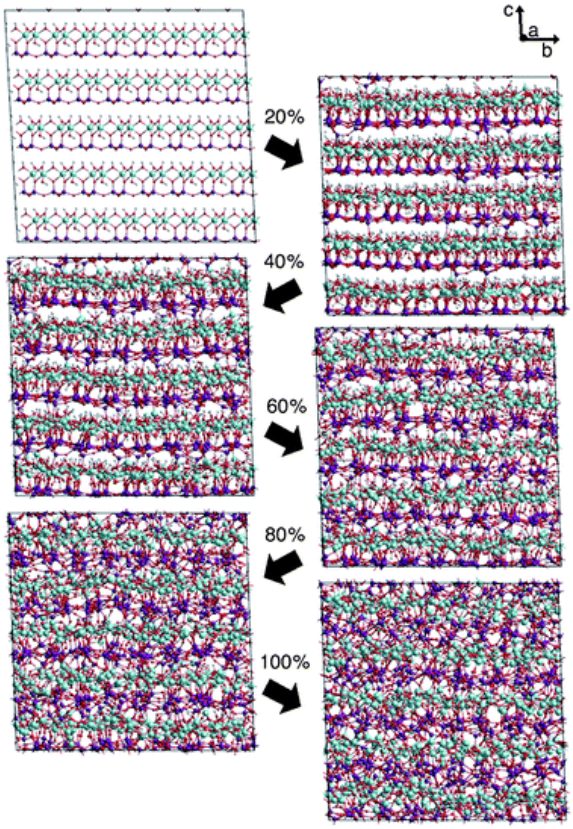

Figure S1-2: Modelled dehydroxylation process from the kaolinite structure (top left) to fully dehydroxylated metakaolin (bottom right), dehydroxylation is shown in 20 % steps [24]. © 2011 used with permission of ROYAL SOCIETY OF CHEMISTRY from [24]; permission conveyed through Copyright Clearance Center, Inc..

8.1.3 Supplementary Tables

Table S1-1: Main publications on the reactivity of MK with CH selected by the authors, dating from 1983 to current year, without claim to exclusivity.

Ref.	Authors	Year	Title	No. references	No. citing articles
[106]	Beuntner & Thienel	2022	Pozzolanic efficiency of calcined clays in blended cements with focus on the early hydration	36	1
[173]	Maier et al.	2022	Particle characteristics of calcined clays and limestone and their impact on early hydration and sulfate demand of blended cement	77	3
[143]	Zunino & Scrivener	2021	The reaction between metakaolin and limestone and its effect in porosity refinement and mechanical properties	27	20
[107]	Scherb et al.	2021	Reaction kinetics during early hydration of calcined phyllosilicates in clinker-free model systems	89	3
[62]	Deng et al.	2020	The effect of activators on the dissolution characteristics and occurrence state of aluminum of alkali-activated metakaolin	31	5
[58]	Žemlička et al.	2015	Study of hydration products in the model systems MK-CH and MK-CH-gypsum	48	18
[54]	Gameiro et al.	2012	Hydration products of lime–metakaolin pastes at ambient temperature with ageing	8	25
[63]	Fernandez et al.	2010	Mineralogical and chemical evolution of hydrated phases in the pozzolanic reaction of calcined paper sludge	44	35
[74]	Cabrera & Rojas	2001	Mechanism of hydration of the MK-CH-water system	22	138
[53]	Frias & Cabrera	2001	Influence of MK on the reaction kinetics in MK/lime and MK-blended cement systems at 20°C	17	116
[69]	De Silva & Glasser	1993	Phase relations in the system $CaO-Al_2O_3-SiO_2-H_2O$ relevant to metakaolin - calcium hydroxide hydration	20	116
[75]	De Silva & Glasser	1990	Hydration of cements based on metakaolin: thermochemistry	14	*
[51]	Murat	1983	Hydration reaction and hardening of calcined clays and related minerals - I. Preliminary investigations on metakaolinite	7	165

*Forward citation search method was not applied for this article as it was not found in the Web of Science database.

Table S1-2: Systematic summary of the results grouped into four MK/CH ranges, indicating observed reaction products of MK with CH where the studies include the presence of carbonate impurities, but no sulfates. The results refer to ambient curing temperatures, while higher curing temperatures of 55 and 60 °C are shown in italic for available data.

MK/CH	C_2ASH_8 (stratlingite)	C_4AH_{13}	$C_3AS_yH_z$ (hydrogarnet)
0.05 - 0.2	Not observed [54, 65, 68]	Observed from 1d to approx. 28d [54, 65, 68]	Not observed [54, 65, 68] as no C_2ASH_8 present
0.3 - 0.6	Observed [65, 69] with increase from 1d to 28d [56, 68], followed by a decrease up to 1.5y [65] due to formation of hydrogarnet [65, 68] *Not observed due to transformation to hydrogarnet [69]*	Possible transformation to $C_3AS_yH_z$ and/or $Ca_2Al(OH)_7 \cdot 6.5\ H_2O$ [54, 65] In some cases not observed due to small amount [66], low crystallinity [53, 57, 66, 70] and/or overlapping with other phases in TGA/XRD [51, 53, 57, 70, 71]	Observed from 28d to 1.5y [65, 68] due to transformation reactions of C_2ASH_8 and C_4AH_{13} [65, 68, 70] *Earlier detection (from 3d) with higher temperatures [69]*
1.0	Observed [51, 53, 69, 72] with increase from 1d to 180d [54, 56, 65, 68] and stable up to 1.5y [65] *Observed earlier for higher temperatures [69, 70, 74]*	a) Observed from 1d to approx. 28d [51, 53, 54, 65, 68, 69], later transformation to $C_3AS_yH_z$ and/or $Ca_2Al(OH)_7 \cdot 6.5\ H_2O$ [65, 68] b) Increasing amount from 7 to 360d [53, 206], as it is stable in the absence of CH [71]	Not observed [51, 53, 54, 56, 65, 68, 69, 72] as the amount of CH is too low *Detected with higher temperatures from 21h [70] to 5y [57] with increase up to 34d [70]*
2.0	*MK/CH=1.0: Not observed due to transformation to hydrogarnet [69]* *MK/CH=2.0: Observed [65]*	Not observed [56, 69, 72], but probably lack of data	*Increasing Si content compared to MK/CH=0.5 [65]* *Direct formation at early ages (without the transformation reaction) [55, 74]*

h: hours; d: days; y: years.

Table S1-3: Overview of the analyzed literature regarding phase formations from the reaction of MK, CH and water (studies include the presence of carbonate impurities, but no sulfates) depending on MK/CH, temperature, testing time.

MK/CH	w/s	Temp. in °C	Relative humidity in %	Time	C-S-H	C_4AH_{13}	C_2ASH_8	$C_3AS_yH_z$	$C_4Ac_{0.5}H_{12}$/ C_4AcH_{11}	Ref.	Comments/ MK source
0.05	1.0	23	> 95	1-180d	1-180d	1-28d			x (de)	[68]	Transformation of C_4AH_{13} to $Ca_2Al(OH)_7 \cdot 6.5\ H_2O$; Carbonate source not specified; MK: ARGICAL M1200S from IMERYS (SiO_2 = 54.39 %; Al_2O_3 = 39.36 % [65])
0.05	1.0	23	95	28d-1,5y	28d-1.5y	28d			28d-1.5y	[65]	
0.1	1.0	23	> 95	1-180d	1-180d	1-7d			x (de)	[68]	
0.1	1.0	23	95	28d-1,5y	28d-1.5y	28d			28d-1.5y	[65]	
0.2	1.0	23	> 95	1-90d	1-90d	1-28d			1-28d	[54]	w/s of 1.0 [64]; Carbonate source not specified; MK: ARGICAL M1200S from IMERYS (SiO_2 = 55 %; Al_2O_3 = 39 %)
0.2	1.0	23	> 95	1-180d	1-180d	1-56d			x (de)	[68]	Transformation of C_4AH_{13} to $Ca_2Al(OH)_7 \cdot 6.5\ H_2O$; Carbonate source not specified; MK: ARGICAL M1200S from IMERYS (SiO_2 = 54.39 %; Al_2O_3 = 39.36 % [65])
0.2	1.0	23	95	28d-1,5y	28d-1.5y	28d			28d-1.5y	[65]	
0.3	1.0	23	> 95	1-180d	1-180d	1-7d	1-180d	28-180d	x (de)	[68]	
0.3	1.0	23	95	28d-1,5y	28d-1.5y	28d	28d-1.5y	28d-1.5y (i)	28d-1.5y (de)	[65]	
0.5	1.0	23	> 95	1-180d	1-180d	1-28d	(de)	28-180d	x (de)	[68]	
0.5	0.8	20	98	10-180d	10-180d	10d	1-180d (i)			[69]	Traces not included; Investigated times: 10, 90, 180d MK: Kaolin (SiO_2 = 55.23 %; Al_2O_3 = 41.23 %) heated at 730 °C for 6h
0.5	1.0	25	99	0-270d	0-270d		10-180d		3-270d (de)	[56]	5 % Cc in CH; MK: Metastar 501 of IMERYS Minerals Ltd. (SiO_2 = 51.70 %; Al_2O_3 = 40.60 %)

Table S1-3: Overview of the analyzed literature regarding phase formations from the reaction of MK, CH and water (studies include the presence of carbonate impurities, but no sulfates) depending on MK/CH, temperature, testing time (continued).

MK/CH	w/s	Temp. in °C	Relative humidity in %	Time	C-S-H	C_4AH_{13}	C_2ASH_8	$C_3AS_yH_z$	$C_4Ac_{0.5}H_{12}$/ C_4AcH_{11}	Ref.	Comments/ MK source
0.5	1.0	23	95	28d-1,5y	28d-1.5y	28d	28d-1.5y (de)	28d-1.5y (i)	28d-1.5y (de)	[65]	Transformation of C_4AH_{13} to $Ca_2Al(OH)_7 \cdot 6.5\ H_2O$; Carbonate source not specified; MK: ARGICAL M1200S from IMERYS (SiO_2 = 54.39 %; Al_2O_3 = 39.36 %)
0.5	0.8	55	98	3-90d	3-90d		1-180d (i)	3-90d	x (de)	[69]	Traces not included; Investigated times: 3, 28, 90d; MK: Kaolin (SiO_2 = 55.23 %; Al_2O_3 = 41.23 %) heated at 730 °C for 6h
0.6	1.0	23	> 95	1-180d	1-180d	1-28d	28d-1.5y (de)	28-180d	28d-1.5y (de)	[68]	Transformation of C_4AH_{13} to $Ca_2Al(OH)_7 \cdot 6.5\ H_2O$; Carbonate source not specified; MK: ARGICAL M1200S from IMERYS (SiO_2 = 54.39 %; Al_2O_3 = 39.36 % [65])
0.6	1.0	23	95	28d-1,5y	28d-1.5y	28d	1-90d (i)	28d-1.5y (i)	1-28d	[65]	Transformation of C_4AH_{13} to $Ca_2Al(OH)_7 \cdot 6.5\ H_2O$; Carbonate source not specified; MK: ARGICAL M1200S from IMERYS (SiO_2 = 54.39 %; Al_2O_3 = 39.36 %)
1.0	1.0	23	> 95	1-90d	1-90d	1-28d	1-180d (i)		x (de)	[54]	Carbonate source not specified; MK: ARGICAL M1200S from IMERYS (SiO_2 = 55 %; Al_2O_3 = 39 %)
1.0	1.0	23	> 95	1-180d	1-180d	1-28d	9-360d (i)		23-360d	[68]	Transformation of C_4AH_{13} to $Ca_2Al(OH)_7 \cdot 6.5\ H_2O$; Carbonate source not specified; MK: ARGICAL M1200S from IMERYS (SiO_2 = 54.39 %; Al_2O_3 = 39.36 % [65])

Table S1-3: Overview of the analyzed literature regarding phase formations from the reaction of MK, CH and water (studies include the presence of carbonate impurities, but no sulfates) depending on MK/CH, temperature, testing time (continued).

MK/CH	w/s	Temp. in °C	Relative humidity in %	Time	C-S-H	C_4AH_{13}	C_2ASH_8	$C_3AS_yH_z$	$C_4Ac_{0.5}H_{12}$/ C_4AcH_{11}	Ref.	Comments/ MK source
1.0	2.37	20	100	2h-360d	2-360d	9-360d (i)	3-28d			[53]	Carbonate source not specified; MK: SiO_2 = 51.60 %; Al_2O_3 = 41.30 % (XRD shows the low crystalline nature with low-intensity peaks corresponding to quartz and mica (muscovite))
1.0	0.75	20	Not specified.	3-28d	3-28d	7-28d	28d-1.5y (de)		28d-1.5y (de)	[51]	MK: Kaolin with 97 – 98 % kaolinite heated at 730 °C for 6h
1.0	1.0	25	99	0-270d	0-270d (i-28d; de)		3-270d (i)		3-14d	[56]	5 % Cc in CH; MK: Metastar 501 of IMERYS Minerals Ltd. (SiO_2 = 51.70 %; Al_2O_3 = 40.60 %)
1.0	0.8	20	98	10-180d	10-180d	10d	10-180d			[69]	Traces not included; Investigated times: 3, 28, 90d; MK: Kaolin (SiO_2 = 55.23 %; Al_2O_3 = 41.23 %) heated at 730 °C for 6h
1.0	2.25	20	Not specified.	1-120d	1-120d (i)	7-120d (i)	7-120d (i)			[206]	MK: Kaolin (from SIGMA–ALDRICH Company; SiO_2 = 45.06 %; Al_2O_3 = 39.87 %) heated for 1h at 800 °C
1.0	1.0	22	100	28-180d	(28-180d)		28-180d		28-180d (de)	[72]	Formation of $Ca_2Al(OH)_7 \cdot 3\ H_2O$; Investigated times: 28, 90 and 180d; Traces of Cc in CH and possibly exposure to atmospheric CO_2; MK: Kaolin production wastes heated at 700 °C for 2h (MK: SiO_2 = 54.44 %; Al_2O_3 = 41.82 %)

Table S1-3: Overview of the analyzed literature regarding phase formations from the reaction of MK, CH and water (studies include the presence of carbonate impurities, but no sulfates) depending on MK/CH, temperature, testing time (continued).

MK/CH	w/s	Temp. in °C	Relative humidity in %	Time	C-S-H	C_4AH_{13}	C_2ASH_8	$C_3AS_yH_z$	$C_4Ac_{0.5}H_{12}$/ C_4AcH_{11}	Ref.	Comments/ MK source
1.0	1.0	22	65	28-180d	(28-180d)				28-180d (de)	[72]	Formation of $Ca_2Al(OH)_7 \cdot 3 H_2O$; Investigated times: 28, 90 and 180d Traces of Cc in CH and possibly exposure to atmospheric CO_2; MK: Kaolin production wastes heated at 700 °C for 2h (MK: SiO_2 = 54.44 %; Al_2O_3 = 41.82 %)
1.0	1.0	23	95	28d-1.5y	28d-1.5y	28d	28d-1.5y (i-180d)		28d-1.5y (de)	[65]	Transformation of C_4AH_{13} to $Ca_2Al(OH)_7 \cdot 6.5 H_2O$; Carbonate source not specified; MK: ARGICAL M1200S from IMERYS (SiO_2 = 54.39 %; Al_2O_3 = 39.36 %)
1.0	1.0	25	-	0-50h	10-50h		10-180d			[107]	Solution with 0.1 M NaOH and 0.5 M KOH; 3.5 % Cc in CH; MK: PowerPozz w, Temcom Solutions GmbH (SiO_2 = 54.5 %; Al_2O_3 = 40.2 %)
1.0	0.8	40	98	3h-180d	1-180d	6h-90d	1-28d	10-180d		[59]	Traces not included; MK: Kaolin (SiO_2 = 56.23 %; Al_2O_3 = 42.91 %) heated at 730 °C for 6h; XRD disclosed the presence of feldspar and muscovite-like impurities
1.0	0.8	40	98	3h-180d	6h-180d	3h-28d		10-180d		[59]	Traces not included 0.5 M NaOH solution; MK: Kaolin (SiO_2 = 56.23 %; Al_2O_3 = 42.91 %) heated at 730 °C for 6h; XRD disclosed the presence of feldspar and muscovite-like impurities

Table S1-3: Overview of the analyzed literature regarding phase formations from the reaction of MK, CH and water (studies include the presence of carbonate impurities, but no sulfates) depending on MK/CH, temperature, testing time (continued).

MK/CH	w/s	Temp. in °C	Relative humidity in %	Time	C-S-H	C_4AH_{13}	C_2ASH_8	$C_3AS_yH_z$	$C_4Ac_{0.5}H_{12}$/ C_4AcH_{11}	Ref.	Comments/ MK source
1.0	0.8	55	98	3-90d	3-90d	3d		3-90d		[69]	Traces not included; Investigated times: 3, 28, 90d; MK: Kaolin (SiO_2 = 55.23 %; Al_2O_3 = 41.23 %) heated at 730 °C for 6h
1.0	2.37	60	Sealed in water bath.	0-9d	6h-9d (i)	12h-9d (i)	12h-9d (i)	30h-9d (i)		[74]	MK: SiO_2 = 51.60 %; Al_2O_3 = 41.30 %
1.0	2.37	60	Sealed in water bath.	0-123d	6h-123d	6h-123d	6h-123d	21h-123d (i-34d)	(x)	[70]	Carbonate source not specified; MK: SiO_2 = 51.60 %; Al_2O_3 = 41.30 % (XRD shows the low crystalline nature with low-intensity peaks corresponding to quartz and mica (muscovite))
1.0	2.37	60	Sealed in water bath.	5y	5y	(5y)	5y	5y		[57]	Presence of vertumnite MK: SiO_2 = 51.6 %; Al_2O_3 = 41.6 %
2.0	1.0	25	99	0-270d	0-270d (i-28d; de)		3-270d (i)		3-14d	[56]	5 % Cc in CH; MK: Metastar 501 of IMERYS Minerals Ltd. (SiO_2 = 51.70 %; Al_2O_3 = 40.60 %)
2.0	0.8	20	98	10-180d	10-180d		10-180d			[69]	Traces not included; Investigated times: 10, 90, 180d
2.0	1.0	22	100	28-180d	(28-180d)		28-180d		28-180d (de)	[72]	Formation of $Ca_2Al(OH)_7 \cdot 3 H_2O$; Investigated times: 28, 90 and 180d; Traces of Cc in CH and possibly exposure to atmospheric CO_2
2.0	1.0	22	65	28-180d	(28-180d)				28-180d (de)	[72]	Formation of $Ca_2Al(OH)_7 \cdot 3 H_2O$; Investigated times: 28, 90 and 180d; Traces of Cc in CH and possibly exposure to atmospheric CO_2

Table S1-3: Overview of the analyzed literature regarding phase formations from the reaction of MK, CH and water (studies include the presence of carbonate impurities, but no sulfates) depending on MK/CH, temperature, testing time (continued).

MK/CH	w/s	Temp. in °C	Relative humidity in %	Time	C-S-H	C_4AH_{13}	C_2ASH_8	$C_3AS_yH_z$	$C_4Ac_{0.5}H_{12}$/ C_4AcH_{11}	Ref.	Comments/ MK source
2.0	0.8	55	98	3-90d	3-90d		3-90d	3-90d		[69]	Traces not included; Investigated times: 3, 28, 90d; MK: Kaolin (SiO_2 = 55.23 %; Al_2O_3 = 41.23 %) heated at 730 °C for 6h
4.0	0.8	20	98	10-180d	10-180d		10-180d			[69]	Traces not included; Investigated times: 10, 90, 180d Corrected to MK:CH=1:0.75 (molar ratios); MK: Kaolin (SiO_2 = 55.23 %; Al_2O_3 = 41.23 %) heated at 730 °C for 6h
4.0	0.8	55	98	3-90d	3-90d	3-28d	3-90d			[69]	Traces not included; Investigated times: 3, 28, 90d; Corrected to MK:CH=1:0.75 (molar ratios); MK: Kaolin (SiO_2 = 55.23 %; Al_2O_3 = 41.23 %) heated at 730 °C for 6h
7.6	0.8	20	98	10-180d	10-180d	10d	90-180d			[69]	Traces not included; Investigated times: 10, 90, 180d; MK: Kaolin (SiO_2 = 55.23 %; Al_2O_3 = 41.23 %) heated at 730 °C for 6h
7.6	0.8	55	98	3-90d	3-90d		3-90d			[69]	Traces not included; Investigated times: 3, 28, 90d; MK: Kaolin (SiO_2 = 55.23 %; Al_2O_3 = 41.23 %) heated at 730 °C for 6h

h: hours; d: days; y: years; i: increasing; de: decreasing; (): not clearly detected.

Table S1-4: Summary of MK specifications from Table S1-2.

MK source	Name of product/ Calcination program	SiO_2	Al_2O_3	SiO_2 + Al_2O_3	SiO_2/ Al_2O_3	References
Commercial MK used	ARGICAL M1200S from IMERYS	55	39	94	1.41	[54]
	ARGICAL M1200S from IMERYS	54.39	39.36	93.75	1.38	[65]
	Metastar 501 from IMERYS	51.7	40.6	92.3	1.27	[56]
	PowerPozz w from Temcom Solutions GmbH	54.5	40.2	94.7	1.36	[107]
	Not provided.	51.6	41.3	92.9	1.25	[53, 70, 74]
	Not provided.	51.6	41.6	93.2	1.24	[57]
Kaolin calcined	730 °C; 6h	55.23	41.23	(96.46)	1.34	[69]
	730 °C; 6h	56.23	42.91	(99.14)	1.31	[59]
	800 °C; 1h	45.06	39.87	(84.93)	1.13	[206]

h: hours.

8.2 Publication 2

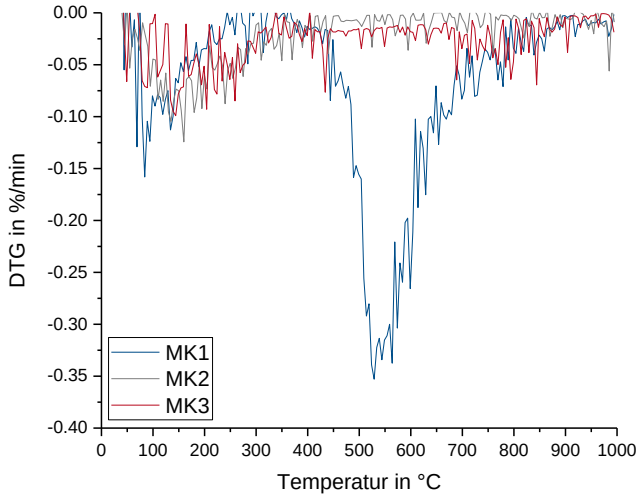

Figure S2-1: DTG-curves of the three different metakaolin (MK1, MK2 and MK3)

8.3 Publication 4

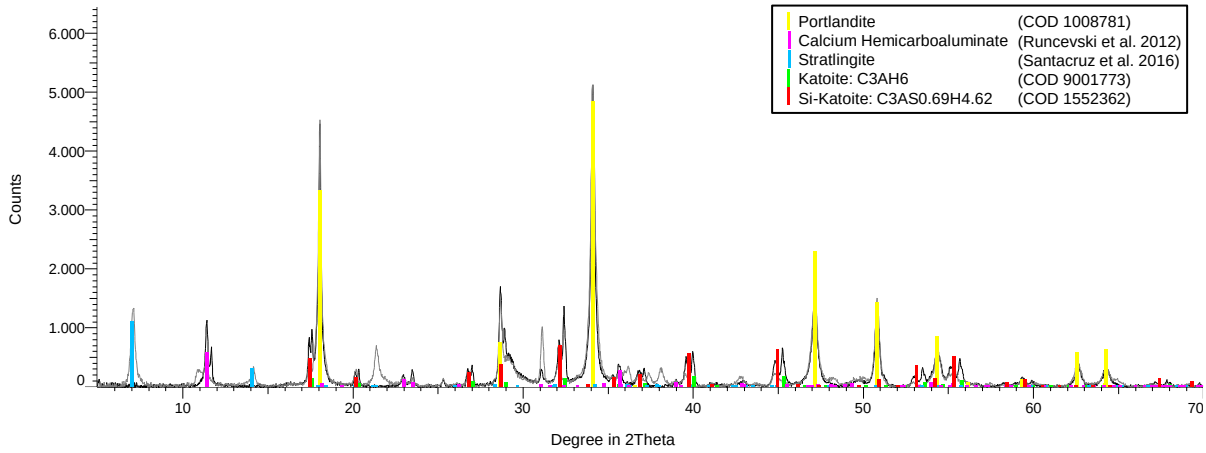

Figure S4-1: Phases used in quantitative XRD analysis exemplarily shown for 0.33MK_1.28NaOH_2d (grey) and 0.33MK_1.28NaOH_245d (black).

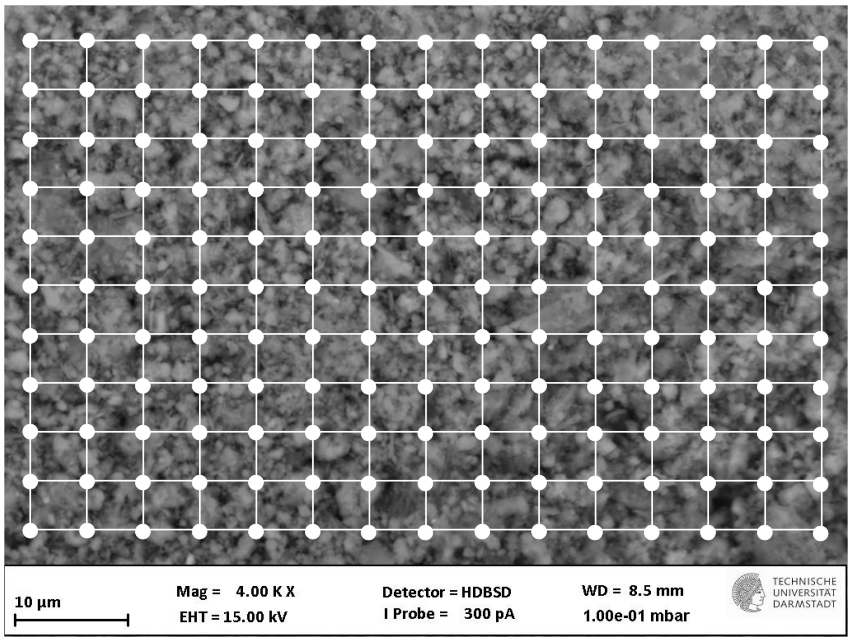

Figure S4-2: Mesh for EDX point analysis, exemplarily shown for one area of 0.33MK_0K_2d (10 x 14 points = 140 points per measuring area).

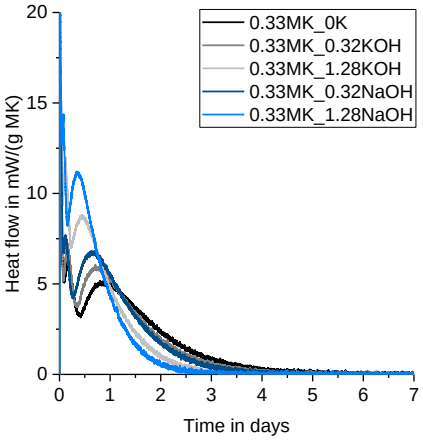

Figure S4-3: Results from isothermal calorimetry measurements at 40 °C of all samples with MK/CH of 0.33 without added sulfates up to 7 days of reaction.

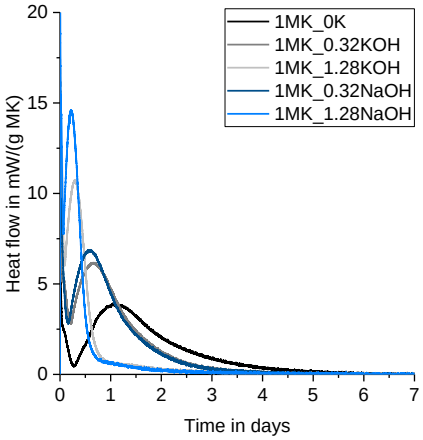

Figure S4-4: Results from isothermal calorimetry measurements at 40 °C of all samples with MK/CH of 1.0 without added sulfates up to 7 days of reaction.

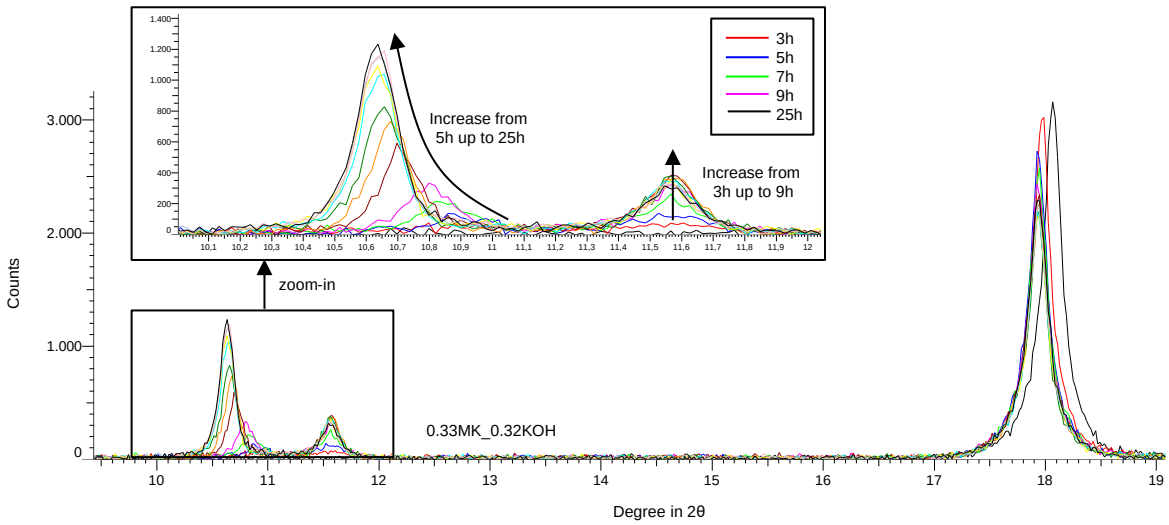

Figure S4-5: In-situ XRD results shown for 0.33MK_0.32KOH from 1h up to 25h (data shown for every two hours); peaks related to C_4AH_{13}.

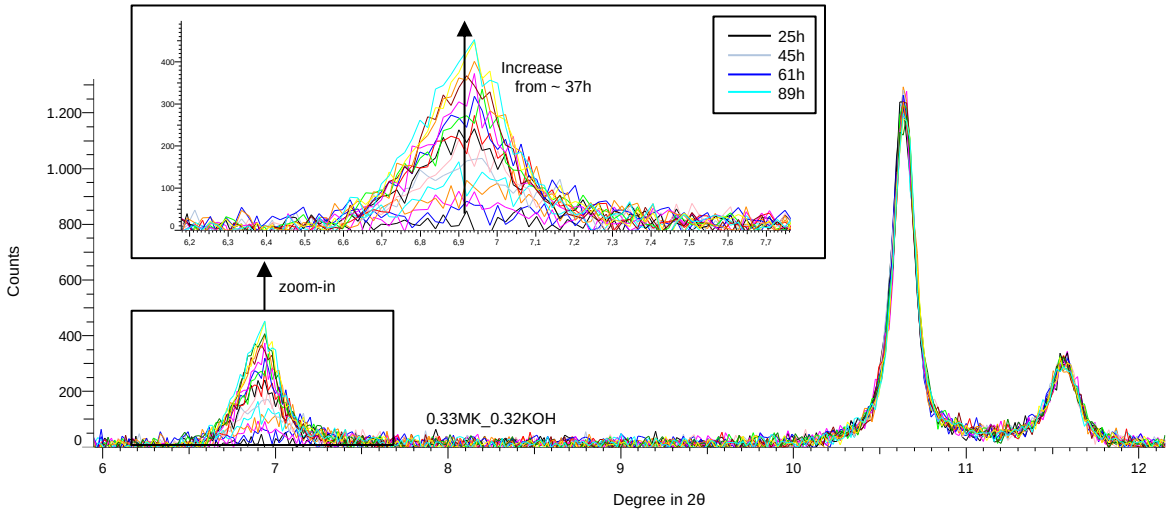

Figure S4-6: In-situ XRD results shown for 0.33MK_0.32KOH from 25h up to 89h (data shown for every four hours); peak related to C_2ASH_8.

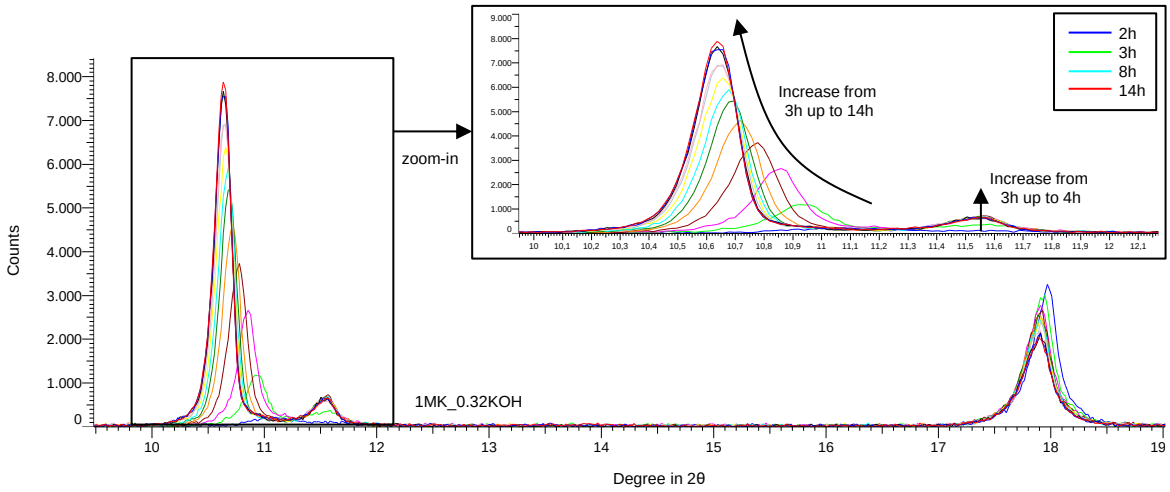

Figure S4-7: In-situ XRD results shown for 1MK_0.32KOH from 2h up to 14h (data shown for every hour); peak related to C_4AH_{13}.

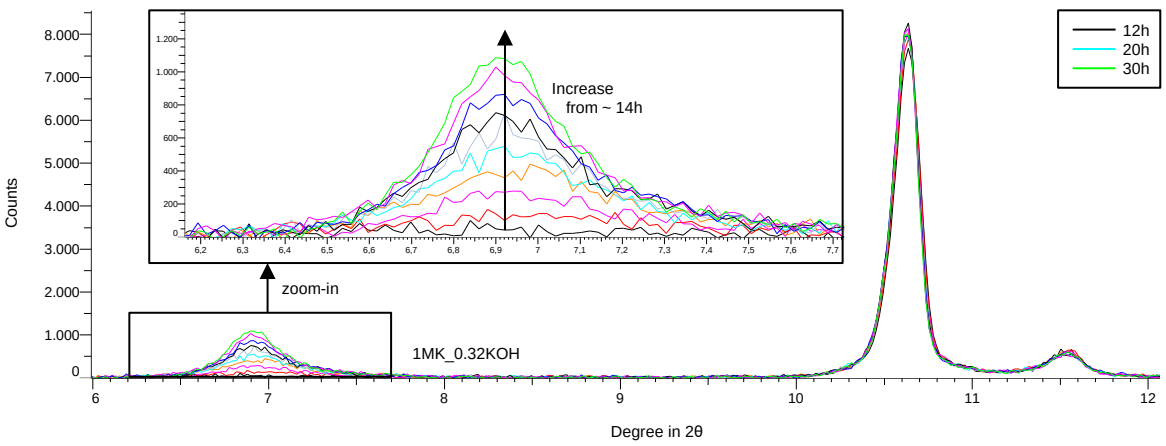

Figure S4-8: In-situ XRD results shown for 1MK_0.32KOH from 12h up to 30h (data shown for every two hours); peak related to C_2ASH_8.

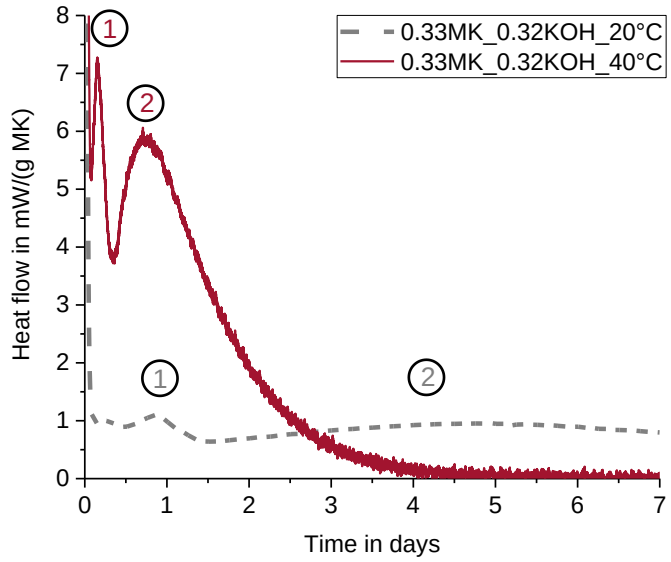

Figure S4-9: Isothermal calorimetry results shown for 0.33MK_0.32KOH at 20 °C and 40 °C; peak 1 related to C_4AH_{13} and peak 2 to C_2ASH_8 formation.

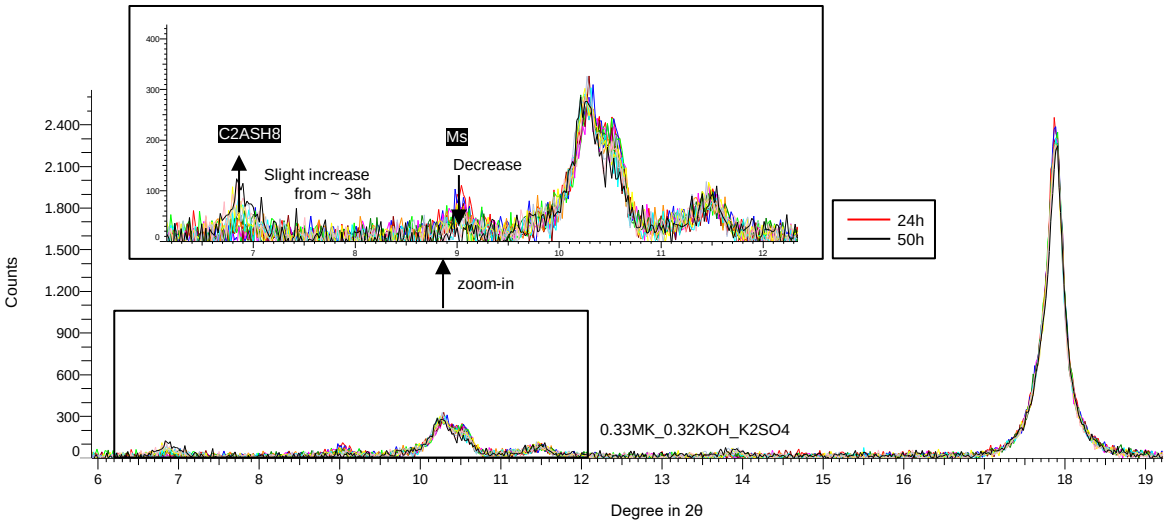

Figure S4-10: In-situ XRD results shown for 0.33MK_0.32KOH_K2SO4 from 24h up to 50h (data shown for every two hours up to 44 h and additionally one measurement after 50 h).

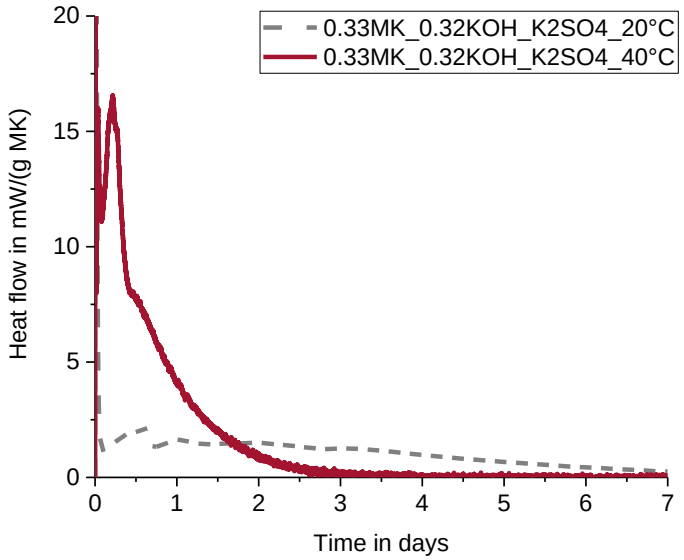

Figure S4-11: Isothermal calorimetry results shown for 0.33MK_0.32KOH_K2SO4 at 20 °C and 40 °C up to 7 days.

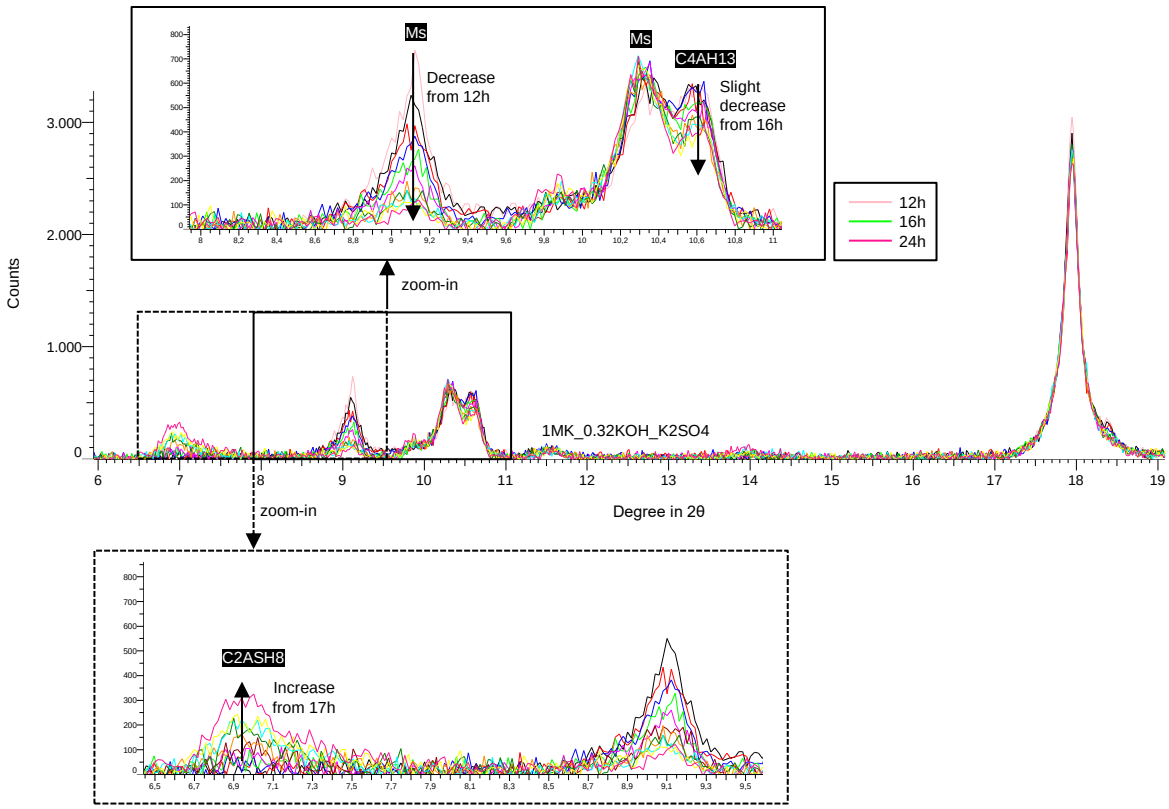

Figure S4-12: In-situ XRD results shown for 1MK_0.32KOH_K2SO4 from 12h up to 24h (data shown for every hour).

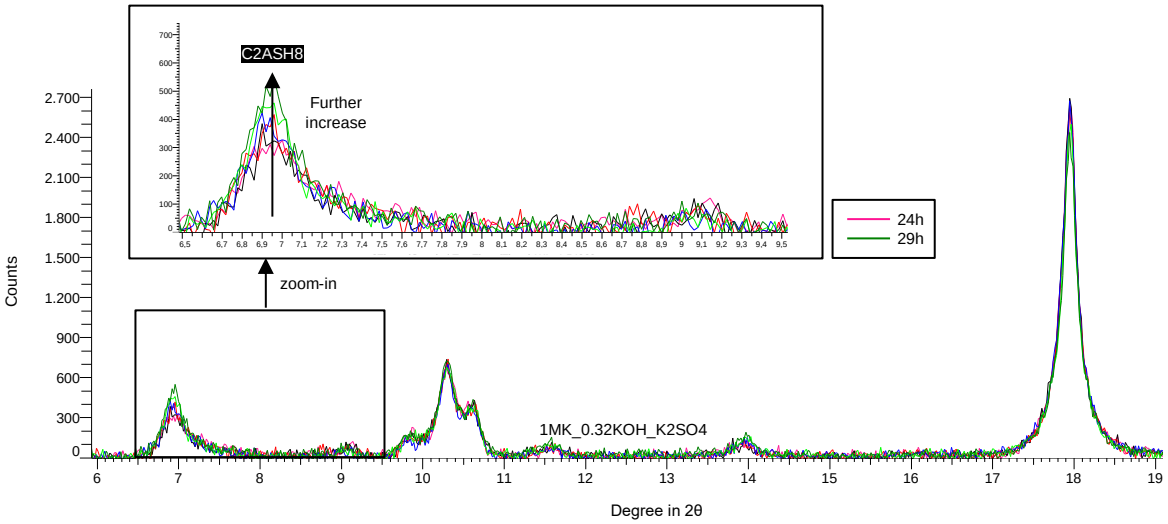

Figure S4-13: In-situ XRD results shown for 1MK_0.32KOH_K2SO4 from 24h up to 29h (data shown for every hour).

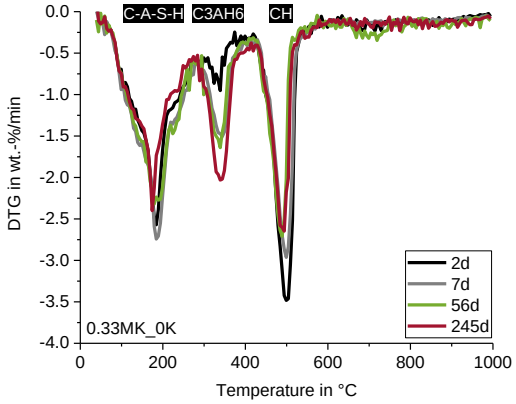

Figure S4-14: DTG-curves of sample 0.33MK_0K with reaction time.

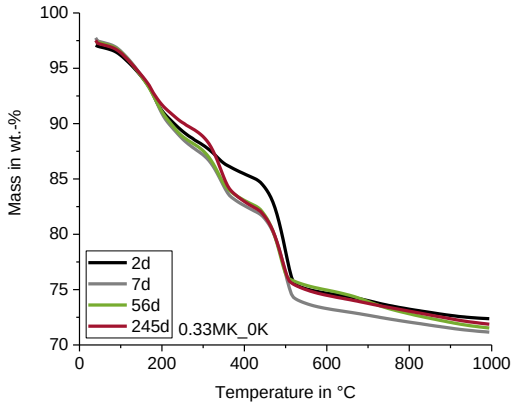

Figure S4-15: TG-curves of 0.33MK_0K with time cured at 40 °C.

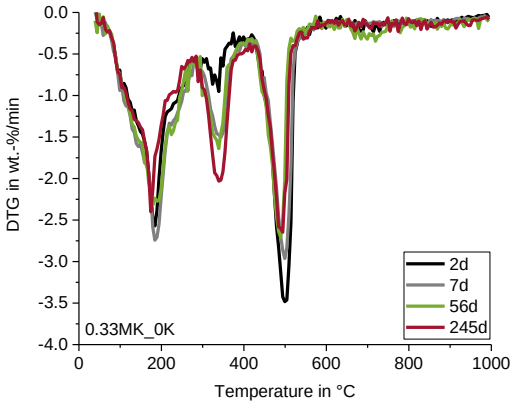

Figure S4-16: DTG-curves of 0.33MK_0K with time cured at 40 °C.

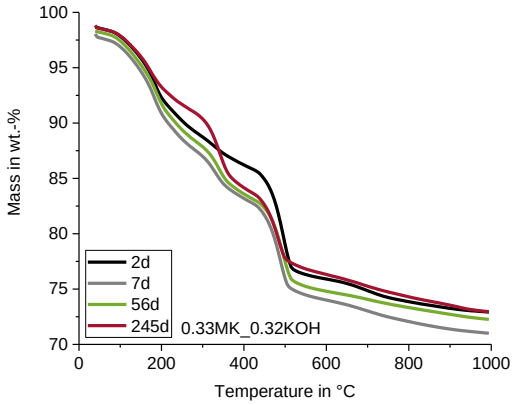

Figure S4-17: TG-curves of 0.33MK_0.32KOH with time cured at 40 °C.

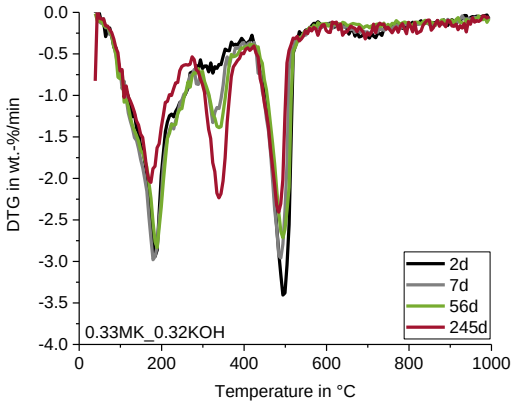

Figure S4-18: DTG-curves of 0.33MK_0.32KOH with time cured at 40 °C.

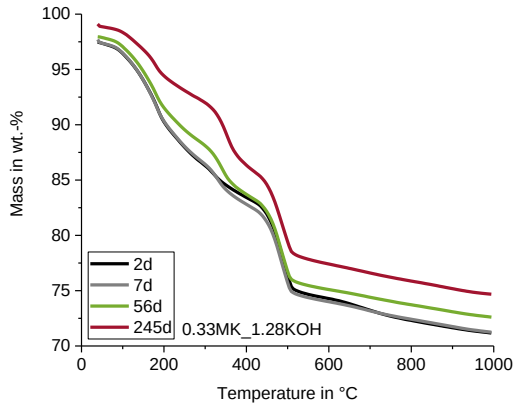

Figure S4-19: TG-curves of 0.33MK_1.28KOH with time cured at 40 °C.

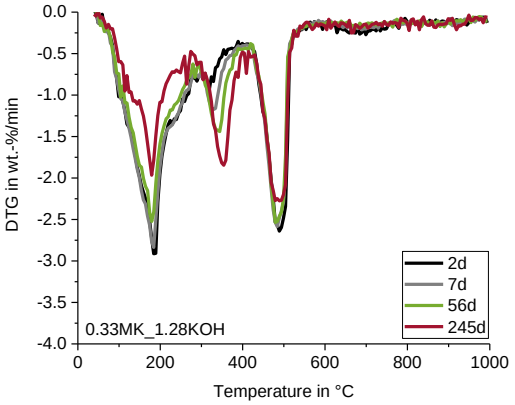

Figure S4-20: DTG-curves of 0.33MK_1.28KOH with time cured at 40 °C.

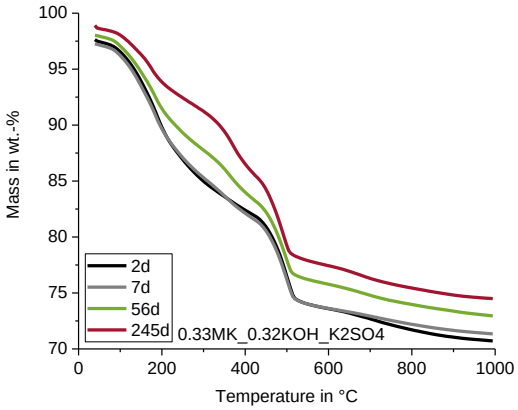

Figure S4-21: TG-curves of 0.33MK_0.32KOH_K2SO4 with time cured at 40 °C.

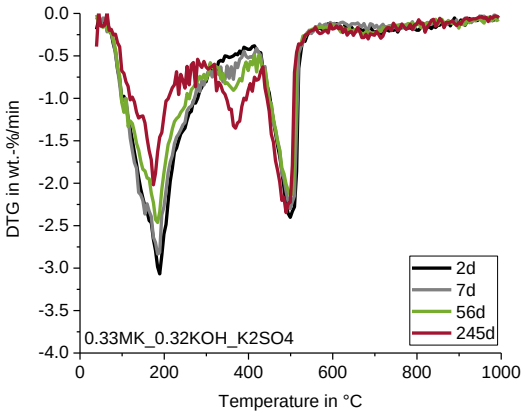

Figure S4-22: DTG-curves of 0.33MK_0.32KOH_K2SO4 with time cured at 40 °C.

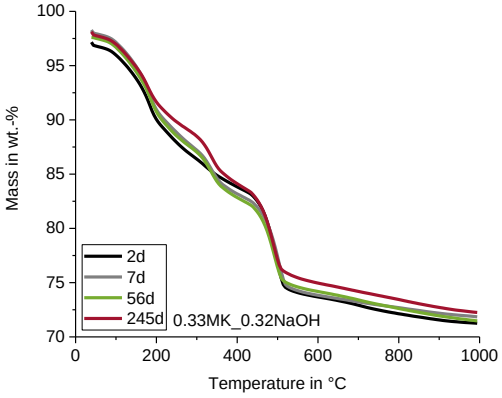

Figure S4-23: TG-curves of 0.33MK_0.32NaOH with time cured at 40 °C.

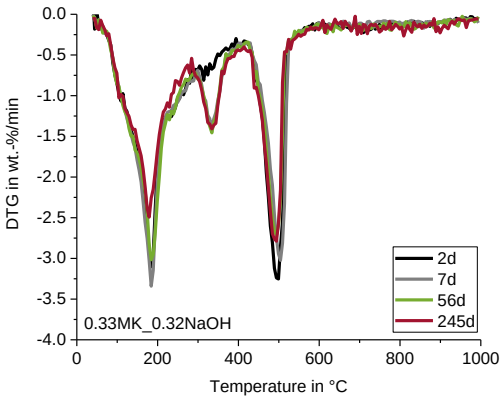

Figure S4-24: DTG-curves of 0.33MK_0.32NaOH with time cured at 40 °C.

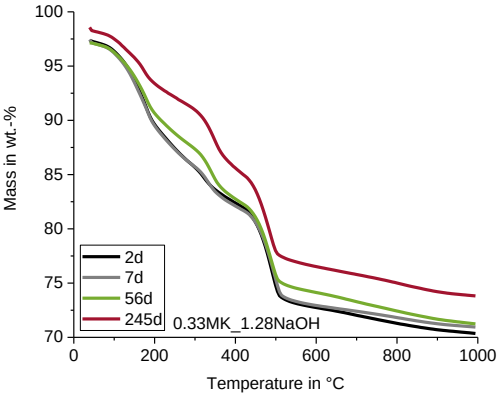

Figure S4-25: TG-curves of 0.33MK_1.28NaOH with time cured at 40 °C.

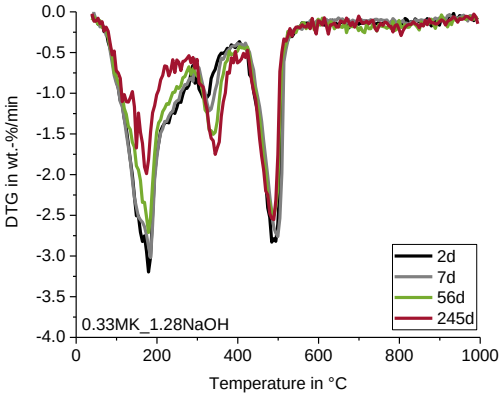

Figure S4-26: DTG-curves of 0.33MK_1.28NaOH with time cured at 40 °C.

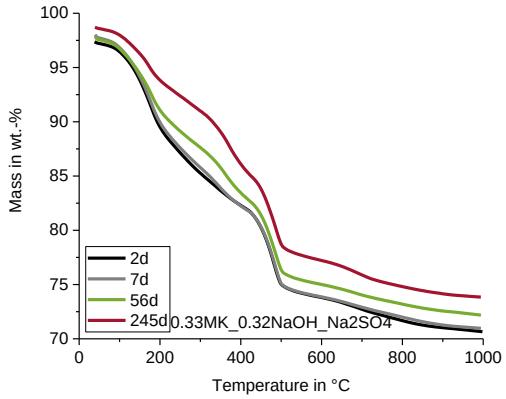

Figure S4-27: TG-curves of 0.33MK_0.32NaOH_Na2SO4 with time cured at 40 °C.

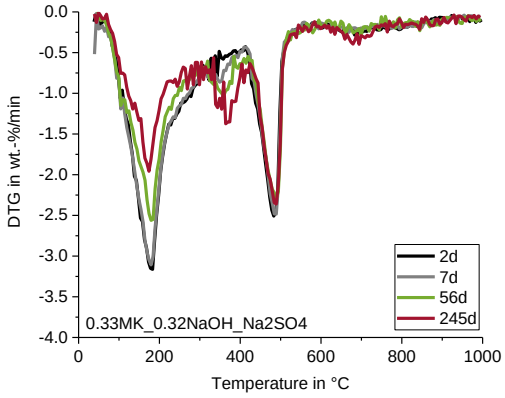

Figure S4-28: DTG-curves of 0.33MK_0.32NaOH_Na2SO4 with time cured at 40 °C.

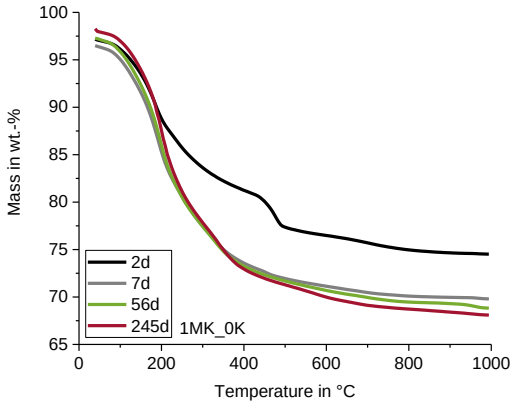

Figure S4-29: TG-curves of 1MK_0K with time cured at 40 °C.

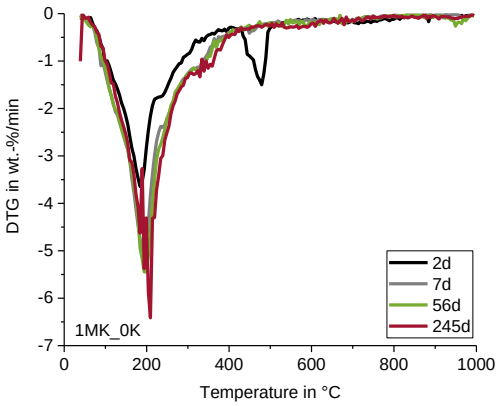

Figure S4-30: DTG-curves of 1MK_0K with time cured at 40 °C.

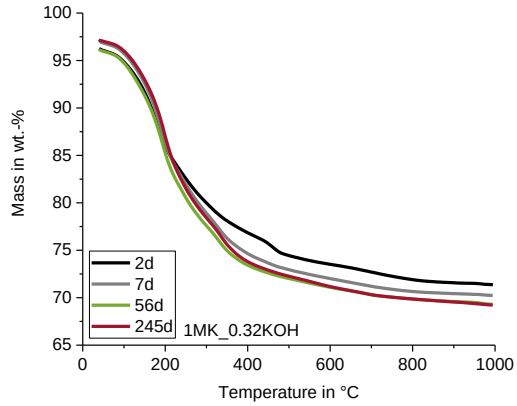

Figure S4-31: TG-curves of 1MK_0.32KOH with time cured at 40 °C.

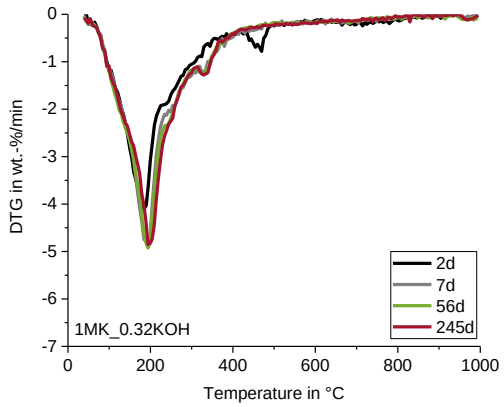

Figure S4-32: DTG-curves of 1MK_0.32KOH with time cured at 40 °C.

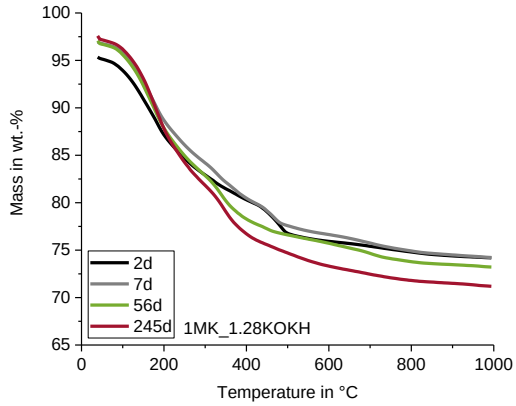

Figure S4-33: TG-curves of 1MK_1.28KOH with time cured at 40 °C.

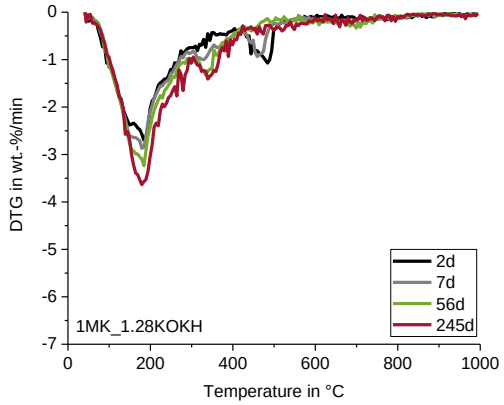

Figure S4-34: DTG-curves of 1MK_1.28KOH with time cured at 40 °C.

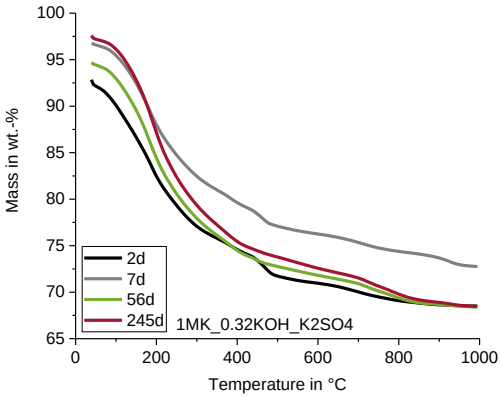

Figure S4-35: TG-curves of 1MK_0.32KOH_K2SO4 with time cured at 40 °C.

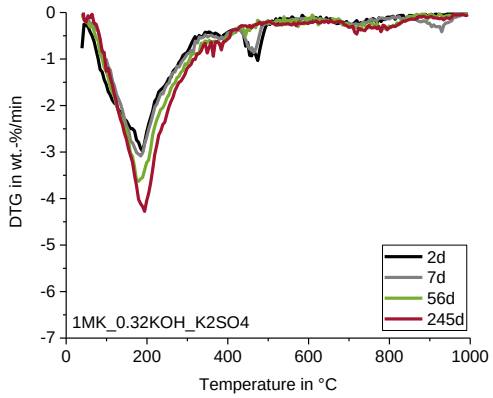

Figure S4-36: DTG-curves of 1MK_0.32KOH_K2SO4 with time cured at 40 °C.

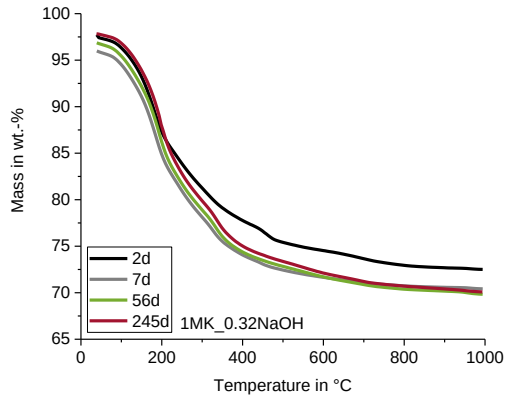

Figure S4-37: TG-curves of 1MK_0.32NaOH with time cured at 40 °C.

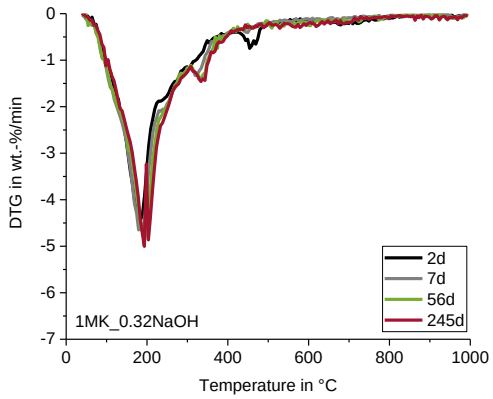

Figure S4-38: DTG-curves of 1MK_0.32NaOH with time cured at 40 °C.

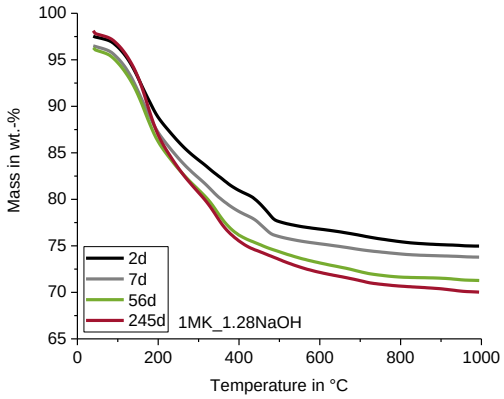

Figure S4-39: TG-curves of 1MK_1.28NaOH with time cured at 40 °C.

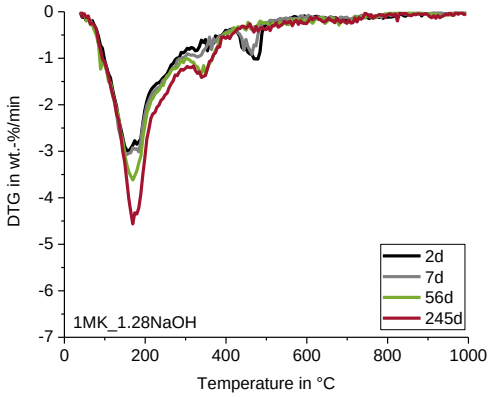

Figure S4-40: DTG-curves of 1MK_1.28NaOH with time cured at 40 °C.

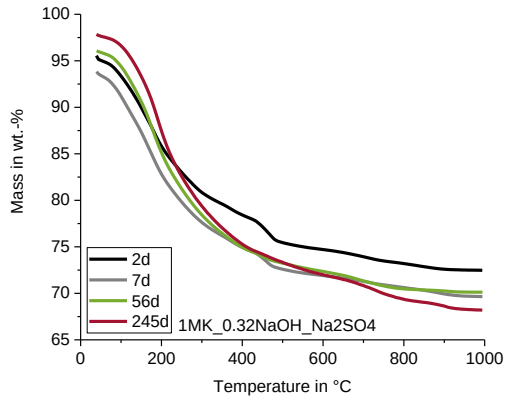

Figure S4-41: TG-curves of 1MK_0.32NaOH_Na2SO4 with time cured at 40 °C.

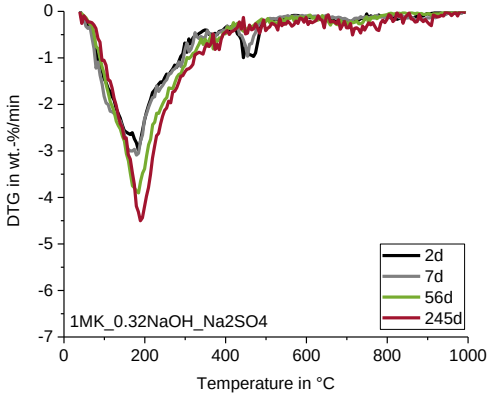

Figure S4-42: DTG-curves of 1MK_0.32NaOH_Na2SO4 with time cured at 40 °C.

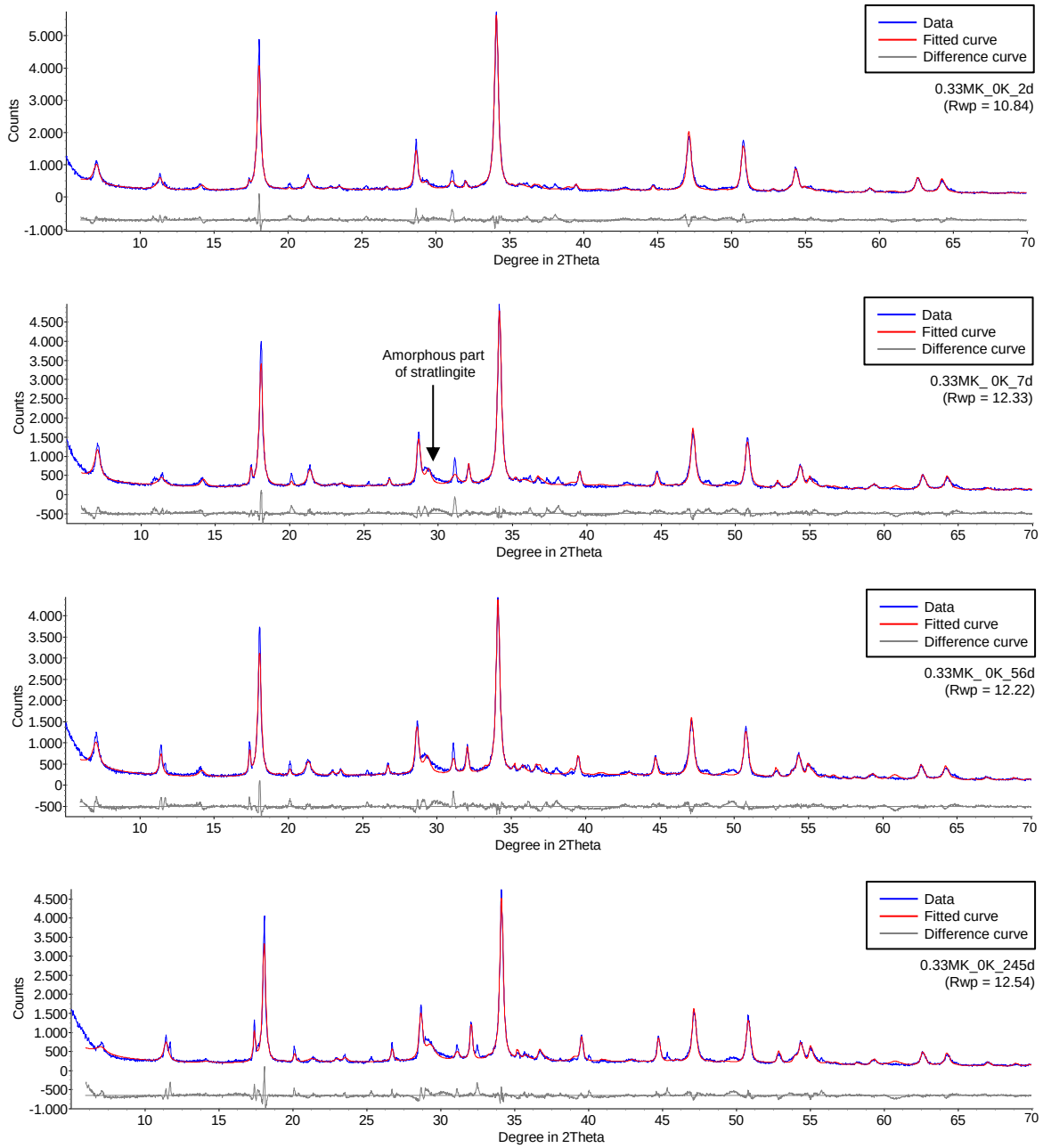

Figure S4-43: qXRD results shown for 0.33MK_0K after 2, 7, 56 and 245 days; amorphous part of stratlingite is indicated.

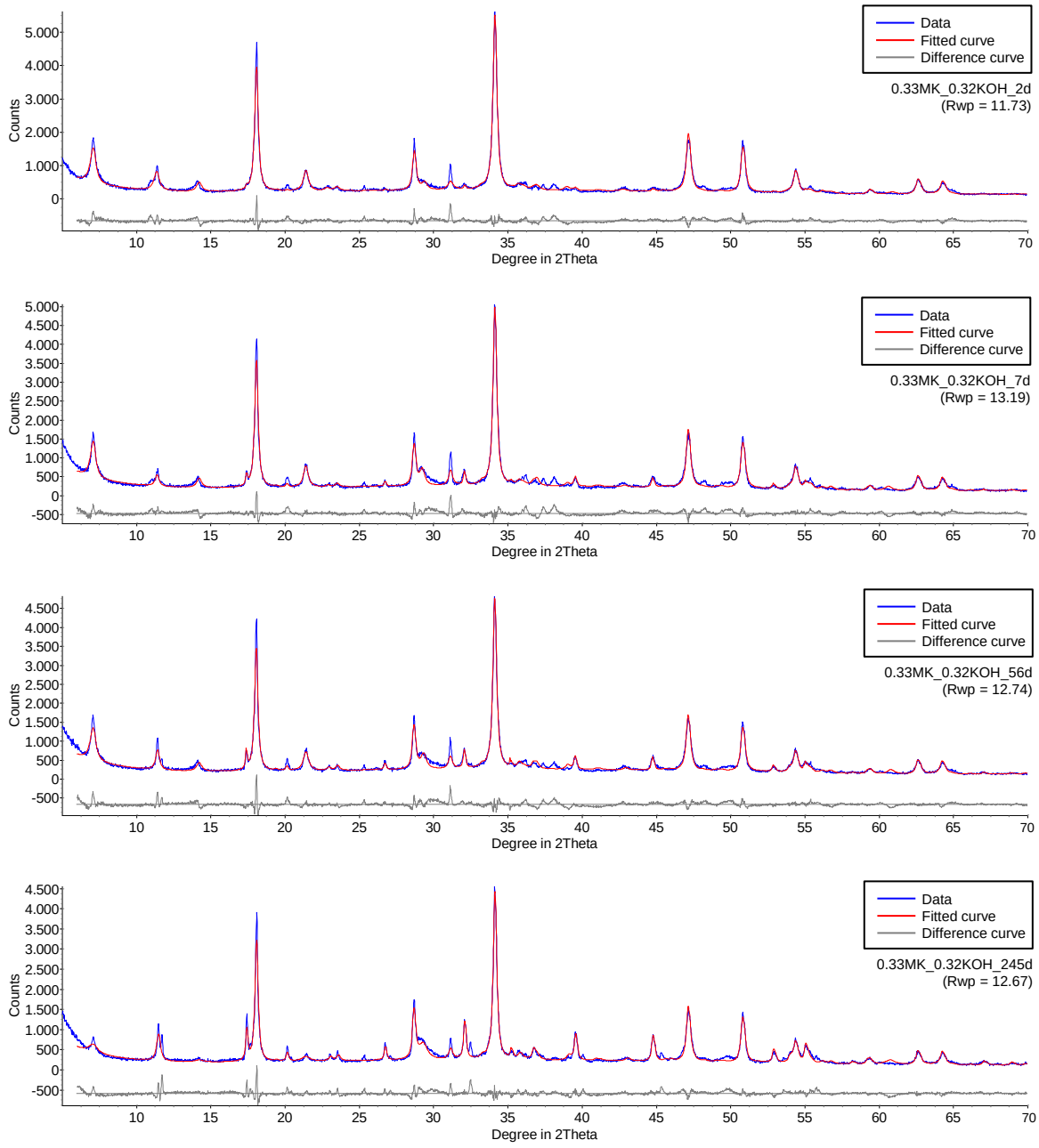

Figure S4-44: qXRD results shown for 0.33MK_0.32KOH after 2, 7, 56 and 245 days.

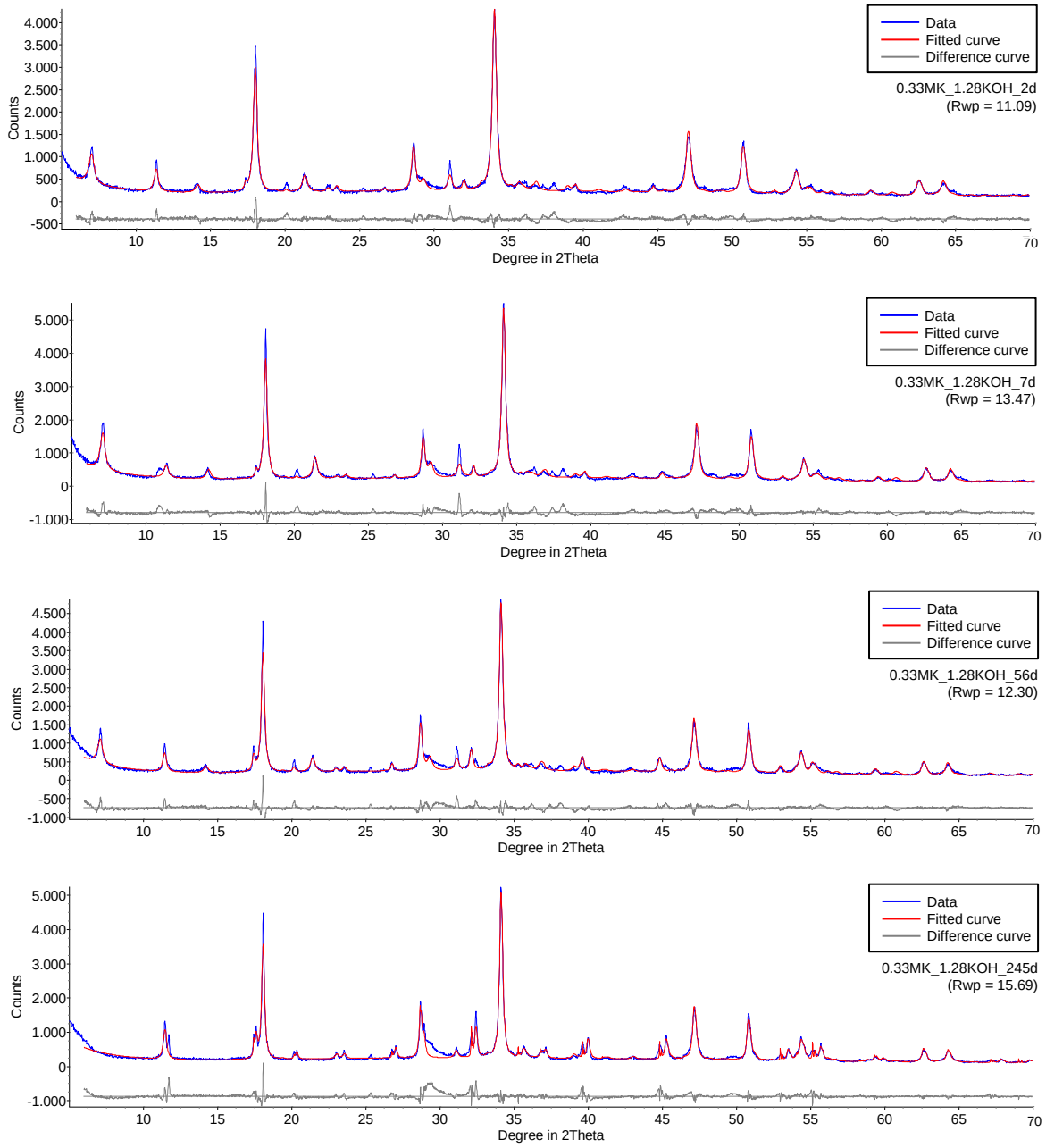

Figure S4-45: qXRD results shown for 0.33MK_1.28KOH after 2, 7, 56 and 245 days.

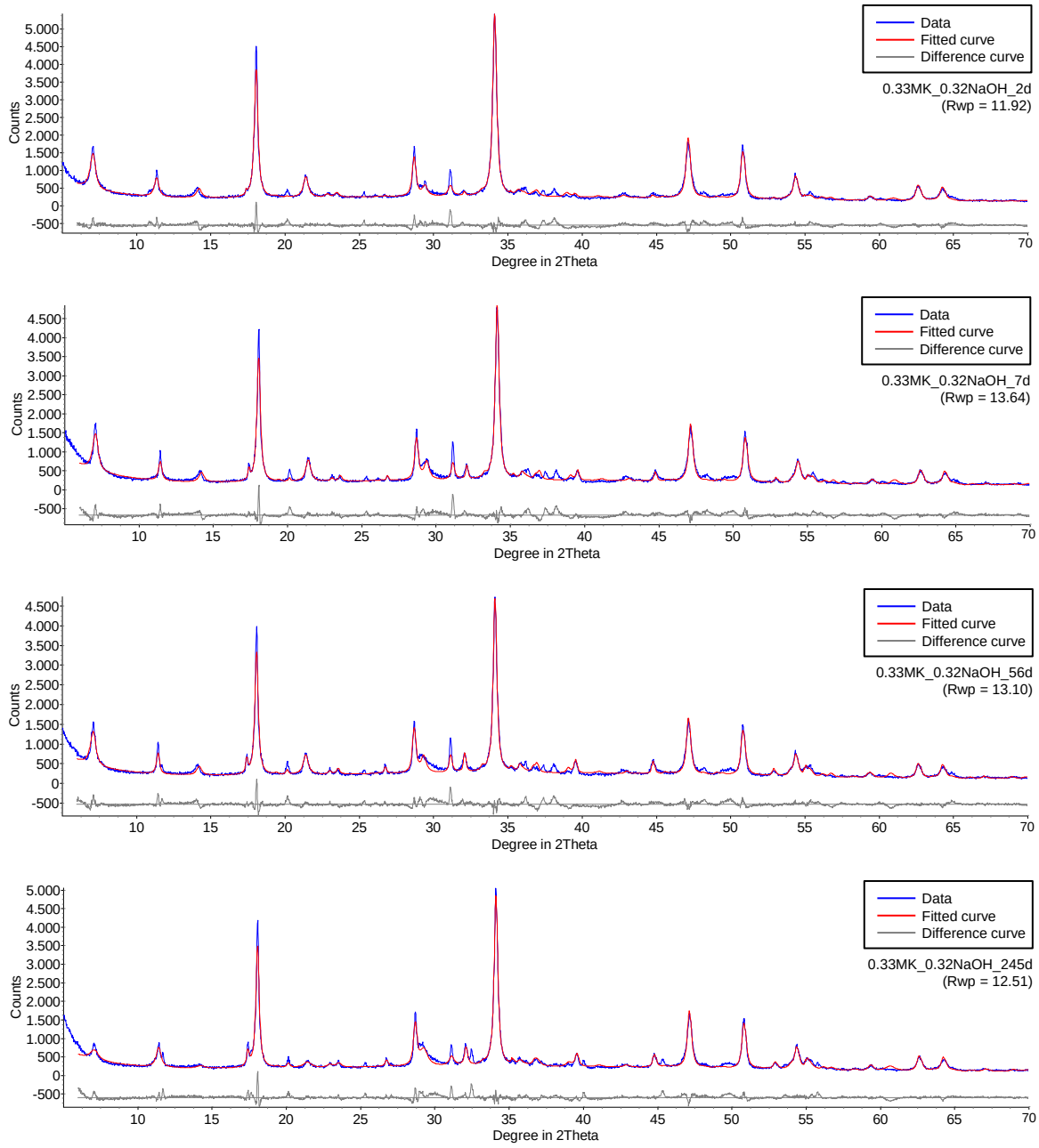

Figure S4-46: qXRD results shown for 0.33MK_0.32NaOH after 2, 7, 56 and 245 days.

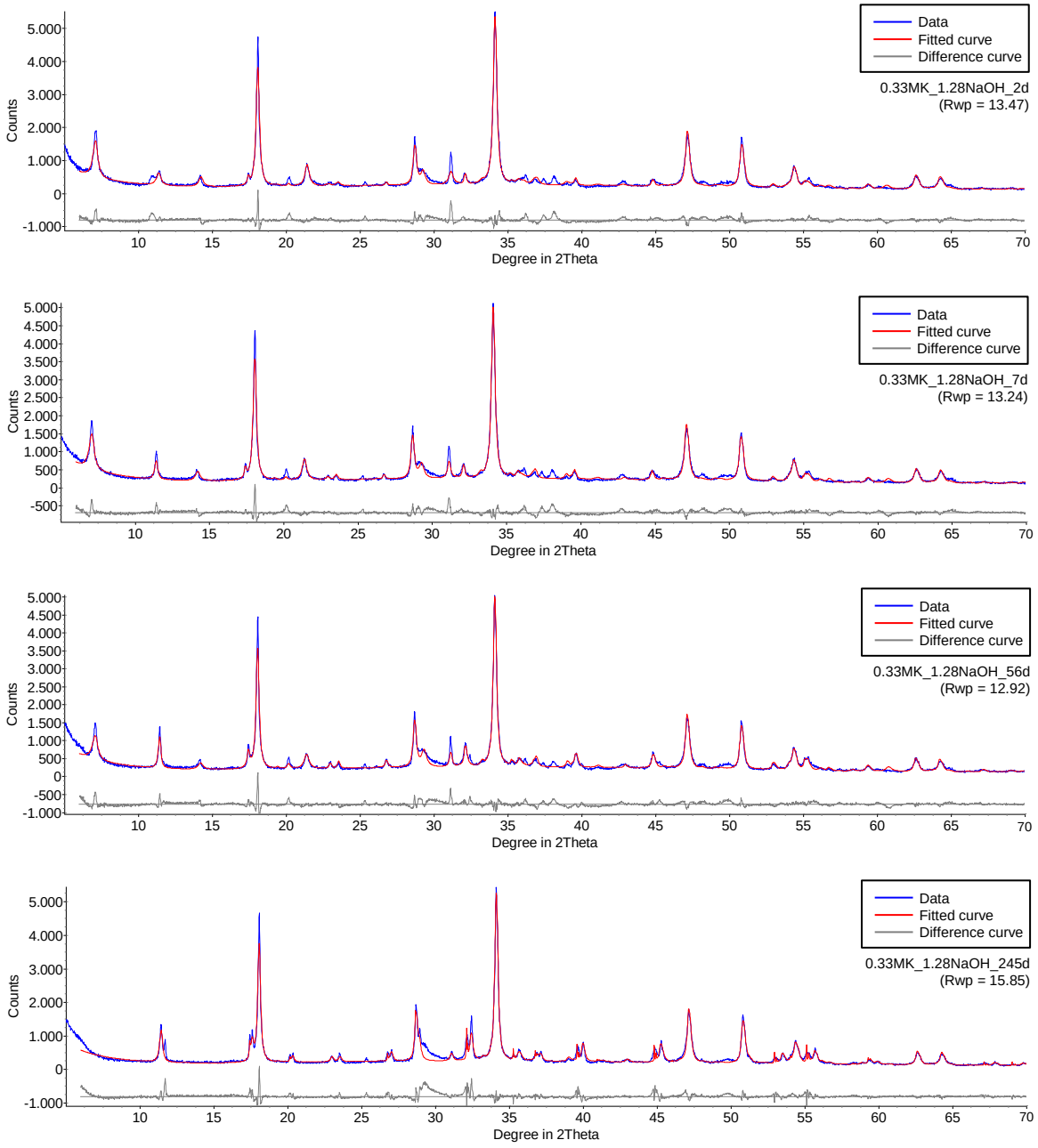

Figure S4-47: qXRD results shown for 0.33MK_1.28NaOH after 2, 7, 56 and 245 days.

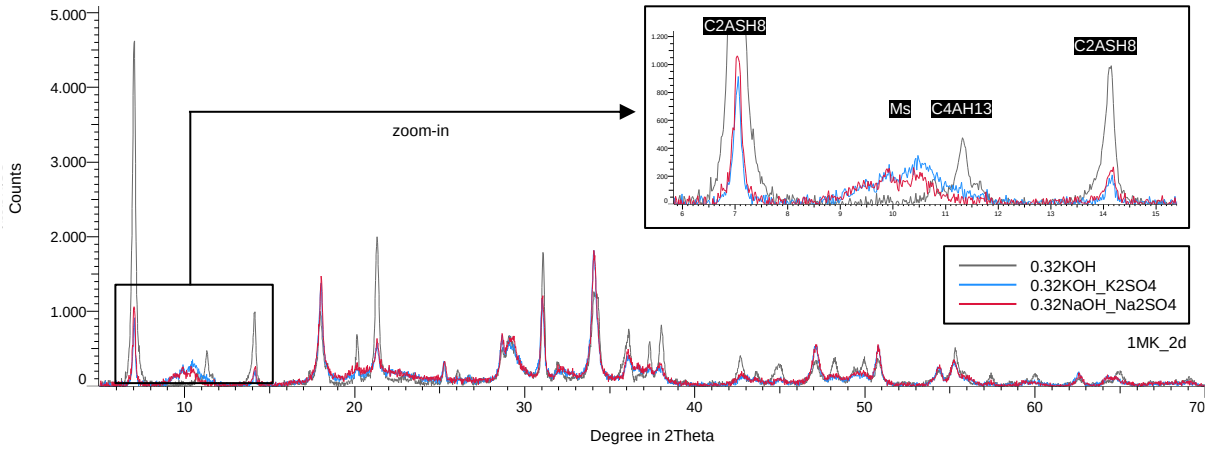

Figure S4-48: Qualitative XRD results for the samples 1MK_0.32KOH, 1MK_0.32KOH_K2SO4 and 1MK_0.32NaOH_Na2SO4 after a reaction time of two days at 40 °C.

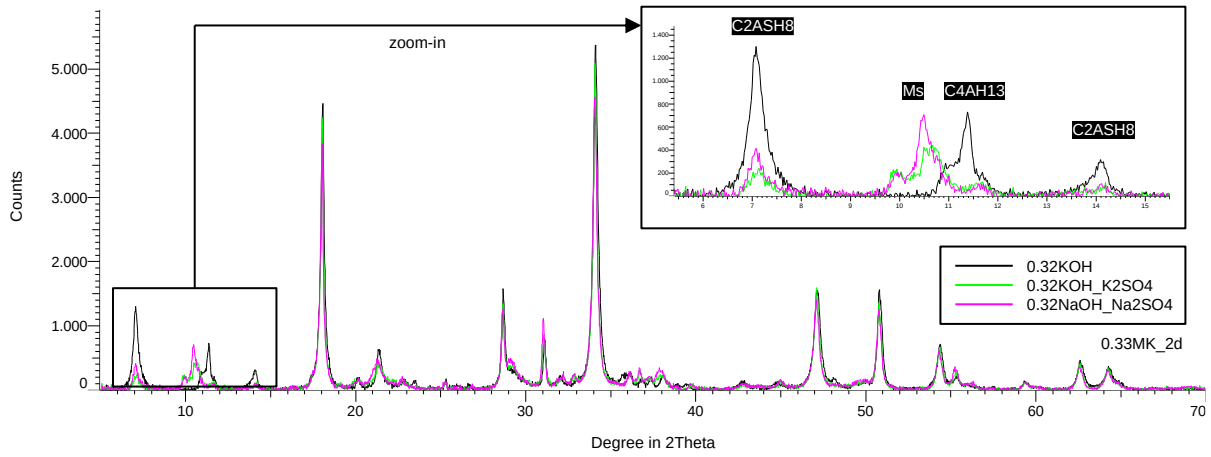

Figure S4-49: Qualitative XRD results for the samples 0.33MK_0.32KOH, 0.33MK_0.32KOH_K2SO4 and 0.33MK_0.32NaOH_Na2SO4 after a reaction time of two days at 40 °C.

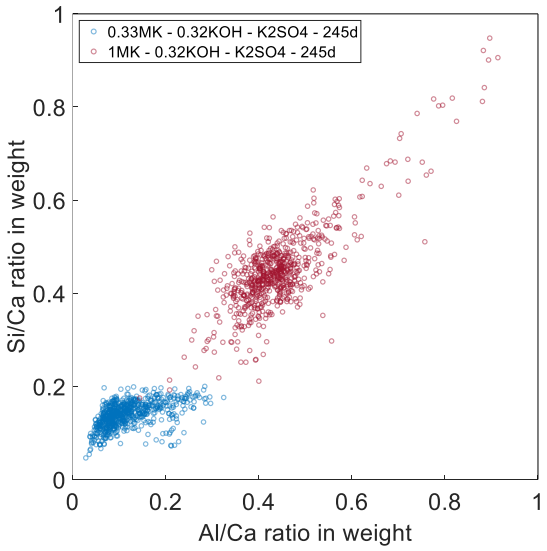

Figure S4-50: SEM/EDX results for 0.33MK_0.32KOH_K2SO4 and 1MK_0.32KOH_K2SO4 after 245 days of reaction.

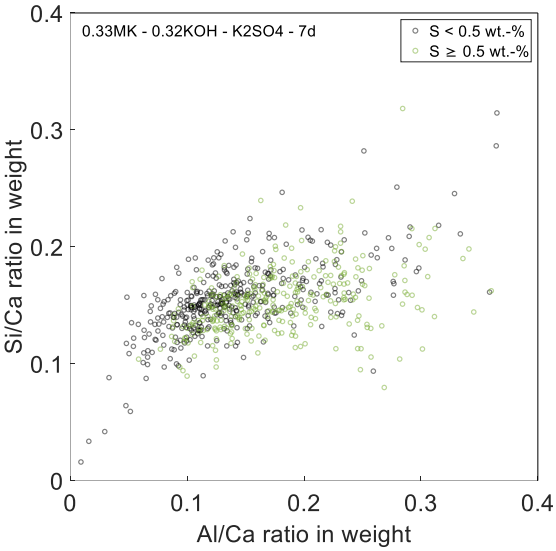

Figure S4-51: SEM/EDX results for 0.33MK_0.32KOH_K2SO4 after 7 days of reaction, green circles represent data points with S ≥ 0.5 wt.-%.

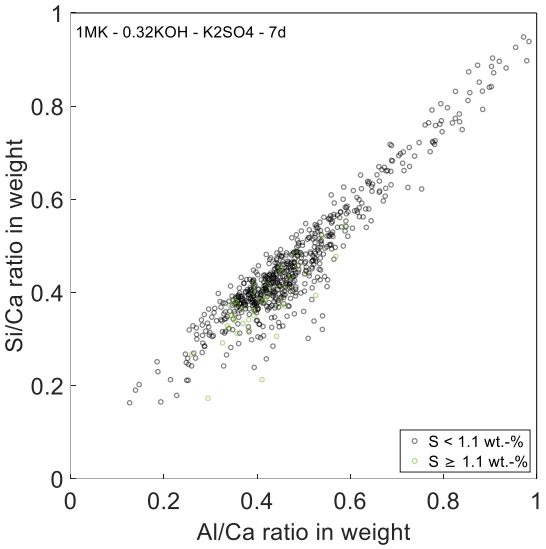

Figure S4-52: SEM/EDX results for 1MK_0.32KOH_K2SO4 after 7 days of reaction, green circles represent data points with S ≥ 1.1 wt.-%.

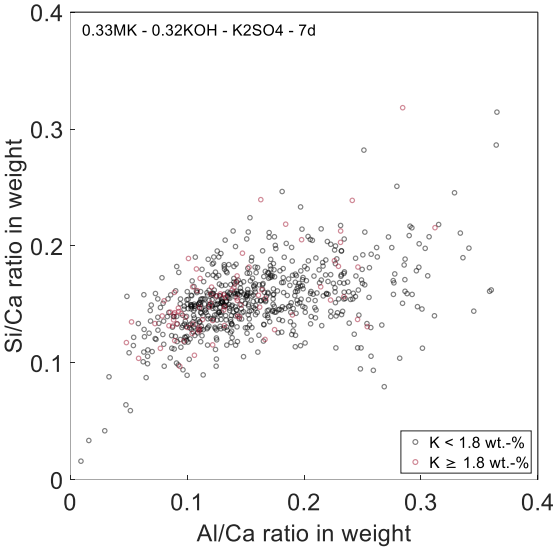

Figure S4-53: SEM/EDX results for 0.33MK_0.32KOH_K2SO4 after 7 days of reaction, red circles represent data points with K ≥ 1.8 wt.-%.

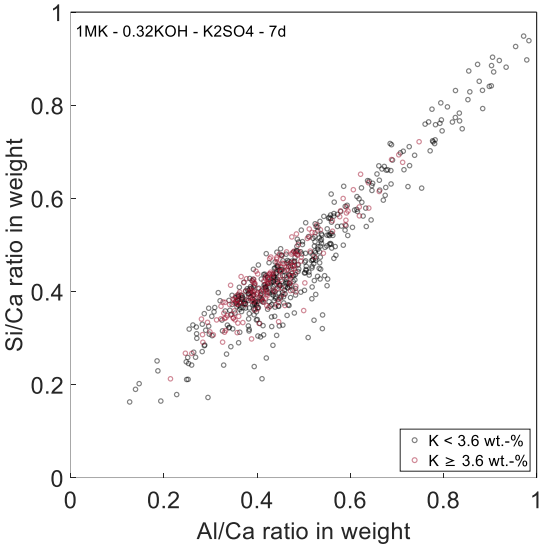

Figure S4-54: SEM/EDX results for 1MK_0.32KOH_K2SO4 after 7 days of reaction, red circles represent data points with K ≥ 3.6 wt.-%.

8.4 Publication 5

8.4.1 Supplementary Figures

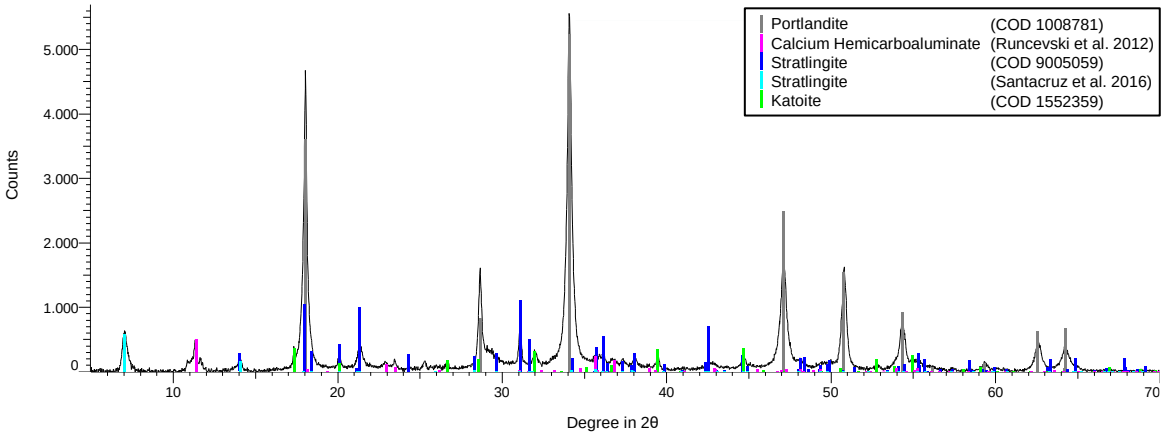

Figure S5-1: XRD result exemplarily shown for 0.33MK_0K_2d.

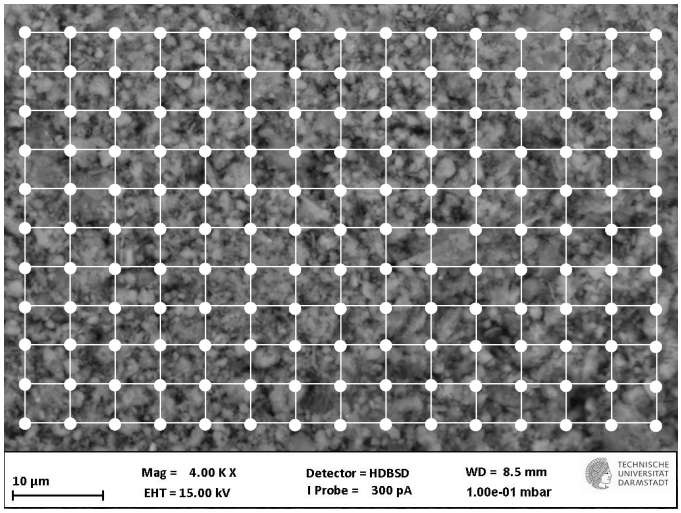

Figure S5-2: Mesh for EDX point analysis, exemplarily shown for one area of 0.33MK_0K_2d (10 x 14 points = 140 points per measuring area).

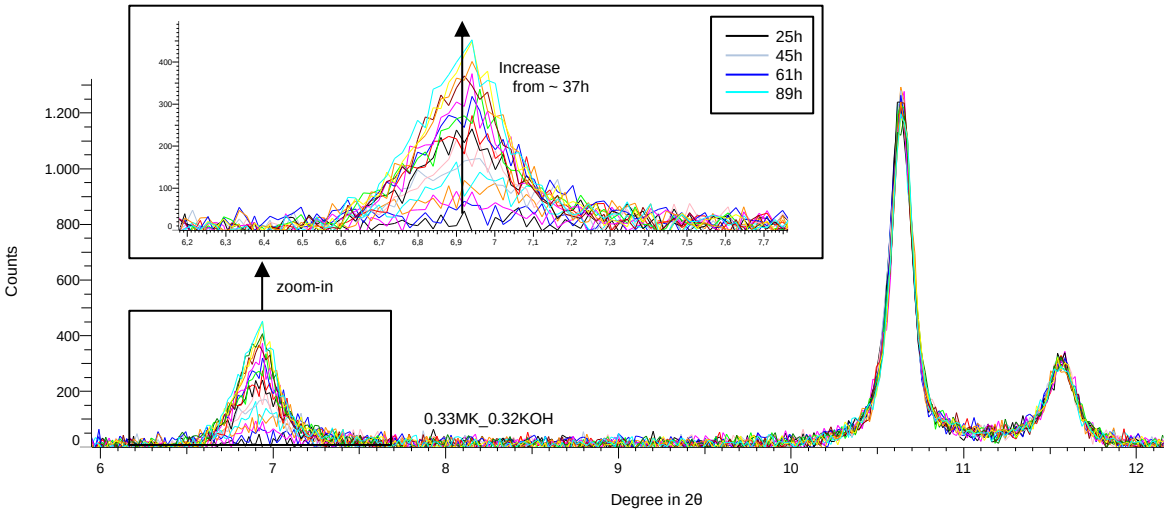

Figure S5-3: In-situ XRD results shown for 0.33MK_0.32KOH from 25h up to 89h (data shown for every four hours); peak related to C_2ASH_8.

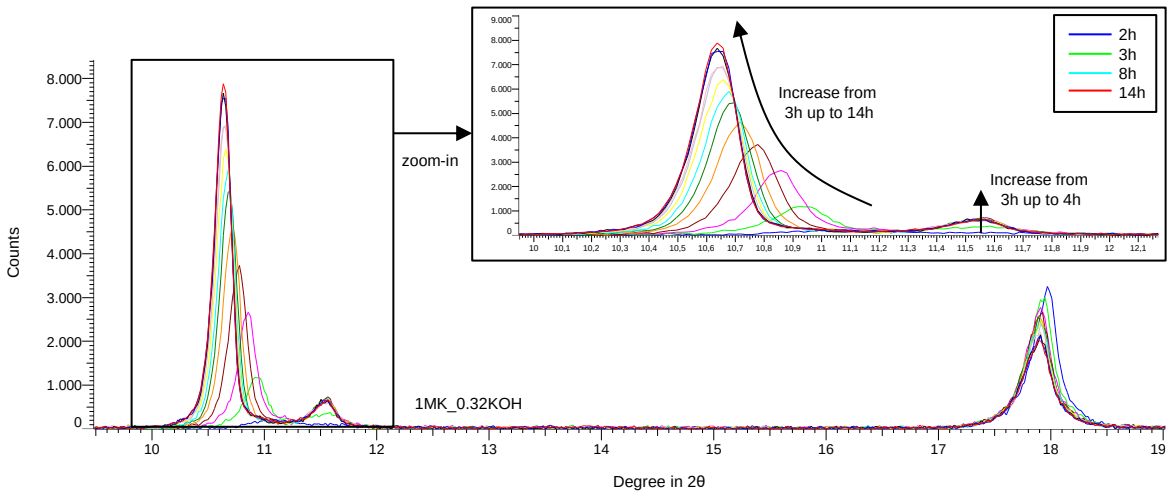

Figure S5-4: In-situ XRD results shown for 1MK_0.32KOH from 2h up to 14h (data shown for every hour); peak related to C_4AH_{13}.

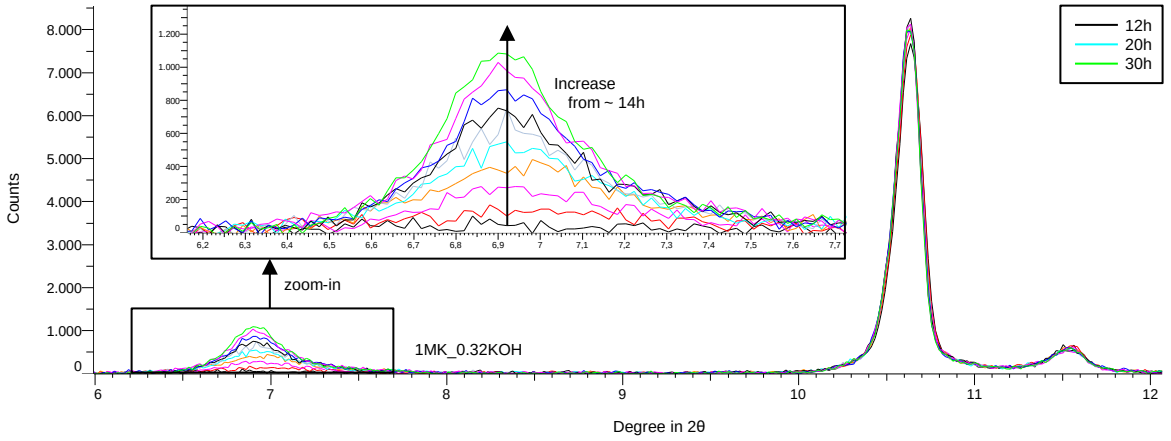

Figure S5-5: In-situ XRD results shown for 1MK_0.32KOH from 12h up to 30h (data shown for every two hours); peak related to C_2ASH_8.

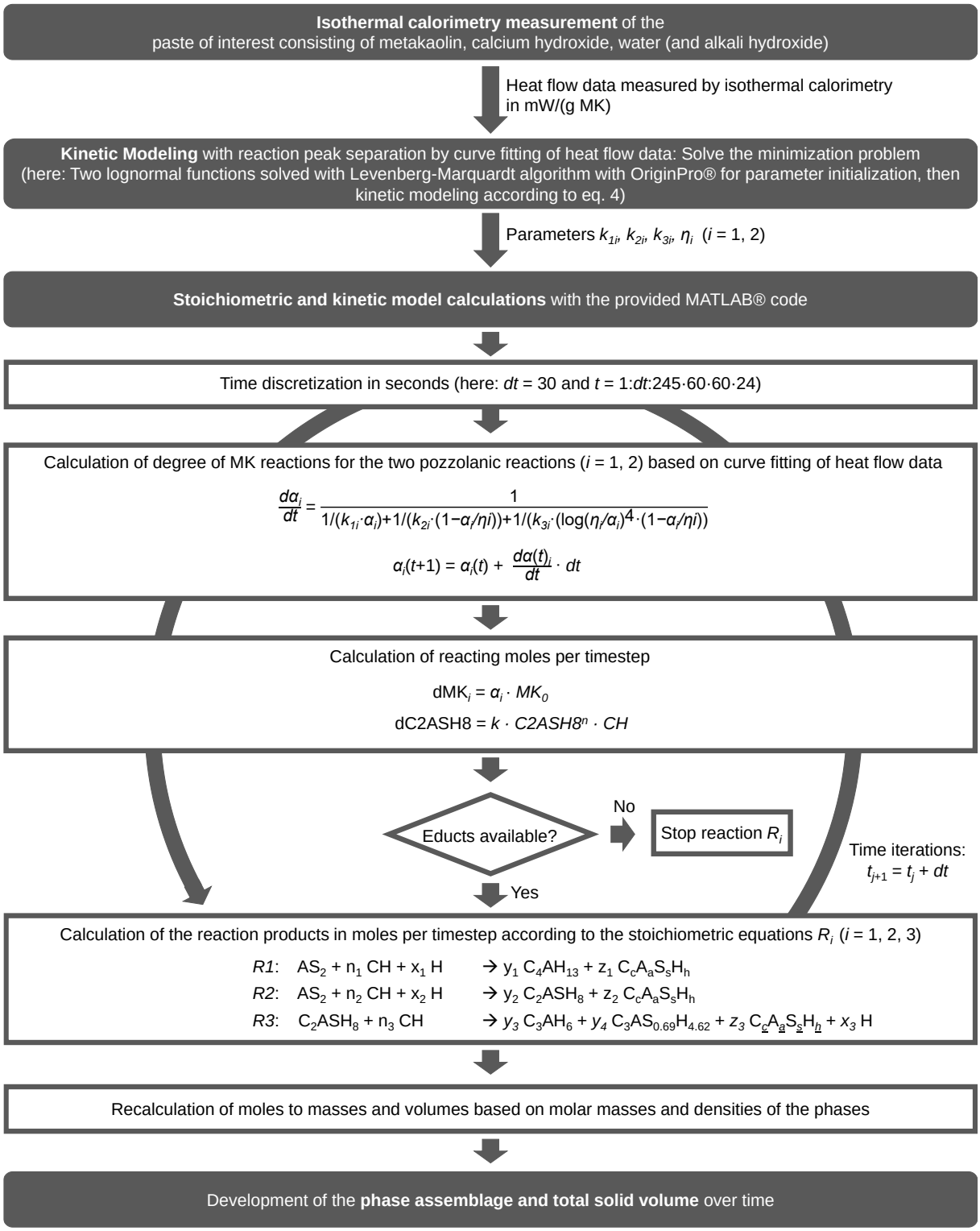

Figure S5-6: Detailed flow chart of the proposed reaction model.

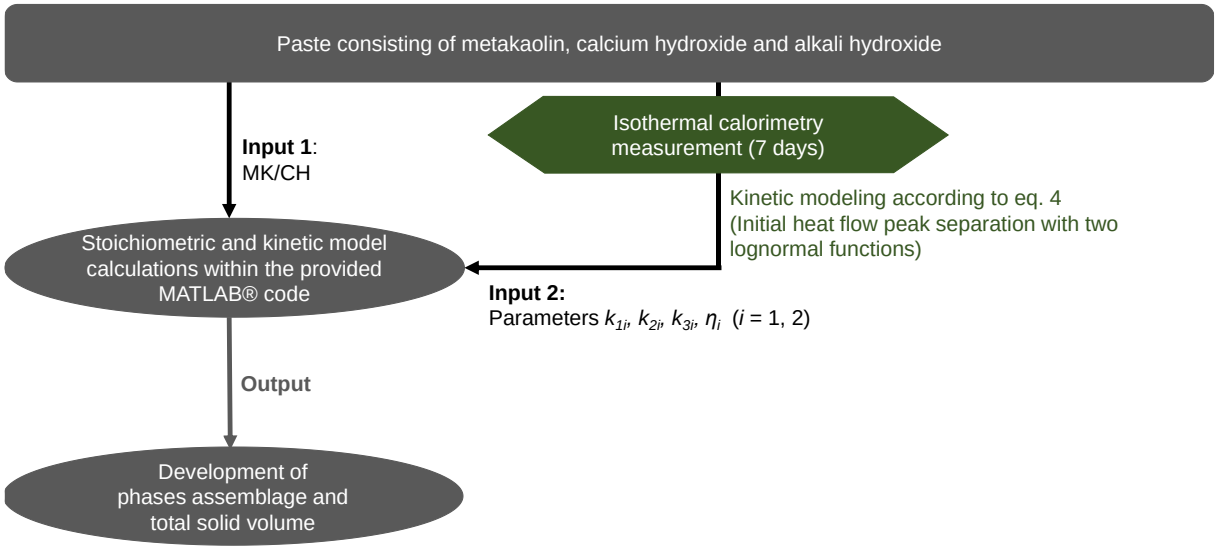

Figure S5-7: Overview of input and output parameters of the proposed reaction model (simplified scheme).

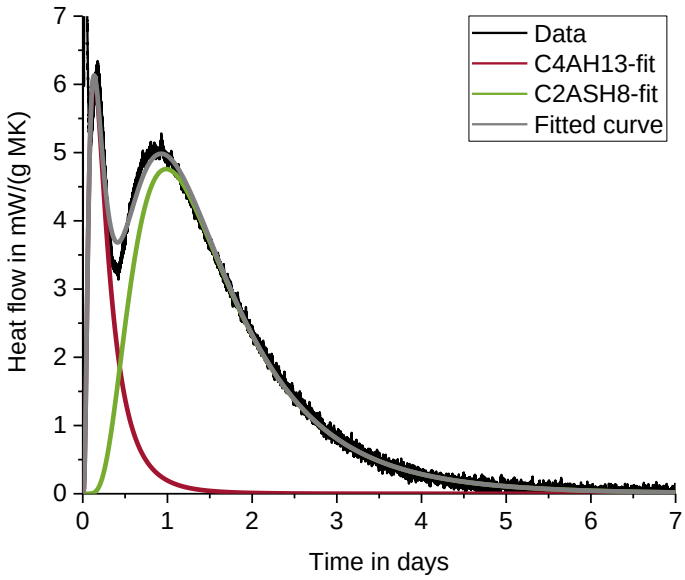

Figure S5-8: Curve fitting of the calorimetry heat flow measurement with two lognormal functions (exemplarily shown on the sample 0.33MK_0K).

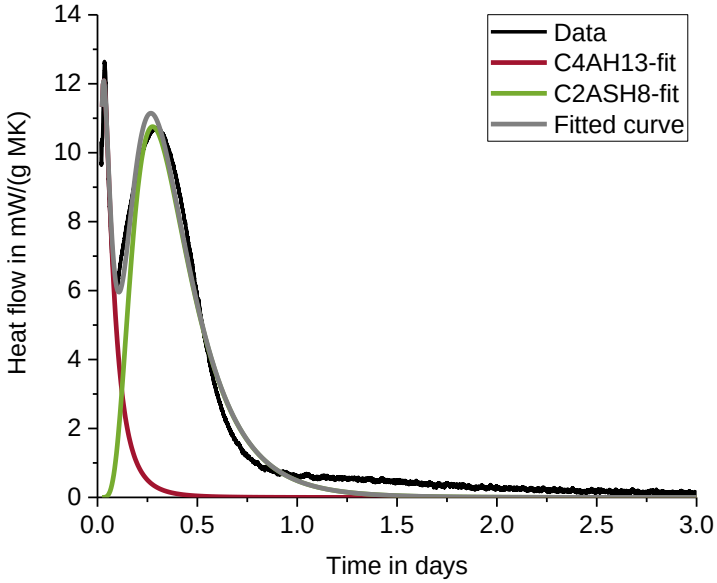

Figure S5-9: Curve fitting of the calorimetry heat flow measurement of the sample 1MK_1.28KOH.

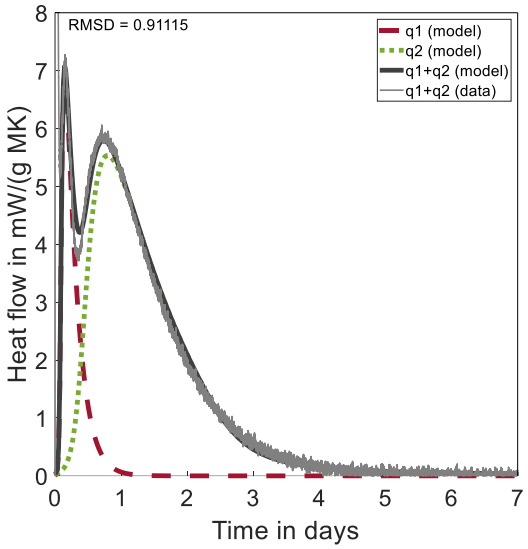

Figure S5-10: Fitting of the calorimetry heat flow (q) measurement with kinetic model equation of 0.33MK_0.32KOH at 40 °C with root mean square deviation (RMSD); $\alpha_1(1) = 5e^{-6}$ and $\alpha_2(1) = 40{\cdot}5e^{-6}$.

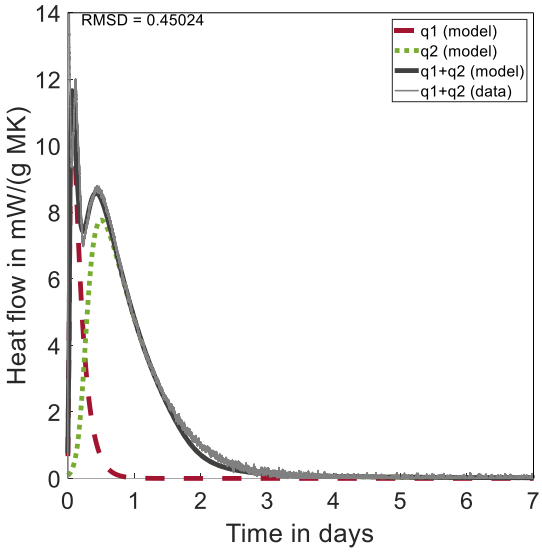

Figure S5-11: Fitting of the calorimetry heat flow (q) measurement with kinetic model equation of 0.33MK_1.28KOH at 40 °C with root mean square deviation (RMSD); $\alpha_1(1) = 80{\cdot}5e^{-6}$ and $\alpha_2(1) = 100{\cdot}5e^{-6}$.

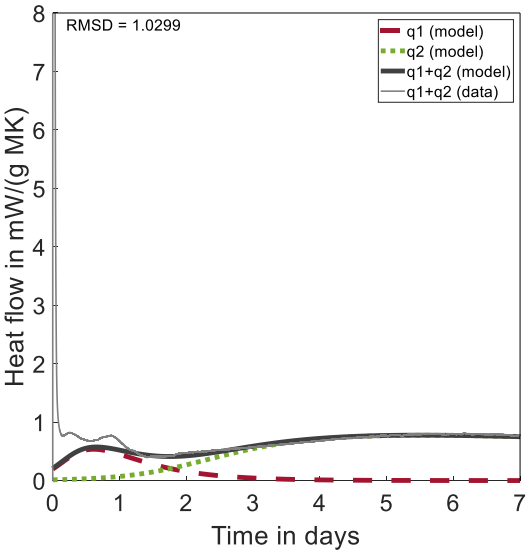

Figure S5-12: Fitting of the calorimetry heat flow (q) measurement with kinetic model equation of 0.33MK_0K at 20 °C with root mean square deviation (RMSD); $\alpha_1(1) = 400 \cdot e^{-6}$ and $\alpha_2(1) = 100 \cdot 5e^{-6}$.

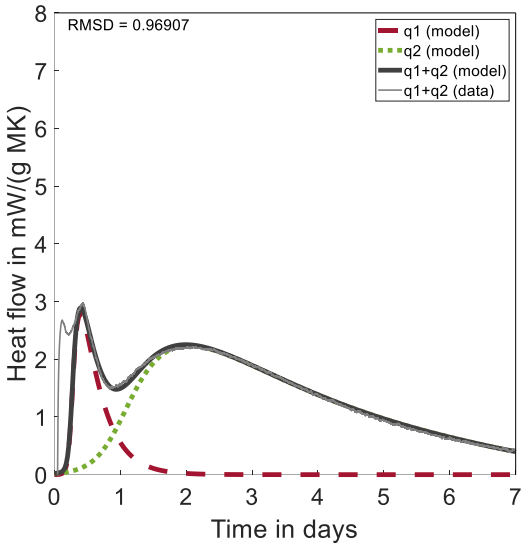

Figure S5-13: Fitting of the calorimetry heat flow (q) measurement with kinetic model equation of 0.33MK_0K at 30 °C with root mean square deviation (RMSD); $\alpha_1(1) = 0.2 \cdot 5e^{-6}$ and $\alpha_2(1) = 80 \cdot 5e^{-6}$.

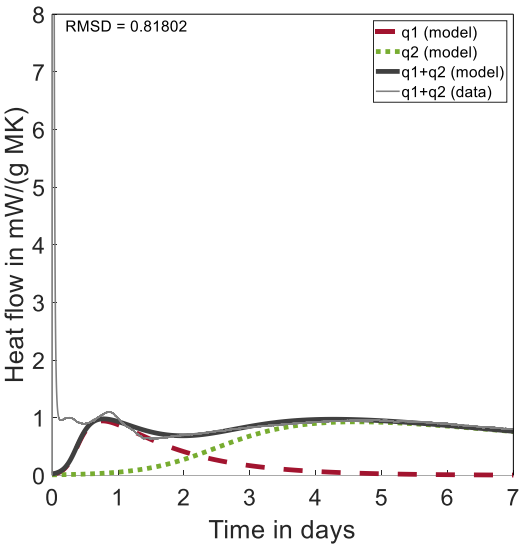

Figure S5-14: Fitting of the calorimetry heat flow (q) measurement with kinetic model equation of 0.33MK_0.32KOH at 20 °C with root mean square deviation (RMSD); $\alpha_1(1) = 20 \cdot e^{-6}$ and $\alpha_2(1) = 80 \cdot 5e^{-6}$.

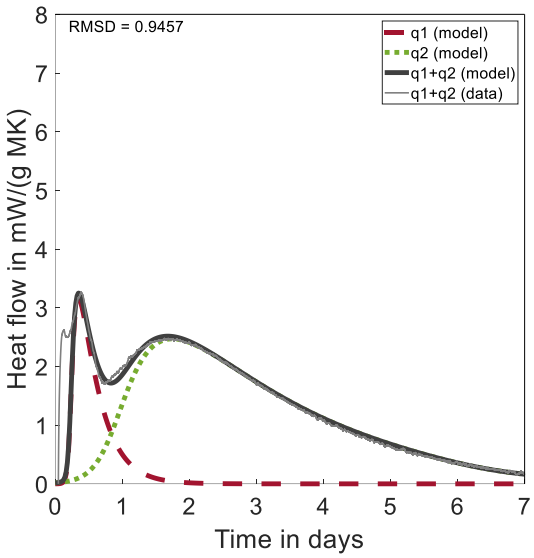

Figure S5-15: Fitting of the calorimetry heat flow (q) measurement with kinetic model equation of 0.33MK_0.32KOH at 30 °C with root mean square deviation (RMSD); $\alpha_1(1) = 0.1 \cdot 5e^{-6}$ and $\alpha_2(1) = 60 \cdot 5e^{-6}$.

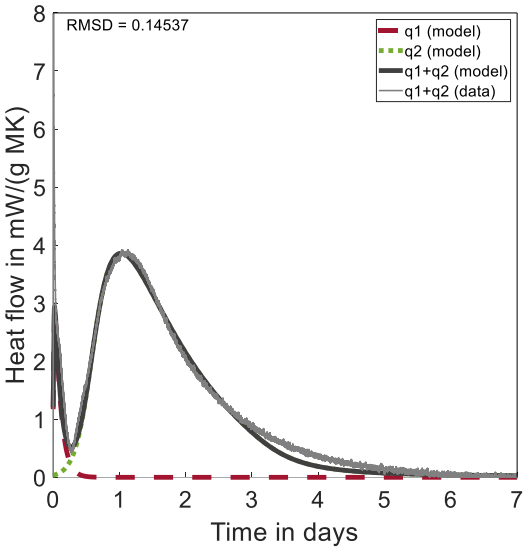

Figure S5-16: Fitting of the calorimetry heat flow (q) measurement with kinetic model equation of 1MK_0K at 40 °C with root mean square deviation (RMSD); $\alpha_1(1) = 80{\cdot}5e^{-6}$ and $\alpha_2(1) = 80{\cdot}5e^{-6}$.

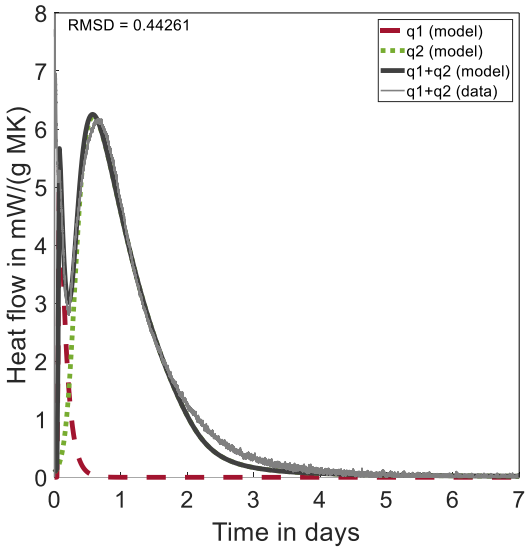

Figure S5-17: Fitting of the calorimetry heat flow (q) measurement with kinetic model equation of 1MK_0.32KOH at 40 °C with root mean square deviation (RMSD); $\alpha_1(1) = 1{\cdot}e^{-13}$ and $\alpha_2(1) = 5{\cdot}e^{-4}$.

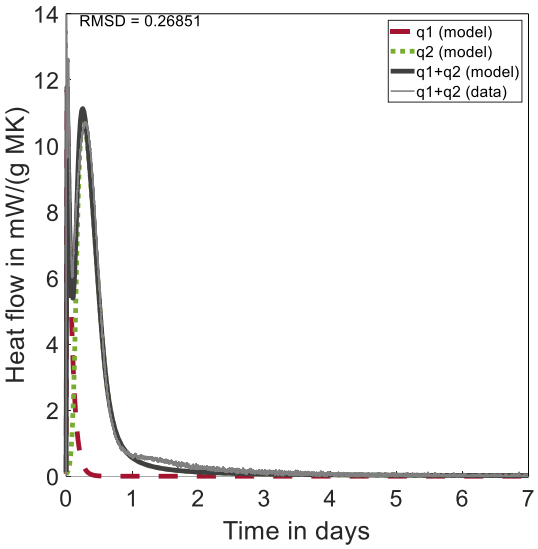

Figure S5-18: Fitting of the calorimetry heat flow (q) measurement with kinetic model equation of 1MK_1.28KOH at 40 °C with root mean square deviation (RMSD); $\alpha_1(1) = 5e^{-6}$ and $\alpha_2(1) = 30{\cdot}5e^{-6}$.

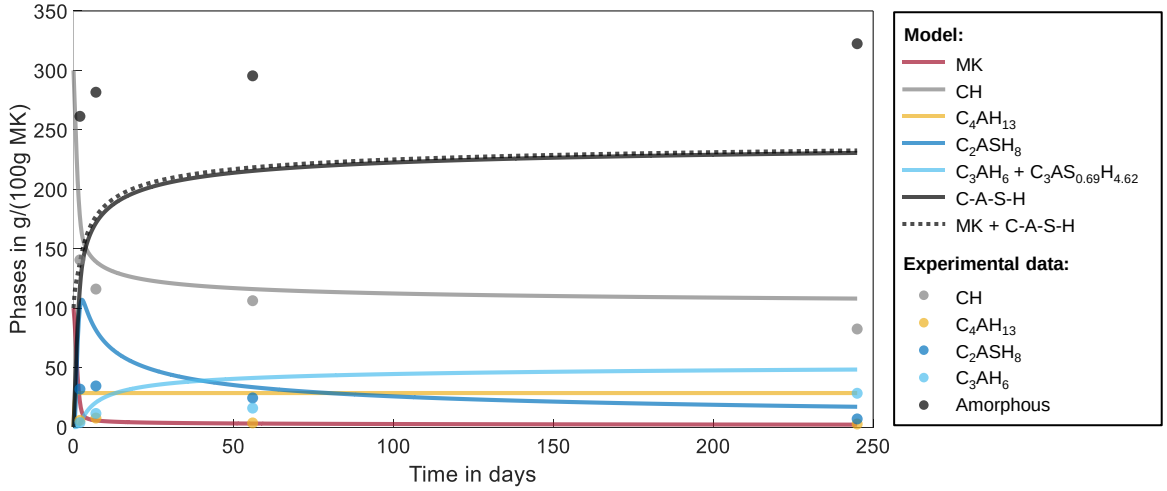

Figure S5-19: Modeled phase assemblage of 0.33MK_0.32KOH, dots are representing qXRD/TGA data.

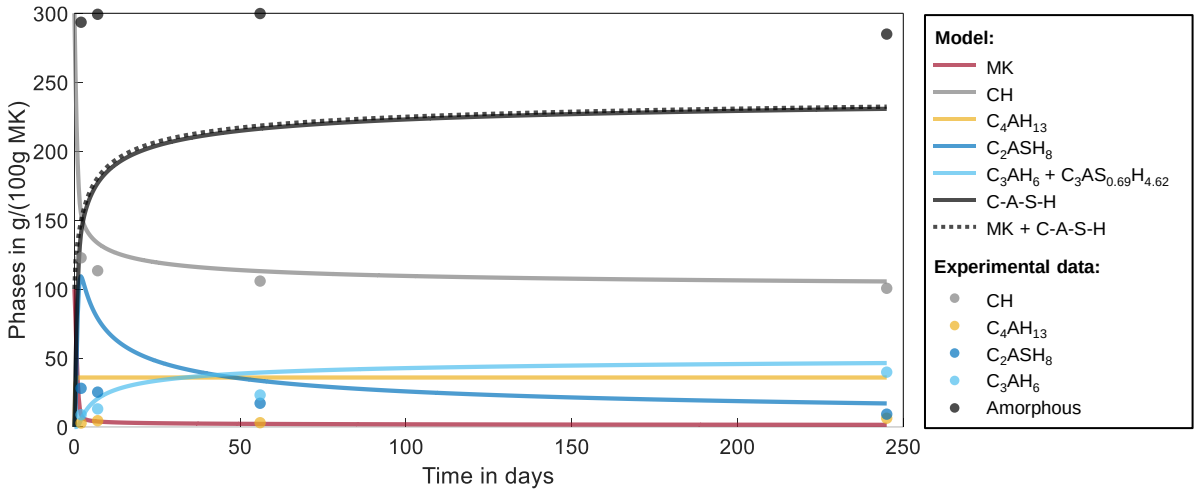

Figure S5-20: Modeled phase assemblage of 0.33MK_1.28KOH, dots are representing qXRD/TGA data.

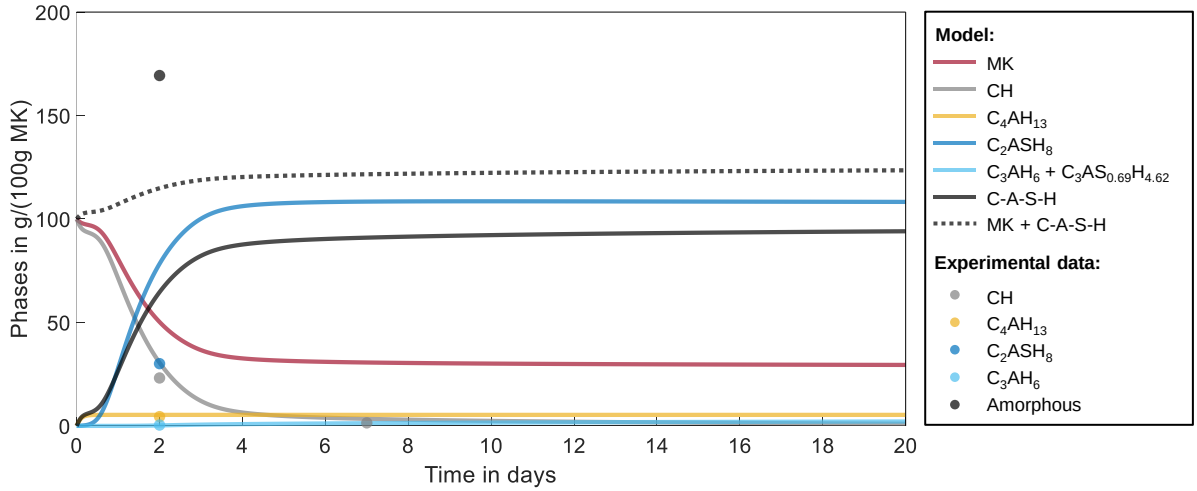

Figure S5-21: Modeled phase assemblage of 1MK_0K, dots are representing qXRD/TGA data.

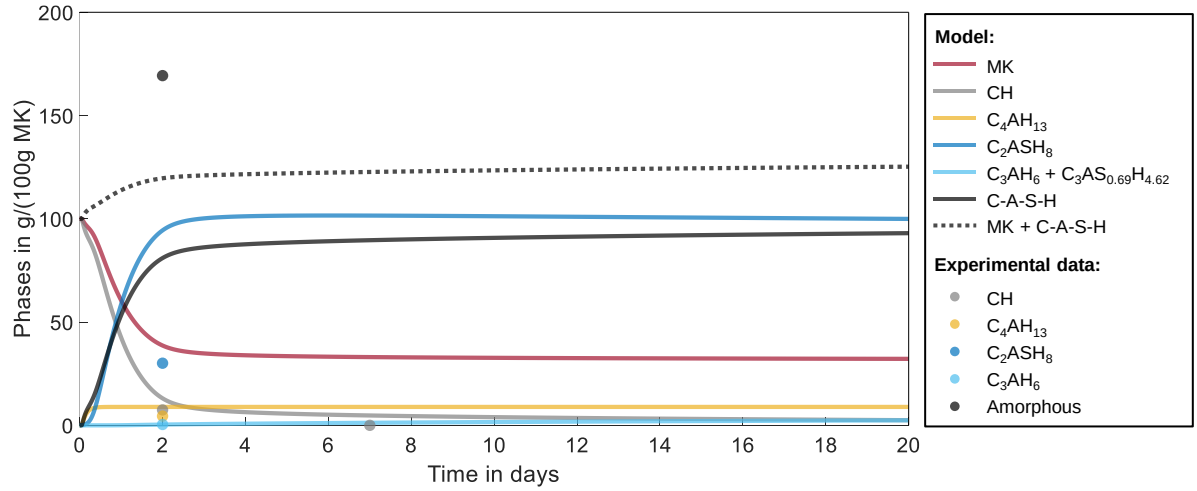

Figure S5-22: Modeled phase assemblage of 1MK_0.32KOH, dots are representing qXRD/TGA data.

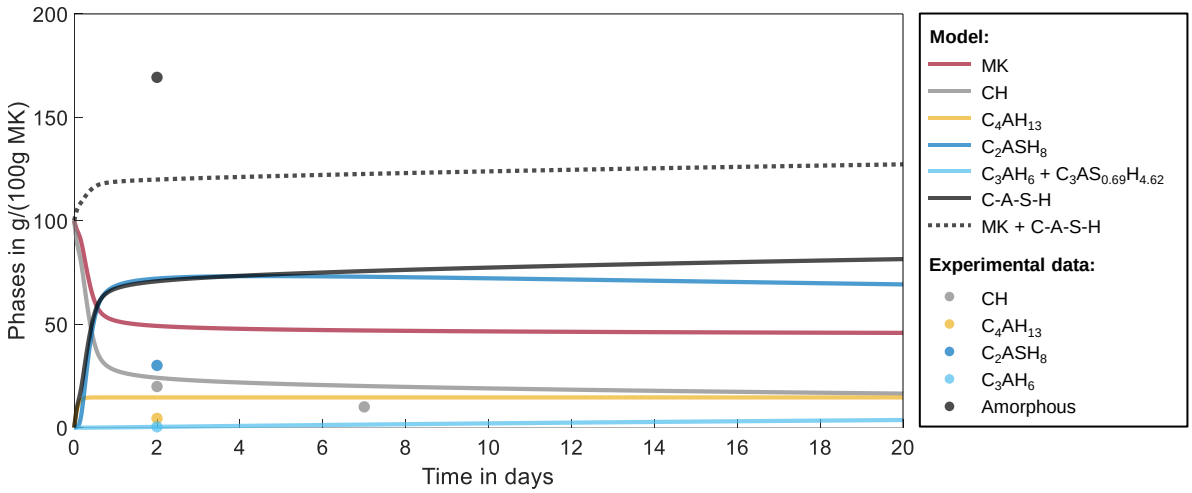

Figure S5-23: Modeled phase assemblage of 1MK_1.28KOH, dots are representing qXRD/TGA data.

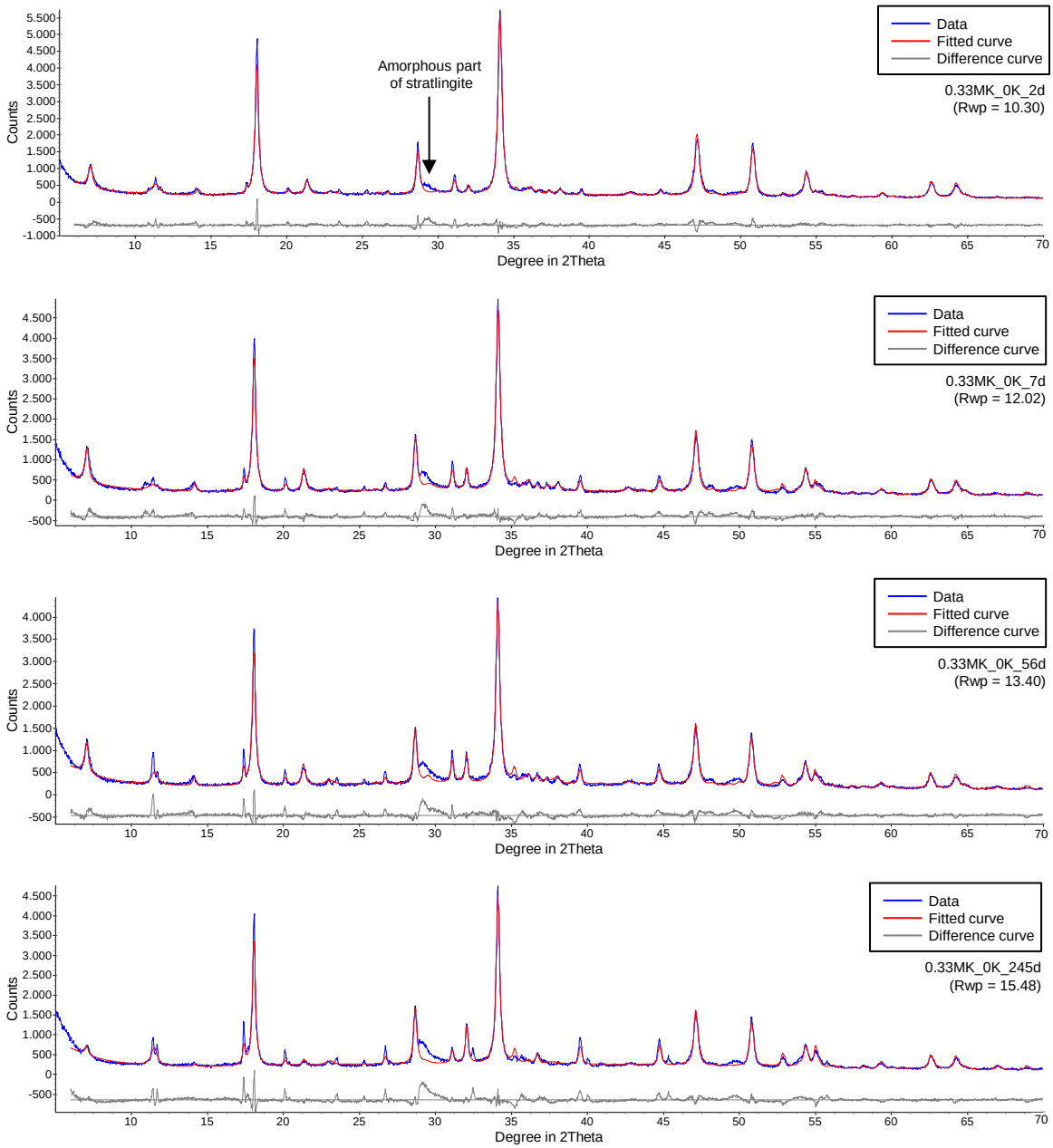

Figure S5-24: qXRD results shown for 0.33MK_0K after 2, 7, 56 and 245 days.

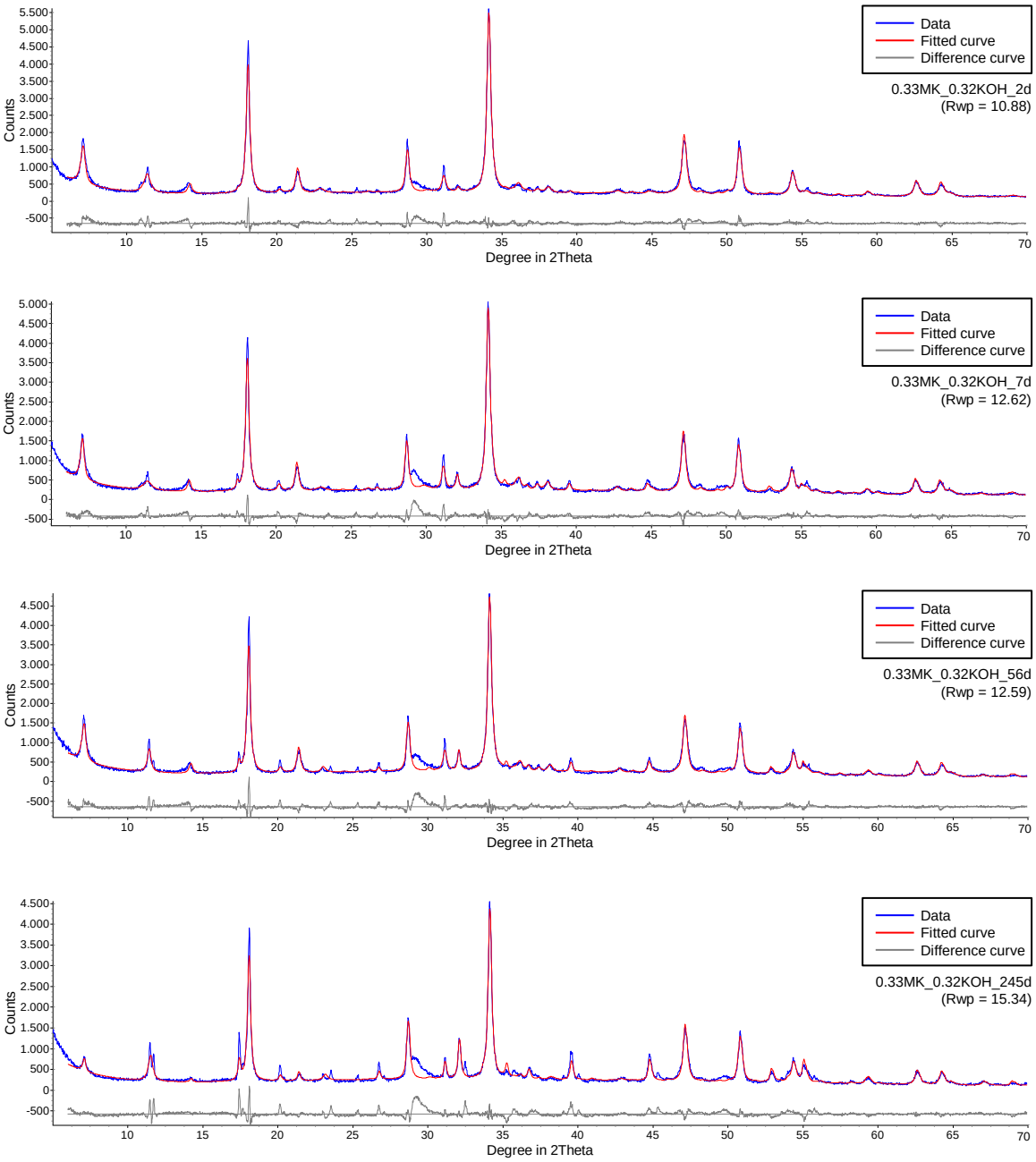

Figure S5-25: qXRD results shown for 0.33MK_0.32KOH after 2, 7, 56 and 245 days.

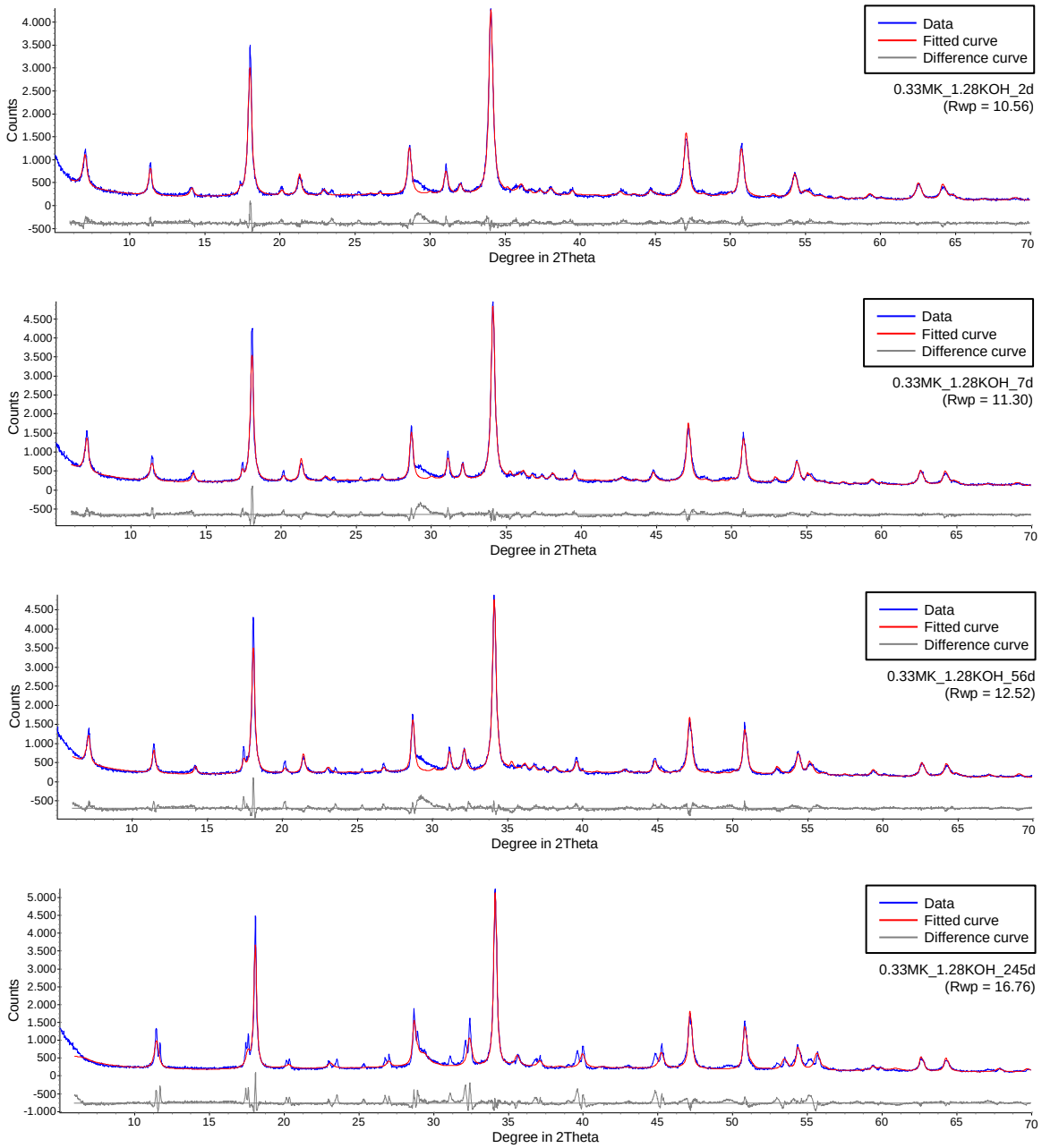

Figure S5-26: qXRD results shown for 0.33MK_1.28KOH after 2, 7, 56 and 245 days.

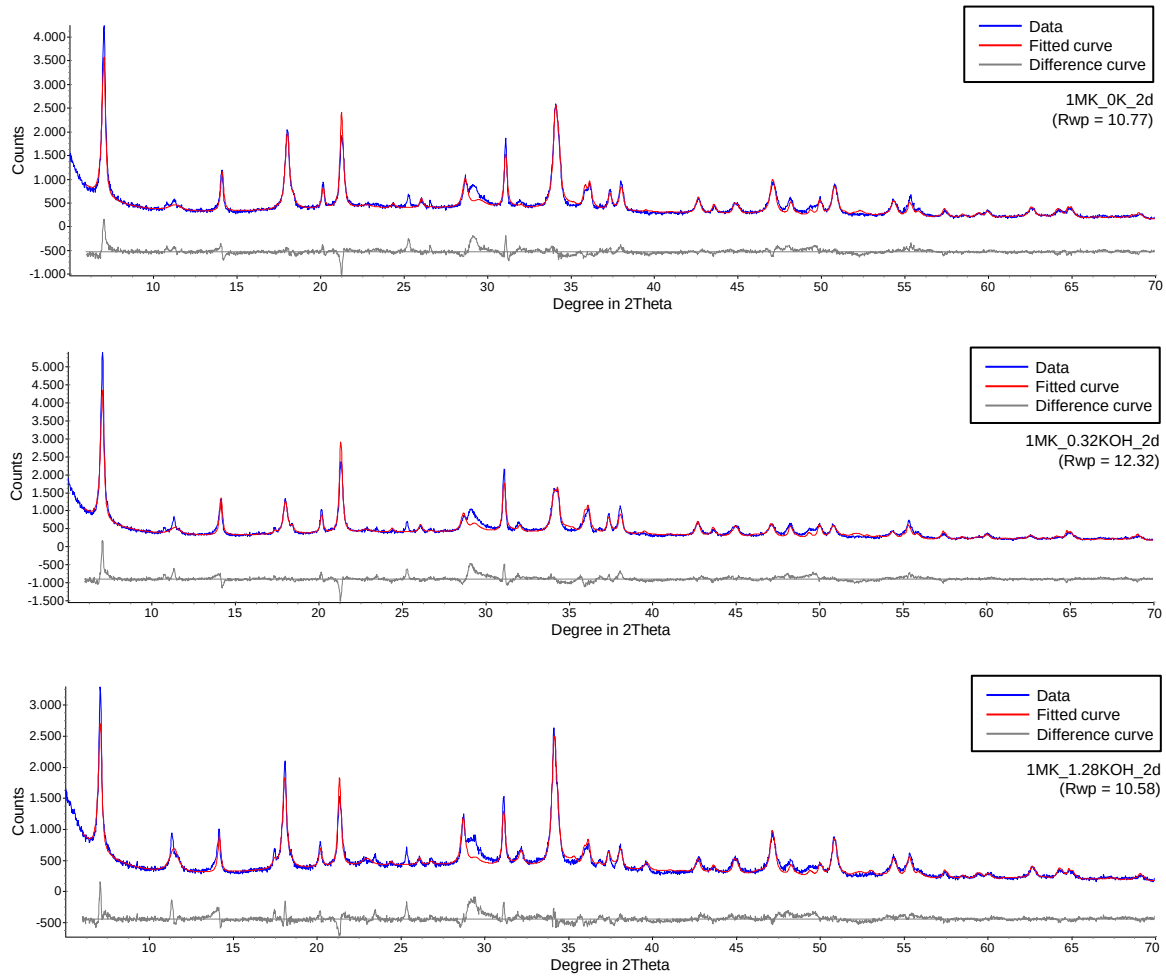

Figure S5-27: qXRD results shown for 1MK_0K, _0.32KOH and _1.28KOH after 2 days.

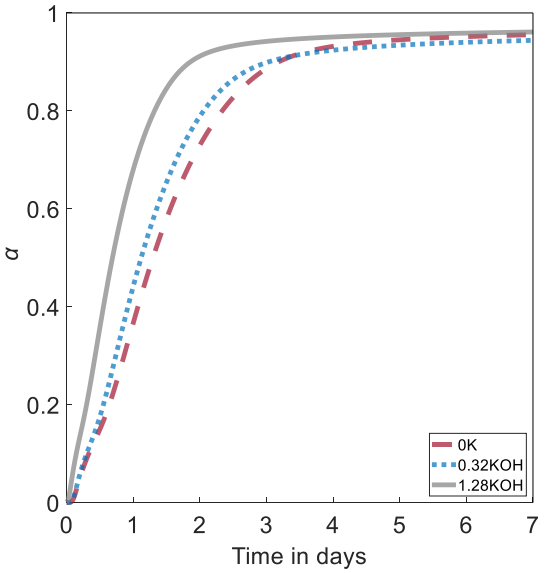

Figure S5-28: Degrees of metakaolin reactions (α) for samples with MK/CH = 0.33 varying with the amount of added KOH.

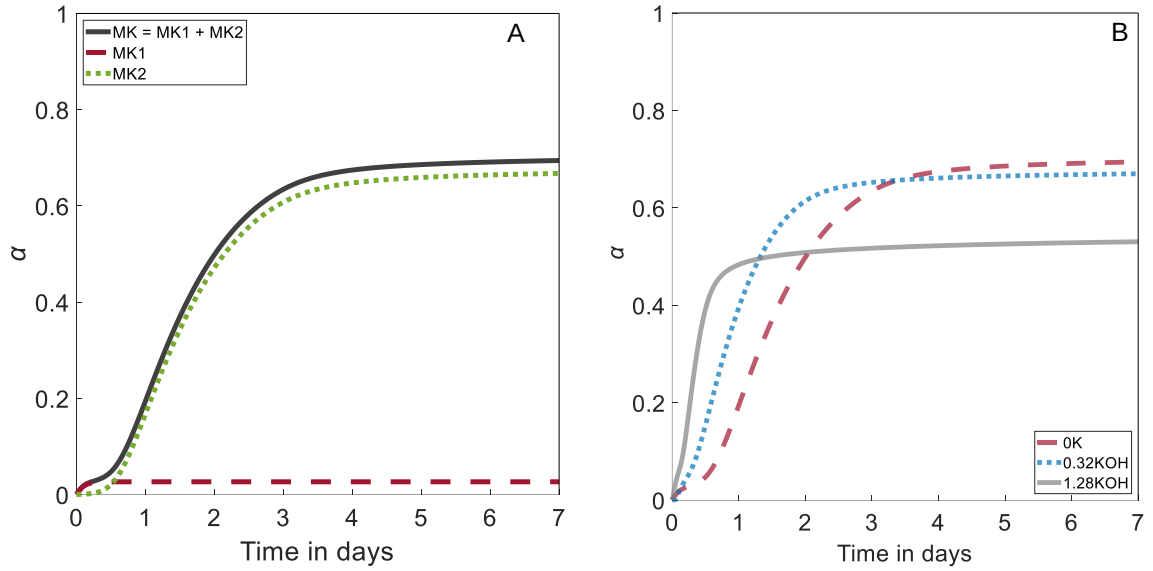

Figure S5-29: Degree of metakaolin reactions (α) for 1MK_0K, divided in the two reaction processes (A) and for samples with MK/CH = 1.0 varying with the amount of added KOH.

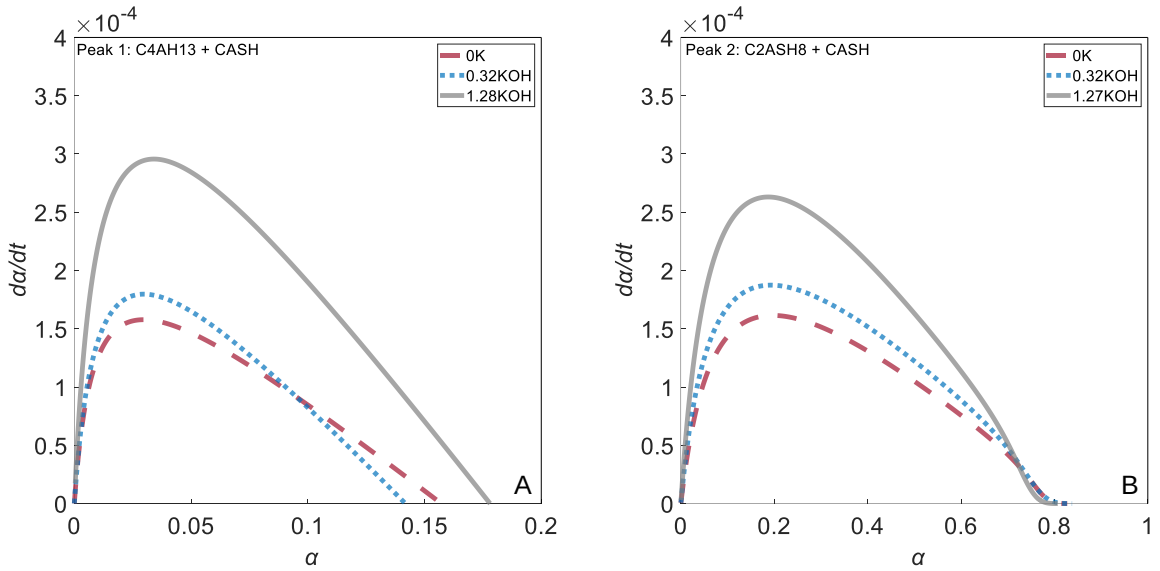

Figure S5-30: Modeled reaction rates ($d\alpha/dt$) of the samples with MK/CH of 0.33 depending on the degree of metakaolin reaction (α) for the first pozzolanic metakaolin reaction (Peak 1, A) and the second pozzolanic metakaolin reaction (Peak 2, B) with varying amounts of KOH.

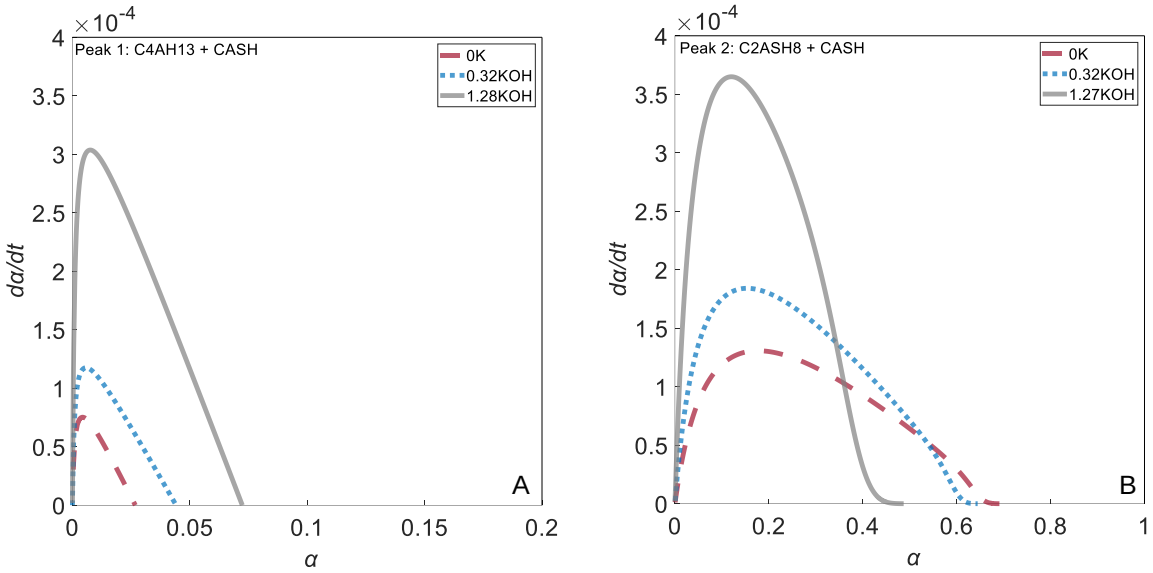

Figure S5-31: Modeled reaction rates ($d\alpha/dt$) of the samples with MK/CH of 1.0 depending on the degree of metakaolin reaction (α) for the first pozzolanic metakaolin reaction (Peak 1, A) and the second pozzolanic metakaolin reaction (Peak 2, B) with varying amounts of KOH.

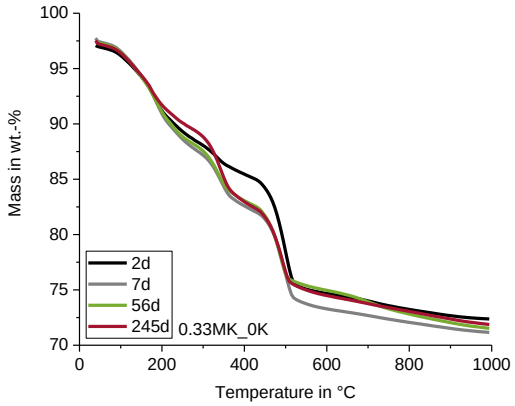

Figure S5-32: TG-curves of 0.33MK_0K with time cured at 40 °C.

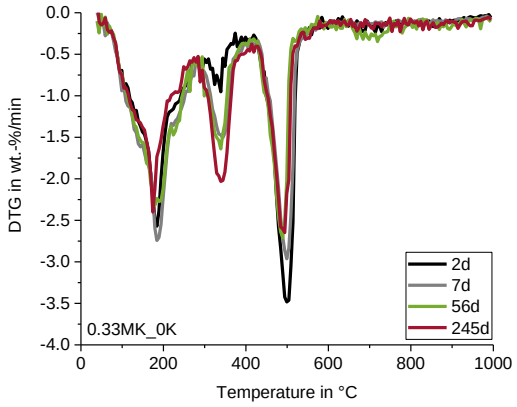

Figure S5-33: DTG-curves of 0.33MK_0K with time cured at 40 °C.

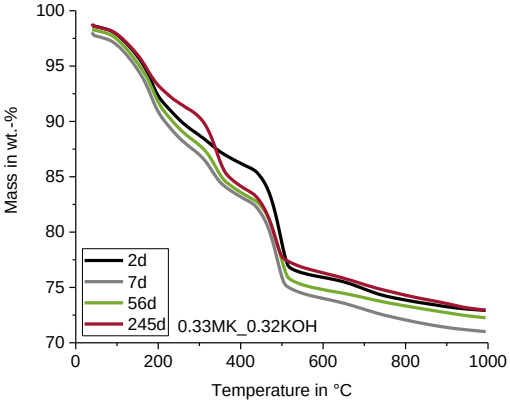

Figure S5-34: TG-curves of 0.33MK_0.32KOH with time cured at 40 °C.

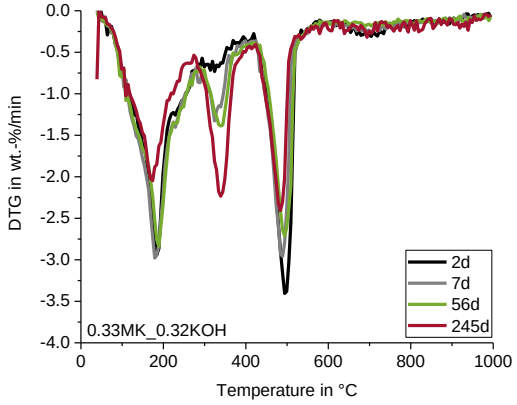

Figure S5-35: DTG-curves of 0.33MK_0.32KOH with time cured at 40 °C.

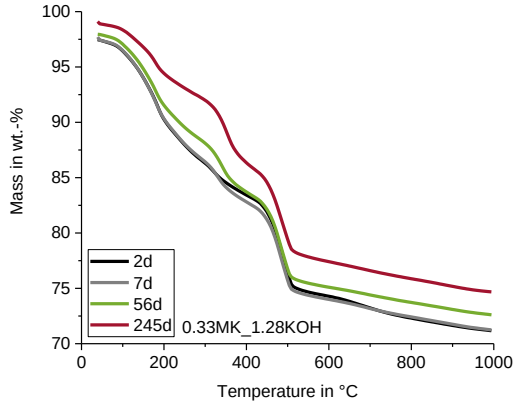

Figure S5-36: TG-curves of 0.33MK_1.28KOH with time cured at 40 °C.

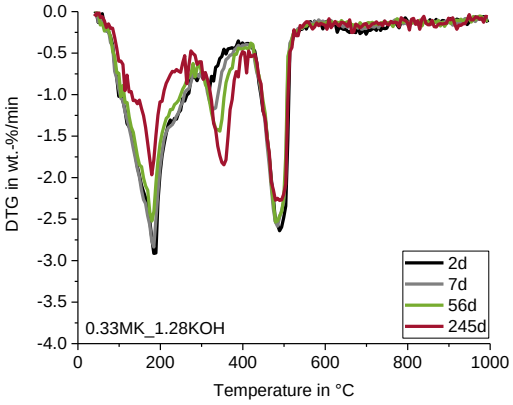

Figure S5-37: DTG-curves of 0.33MK_1.28KOH with time cured at 40 °C.

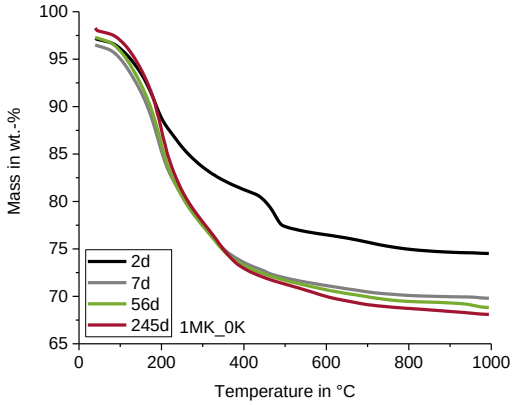

Figure S5-38: TG-curves of 1MK_0K with time cured at 40 °C.

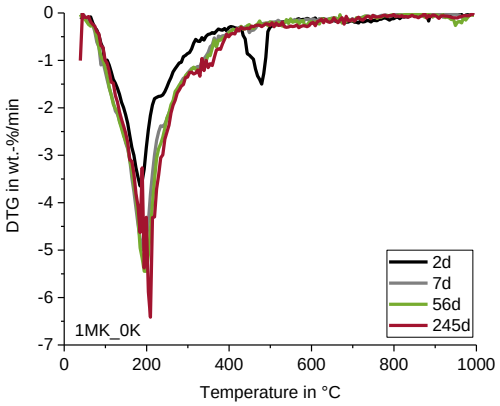

Figure S5-39: DTG-curves of 1MK_0K with time cured at 40 °C.

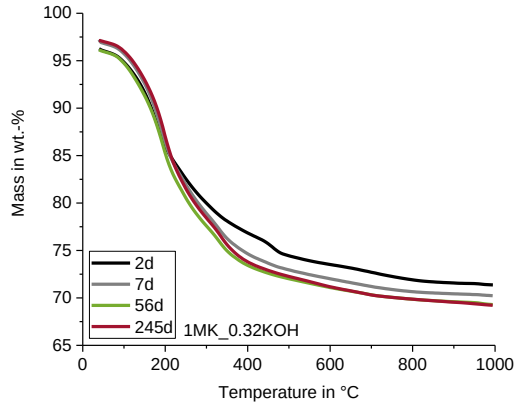

Figure S5-40: TG-curves of 1MK_0.32KOH with time cured at 40 °C.

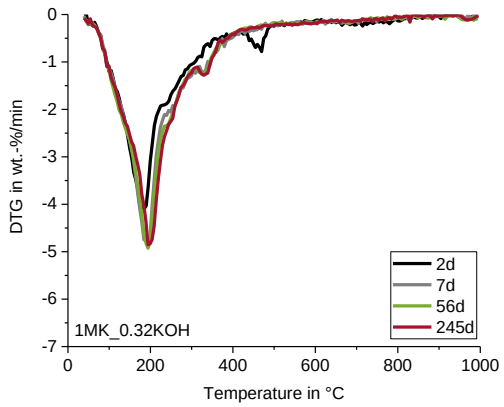

Figure S5-41: DTG-curves of 1MK_0.32KOH with time cured at 40 °C.

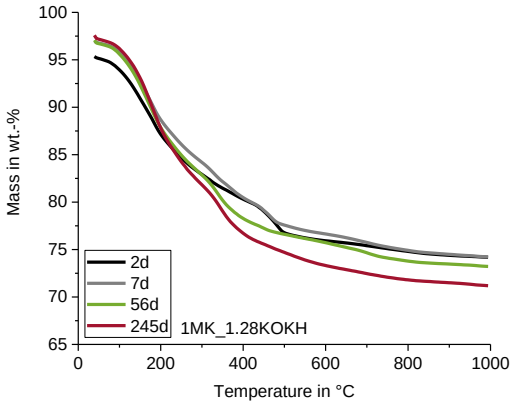

Figure S5-42: TG-curves of 1MK_1.28KOH with time cured at 40 °C.

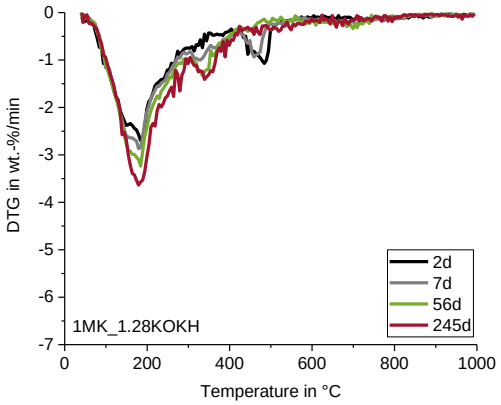

Figure S5-43: DTG-curves of 1MK_1.28KOH with time cured at 40 °C.

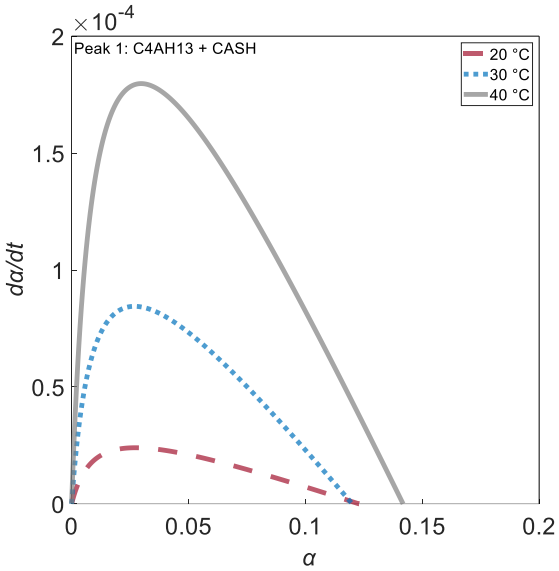

Figure S5-44: Modeled reaction rates (dα/dt) of the sample 0.33MK_0.32KOH depending on the degree of metakaolin reaction (α) for the two proposed pozzolanic metakaolin reactions at 20 °C, 30 °C and 40 °C (Peak 1).

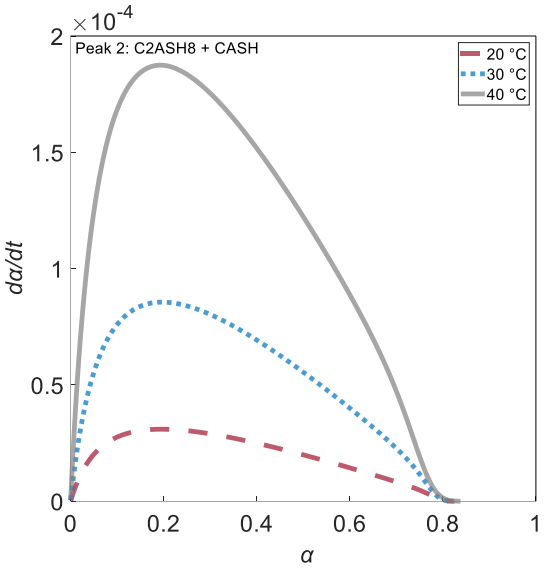

Figure S5-45: Modeled reaction rates (dα/dt) of the sample 0.33MK_0.32KOH depending on the degree of metakaolin reaction (α) for the two proposed pozzolanic metakaolin reactions at 20 °C, 30 °C and 40 °C (Peak 2).

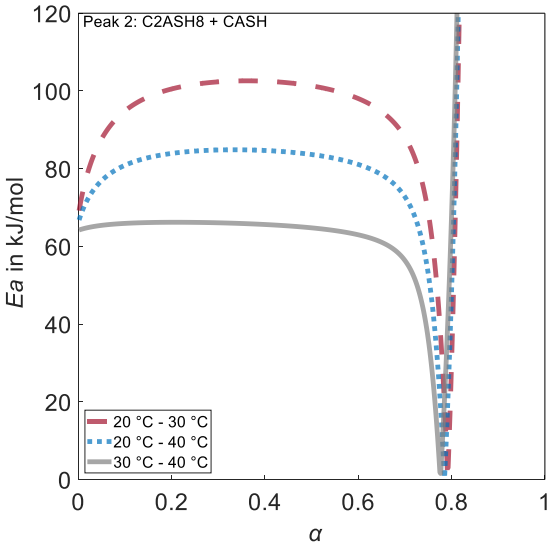

Figure S5-46: Calculated activation energy *Ea* for the sample 0.33MK_0K in kJ/mol.

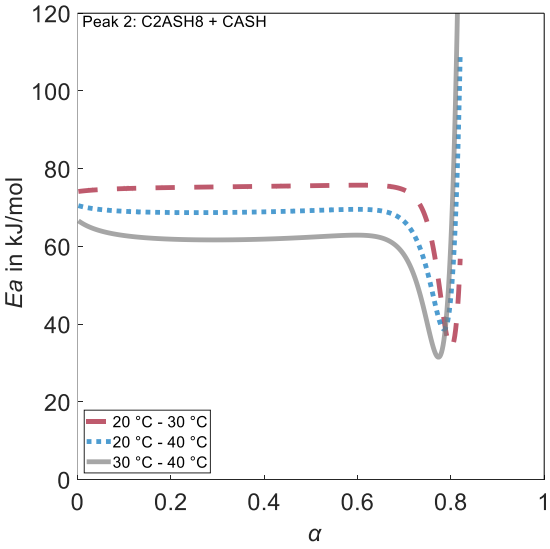

Figure S5-47: Calculated activation energy *Ea* for the sample 0.33MK_0.32KOH in kJ/mol.

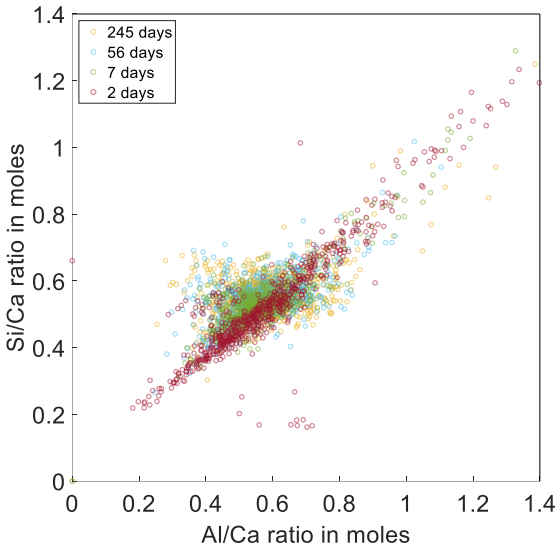

Figure S5-48: SEM/EDX results for 1MK_0K with reaction time.

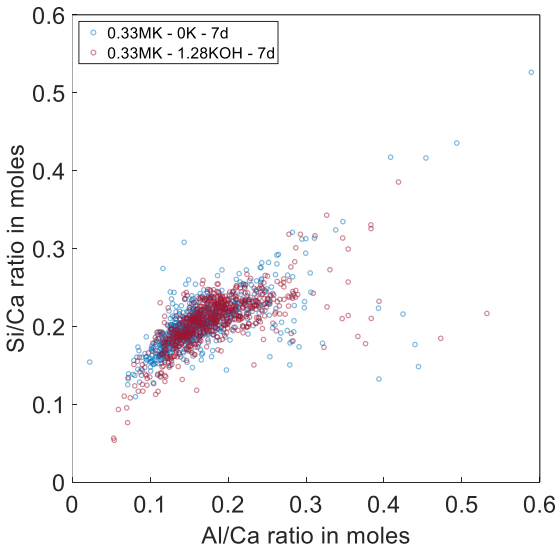

Figure S5-49: SEM/EDX results for 0.33MK_0K and 0.33MK_1.28KOH at 7 days of reaction.

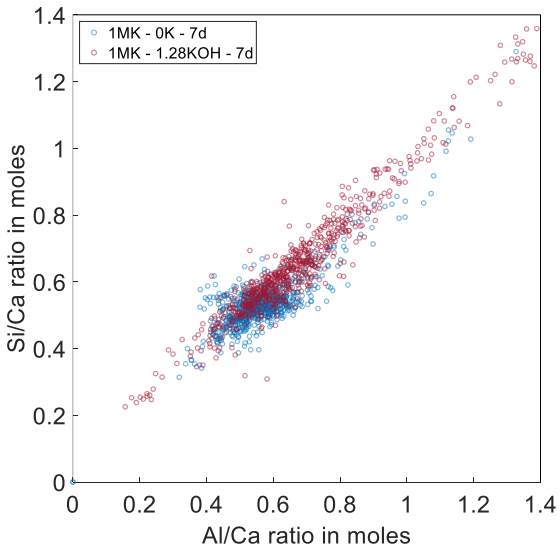

Figure S5-50: SEM/EDX results for 1MK_0K and 1MK_1.28KOH at 7 days of reaction.

8.4.2 Supplementary Tables

Table S5-1: Results of the lognormal fitting parameters (isothermal calorimetry 40 °C) with RSS (Residual Sum of Squares).

Sample	xc_1	w_1	A_1	xc_2	w_2	A_2	RSS
0.33MK_0K	20770	0.76	181865	120715	0.59	714735	316
0.33MK_0.32KOH	17545	0.70	164065	102048	0.60	713805	442
0.33MK_1.28KOH	13350	0.73	206038	70520	0.64	709939	651
1MK_0K	10251	0.63	30987	131025	0.59	616829	79
1MK_0.32KOH	9854	0.70	71720	82184	0.65	658581	52
1MK_1.28KOH*	5317	0.83	94812	31153	0.52	379857	1104

* Fitting curve does not represent the data very well, fit has not converged (see Fig. S9 in the Supplementary Material).

Table S5-2: Summary of TGA results (mean values of two samples), samples cured at 40 °C.

Sample	Chemically bound water in reaction products (CBW) in g/(100g MK)	CH-Consumption in g/(100g MK)
0.33MK_0K_2d	65.6	145.8
0.33MK_0K_7d	85.0	175.5
0.33MK_0K_56d	81.9	194.5
0.33MK_0K_245d	81.4	201.1
0.33MK_0.32KOH_2d	70.9	162.2
0.33MK_0.32KOH_7d	83.1	188.3
0.33MK_0.32KOH_56d	82.7	191.2
0.33MK_0.32KOH_245d	80.6	211.3
0.33MK_1.28KOH_2d	80.6	171.6
0.33MK_1.28KOH_7d	85.5	186.8
0.33MK_1.28KOH_56d	81.1	189.0
0.33MK_1.28KOH_245d	72.8	200.2
1MK_0K_2d	43.4	76.3
1MK_0K_7d	66.1	98.5
1MK_0K_56d	69.9	100.0
1MK_0K_245d	70.7	100.0
1MK_0.32KOH_2d	59.7	92.5
1MK_0.32KOH_7d	64.2	100.0
1MK_0.32KOH_56d	68.5	100.0
1MK_0.32KOH_245d	69.0	100.0
1MK_1.28KOH_2d	45.4	82.4
1MK_1.28KOH_7d	48.3	90.3
1MK_1.28KOH_56d	55.1	98.4
1MK_1.28KOH_245d	62.2	100.0

Table S5-3: Summary of total solid volume results in $cm^3/(g\ MK)$ with time, samples cured at 40 °C.

Sample	2d	7d	56d	245d
0.33MK_0K	2.53	2.39	2.20	2.17
0.33MK_0.32KOH	2.20	2.52	2.24	2.29
0.33MK_1.28KOH	2.23	2.07	1.99	1.97
1MK_0K	1.43	1.48	1.31*	1.75
1MK_0.32KOH	1.50	1.50	1.64	1.63
1MK_1.28KOH	1.09	1.06	1.21	1.60

* Outlier.

Table S5-4: Results of the lognormal fitting parameters (isothermal calorimetry of selected samples at 20 and 30 °C) with RSS (Residual Sum of Squares).

Sample	xc_1	w_1	A_1	xc_2	w_2	A_2	RSS
0.33MK_0K_20°C	85139	0.65	77771	1026210	0.81	1181840	21
0.33MK_0K_30°C	40446	0.53	136541	280611	0.66	819623	35
0.33MK_0.32KOH_20°C	102482	0.76	146397	624099	0.62	740462	30
0.33MK_0.32KOH_30°C	37083	0.57	142145	227133	0.62	710725	75

Table S5-5: Results of the kinetic fitting parameters; $k_{31} = 0$ with root mean square deviation (RMSD).

Sample	k_{11}	k_{21}	η_1	k_{12}	k_{22}	k_{32}	η_2	RMSD
0.33MK_0K_20°C	6.3529e-05	6.3529e-07	0.041373	2.0679e-05	8.9191e-07	0.09	0.91863	1.03
0.33MK_0K_30°C	3.7586e-04	3.7586e-06	0.098163	5.1914e-05	3.9048e-06	0.045821	0.86184	0.97
0.33MK_0.32KOH_20°C	1.3217e-04	1.3217e-06	0.12291	2.2715e-05	1.7542e-06	0.09	0.83709	0.82
0.33MK_0.32KOH_30°C	4.6756e-04	4.6756e-06	0.12004	6.1924e-05	4.8649e-06	0.09	0.83996	0.95

Table S5-6: Calibration of the formation enthalpy of the average solid solution phase "$C_{1.5}A_{0.075}S_{0.75}H_{2.7}$" and the corresponding heat of pozzolanic reactions.

Sample	Formation enthalpy of "$C_{1.5}A_{0.075}S_{0.75}H_{2.7}$"	Explanation	Heat of reaction i (i = 1, 2)
0.33MK_0K_20°C	-2756 kJ/mol	Calibrated to achieve α = 0.96 in the long-term.	H_1 = -417 kJ/mol H_2 = -286 kJ/mol
0.33MK_0K_30°C	-2707 kJ/mol	Calibrated to achieve α = 0.96 in the long-term.	H_1 = -286 kJ/mol H_2 = -213 kJ/mol
0.33MK_0K_40°C	-2696 kJ/mol	Calibrated based on the assumption of α = 0.96 after seven days of reaction at 40 °C	H_1 = -257 kJ/mol H_2 = -197 kJ/mol
0.33MK_0.32KOH_20°C	-2698 kJ/mol	Calibrated to achieve α = 0.95 in the long-term	H_1 = -262 kJ/mol H_2 = -200 kJ/mol
0.33MK_0.32KOH_30°C	-2693 kJ/mol	Calibrated to achieve α = 0.95 in the long-term	H_1 = -249 kJ/mol H_2 = -192 kJ/mol
0.33MK_0.32KOH_40°C	-2696 kJ/mol	Same value as calibrated for sample 0.33MK_0K_40°C leads to a maximum α = 0.95	H_1 = -257 kJ/mol H_2 = -197 kJ/mol
1MK_0.32KOH_40°C	-2715 kJ/mol	Realize better model fitting with experimental data (α_max = 0.7)	H_1 = -307 kJ/mol H_2 = -225 kJ/mol

8.4.3 Documentation of Supplementary MATLAB® File

The MATLAB® code for the calculation of the modeling results is provided in a separate file. The detailed documentation is done in the MATLAB® file and a short overview is given below.

Line 4-7 **Import calorimetry data**

Line 9-56 **Definition of relevant parameters**

Line 10: MK/CH weight ratio (mkch)

Line 11: water-to-solid weight ratio (ws)

Line 12: Formation enthalpy of the pozzolanic C-A-S-H phase (Hf_CASH)

Line 13: Definition of the transformation rate constant k (eq. 42)

Line 17-38: Kinetic modeling parameters from fitting of heat flow curves (vector) and initialization

Line 40-44: Definition of C-A-S-H composition of main (second) pozzolanic reaction (eq. 39)

Line 46-50: Definition of C-A-S-H composition of first pozzolanic reaction (eq. 38)

Line 52-56: Definition of C-A-S-H composition of transformation reaction (eq. 41)

Line 58-77 **Relevant material properties**

Line 58-68: Molar masses of relevant phases

Line 70-77: Densities of relevant phases

Line 79-123 **Initializing and discretization**

Line 79-81: Time discretization

Line 85-95: Initializing vectors for the relevant phases in mol/(g MK)

Line 97-105: Initializing vectors for the relevant phases in g/(g MK)

Line 107-114: Initializing vectors for the relevant phases in $cm^3/(g\ MK)$

Line 117: Initializing CH-consumption vector

Line 119-123: Initializing alpha vectors for the two pozzolanic reactions

Line 125-166 Calculation of the reacting moles of MK for the individual equations (kinetics)

Line 125-131: Formation enthalpies of the relevant phases

Line 133-135: Calculation of the theoretical heat of reactions for eq. 38 and eq. 39 according to Hesse Law

Line 137-140: Initializing of reacting phases vectors

Line 142-148: Calculation of the degree of MK reaction for the individual pozzolanic reactions based on the kinetic model (eq. 41)

Line 150-156: Calculation of the reacting moles of MK in each of the two pozzolanic reactions

Line 158-160: Calculation of the modeled heat flow from the two pozzolanic reactions

Line 162-166: Calculation of parameters for transformation reaction (eq. 40)

Line 171-224 Calculation of the phase assemblage according to the three stoichiometric reaction equations (eq. 38-40) for each timestep

Line 171-172: Calculation of the reacting moles in the transformation reaction according to eq. 42

Line 174-195: Calculation of the phase assemblage (in moles) according to eq. 38 (first pozzolanic reaction)

Line 197-211: Calculation of the phase assemblage (in moles) according to eq. 39 (second pozzolanic reaction)

Line 213-222: Calculation of the phase assemblage (in moles) according to eq. 40 (transformation of C_2ASH_8)

Line 224: Calculation of the consumed CH

Line 227-253 Recalculation to masses and volumes from the results in moles

Line 227-240: Calculation of the phase assemblage in g/(g MK)

Line 242-253: Calculation of the respective volumes of the phases in $cm^3/(g\ MK)$

Line 255-268 Calculation of the statistical value RMSD (root mean square deviation)

Line 270-595 Plotting the results

Line 597-603 Saving the results

References

[1] Tiseo. 2023. Carbon dioxide emissions from the manufacture of cement worldwide from 1960 to 2021. https://www.statista.com/statistics/1299532/carbon-dioxide-emissions-worldwide-cement-manufacturing/. Accessed 18 October 2023.

[2] IEA. 2018. Technology Roadmap. *Low-Carbon Transition in the Cement Industry*. https://www.iea.org/reports/technology-roadmap-low-carbon-transition-in-the-cement-industry. Accessed 18 October 2023.

[3] Flatt, Roussel, and Cheeseman. 2012. Concrete: An eco material that needs to be improved. *Journal of the European Ceramic Society* 32, 11, 2787–2798. https://doi.org/10.1016/j.jeurceramsoc.2011.11.012.

[4] Lee et al. 2023. IPCC, 2023: Climate Change 2023: Synthesis Report. Contribution of Working Groups I, II and III to the Sixth Assessment Report of the Intergovernmental Panel on Climate Change [Core Writing Team, H. Lee and J. Romero (eds.)]. IPCC, Geneva, Switzerland. https://doi.org/10.59327/IPCC/AR6-9789291691647.

[5] Bumanis, Korjakins, and Bajare. 2022. Environmental Benefit of Alternative Binders in Construction Industry: Life Cycle Assessment. *Environments* 9, 1. https://doi.org/10.3390/environments9010006.

[6] Turk et al. 2015. Environmental evaluation of green concretes versus conventional concrete by means of LCA. *Waste management (New York, N.Y.)* 45, 194–205. https://doi.org/10.1016/j.wasman.2015.06.035.

[7] Beuntner. 2017. Zur Eignung und Wirkungsweise calcinierter Tone als reaktive Bindemittelkomponente im Zement, *Universität der Bundeswehr München*.

[8] Trümer. 2020. Calcinierte Tone als Puzzolane der Zukunft - Von den Rohstoffen bis zur Wirkung im Beton. *Dissertation, Bauhaus-Universität Weimar*.

[9] Danner. 2013. Reactivity of Calcined Clays. *Dissertation, Norwegian University of Science and Technology*.

[10] Ito, A. & Wagai, R. 2017. Global distribution of clay-size minerals on land surface for biogeochemical and climatological studies. *Sci Data,* 4.

[11] He, Osbaeck, and Makovicky. 1995. Pozzolanic reactions of six principal clay minerals: Activation, reactivity assessments and technological effects. *Cement and Concrete Research,* 25, 1691–1702. https://doi.org/10.1016/0008-8846(95)00165-4.

[12] Hollanders et al. 2016. Pozzolanic reactivity of pure calcined clays. *Applied Clay Science,* 132-133, 552–560. https://doi.org/10.1016/j.clay.2016.08.003.

[13] Berriel et al. 2015. Assessment of Sustainability of Low Carbon Cement in Cuba. Cement Pilot Production and Prospective Case. In *Calcined Clays for Sustainable Concrete*, K. Scrivener and A. Favier, Eds. RILEM Bookseries. Springer Netherlands, Dordrecht, 189–194. https://doi.org/10.1007/978-94-017-9939-3_23.

[14] Thienel and Beuntner. 2012. Effects of Calcined Clay as Low Carbon Cementing Materials on the Properties of Concrete, Dundee.

[15] Weise. 2020. Über das Potenzial von calciniertem Ton in zementgebundenen Systemen. Springer Vieweg.

[16] Fernandez, Martirena, and Scrivener. 2011. The origin of the pozzolanic activity of calcined clay minerals: A comparison between kaolinite, illite and montmorillonite. *Cement and Concrete Research,* 41, 113–122. https://doi.org/10.1016/j.cemconres.2010.09.013.

[17] Bratoev et al. 2018. Pozzolanic activity assessment of calcined clays with complex minerals content. *Advances in Cement Research* 30, 3, 103–112. https://doi.org/10.1680/jadcr.17.00057.

[18] Maier, Beuntner, and Thienel. 2020. An Approach for the Evaluation of Local Raw Material Potential for Calcined Clay as SCM, Based on Geological and Mineralogical Data: Examples from German Clay Deposits. In *Calcined Clays for Sustainable Concrete*, S. Bishnoi, Ed. RILEM Bookseries. Springer Singapore, Singapore, 37–47. https://doi.org/10.1007/978-981-15-2806-4_5.

[19] Zunino et al. 2022. Hydration and mixture design of calcined clay blended cements: review by the RILEM TC 282-CCL. *Mater Struct* 55, 9. https://doi.org/10.1617/s11527-022-02060-1.
[20] Cardinaud et al. 2021. Calcined clay – Limestone cements: Hydration processes with high and low-grade kaolinite clays. *Construction and Building Materials* 277, 122271. https://doi.org/10.1016/j.conbuildmat.2021.122271.
[21] Christian Ramadji et al. Microstructural Analysis of the Reactivity Parameters of Calcined Clays.
[22] Piga. 1995. Thermogravimetry of a kaolinite-alunite ore. *Thermochimica Acta* 265, 177–187. https://doi.org/10.1016/0040-6031(95)02429-6.
[23] Shvarzman et al. 2003. The effect of dehydroxylation/amorphization degree on pozzolanic activity of kaolinite. *Cement and Concrete Research* 33, 3, 405–416. https://doi.org/10.1016/S0008-8846(02)00975-4.
[24] Sperinck et al. 2011. Dehydroxylation of kaolinite to metakaolin—a molecular dynamics study. *J. Mater. Chem.* 21, 7, 2118–2125. https://doi.org/10.1039/C0JM01748E.
[25] Ilic, Mitrović, and Ljiljana. 2010. Thermal treatment of kaolin clay to obtain metakaolin. *Hemijska Industrija* 64, 4, 351–356. https://doi.org/10.2298/HEMIND100322014I.
[26] Hanein et al. 2022. Clay calcination technology: state-of-the-art review by the RILEM TC 282-CCL. *Mater Struct* 55, 1. https://doi.org/10.1617/s11527-021-01807-6.
[27] Konan et al. 2009. Comparison of surface properties between kaolin and metakaolin in concentrated lime solutions. *Journal of colloid and interface science* 339, 1, 103–109. https://doi.org/10.1016/j.jcis.2009.07.019.
[28] Fernandez, Martirena, and Scrivener. 2011. The origin of the pozzolanic activity of calcined clay minerals: A comparison between kaolinite, illite and montmorillonite. *Cement and Concrete Research* 41, 1, 113–122. https://doi.org/10.1016/j.cemconres.2010.09.013.
[29] Garg and Skibsted. 2019. Dissolution kinetics of calcined kaolinite and montmorillonite in alkaline conditions: Evidence for reactive Al(V) sites. *J Am Ceram Soc* 102, 12, 7720–7734. https://doi.org/10.1111/jace.16663.
[30] Li, Sun, and Li. 2010. A review: The comparison between alkali-activated slag (Si+Ca) and metakaolin (Si+Al) cements. *Cement and Concrete Research* 40, 9, 1341–1349. https://doi.org/10.1016/j.cemconres.2010.03.020.
[31] Hanzlíček and Steinerová-Vondráková. 2002. Investigation of dissolution of alumosilicates in aqueous alkaline solution under laboratory conditions. *Ceramics-Silikáty* 46, 3, 97–103.
[32] Romero and Garg. 2022. Evolution of kaolinite morphology upon exfoliation and dissolution: Evidence for nanoscale layer thinning in metakaolin. *Applied Clay Science* 222, 106486. https://doi.org/10.1016/j.clay.2022.106486.
[33] Da Silva Andrade et al. 2018. Chemical and mechanical characterization of ternary cement pastes containing metakaolin and nanosilica. *Construction and Building Materials* 159, 18–26. https://doi.org/10.1016/j.conbuildmat.2017.10.123.
[34] Figueiredo et al. 2014. O papel do metacaulim na proteção dos concretos contra a ação deletéria de cloretos. *Rev. IBRACON Estrut. Mater.* 7, 4, 685–708. https://doi.org/10.1590/S1983-41952014000400008.
[35] Tongbo et al. 2015. Meta-Kaolin for High Performance Concrete. In *Calcined Clays for Sustainable Concrete*, K. Scrivener and A. Favier, Eds. RILEM Bookseries. Springer Netherlands, Dordrecht, 467–477. https://doi.org/10.1007/978-94-017-9939-3_58.
[36] Khater. 2011. Influence of Metakaolin on Resistivity of Cement Mortar to Magnesium Chloride Solution. *J. Mater. Civ. Eng.* 23, 9, 1295–1301. https://doi.org/10.1061/(ASCE)MT.1943-5533.0000294.
[37] Barbhuiya, Chow, and Memon. 2015. Microstructure, hydration and nanomechanical properties of concrete containing metakaolin. *Construction and Building Materials* 95, 696–702. https://doi.org/10.1016/j.conbuildmat.2015.07.101.
[38] Sfikas, Badogiannis, and Trezos. 2014. Rheology and mechanical characteristics of self-compacting concrete mixtures containing metakaolin. *Construction and Building Materials* 64, 121–129. https://doi.org/10.1016/j.conbuildmat.2014.04.048.

[39] Abiodun et al. 2022. Cutting Cement Industry CO2 Emissions through Metakaolin Use in Construction. *Atmosphere* 13, 9, 1494. https://doi.org/10.3390/atmos13091494.
[40] Abdelli et al. 2017. Influence of the pozzolanic reactivity of the Blast Furnace Slag (BFS) and metakaolin on mortars. *Energy Procedia* 139, 224–229. https://doi.org/10.1016/j.egypro.2017.11.200.
[41] Ramezanianpour and Bahrami Jovein. 2012. Influence of metakaolin as supplementary cementing material on strength and durability of concretes. *Construction and Building Materials* 30, 470–479. https://doi.org/10.1016/j.conbuildmat.2011.12.050.
[42] Wild and Khatib. 1997. Portlandite consumption in metakaolin cement pastes and mortars. *Cement and Concrete Research* 27, 1, 137–146. https://doi.org/10.1016/S0008-8846(96)00187-1.
[43] Justice and Kurtis. 2007. Influence of Metakaolin Surface Area on Properties of Cement-Based Materials. *J. Mater. Civ. Eng.* 19, 9, 762–771. https://doi.org/10.1061/(ASCE)0899-1561(2007)19:9(762).
[44] Aramburo, Pedrajas, and Talero. 2020. Portland Cements with High Content of Calcined Clay: Mechanical Strength Behaviour and Sulfate Durability. *Materials (Basel, Switzerland)* 13, 18. https://doi.org/10.3390/ma13184206.
[45] Tironi et al. 2014. Kaolinitic calcined clays – Portland cement system: Hydration and properties. *Construction and Building Materials* 64, 215–221. https://doi.org/10.1016/j.conbuildmat.2014.04.065.
[46] SANTOS, ALBUQUERQUE, and RIBEIRO. 2020. Effect of the addition of metakaolin on the carbonation of Portland cement concretes. *Rev. IBRACON Estrut. Mater.* 13, 1, 1–18. https://doi.org/10.1590/S1983-41952020000100002.
[47] Saji and Unnikrishnan. 2023. Effect of Dolomite and Metakaolin on the Properties of High-Performance Concrete. *IOP Conf. Ser.: Earth Environ. Sci.* 1237, 1, 12005. https://doi.org/10.1088/1755-1315/1237/1/012005.
[48] Dubey, Deo, and Ramtekkar. 2023. Accelerated curing effects on performance of metakaolin concrete. *IRASE* 14, 3, 342–348. https://doi.org/10.1556/1848.2022.00558.
[49] Parashar and Bishnoi. 2024. Influence of the availability of calcium hydroxide, sulphates, and alkalis on hydration of supplementary cementitious materials. *Cement and Concrete Research* 175, 107388. https://doi.org/10.1016/j.cemconres.2023.107388.
[50] Serry et al. 1984. Metakaolin-Lime Hydration Products. *Thermochimica Acta,* 79 (1984), 103–110.
[51] Murat. 1983. Hydration reaction and hardening of calcined clays and related minerals. I. Preliminary investigation on metakaolinite. *Cement and Concrete Research* 13, 2, 259–266. https://doi.org/10.1016/0008-8846(83)90109-6.
[52] He, Osbaeck, and Makovicky. 1995. Pozzolanic reactions of six principal clay minerals: Activation, reactivity assessments and technological effects. *Cement and Concrete Research* 25, 8, 1691–1702. https://doi.org/10.1016/0008-8846(95)00165-4.
[53] Frías and Cabrera. 2001. Influence of MK on the reaction kinetics in MK/lime and MK-blended cement systems at 20°C. *Cement and Concrete Research* 31, 4, 519–527. https://doi.org/10.1016/S0008-8846(00)00465-8.
[54] Gameiro et al. 2012. Lime-metakaolin hydration products: a microscopy analysis. *Materials and Technologies* 46, 2.
[55] Frías et al. 2013. Evolution of Mineralogical Phases by 27 Al and 29 Si NMR in MK-Ca(OH) 2 System Cured at 60°C. *J. Am. Ceram. Soc.* 96, 7, 2306–2310. https://doi.org/10.1111/jace.12274.
[56] Bakolas et al. 2006. Evaluation of pozzolanic activity and physicomechanical characteristics in metakaolin-lime pastes. *J Therm Anal Calorim* 84, 1, 157–163. https://doi.org/10.1007/s10973-005-7262-y.
[57] Rojas. 2006. Study of hydrated phases present in a MK–lime system cured at 60 °C and 60 months of reaction. *Cement and Concrete Research* 36, 5, 827–831. https://doi.org/10.1016/j.cemconres.2006.01.001.

[58] Zemlicka et al. 2015. Study of hydration products in the model systems metakaolin-lime and metakaolin-lime-gypsum. *Ceramics Silikaty* 59, 4, 283–291.
[59] De Silva and Glasser. 1992. Pozzolanic activation of metakaolin. *Advances in Cement Research* 4, 16, 167–178. https://doi.org/10.1680/adcr.1992.4.16.167.
[60] Pesce et al. 2014. Monitoring hydration in lime-metakaolin composites using electrochemical impedance spectroscopy and nuclear magnetic resonance spectroscopy. *Clay miner.* 49, 3, 341–358. https://doi.org/10.1180/claymin.2014.049.3.01.
[61] Morsy et al. 2017. Mechanical Properties, Phase Composition and Microstructure of Activated Metakaolin-slaked Lime Binder. *KSCE Journal of Civil Engineering* 21, 3, 863–871. https://doi.org/10.1007/s12205-016-0667-2.
[62] Deng et al. 2020. The effect of activators on the dissolution characteristics and occurrence state of aluminum of alkali-activated metakaolin. *Construction and Building Materials* 235, 117451. https://doi.org/10.1016/j.conbuildmat.2019.117451.
[63] Fernández et al. 2010. Mineralogical and chemical evolution of hydrated phases in the pozzolanic reaction of calcined paper sludge. *Cement and Concrete Composites* 32, 10, 775–782. https://doi.org/10.1016/j.cemconcomp.2010.08.003.
[64] Gameiro et al. 2012. Phase and Microstructural Characterization of Lime-MK Blended Mixes 730-732, 135–140. https://doi.org/10.4028/www.scientific.net/MSF.730-732.135.
[65] Silva et al. 2014. Long-term behavior of lime–metakaolin pastes at ambient temperature and humid curing condition. *Applied Clay Science* 88-89, 49–55. https://doi.org/10.1016/j.clay.2013.12.016.
[66] Wang et al. 2019. Chloride binding behaviors of metakaolin-lime hydrated blends: Influence of gypsum and atmospheric carbonation. *Construction and Building Materials* 201, 380–390. https://doi.org/10.1016/j.conbuildmat.2018.12.162.
[67] Tydlitát et al. 2015. Application of isothermal calorimetry and thermal analysis for the investigation of calcined gypsum–lime–metakaolin–water system. *J Therm Anal Calorim* 122, 1, 115–122. https://doi.org/10.1007/s10973-015-4727-5.
[68] Gameiro et al. 2012. Hydration products of lime–metakaolin pastes at ambient temperature with ageing. *Thermochimica Acta* 535, 36–41. https://doi.org/10.1016/j.tca.2012.02.013.
[69] De Silva and Glasser. 1993. Phase relations in the system CaO-Al2O3-SiO2-H2O relevant to metakaolin - calcium hydroxide hydration. *Cement and Concrete Research* 23, 3, 627–639. https://doi.org/10.1016/0008-8846(93)90014-Z.
[70] Rojas and Sánchez de Rojas. 2003. The effect of high curing temperature on the reaction kinetics in MK/lime and MK-blended cement matrices at 60 °C. *Cement and Concrete Research* 33, 5, 643–649. https://doi.org/10.1016/S0008-8846(02)01040-2.
[71] Rojas and Cabrera. 2002. The effect of temperature on the hydration rate and stability of the hydration phases of metakaolin–lime–water systems. *Cement and Concrete Research* 32, 1, 133–138. https://doi.org/10.1016/S0008-8846(01)00642-1.
[72] Azeredo, Struble, and Carneiro. 2015. Microstructural characteristics of lime-pozzolan pastes made from kaolin production wastes. *Mater Struct* 48, 7, 2123–2132. https://doi.org/10.1617/s11527-014-0297-4.
[73] Ambroise, Murat, and Pera. 1985. Hydration reaction and hardening of calcined clays and related minerals. IV. Experimental conditions for strength improvement on metakaolinite minicylinders. *Cement and Concrete Research* 15 (1985), 83–88.
[74] Cabrera and Rojas. 2001. Mechanism of hydration of the metakaolin–lime–water system. *Cement and Concrete Research* 31, 2, 177–182. https://doi.org/10.1016/S0008-8846(00)00456-7.
[75] De Silva and Glasser. 1990. Hydration of cements based on metakaolin: thermochemistry. *Advances in Cement Research* 3, 12, 167–177. https://doi.org/10.1680/adcr.1990.3.12.167.
[76] Beuntner and Thienel. 2016. Solubility and kinetics of calcined clay: study of interaction by pore solution, München.
[77] Kunther, Dai, and Skibsted. 2015. Thermodynamic Modeling of Portland Cement—Metakaolin—Limestone Blends. In *Calcined Clays for Sustainable Concrete*, K. Scrivener and A. Favier, Eds.

RILEM Bookseries. Springer Netherlands, Dordrecht, 143–149. https://doi.org/10.1007/978-94-017-9939-3_18.
[78] Damidot and Glasser. 1995. Investigation of the CaO-Al2O3-SiO2-H2O system at 25 °C by thermodynamic calculations. *Cement and Concrete Research* 25, 1, 22–28. https://doi.org/10.1016/0008-8846(94)00108-B.
[79] Weise, Ukrainczyk, and Koenders. 2023. Pozzolanic Reactions of Metakaolin with Calcium Hydroxide: Review on Hydrate Phase Formations and Effect of Alkali Hydroxides, Carbonates and Sulfates. *Materials & Design* 231, 112062. https://doi.org/10.1016/j.matdes.2023.112062.
[80] Zajac et al. 2018. Influence of calcium and magnesium carbonates on hydration kinetics, hydrate assemblage and microstructural development of metakaolin containing composite cements. *Cement and Concrete Research* 106, 91–102. https://doi.org/10.1016/j.cemconres.2018.01.008.
[81] Zunino et al. 2022. Hydration and mixture design of calcined clay blended cements: review by the RILEM TC 282-CCL. *Mater Struct* 55, 9. https://doi.org/10.1617/s11527-022-02060-1.
[82] Weise et al. 2023. R3-Test for Pozzolanic Reactivity: Experimental Issues and Practical Recommendations for Hydration Stoppage with Isopropanol. In *International RILEM Conference on Synergising Expertise towards Sustainability and Robustness of Cement-based Materials and Concrete Structures*, A. Jędrzejewska, F. Kanavaris, M. Azenha, F. Benboudjema and D. Schlicke, Eds. RILEM Bookseries. Springer Nature Switzerland, Cham, 55–64. https://doi.org/10.1007/978-3-031-33187-9_6.
[83] Weise, Ukrainczyk, and Koenders. 2023. Early metakaolin reactions in pozzolanic R3-test: calorimetry baseline correction of initial temperature jump due to ex-situ mixing. *Mater Struct* 56, 7. https://doi.org/10.1617/s11527-023-02217-6.
[84] Weise, Ukrainczyk, and Koenders. 2021. A Mass Balance Approach for Thermogravimetric Analysis in Pozzolanic Reactivity R3 Test and Effect of Drying Methods. *Materials (Basel, Switzerland)* 14, 19. https://doi.org/10.3390/ma14195859.
[85] Avet et al. 2022. Report of RILEM TC 267-TRM phase 2: optimization and testing of the robustness of the R3 reactivity tests for supplementary cementitious materials. *Mater Struct* 55, 3. https://doi.org/10.1617/s11527-022-01928-6.
[86] Londono-Zuluaga et al. 2022. Report of RILEM TC 267-TRM phase 3: validation of the R3 reactivity test across a wide range of materials. *Mater Struct* 55, 5. https://doi.org/10.1617/s11527-022-01947-3.
[87] Avet et al. 2016. Development of a new rapid, relevant and reliable (R3) test method to evaluate the pozzolanic reactivity of calcined kaolinitic clays. *Cement and Concrete Research* 85, 1–11. https://doi.org/10.1016/j.cemconres.2016.02.015.
[88] Singh. 2022. Clays and Clay Minerals in the Construction Industry. *Minerals* 12, 3, 301. https://doi.org/10.3390/min12030301.
[89] Kavitha et al. 2016. Microstructural studies on eco-friendly and durable Self-compacting concrete blended with metakaolin. *Applied Clay Science* 124-125, 143–149. https://doi.org/10.1016/j.clay.2016.02.011.
[90] Madandoust and Mousavi. 2012. Fresh and hardened properties of self-compacting concrete containing metakaolin. *Construction and Building Materials* 35, 752–760. https://doi.org/10.1016/j.conbuildmat.2012.04.109.
[91] Arikan et al. 2009. Properties of blended cements with thermally activated kaolin. *Construction and Building Materials* 23, 1, 62–70. https://doi.org/10.1016/j.conbuildmat.2008.02.008.
[92] Hwalla, Saba, and Assaad. 2020. Suitability of metakaolin-based geopolymers for underwater applications. *Mater Struct* 53, 5. https://doi.org/10.1617/s11527-020-01546-0.
[93] Thankam and Thurvas Renganathan. 2020. Ideal supplementary cementing material – Metakaolin: A review. *IRASE* 11, 1, 58–65. https://doi.org/10.1556/1848.2020.00008.
[94] Li et al. 2022. Natural hydraulic lime versus lime-metakaolin modified silt in earthen heritages. *Mater Struct* 55, 7. https://doi.org/10.1617/s11527-022-02034-3.
[95] Frías, Sánchez de Rojas, and Cabrera. 2000. The effect that the pozzolanic reaction of metakaolin has on the heat evolution in metakaolin-cement mortars. *Cement and Concrete Research* 30, 2, 209–216. https://doi.org/10.1016/S0008-8846(99)00231-8.

[96] Tironi et al. 2013. Assessment of pozzolanic activity of different calcined clays. *Cement and Concrete Composites* 37, 319–327. https://doi.org/10.1016/j.cemconcomp.2013.01.002.
[97] Wang. 2017. Analysis of Hydration-Mechanical-Durability Properties of Metakaolin Blended Concrete. *Applied Sciences* 7, 10, 1087. https://doi.org/10.3390/app7101087.
[98] Cassagnabère, Escadeillas, and Mouret. 2009. Study of the reactivity of cement/metakaolin binders at early age for specific use in steam cured precast concrete. *Construction and Building Materials* 23, 2, 775–784. https://doi.org/10.1016/j.conbuildmat.2008.02.022.
[99] Dong et al. 2022. Investigating the Mechanical Properties and Durability of Metakaolin-Incorporated Mortar by Different Curing Methods. *Materials (Basel, Switzerland)* 15, 6. https://doi.org/10.3390/ma15062035.
[100] Zhang and Malhotra. 1995. Characteristics of a thermally activated alumino-silicate pozzolanic material and its use in concrete. *Cement and Concrete Research* 25, 8, 1713–1725. https://doi.org/10.1016/0008-8846(95)00167-0.
[101] Schulze and Rickert. 2019. Suitability of natural calcined clays as supplementary cementitious material. *Cement and Concrete Composites* 95, 92–97. https://doi.org/10.1016/j.cemconcomp.2018.07.006.
[102] Maier, Beuntner, and Thienel. 2021. Mineralogical characterization and reactivity test of common clays suitable as supplementary cementitious material. *Applied Clay Science* 202, 105990. https://doi.org/10.1016/j.clay.2021.105990.
[103] Avet and Scrivener. 2018. Investigation of the calcined kaolinite content on the hydration of Limestone Calcined Clay Cement (LC3). *Cement and Concrete Research* 107, 124–135. https://doi.org/10.1016/j.cemconres.2018.02.016.
[104] Hollanders et al. 2016. Pozzolanic reactivity of pure calcined clays. *Applied Clay Science* 132-133, 552–560. https://doi.org/10.1016/j.clay.2016.08.003.
[105] Scherb, Beuntner, and Thienel. 2018. Reaction Kinetics of Basic Clay Components Present in Natural Mixed Clays. In *Calcined Clays for Sustainable Concrete*, F. Martirena, A. Favier and K. Scrivener, Eds. RILEM Bookseries. Springer Netherlands, Dordrecht, 427–433. https://doi.org/10.1007/978-94-024-1207-9_69.
[106] Beuntner and Thienel. 2022. Pozzolanic efficiency of calcined clays in blended cements with a focus on early hydration. *Advances in Cement Research*, 1–15. https://doi.org/10.1680/jadcr.21.00034.
[107] Scherb et al. 2021. Reaction kinetics during early hydration of calcined phyllosilicates in clinker-free model systems. *Cement and Concrete Research* 143, 106382. https://doi.org/10.1016/j.cemconres.2021.106382.
[108] Aiswarya, Prince Arulraj, and Dilip. 2013. A Review on Use of Metakaolin in Concrete. *IRACST - Engineering Science and Technology: An International Journal (ESTIJ)* 3, 3 (2013), 592–597. https://doi.org/10.2307/j.ctt46nrzt.12.
[109] Homayoonmehr, Ramezanianpour, and Mirdarsoltany. 2021. Influence of metakaolin on fresh properties, mechanical properties and corrosion resistance of concrete and its sustainability issues: A review. *Journal of Building Engineering* 44, 103011. https://doi.org/10.1016/j.jobe.2021.103011.
[110] Raheem, Abdulwahab, and Kareem. 2021. Incorporation of metakaolin and nanosilica in blended cement mortar and concrete- A review. *Journal of Cleaner Production* 290, 125852. https://doi.org/10.1016/j.jclepro.2021.125852.
[111] Brooks and Megat Johari. 2001. Effect of metakaolin on creep and shrinkage of concrete. *Cement and Concrete Composites* 23, 6, 495–502. https://doi.org/10.1016/S0958-9465(00)00095-0.
[112] Si-Ahmed, Belakrouf, and Kenai. 2012. Influence Of Metakaolin On The Performance Of Mortars And Concretes. *International Journal of Civil and Environmental Engineering* 6, 11, 1010–1013. https://doi.org/10.5281/ZENODO.1331725.
[113] Sabir, Wild, and Bai. 2001. Metakaolin and calcined clays as pozzolans for concrete: a review. *Cement and Concrete Composites* 23, 6, 441–454. https://doi.org/10.1016/S0958-9465(00)00092-5.

[114] Siddique and Klaus. 2009. Influence of metakaolin on the properties of mortar and concrete: A review. *Applied Clay Science* 43, 3-4, 392–400. https://doi.org/10.1016/j.clay.2008.11.007.
[115] Mo, Wang, and Gao. 2020. Hydration and mechanical properties of UHPC matrix containing limestone and different levels of metakaolin. *Construction and Building Materials* 256, 119454. https://doi.org/10.1016/j.conbuildmat.2020.119454.
[116] Potapova and Dmitrieva. 2019. The effect of metakaolin on the processes of hydration and hardening of cement. *Materials Today: Proceedings* 19, 2193–2196. https://doi.org/10.1016/j.matpr.2019.07.373.
[117] Li et al. 2022. Influence of metakaolin on the hydration and microstructure evolution of cement paste during the early stage. *Applied Clay Science* 229, 106674. https://doi.org/10.1016/j.clay.2022.106674.
[118] Zhang et al. 2023. Evaluation of the environmental medium erosion resistance of natural hydraulic lime and metakaolin-air lime mortars. *Case Studies in Construction Materials* 18, e02044. https://doi.org/10.1016/j.cscm.2023.e02044.
[119] Rashad. 2013. Metakaolin as cementitious material: History, scours, production and composition – A comprehensive overview. *Construction and Building Materials* 41, 303–318. https://doi.org/10.1016/j.conbuildmat.2012.12.001.
[120] Daher et al. 2023. Performance Improved of a Lime and Hemp-Based Concrete through the Addition of Metakaolin. *Fluid Dynamics & Materials Processing* 19, 5, 1091–1113. https://doi.org/10.32604/fdmp.2023.020348.
[121] Loureiro et al. 2020. Assessment of compatibility between historic mortars and lime-METAKAOLIN restoration mortars made from amazon industrial waste. *Applied Clay Science* 198, 105843. https://doi.org/10.1016/j.clay.2020.105843.
[122] Aggelakopoulou, Ksinopoulou, and Eleftheriou. 2022. Evaluation of mortar mix designs for the conservation of the Acropolis monuments. *Journal of Cultural Heritage* 55, 300–308. https://doi.org/10.1016/j.culher.2022.04.004.
[123] Monteiro, Silva, and Faria. 2021. Effect of Type of Curing and Metakaolin Replacement on Air Lime Mortars for the Durability of Masonries. *Infrastructures* 6, 10, 143. https://doi.org/10.3390/infrastructures6100143.
[124] Vejmelková et al. 2012. Mechanical, fracture-mechanical, hydric, thermal, and durability properties of lime–metakaolin plasters for renovation of historical buildings. *Construction and Building Materials* 31, 22–28. https://doi.org/10.1016/j.conbuildmat.2011.12.084.
[125] Velosa and Veiga. Lime-metakaolin mortars - Properties and applications.
[126] Qiao et al. 2022. Enhanced mechanical properties and environmental erosion resistance with metakaolin in a kind of Chinese traditional Lime-based mortar. *Construction and Building Materials* 317, 126110. https://doi.org/10.1016/j.conbuildmat.2021.126110.
[127] Zhang et al. 2022. Effect of water to binder ratio, polycarboxylate superplasticizer and metakaolin dosages on rheological and viscoelastic properties of fresh metakaolin-air lime pastes. *Journal of Building Engineering* 62, 105351. https://doi.org/10.1016/j.jobe.2022.105351.
[128] Aggelakopoulou, Bakolas, and Moropoulou. 2011. Properties of lime–metakolin mortars for the restoration of historic masonries. *Applied Clay Science* 53, 1, 15–19. https://doi.org/10.1016/j.clay.2011.04.005.
[129] Andrejkovičová et al. 2014. Influence of clay minerals addition on mechanical properties of air lime–metakaolin mortars. *Construction and Building Materials* 65, 132–139. https://doi.org/10.1016/j.conbuildmat.2014.04.118.
[130] Arizzi and Cultrone. 2012. Aerial lime-based mortars blended with a pozzolanic additive and different admixtures: A mineralogical, textural and physical-mechanical study. *Construction and Building Materials* 31, 135–143. https://doi.org/10.1016/j.conbuildmat.2011.12.069.
[131] Gameiro et al. 2014. Physical and chemical assessment of lime–metakaolin mortars: Influence of binder:aggregate ratio. *Cement and Concrete Composites* 45, 264–271. https://doi.org/10.1016/j.cemconcomp.2013.06.010.

[132] Pavlík and Užáková. 2016. Effect of curing conditions on the properties of lime, lime–metakaolin and lime–zeolite mortars. *Construction and Building Materials* 102, 14–25. https://doi.org/10.1016/j.conbuildmat.2015.10.128.
[133] Grilo et al. 2014. New natural hydraulic lime mortars – Physical and microstructural properties in different curing conditions. *Construction and Building Materials* 54, 378–384. https://doi.org/10.1016/j.conbuildmat.2013.12.078.
[134] Espitia Morales and Torres Castellanos. 2022. Assessment of the Compressive Strength of Lime Mortars with Admixtures, Subjected to Two Curing Environments. *Ing. Inv.* 42, 2, e91364. https://doi.org/10.15446/ing.investig.91364.
[135] Zhang et al. 2020. Assessment of the thermal and microstructural properties of metakaolin-air lime based materials at an early age. *Applied Clay Science* 191, 105619. https://doi.org/10.1016/j.clay.2020.105619.
[136] C09 Committee. Standard Test Methods for Measuring the Reactivity of Supplementary Cementitious Materials by Isothermal Calorimetry and Bound Water Measurements. ASTM International, West Conshohocken, PA.
[137] Bharadwaj, Isgor, and Weiss. 2023. Pozzolanic Reactivity of Supplementary Cementitious Materials. *Materials Journal. https://doi.org/*10.14359/51738817.
[138] Parashar et al. 2022. Report of RILEM TC 267—TRM: Improvement and robustness study of lime mortar strength test for assessing reactivity of SCMs. *Mater Struct* 55, 3. https://doi.org/10.1617/s11527-022-01911-1.
[139] Kakali et al. 2001. Thermal treatment of kaolin: the effect of mineralogy on the pozzolanic activity. *Applied Clay Science* 20, 1-2, 73–80. https://doi.org/10.1016/S0169-1317(01)00040-0.
[140] Valentini et al. 2015. In-Situ XRD Measurement and Quantitative Analysis of Hydrating Cement: Implications for Sulfate Incorporation in C-S-H. *J. Am. Ceram. Soc.* 98, 4, 1259–1264. https://doi.org/10.1111/jace.13401.
[141] Badogiannis, Kakali, and Tsivilis. 2005. Metakaolin as supplementary cementitious material - Optimization of kaolin to metakaolin conversion. *Journal of Thermal Analysis and Calorimetry,* 81, 457–462. https://doi.org/10.1007/s10973-005-0806-3.
[142] Izadifar et al. 2020. Comprehensive Examination of Dehydroxylation of Kaolinite, Disordered Kaolinite, and Dickite: experimental Studies and Density Functional Theory. *Clays Clay Miner.* 68, 4, 319–333. https://doi.org/10.1007/s42860-020-00082-w.
[143] Zunino and Scrivener. 2021. The reaction between metakaolin and limestone and its effect in porosity refinement and mechanical properties. *Cement and Concrete Research* 140, 106307. https://doi.org/10.1016/j.cemconres.2020.106307.
[144] Matschei, Lothenbach, and Glasser. 2007. The AFm phase in Portland cement. *Cement and Concrete Research* 37, 2, 118–130. https://doi.org/10.1016/j.cemconres.2006.10.010.
[145] Tironi et al. 2014. Thermal analysis to assess pozzolanic activity of calcined kaolinitic clays. *J Therm Anal Calorim* 117, 2, 547–556. https://doi.org/10.1007/s10973-014-3816-1.
[146] Herrmann, Koenig, and Dehn. 2017. Structural concrete based on alkali-activated binders: Terminology, reaction mechanisms, mix designs and performance. *Structural Concrete* 19, 3, 918–929. https://doi.org/10.1002/suco.201700016.
[147] Boonjaeng, Chindaprasirt, and Pimraksa. 2014. Lime-calcined clay materials with alkaline activation: Phase development and reaction transition zone. *Applied Clay Science* 95, 357–364. https://doi.org/10.1016/j.clay.2014.05.002.
[148] Alujas Diaz et al. 2022. Properties and occurrence of clay resources for use as supplementary cementitious materials: a paper of RILEM TC 282-CCL. *Mater Struct* 55, 5. https://doi.org/10.1617/s11527-022-01972-2.
[149] Souri et al. 2015. Pozzolanic activity of mechanochemically and thermally activated kaolins in cement. *Cement and Concrete Research* 77, 47–59. https://doi.org/10.1016/j.cemconres.2015.04.017.
[150] Balek and Murat. 1996. The emanation thermal analysis of kaolinite clay minerals. *Thermochimica Acta* 282-283, 385–397. https://doi.org/10.1016/0040-6031(96)02886-9.

[151] Fripiat and Toussaint. 1963. Dehydroxylation of Kaolinite. II. Conductometric Measurements and Infrared Spectroscopy. *J. Phys. Chem.* 67, 1, 30–36. https://doi.org/10.1021/j100795a008.
[152] Kaloumenou et al. 1999. Effect of the Kaolin Particle Size on the Pozzolanic Behaviour of the Metakaolinite Produced. *J Therm Anal Calorim* 56, 2, 901–907. https://doi.org/10.1023/A:1010143214686.
[153] Souri et al. 2015. An investigation on pozzolanic activity of Iranian kaolins obtained by thermal treatment. *Applied Clay Science* 103, 34–39. https://doi.org/10.1016/j.clay.2014.11.001.
[154] Bellotto et al. 1995. Kinetic study of the kaolinite-mullite reaction sequence. Part I: Kaolinite dehydroxylation. *Phys Chem Minerals* 22, 4. https://doi.org/10.1007/BF00202253.
[155] Ptáček et al. 2014. Kinetics and mechanism of three stages of thermal transformation of kaolinite to metakaolinite. *Powder Technology* 264, 439–445. https://doi.org/10.1016/j.powtec.2014.05.047.
[156] Alujas et al. 2015. Pozzolanic reactivity of low grade kaolinitic clays: Influence of calcination temperature and impact of calcination products on OPC hydration. *Applied Clay Science* 108, 94–101. https://doi.org/10.1016/j.clay.2015.01.028.
[157] Valentini. 2018. Modeling Dissolution-Precipitation Kinetics of Alkali-Activated Metakaolin. *ACS omega* 3, 12, 18100–18108. https://doi.org/10.1021/acsomega.8b02380.
[158] Abo-El-Enein, Abbas, and Ezzat. 2010. Propiedades y durabilidad de los cementos adicionados con metacaolín. *Mater. construcc.* 60, 299, 21–35. https://doi.org/10.3989/mc.2010.50509.
[159] Lei and Plank. 2014. A study on the impact of different clay minerals on the dispersing force of conventional and modified vinyl ether based polycarboxylate superplasticizers. *Cement and Concrete Research* 60, 1–10. https://doi.org/10.1016/j.cemconres.2014.02.009.
[160] Ekosse. 2001. Provenance of the Kgwakgwe kaolin deposit in Southeastern Botswana and its possible utilization. *Applied Clay Science* 20, 3, 137–152. https://doi.org/10.1016/S0169-1317(01)00064-3.
[161] Brindley and NAKAHIRA. 1958. A New Concept of the Transformation Sequence of Kaolinite to Mullite. *Nature* 181, 4619, 1333–1334. https://doi.org/10.1038/1811333a0.
[162] Rashad. 2013. Metakaolin as cementitious material: History, scours, production and composition – A comprehensive overview. *Construction and Building Materials* 41, 303–318. https://doi.org/10.1016/j.conbuildmat.2012.12.001.
[163] Wardle and Brindley. 1972. The crystal structures of pyrophyllite, 1Tc, and of its dehydroxylate. *American Mineralogist,* 57 (1972), 732–750.
[164] White et al. 2010. Density functional modeling of the local structure of kaolinite subjected to thermal dehydroxylation. *The journal of physical chemistry. A* 114, 14, 4988–4996. https://doi.org/10.1021/jp911108d.
[165] Davidovits. 2020. Geopolymer chemistry and applications. Institut Géopolymère, Saint-Quentin.
[166] J. Davidovits. 2017. Geopolymers: Ceramic-Like Inorganic Polymers, 03. https://doi.org/10.4416/JCST2017-00038.
[167] Coleman and Mcwhinnie. 2000. The solid state chemistry of metakaolin-blended ordinary Portland cement. *Journal of Materials Science* 35, 2701–2710. https://doi.org/10.1023/A:1004753926277.
[168] Walkley and Provis. 2019. Solid-state nuclear magnetic resonance spectroscopy of cements. *Materials Today Advances* 1, 100007. https://doi.org/10.1016/j.mtadv.2019.100007.
[169] Granizo, Palomo, and Fernandez-Jiménez. 2014. Effect of temperature and alkaline concentration on metakaolin leaching kinetics. *Ceramics International* 40, 7, 8975–8985. https://doi.org/10.1016/j.ceramint.2014.02.071.
[170] Schmid and Plank. 2021. Interaction of individual meta clays with polycarboxylate (PCE) superplasticizers in cement investigated via dispersion, zeta potential and sorption measurements. *undefined. https://doi.org/*10.1016/j.clay.2021.106092.
[171] Sposito, Beuntner, and Thienel. 2020. Characteristics of components in calcined clays and their influence on the efficiency of superplasticizers. *Cement and Concrete Composites* 110, 103594. https://doi.org/10.1016/j.cemconcomp.2020.103594.

[172] Li, Lei, and Plank. 2022. Impact of metakaolin content and fineness on the behavior of calcined clay blended cements admixed with HPEG PCE superplasticizer. *Cement and Concrete Composites* 133, 104654. https://doi.org/10.1016/j.cemconcomp.2022.104654.
[173] Maier et al. 2022. Particle characteristics of calcined clays and limestone and their impact on early hydration and sulfate demand of blended cement. *Cement and Concrete Research* 154, 106736. https://doi.org/10.1016/j.cemconres.2022.106736.
[174] Li et al. 2021. Effectiveness of PCE superplasticizers in calcined clay blended cements. *Cement and Concrete Research* 141, 106334. https://doi.org/10.1016/j.cemconres.2020.106334.
[175] Maier et al. 2021. Hydration of cubic tricalcium aluminate in the presence of calcined clays. *J. Am. Ceram. Soc.* 104, 7, 3619–3631. https://doi.org/10.1111/jace.17745.
[176] Quennoz and Scrivener. 2013. Interactions between alite and C3A-gypsum hydrations in model cements. *Cement and Concrete Research* 44, 46–54. https://doi.org/10.1016/j.cemconres.2012.10.018.
[177] Mota, Matschei, and Scrivener. 2015. The influence of sodium salts and gypsum on alite hydration. *Cement and Concrete Research* 75, 53–65. https://doi.org/10.1016/j.cemconres.2015.04.015.
[178] Zunino and Scrivener. 2020. Factors influencing the sulfate balance in pure phase C3S/C3A systems. *Cement and Concrete Research* 133, 106085. https://doi.org/10.1016/j.cemconres.2020.106085.
[179] Zunino and Scrivener. 2019. The influence of the filler effect on the sulfate requirement of blended cements. *Cement and Concrete Research* 126, 105918. https://doi.org/10.1016/j.cemconres.2019.105918.
[180] Hajimohammadi and van Deventer. 2016. Dissolution behaviour of source materials for synthesis of geopolymer binders: A kinetic approach. *International Journal of Mineral Processing* 153, 80–86. https://doi.org/10.1016/j.minpro.2016.05.014.
[181] Panagiotopoulou et al. 2007. Dissolution of aluminosilicate minerals and by-products in alkaline media. *J Mater Sci* 42, 9, 2967–2973. https://doi.org/10.1007/s10853-006-0531-8.
[182] Weng and Sagoe-Crentsil. 2007. Dissolution processes, hydrolysis and condensation reactions during geopolymer synthesis: Part I—Low Si/Al ratio systems. *J Mater Sci* 42, 9, 2997–3006. https://doi.org/10.1007/s10853-006-0820-2.
[183] Granizo et al. 2002. Alkaline Activation of Metakaolin: Effect of Calcium Hydroxide in the Products of Reaction. *Journal of the American Ceramic Society* 85, 1, 225–231. https://doi.org/10.1111/j.1151-2916.2002.tb00070.x.
[184] Scherb et al. 2020. Reactivity of Metakaolin in Alkaline Environment: Correlation of Results from Dissolution Experiments with XRD Quantifications. *Materials (Basel, Switzerland)* 13, 10. https://doi.org/10.3390/ma13102214.
[185] Silva, Sagoe-Crenstil, and Sirivivatnanon. 2007. Kinetics of geopolymerization: Role of Al2O3 and SiO2. *Cement and Concrete Research* 37, 4, 512–518. https://doi.org/10.1016/j.cemconres.2007.01.003.
[186] Caullet and Guth. 1989. Observed and Calculated Silicate and Aluminosilicate Oligomer Concentrations in Alkaline Aqueous Solutions. In *Zeolite synthesis*. *Developed from a symposium sponsored by the Division of Colloid and Surface Chemistry at the 196th national meeting of the American Chemical Society, Los Angeles, California, September 25 - 30, 1988*, M. L. Occelli, Ed. ACS Symposium Series 398. American Chemical Society, Washington, DC, 83–97. https://doi.org/10.1021/bk-1989-0398.ch006.
[187] Weng et al. 2005. Effects of aluminates on the formation of geopolymers. *Materials Science and Engineering: B* 117, 2, 163–168. https://doi.org/10.1016/j.mseb.2004.11.008.
[188] Siline and Mehsas. 2022. Effect of increasing the Blaine fineness of Metakaolin on its chemical reactivity. *Journal of Building Engineering* 56, 104778. https://doi.org/10.1016/j.jobe.2022.104778.
[189] He, Makovicky, and Osback. 1994. Thermal stability and pozzolanic activity of calcined kaolin. *Applied Clay Science* 9, 3, 165–187. https://doi.org/10.1016/0169-1317(94)90018-3.

[190] Oelkers, Schott, and Devidal. 1994. The effect of aluminum, pH, and chemical affinity on the rates of aluminosilicate dissolution reactions. *Geochimica et Cosmochimica Acta* 58, 9, 2011–2024. https://doi.org/10.1016/0016-7037(94)90281-X.
[191] Hajimohammadi, Provis, and van Deventer. 2010. Effect of Alumina Release Rate on the Mechanism of Geopolymer Gel Formation. *Chem. Mater.* 22, 18, 5199–5208. https://doi.org/10.1021/cm101151n.
[192] Love, Richardson, and Brough. 2007. Composition and structure of C–S–H in white Portland cement–20% metakaolin pastes hydrated at 25 °C. *Cement and Concrete Research* 37, 2, 109–117. https://doi.org/10.1016/j.cemconres.2006.11.012.
[193] Lagier and Kurtis. 2007. Influence of Portland cement composition on early age reactions with metakaolin. *Cement and Concrete Research* 37, 10, 1411–1417. https://doi.org/10.1016/j.cemconres.2007.07.002.
[194] Sun and Vollpracht. 2018. Isothermal calorimetry and in-situ XRD study of the NaOH activated fly ash, metakaolin and slag. *Cement and Concrete Research* 103, 110–122. https://doi.org/10.1016/j.cemconres.2017.10.004.
[195] Xu and van Deventer. 2000. The geopolymerisation of alumino-silicate minerals. *International Journal of Mineral Processing* 59, 3, 247–266. https://doi.org/10.1016/S0301-7516(99)00074-5.
[196] 2021. CENTRAL EUROPEAN SYMPOSIUM ON THERMOPHYSICS 2021 (CEST 2021). *AIP Conference Proceedings*. AIP Publishing.
[197] Alonso and Palomo. 2001. Calorimetric study of alkaline activation of calcium hydroxide±metakaolin solid mixtures. *Cement and Concrete Research* 31, 25–30. https://doi.org/10.1016/S0008-8846(00)00435-X.
[198] Ambroise, Maximilien, and Pera. 1994. Properties of Metakaolin blended cements. *Advanced Cement Based Materials* 1, 4, 161–168. https://doi.org/10.1016/1065-7355(94)90007-8.
[199] Zhao and Khoshnazar. 2020. Microstructure of cement paste incorporating high volume of low-grade metakaolin. *Cement and Concrete Composites* 106, 103453. https://doi.org/10.1016/j.cemconcomp.2019.103453.
[200] Richardson and Groves. 1993. Microstructure and microanalysis of hardened ordinary Portland cement pastes. *JOURNAL OF MATERIALS SCIENCE* 28, 1, 265–277. https://doi.org/10.1007/BF00349061.
[201] Chatterji. 1980. CaO/SiO2 mole ratio of calcium silicate hydrate in fully hydrated tricalcium silicate paste. *Cement and Concrete Research* 10, 6, 783–787. https://doi.org/10.1016/0008-8846(80)90006-X.
[202] Richardson. 2000. The nature of the hydration products in hardened cement pastes. *Cement and Concrete Composites* 22, 2, 97–113. https://doi.org/10.1016/S0958-9465(99)00036-0.
[203] Schmidt-Döhl et al. 2022. Quantitative analysis of the strength generating C-S-H-phase in concrete by IR-spectroscopy. *APP* 33, 539–545. https://doi.org/10.14311/APP.2022.33.0539.
[204] Dousti, Beaudoin, and Shekarchi. 2017. Chloride binding in hydrated MK, SF and natural zeolite-lime mixtures. *Construction and Building Materials* 154, 1035–1047. https://doi.org/10.1016/j.conbuildmat.2017.08.034.
[205] Zibara et al. 2008. Influence of the C/S and C/A ratios of hydration products on the chloride ion binding capacity of lime-SF and lime-MK mixtures. *Cement and Concrete Research* 38, 3, 422–426. https://doi.org/10.1016/j.cemconres.2007.08.024.
[206] Saikia, Kato, and Kojima. 2006. Thermogravimetric investigation on the chloride binding behaviour of MK–lime paste. *Thermochimica Acta* 444, 1, 16–25. https://doi.org/10.1016/j.tca.2006.02.012.
[207] Moropoulou, Bakolas, and Aggelakopoulou. 2004. Evaluation of pozzolanic activity of natural and artificial pozzolans by thermal analysis. *Thermochimica Acta* 420, 1-2, 135–140. https://doi.org/10.1016/j.tca.2003.11.059.
[208] Midgley and Bhaskara Rao. 1978. Formation of stratlingite, 2CaO.SiO2.Al2O3.8H2O, in relation to the hydration of high alumina cement. *Cement and Concrete Research* 8, 2, 169–172. https://doi.org/10.1016/0008-8846(78)90005-4.

[209] Martínez-Ramírez and Frias. 2011. Micro-Raman study of stable and metastable phases in metakaolin/Ca(OH)2 system cured at 60°C. *Applied Clay Science* 51, 3, 283–286. https://doi.org/10.1016/j.clay.2010.12.001.
[210] Frías et al. 2020. Mineral phases in metakaolin-portlandite pastes cured 15 years at 60 °C. New data for scientific advancement. *Applied Clay Science* 184, 105368. https://doi.org/10.1016/j.clay.2019.105368.
[211] Frías et al. 2022. New scientific evidence of the effect of high temperatures and long curing times on MK-blended cement paste mineralogy. *Cement and Concrete Research* 152, 106657. https://doi.org/10.1016/j.cemconres.2021.106657.
[212] Morsy. 2005. Effect of temperature on hydration kinetics and stability of hydration phases of metakaolin-lime sludge-silica fume system. *Ceramics − Silikáty* 49, 225–229.
[213] Okoronkwo and Glasser. 2016. Stability of strätlingite in the CASH system. *Mater Struct* 49, 10, 4305–4318. https://doi.org/10.1617/s11527-015-0789-x.
[214] Dilnesa et al. 2014. Synthesis and characterization of hydrogarnet Ca3(AlxFe1−x)2(SiO4)y(OH)4(3−y). *Cement and Concrete Research* 59, 96–111. https://doi.org/10.1016/j.cemconres.2014.02.001.
[215] Paul and Glasser. 2000. Impact of prolonged warm (85°C) moist cure on Portland cement paste. *Cement and Concrete Research* 30, 12, 1869–1877. https://doi.org/10.1016/S0008-8846(00)00286-6.
[216] Passaglia and Rinaldi. 1984. Katoite, a new member of the Ca3Al2(SiO4)3-Ca3Al2(OH)12 series and a new nomenclature for the hydrogrossular group of minerals. *bulmi* 107, 5, 605–618. https://doi.org/10.3406/bulmi.1984.7804.
[217] Bakolas and Aggelakopoulou. 2019. Pozzolanic activity of natural pozzolan–lime pastes and physicomechanical characteristics. *J Therm Anal Calorim* 135, 6, 2953–2961. https://doi.org/10.1007/s10973-018-7612-1.
[218] Antoni et al. 2012. Cement substitution by a combination of metakaolin and limestone. *Cement and Concrete Research* 42, 12, 1579–1589. https://doi.org/10.1016/j.cemconres.2012.09.006.
[219] Frankeová and Slížková. 2016. Determination of the pozzolanic activity of mortar's components by thermal analysis. *J Therm Anal Calorim* 125, 3, 1115–1123. https://doi.org/10.1007/s10973-016-5360-7.
[220] Ninov et al. 2011. On the kinetics of pozzolanic reaction in metakaolin–lime–water system. *J Therm Anal Calorim* 105, 1, 245–250. https://doi.org/10.1007/s10973-011-1419-7.
[221] Davidovits, Pélegris, and Davidovits. 2019. Standardized Method in Testing Commercial Metakaolins for Geopolymer Formulations. https://doi.org/10.13140/RG.2.2.18109.10727/1.
[222] Skocek et al. 2017. Predictive modelling of hydration and mechanical performance of low Ca composite cements: Possibilities and limitations from industrial perspective. *Cement and Concrete Research* 100, 68–83. https://doi.org/10.1016/j.cemconres.2017.05.020.
[223] Berodier and Scrivener. 2015. Evolution of pore structure in blended systems. *Cement and Concrete Research* 73, 25–35. https://doi.org/10.1016/j.cemconres.2015.02.025.
[224] Palou et al. 2018. The effect of metakaolin upon the formation of ettringite in metakaolin–lime–gypsum ternary systems. *J Therm Anal Calorim* 133, 1, 77–86. https://doi.org/10.1007/s10973-017-6885-0.
[225] Pera and Amrouz. 1998. Development of Highly Reactive Metakaolin from Paper Sludge. *Advanced Cement Based Materials* 7, 2, 49–56. https://doi.org/10.1016/S1065-7355(97)00016-3.
[226] Pera and Amrouz. 1998. Development of Highly Reactive Metakaolin from Paper Sludge. *Advanced Cement Based Materials* 7, 2, 49–56. https://doi.org/10.1016/S1065-7355(97)00016-3.
[227] Matschei, Lothenbach, and Glasser. 2007. The role of calcium carbonate in cement hydration. *Cement and Concrete Research* 37, 4, 551–558. https://doi.org/10.1016/j.cemconres.2006.10.013.

[228] Damidot et al. 1994. Thermodynamic investigation of the CaO-Al2O3-CaCO3-H2O closed system at 25°C and the influence of Na2O. *Cement and Concrete Research* 24, 3, 563–572. https://doi.org/10.1016/0008-8846(94)90145-7.
[229] Georget et al. 2022. Stability of hemicarbonate under cement paste-like conditions. *Cement and Concrete Research* 153, 106692. https://doi.org/10.1016/j.cemconres.2021.106692.
[230] Cardoso, Gameiro, Silva, Faria, Vieira, Veiga, and Velosa. 2013. Influence of curing conditions in air lime-metakaolin blended mortars – A mineralogical and mechanical study, Glasgow.
[231] Matschei, Lothenbach, and Glasser. 2007. Thermodynamic properties of Portland cement hydrates in the system CaO–Al2O3–SiO2–CaSO4–CaCO3–H2O. *Cement and Concrete Research* 37, 10, 1379–1410. https://doi.org/10.1016/j.cemconres.2007.06.002.
[232] Damidot and Glasser. 1992. Thermodynamic investigation of the CaO-Al2O3-CaSO4-H2O system at 50°C and 85°C. *Cement and Concrete Research* 22, 6, 1179–1191. https://doi.org/10.1016/0008-8846(92)90047-Y.
[233] Lothenbach et al. 2019. Cemdata18: A chemical thermodynamic database for hydrated Portland cements and alkali-activated materials. *Cement and Concrete Research* 115, 472–506. https://doi.org/10.1016/j.cemconres.2018.04.018.
[234] Perkins and Palmer. 1999. Solubility of ettringite (Ca6[Al(OH)6]2(SO4)3 z 26H2O) at 5–75°C. *Geochimica et Cosmochimica Acta* 63, 1969–1980. https://doi.org/10.1016/S0883-2927(99)00109-2.
[235] Lothenbach and Winnefeld. 2006. Thermodynamic modelling of the hydration of Portland cement. *Cement and Concrete Research* 36, 2, 209–226. https://doi.org/10.1016/j.cemconres.2005.03.001.
[236] Lothenbach et al. 2008. Thermodynamic modelling of the effect of temperature on the hydration and porosity of Portland cement. *Cement and Concrete Research* 38, 1, 1–18. https://doi.org/10.1016/j.cemconres.2007.08.017.
[237] Skibsted and Snellings. 2019. Reactivity of supplementary cementitious materials (SCMs) in cement blends. *Cement and Concrete Research* 124, 105799. https://doi.org/10.1016/j.cemconres.2019.105799.
[238] Gong et al. 2021. Density functional modeling and total scattering analysis of the atomic structure of a quaternary CaO−MgO−Al2O3−SiO2 (CMAS) glass: Uncovering the local environment of calcium and magnesium. *Phys. Rev. Materials* 5, 1. https://doi.org/10.1103/PhysRevMaterials.5.015603.
[239] Gong and White. 2021. Predicting CaO-(MgO)-Al2O3-SiO2 glass reactivity in alkaline environments from force field molecular dynamics simulations. *Cement and Concrete Research* 150, 106588. https://doi.org/10.1016/j.cemconres.2021.106588.
[240] Li et al. 2018. Reactivity tests for supplementary cementitious materials: RILEM TC 267-TRM phase 1. *Mater Struct* 51, 6. https://doi.org/10.1617/s11527-018-1269-x.
[241] Parashar et al. 2022. Report of RILEM TC 267—TRM: Improvement and robustness study of lime mortar strength test for assessing reactivity of SCMs. *Mater Struct* 55, 3. https://doi.org/10.1617/s11527-022-01911-1.
[242] Evju. 2003. Initial hydration of cementitious systems using a simple isothermal calorimeter and dynamic correction. *J Therm Anal Calorim* 71, 3, 829–840. https://doi.org/10.1023/A:1023374125778.
[243] Wadsö. 2010. Operational issues in isothermal calorimetry. *Cement and Concrete Research* 40, 7, 1129–1137. https://doi.org/10.1016/j.cemconres.2010.03.017.
[244] Aramburo et al. 2019. Calcined clays for low carbon cement: Rheological behaviour in fresh Portland cement pastes. *Materials Letters* 239, 24–28. https://doi.org/10.1016/j.matlet.2018.12.050.
[245] Pott et al. 2023. Characterization data of reference materials used for phase II of the priority program DFG SPP 2005 "Opus Fluidum Futurum - Rheology of reactive, multiscale, multiphase construction materials". *Data in brief* 47, 108902. https://doi.org/10.1016/j.dib.2023.108902.
[246] Weise. 2020. Über das Potenzial von calciniertem Ton in zementgebundenen Systemen. Springer Fachmedien Wiesbaden, Wiesbaden. https://doi.org/10.1007/978-3-658-28791-7.

[247] Scrivener, Snellings, and Lothenbach, Eds. 2016. A practical guide to microstructural analysis of cementitious materials. *A Spon Press Book*. CRC Press Taylor & Francis Group, Boca Raton, London, New York.
[248] Statista. 2021. Worldwide tall building completions in 2019, by structural material. https://www.statista.com/statistics/319931/structural-materials-of-tall-buildings-worldwide/. Accessed 3 May 2021.
[249] CEMBUREAU. 2019. 2019 Activity Report. https://cembureau.eu/media/clkdda45/activity-report-2019.pdf. Accessed 19 December 2023.
[250] VDZ - Verein Deutscher Zementwerke e.V. 2017. Umwelt-Produktdeklaration – Zement.
[251] Schneider et al. 2011. Sustainable cement production - present and future. *Cement and Concrete Research* 41, 642–650. https://doi.org/10.1016/j.cemconres.2011.03.019.
[252] bbs - Bundesverband Baustoffe – Steine und Erden e.V. 2016. Die Nachfrage nach Primär- und Sekundärrohstoffen der Steine-und-Erden-Industrie bis 2035 in Deutschland. https://www.baustoffindustrie.de/fileadmin/user_upload/bbs/Dateien/2016-04-07_BBS_Rohstoffstudie.pdf. Accessed 19 December 2023.
[253] Li et al. 2018. Reactivity tests for supplementary cementitious materials: RILEM TC 267-TRM phase 1. *Materials and Structures,* 51, 151. https://doi.org/10.1617/s11527-018-1269-x.
[254] Blotevogel et al. 2020. Ability of the R3 test to evaluate differences in early age reactivity of 16 industrial ground granulated blast furnace slags (GGBS). *Cement and Concrete Research* 130, 105998. https://doi.org/10.1016/j.cemconres.2020.105998.
[255] Suraneni and Weiss. 2017. Examining the pozzolanicity of supplementary cementitious materials using isothermal calorimetry and thermogravimetric analysis. *Cement and Concrete Composites* 83, 273–278. https://doi.org/10.1016/j.cemconcomp.2017.07.009.
[256] Snellings, Kamyab, Joseph, Nielsen, Loots, and van den Abeele. 2019. Pozzolanic reactivity of size-classified siliceous fly ashes. *2nd International Conference of Sustainable Building Materials*, Eindhoven.
[257] Snellings and Kamyab. 2019. Reactivity of non-ferrous metallurgical slags and sludges measured by the RILEM R³ Test. *6th International Slag Valorisation Symposium*, Mechelen.
[258] Snellings et al. 2018. Report of TC 238-SCM: hydration stoppage methods for phase assemblage studies of blended cements—results of a round robin test. *Mater Struct* 51, 4. https://doi.org/10.1617/s11527-018-1237-5.
[259] Collier et al. 2008. The influence of water removal techniques on the composition and microstructure of hardened cement pastes. *Cement and Concrete Research* 38, 6, 737–744. https://doi.org/10.1016/j.cemconres.2008.02.012.
[260] Zhang and Scherer. 2011. Comparison of methods for arresting hydration of cement. *Cement and Concrete Research* 41, 10, 1024–1036. https://doi.org/10.1016/j.cemconres.2011.06.003.
[261] Röser. 2018. Über die Reaktivität von Betonzusatzstoffen. Ein versuchsbasiertes Hydratationsmodell, *Technische Universität Darmstadt*.
[262] Justnes et al. 2020. Evaluation of Ceramic Waste from Goa as SCM. In *Calcined Clays for Sustainable Concrete*. *Proceedings of the 3rd International Conference on Calcined Clays for Sustainable Concrete*. RILEM Bookseries. Springer, 67-73. https://doi.org/10.1007/978-981-15-2806-4_8.
[263] Sivakumar et al. 2021. Reactivity Assessment of Modified Ferro Silicate Slag by R3 Method. *Applied Sciences* 11, 1, 366. https://doi.org/10.3390/app11010366.
[264] Snellings et al. 2018. RILEM TC-238 SCM recommendation on hydration stoppage by solvent exchange for the study of hydrate assemblages. *Mater Struct* 51, 6. https://doi.org/10.1617/s11527-018-1298-5.
[265] Elkem Materials Inc. 2018. Safety Data Sheet: Elkem Microsilica. https://www.elkem.com/globalassets/silicon-materials/construction/construction-safety/microsilicasafetyna.pdf. Accessed 31 August 2021.
[266] Thienel and Beuntner. 2013. Ökologisch und technisch verbesserte Betone durch den Einsatz alternativer Zusatzstoffe. *Nachhaltigkeit und Innovation, Universität der Bundeswehr München*, München.

[267] Beuntner. 2017. Zur Eignung und Wirkungsweise calcinierter Tone als reaktive Bindemittelkomponente im Zement. *Dissertation, Universität der Bundeswehr München*.
[268] Weise. 2018. Die Reaktivität von Hüttensand als Betonzusatzstoff. Springer Fachmedien Wiesbaden, Wiesbaden. https://doi.org/10.1007/978-3-658-20492-1.
[269] Kim and Olek. 2012. Effects of Sample Preparation and Interpretation of Thermogravimetric Curves on Calcium Hydroxide in Hydrated Pastes and Mortars. *Transportation Research Record* 2290, 1, 10–18. https://doi.org/10.3141/2290-02.
[270] Beuntner and Thienel. 2016. Solubility and kinetics of calcined clay: study of interaction by pore solution. *2nd International Conference on the Chemistry of Construction Materials*, München.
[271] Lothenbach, Durdziński, and Weerdt. 2016. Thermogravimetric analysis. In *A practical guide to microstructural analysis of cementitious materials*, K. Scrivener, R. Snellings and B. Lothenbach, Eds. A Spon Press Book. CRC Press Taylor & Francis Group, Boca Raton, London, New York, 177–211.
[272] Carević et al. 2021. Effect of Wood Biomass Ash Storage on the Properties of Cement Composites. *Materials (Basel, Switzerland)* 14, 7. https://doi.org/10.3390/ma14071632.
[273] Sedić et al. 2020. Carbonation of Portland-Zeolite and geopolymer well-cement composites under geologic CO2 sequestration conditions. *Cement and Concrete Composites* 111, 103615. https://doi.org/10.1016/j.cemconcomp.2020.103615.
[274] Belie, Kratky, and van Vlierberghe. 2010. Influence of pozzolans and slag on the microstructure of partially carbonated cement paste by means of water vapour and nitrogen sorption experiments and BET calculations. *Cement and Concrete Research* 40, 12, 1723–1733. https://doi.org/10.1016/j.cemconres.2010.08.014.
[275] Alarcon-Ruiz et al. 2005. The use of thermal analysis in assessing the effect of temperature on a cement paste. *Cement and Concrete Research* 35, 3, 609–613. https://doi.org/10.1016/j.cemconres.2004.06.015.
[276] Pane and Hansen. 2005. Investigation of blended cement hydration by isothermal calorimetry and thermal analysis. *Cement and Concrete Research* 35, 6, 1155–1164. https://doi.org/10.1016/j.cemconres.2004.10.027.
[277] Gruyaert, Robeyst, and Belie. 2010. Study of the hydration of Portland cement blended with blast-furnace slag by calorimetry and thermogravimetry. *J Therm Anal Calorim* 102, 3, 941–951. https://doi.org/10.1007/s10973-010-0841-6.
[278] Taylor and Turner. 1987. Reactions of tricalcium silicate paste with organic liquids. *Cement and Concrete Research* 17, 4, 613–623. https://doi.org/10.1016/0008-8846(87)90134-7.
[279] Mitchell and Margeson. 2006. The effects of solvents on C–S–H as determined by thermal analysis. *J Therm Anal Calorim* 86, 3, 591–594. https://doi.org/10.1007/s10973-006-7712-1.
[280] Zhang and Scherer. 2017. Supercritical drying of cementitious materials. *Cement and Concrete Research* 99, 137–154. https://doi.org/10.1016/j.cemconres.2017.05.005.
[281] Sagoe-Crentsil and Weng. 2007. Dissolution processes, hydrolysis and condensation reactions during geopolymer synthesis: Part II. High Si/Al ratio systems. *J Mater Sci* 42, 9, 3007–3014. https://doi.org/10.1007/s10853-006-0818-9.
[282] Newman. 1957. A thermochemical study of the reaction of calcium hydroxide, silica gel, and water. *J. RES. NATL. BUR. STAN.* 59, 3, 187. https://doi.org/10.6028/jres.059.018.
[283] DIN EN ISO 11885:2009-09, Wasserbeschaffenheit_- Bestimmung von ausgewählten Elementen durch induktiv gekoppelte Plasma-Atom-Emissionsspektrometrie (ICP-OES) (ISO_11885:2007); Deutsche Fassung EN_ISO_11885:2009. Beuth Verlag GmbH, Berlin.
[284] Runčevski et al. 2012. Crystal structures of calcium hemicarboaluminate and carbonated calcium hemicarboaluminate from synchrotron powder diffraction data. *Acta crystallographica. Section B, Structural science* 68, Pt 5, 493–500. https://doi.org/10.1107/S010876811203042X.
[285] Santacruz et al. Structure of stratlingite and effect of hydration methodology on microstructure. https://doi.org/10.1680/adcr.14.00104.
[286] Baquerizo et al. 2015. Hydration states of AFm cement phases. *Cement and Concrete Research* 73, 143–157. https://doi.org/10.1016/j.cemconres.2015.02.011.

[287] Jing et al. 2019. Effects of graphene oxide on the hydration behavior of ye'elimite. *J Mater Sci* 54, 19, 12582–12591. https://doi.org/10.1007/s10853-019-03801-4.
[288] Danner, Sletnes, and Justnes. 2020. Alkali-reduced Bauxite Residue as Novel SCM. *Nordic Concrete Research* 63, 2, 1–20. https://doi.org/10.2478/ncr-2020-0015.
[289] Urs Mueller, Monica Lundgren, and Arezou Babaahmadi. 2017. Hydration of concrete binders blended with ground granulated blast furnace slag, fly ash and metakaolin. https://doi.org/10.13140/RG.2.2.11577.08809.
[290] Ke, Bernal, and Provis. 2017. Uptake of chloride and carbonate by Mg-Al and Ca-Al layered double hydroxides in simulated pore solutions of alkali-activated slag cement. *Cement and Concrete Research* 100, 1–13. https://doi.org/10.1016/j.cemconres.2017.05.015.
[291] Weise, Ukrainczyk, and Koenders. 2024. Pozzolanic Metakaolin Reactions: Stoichiometric and Kinetic Modeling. *Materials & Design* 239, 112747. https://doi.org/10.1016/j.matdes.2024.112747.
[292] Antao, Duane, and Hassan. 2002. DTA, TG, and XRD Studies of Sturmanite and Ettringite. *The Canadian Mineralogist* 40, 5, 1403–1409. https://doi.org/10.2113/gscanmin.40.5.1403.
[293] Shim et al. 2012. Arsenic removal from artificial arsenic water using CaAl-monosulfate and CaAl-ettringite. *Journal of Korean Society of Water and Wastewater* 26, 1, 141–148. https://doi.org/10.11001/jksww.2012.26.1.141.
[294] Fuchida et al. 2020. Experimental Investigation of Boron Removal Mechanism from Wastewater by Calcined Ettringite. *Water Air Soil Pollut* 231, 7. https://doi.org/10.1007/s11270-020-04713-9.
[295] Zhang et al. 2018. Nanostructural characterization of Al(OH) 3 formed during the hydration of calcium sulfoaluminate cement. *J Am Ceram Soc* 101, 9, 4262–4274. https://doi.org/10.1111/jace.15536.
[296] Li et al. 2023. The Early Age Hydration Products and Mechanical Properties of Cement Paste with Steel Slag Powder as Additive under Steam Curing Conditions. *Buildings* 13, 9, 2192. https://doi.org/10.3390/buildings13092192.
[297] Bergold, Goetz-Neunhoeffer, and Neubauer. 2013. Quantitative analysis of C–S–H in hydrating alite pastes by in-situ XRD. *Cement and Concrete Research* 53, 119–126. https://doi.org/10.1016/j.cemconres.2013.06.001.
[298] Georget, Wilson, and Scrivener. 2021. edxia: Microstructure characterisation from quantified SEM-EDS hypermaps. *Cement and Concrete Research* 141, 106327. https://doi.org/10.1016/j.cemconres.2020.106327.
[299] Pardal et al. 2012. 27Al and 29Si solid-state NMR characterization of calcium-aluminosilicate-hydrate. *Inorganic chemistry* 51, 3, 1827–1836. https://doi.org/10.1021/ic202124x.
[300] Okoronkwo and Glasser. 2016. Compatibility of hydrogarnet, Ca3Al2(SiO4)x(OH)4(3−x), with sulfate and carbonate-bearing cement phases: 5–85 °C. *Cement and Concrete Research* 83, 86–96. https://doi.org/10.1016/j.cemconres.2016.01.013.
[301] Kyritsis, Meller, and Hall. 2009. Chemistry and Morphology of Hydrogarnets Formed in Cement-Based CASH Hydroceramics Cured at 200° to 350°C. *J Am Ceram Soc* 92, 5, 1105–1111. https://doi.org/10.1111/j.1551-2916.2009.02958.x.
[302] Hong and Glasser. 2002. Alkali sorption by C-S-H and C-A-S-H gels. *Cement and Concrete Research* 32, 7, 1101–1111. https://doi.org/10.1016/S0008-8846(02)00753-6.
[303] Miron et al. 2022. Extensions of CASH+ thermodynamic solid solution model for the uptake of alkali metals and alkaline earth metals in C-S-H. *Cement and Concrete Research* 152, 106667. https://doi.org/10.1016/j.cemconres.2021.106667.
[304] Myers et al. 2015. Composition-solubility-structure relationships in calcium (alkali) aluminosilicate hydrate (C-(N,K-)A-S-H). *Dalton transactions (Cambridge, England : 2003)* 44, 30, 13530–13544. https://doi.org/10.1039/C5DT01124H.
[305] Moya et al. 2024. Significance of the formation of pentahedral aluminum in the reactivity of calcined kaolin/metakaolin and its applications. *Ceramics International* 50, 1, 1329–1340. https://doi.org/10.1016/j.ceramint.2023.10.304.

[306] Da Cruz Teixeira et al. 2024. Study of the transition zone of concretes prepared with metakaolin using sem/eds-associated nanoindentation technique. *Construction and Building Materials* 412, 134717. https://doi.org/10.1016/j.conbuildmat.2023.134717.
[307] Hanein et al. 2023. Thermodynamics of calcined clays used in cementitious binders: origin to service life considerations. *J. Mater. Chem. A* 11, 34, 17920–17937. https://doi.org/10.1039/D3TA01896B.
[308] Deschner et al. 2013. Effect of temperature on the hydration of Portland cement blended with siliceous fly ash. *Cement and Concrete Research* 52, 169–181. https://doi.org/10.1016/j.cemconres.2013.07.006.
[309] Girão et al. 2010. Composition, morphology and nanostructure of C–S–H in 70% white Portland cement–30% fly ash blends hydrated at 55 °C. *Cement and Concrete Research* 40, 9, 1350–1359. https://doi.org/10.1016/j.cemconres.2010.03.012.
[310] Rossen, Lothenbach, and Scrivener. 2015. Composition of C–S–H in pastes with increasing levels of silica fume addition. *Cement and Concrete Research* 75, 14–22. https://doi.org/10.1016/j.cemconres.2015.04.016.
[311] Bernal et al. 2014. MgO content of slag controls phase evolution and structural changes induced by accelerated carbonation in alkali-activated binders. *Cement and Concrete Research* 57, 33–43. https://doi.org/10.1016/j.cemconres.2013.12.003.
[312] Ben Haha et al. 2012. Influence of slag chemistry on the hydration of alkali-activated blast-furnace slag — Part II: Effect of Al2O3. *Cement and Concrete Research* 42, 1, 74–83. https://doi.org/10.1016/j.cemconres.2011.08.005.
[313] Kulik, Miron, and Lothenbach. 2022. A structurally-consistent CASH+ sublattice solid solution model for fully hydrated C-S-H phases: Thermodynamic basis, methods, and Ca-Si-H2O core sub-model. *Cement and Concrete Research* 151, 106585. https://doi.org/10.1016/j.cemconres.2021.106585.
[314] Roosz et al. 2018. Thermodynamic properties of C-S-H, C-A-S-H and M-S-H phases: Results from direct measurements and predictive modelling. *Applied Geochemistry* 92, 140–156. https://doi.org/10.1016/j.apgeochem.2018.03.004.
[315] Kassa, Shibeshi, and Tizazu. 2022. Kinetic analysis of dehydroxylation of Ethiopian kaolinite during calcination. *J Therm Anal Calorim* 147, 22, 12837–12853. https://doi.org/10.1007/s10973-022-11452-y.
[316] Ligny and Navrotsky. 1999. Energetics of kaolin polymorphs. *American Mineralogist* 84, 4, 506–516. https://doi.org/10.2138/am-1999-0404.
[317] Ukrainczyk. 2010. Kinetic modeling of calcium aluminate cement hydration. *Chemical Engineering Science* 65, 20, 5605–5614. https://doi.org/10.1016/j.ces.2010.08.012.
[318] Xie and Qian. 2023. A novel numerical method for predicting the hydration heat of concrete based on thermodynamic model and finite element analysis. *Materials & Design* 226, 111675. https://doi.org/10.1016/j.matdes.2023.111675.
[319] Avet, Boehm-Courjault, and Scrivener. 2019. Investigation of C-A-S-H composition, morphology and density in Limestone Calcined Clay Cement (LC3). *Cement and Concrete Research* 115, 70–79. https://doi.org/10.1016/j.cemconres.2018.10.011.
[320] Niemand and Lorsee. Specification CN87 Calcium Hydroxide. https://www.carlroth.com/de/de/calciumsalze-ca/calciumhydroxid/p/cn87.1. Accessed 1 November 2023.
[321] Balonis and Glasser. 2009. The density of cement phases. *Cement and Concrete Research* 39, 9, 733–739. https://doi.org/10.1016/j.cemconres.2009.06.005.
[322] TANAKA et al. 2009. Fundamental Study on Density of C-S-H. *Cement Science and Concrete Technology* 63, 1, 70–76. https://doi.org/10.14250/cement.63.70.
[323] Maruyama et al. 2016. Action Mechanisms of Shrinkage Reducing Admixture in Hardened Cement Paste. *ACT* 14, 6, 311–323. https://doi.org/10.3151/jact.14.311.
[324] Gesoglu et al. 2015. Durability and Shrinkage Characteristics of Self-Compacting Concretes Containing Recycled Coarse and/or Fine Aggregates. *Advances in Materials Science and Engineering* 2015, 1–18. https://doi.org/10.1155/2015/278296.

[325] Sharma et al. 2020. Characterization of paste microstructure for durability properties of concrete. *Construction and Building Materials* 248, 118570. https://doi.org/10.1016/j.conbuildmat.2020.118570.
[326] Svetlana V. Samchenko and Irina V. Kozlova and Andrey V. Korshunov. Optimization of the Composition of Cement Pastes Using Combined Additives of Alumoferrites and Gypsum in Order to Increase the Durability of Concrete. https://doi.org/10.3390/buildings13020565.
[327] Lu, Sun, and YOUNG. 1993. Phase Composition of Hydrated DSP Cement Pastes. *J Am Ceram Soc* 76, 4, 1003–1007. https://doi.org/10.1111/j.1151-2916.1993.tb05326.x.
[328] Brouwers. 2004. The work of Powers and Brownyard revisited: Part 1. *Cement and Concrete Research* 34, 9, 1697–1716. https://doi.org/10.1016/j.cemconres.2004.05.031.
[329] Lothenbach and Nonat. 2015. Calcium silicate hydrates: Solid and liquid phase composition. *Cement and Concrete Research* 78, 57–70. https://doi.org/10.1016/j.cemconres.2015.03.019.
[330] Ukrainczyk. 2009. Razvoj Modela Procesa Hidratacije Cementa. *PhD thesis (in Croatian)*, Zagreb.
[331] Huang and Wang. 2024. The effect of temperature on dissolution activity of fly ash and metakaolin in alkaline conditions. *Cement and Concrete Composites* 146, 105363. https://doi.org/10.1016/j.cemconcomp.2023.105363.
[332] Kim and Moon. 2023. Experimental Study on Activation Energy and Microstructure of Nano- and Micro-Sized Pozzolanic Materials as Cementitious Composite Binder. *Buildings* 13, 12, 3085. https://doi.org/10.3390/buildings13123085.
[333] Yan et al. 2023. Kinetics of Al uptake in synthetic calcium silicate hydrate (C-S-H). *Cement and Concrete Research* 172, 107250. https://doi.org/10.1016/j.cemconres.2023.107250.
[334] Zunino and Scrivener. 2022. Microstructural developments of limestone calcined clay cement (LC3) pastes after long-term (3 years) hydration. *Cement and Concrete Research* 153, 106693. https://doi.org/10.1016/j.cemconres.2021.106693.
[335] Da Silva et al. 2015. Mass density and water content of saturated never-dried calcium silicate hydrates. *Langmuir* 31, 13, 3779–3783. https://doi.org/10.1021/la504478j.
[336] Jing et al. 2023. Hydration kinetics, microstructure and physicochemical performance of metakaolin-blended cementitious composites. *Construction and Building Materials* 408, 133756. https://doi.org/10.1016/j.conbuildmat.2023.133756.
[337] Allen, Thomas, and Jennings. 2007. Composition and density of nanoscale calcium-silicate-hydrate in cement. *Nature materials* 6, 4, 311–316. https://doi.org/10.1038/nmat1871.
[338] Gallucci, Zhang, and Scrivener. 2013. Effect of temperature on the microstructure of calcium silicate hydrate (C-S-H). *Cement and Concrete Research* 53, 185–195. https://doi.org/10.1016/j.cemconres.2013.06.008.
[339] Yan and Geng. 2024. Does nano basic building-block of C-S-H exist? – A review of direct morphological observations. *Materials & Design* 238, 112699. https://doi.org/10.1016/j.matdes.2024.112699.
[340] Li, Yang, and Li. 2023. Quantifying the microstructure and phase assemblage of alkali-activated fly ash/slag materials by EDS mapping analysis. *Materials & Design* 234, 112320. https://doi.org/10.1016/j.matdes.2023.112320.
[341] Clarivate. 2023. Document search - Web of Science. www.webofscience.com.
[342] Clarivate. 2023. Search Results - Web of Science. *AB=((metakaolin OR "calcined kaolin") AND ("calcium hydroxide" OR "lime" OR "Ca(OH)2" OR "portlandite") NOT geopolymer)*. https://www.webofscience.com/wos/woscc/summary/043d0116-cb34-4c50-82f5-377e7f037585-433fab33/relevance/9.